



Synthesis and characterisation of perfluorinated
lanthanide complexes for near-infrared
applications

Rendy Howe Choong Tan

Department of Physics
School of biological and chemical sciences
Queen Mary, University of London

Supervisors – Dr. William Gillin (Physics)
Dr. Peter Wyatt (School of biological and chemical sciences)

Thesis submitted to the University of London for the Degree of
Doctor of Philosophy

2009

Declaration

All the work contained within this thesis is my own and has not previously been submitted to satisfy any of other degree requirements at this or any other University. This thesis contains no material published or written by another person except where due reference is made in this thesis itself.

Abstract

Lanthanide (Er^{3+} , Nd^{3+} and Yb^{3+}) complexes of 1,1,1,5,5,5-hexafluoroacetylacetone (HHFA) have been deuterated to levels of 98% and increases in luminescence lifetimes of more than 150% were observed over their undeuterated analogues. From the crystal structures of erbium HFA complexes, we deduced that any hydrogen within a radius of ~ 20 Å from the erbium center will effectively quench the radiative lifetimes. The synthesis of the β -diketone, 1,1,1,5,5,5-hexafluoro-3-(pentafluorophenyl)-pentane-2,4-dione was attempted by several approaches, including perfluoroarylation of HHFA. However, this preparation was not achieved.

Four new fluorinated phosphinic acids, bis(pentafluorophenyl)phosphinic acid, bis[2,3,5,6-tetrafluoro-4(trifluoromethyl)phenyl] phosphinic acid, nonafluorobiphenyl-4-yl(pentafluorophenyl)phosphinic acid and bis(nonafluorobiphenyl-4-yl)phosphinic acid were successfully synthesized by treating phosphinamide dichloride with perfluoroaryllithium reagents, followed by acid hydrolysis and then used to form lanthanide complexes. The morphology of these lanthanide complexes were found to be rod-like with dimensions of 200 nm and below in diameter. These complexes demonstrated remarkable luminescence lifetimes and by diluting them with yttrium, we have minimized the concentration quenching effects and achieved unprecedented luminescence lifetimes. Increasing lifetimes were observed with decreasing lanthanide concentrations. In erbium, for example, more than two-fold improvement in the luminescence efficiency over the 100% erbium concentration samples was reported when the erbium concentration was at 10%. This is the first time that concentration quenching effects have been studied in organic lanthanide complexes and we have found that energy migration is the dominant process affecting the luminescence lifetimes. Our detailed studies on these organic complexes have also shown that upconversion, a phenomenon observed in doped glasses, was not present.

This thesis is dedicated to my mother, Magdalene Chan,
my uncle, Cheow Keng Chan and my wife, Jan Chiew Ping Neo



But they that wait upon the LORD shall renew their strength; they shall mount up with wings as eagles; they shall run, and not be weary; and they shall walk, and not faint. *Isaiah 40:31*

Acknowledgements

My utmost gratefulness to The Creator, for including me as part of His plans for creation.

I thank my mother Magdalene Chan, my uncle, Cheow Keng Chan and my wife, Jan Chiew Ping Neo, who have showered me with unconditional love and support these few years. Grandma, Auntie Maureen, Auntie Edalene, Uncle Andre, Uncle Ju and Auntie Selina have been exceptional and I am eternally grateful for their kindness.

I would like to express my sincere gratitude to my supervisors, Dr William Gillin from physics and Dr Peter Wyatt from chemistry. They have invested tremendous amount of time and provided excellent guidance during the course of my PhD. Their patience and time taken to read and correct this thesis are deeply appreciated.

Dr Ignacia Hernandez has provided a lot of guidance to my research and I am appreciative for his time. Special thanks are also reserved for the members of the physics department especially, Pratik Desai, Pabitra Shakya, Sijie Zhang, Jingyao Song, Dr Theo Kreouzis, Prof David Dunstan, Geoff Gannaway, Jim Murphy, George Anderson, Seema Barard, Ahmad Ghandour, Nicola Rolfe, Tyler Robb-Smith, Kate Shine and Kathy Boydon. They have made my time at Queen Mary, University of London a very memorable one. I would also like to thank Dr Ken Png and Dr Zofia Luklinska from Nanovision for helping me to obtain the microscopy images of my phosphates.

The chemistry department has been an integral part of my research life for the past three years. I am very appreciative of the friends that I have made especially, Jem Pearson, Alexandra Tsami, Hannah Wright, Farid Uddin, Jonathan Dunn, Ramla Awais, Ana Maria Blanco, Davide Carboni, Patrick Gilbert, Asma Qazi, Julie Warne, Ania Servant, Mark Penny, Krystelle Mafina, Halima Nasir Ali, Yuen-Ki Cheong, Eileen Cheng and Mohammed Al-Hashimi. Many thanks also to the store manager Alan Bradshaw and technicians Jalal Hamdan and John Hayes. I thank Dr Isaac Abrahams and Majid Motevalli for their kind assistance with crystallography data collection and Greg Coumbarides for assistance with NMR.

Last but not least, I thank my good friends; Pete Stacey, Susan Walker, Charles Dibor and Mary Rundle for just being there when I needed it most.

Table of contents

Declaration	2
Abstract	3
Dedication	4
Acknowledgements	5
Table of contents	6
List of figures	12
List of tables	21
List of schemes	24
List of charts	26
List of publications	27
Chapter 1 – Introduction	28
1.1 General introduction	28
1.2 History of optical amplifiers	30
1.3 Polymer waveguides	31
1.4 Polymer waveguide doped with Ln ³⁺ complexes	35
1.5 Optical amplification	37
1.6 Laser systems	37
1.7 Radiative and nonradiative recombination	38
1.8 Characteristics of lanthanides	39
1.9 Electronic transitions of Ln ³⁺ ions	42
1.10 Ln ³⁺ emission	44
1.11 The energy gap law	46
1.12 Excitation of Ln ³⁺ ions	47
1.12.1 <i>Direct excitation</i>	48
1.12.2 <i>Indirect excitation</i>	48
1.13 Sensitizing moieties	51
1.13.1 <i>Fluorescein derivatives</i>	51
1.13.2 <i>Complexes of d-block metals</i>	53
1.14 Design of organic ligands	55
1.15 Lifetime measurements	56
1.16 Photoluminescence	59
1.17 Outline of thesis	61
1.18 References for chapter 1	63

Chapter 2 – Results and discussion 1 : The role of high energy oscillators in luminescence quenching	70
2.1 Introduction	70
2.1.1 <i>Effects of high vibrational energy bonds on Ln³⁺ ions</i>	71
2.1.2 <i>Overview of experimental studies for chapter 2</i>	80
2.2 Preparation of Ln ³⁺ complexes	80
2.3 Determination of the deuteration levels	81
2.3.1 <i>MALDI Mass Spectroscopy</i>	82
2.3.2 <i>Determination of the deuteration levels of complexes</i>	82
2.4 Lifetime measurements	83
2.5 Crystal structure of Er ³⁺ complexes	84
2.6 Effects of coordinated H ₂ O	86
2.7 Luminescence of Er ³⁺ tetrakis HFA complexes	89
2.7.1 <i>Partially deuterated Er³⁺ samples</i>	91
2.8 Luminescence of Nd ³⁺ complexes	95
2.8.1 <i>Partially deuterated Nd³⁺ samples</i>	98
2.9 Luminescence of Yb ³⁺ complexes	102
2.9.1 <i>Partially deuterated Yb³⁺ samples</i>	103
2.10 Conclusions for chapter 2	105
2.11 References for chapter 2	107
Chapter 3 - Results and discussion 2 : Attempted preparation of fluorinated complexes	110
3.1 Introduction	110
3.1.1 <i>Outline of chapter</i>	121
3.2 Attempt to prepare Cs[Er(pentafluorobenzoate) ₄]	122
3.3 Attempted preparation of Cs[Er(3-[(4-methoxyphenyl) (pentafluorophenylsulfanyl)methyl] -1,1,1,5,5,5-hexafluoro-pentane-2,4-dione) ₄]	126
3.4 Attempted preparation of 1,1,1,5,5,5-hexafluoro-3-pentafluorophenyl-pentane-2,4-dione	128
3.4.1 <i>Grignard reaction</i>	129
3.4.2 <i>Wittig reaction</i>	134
3.4.3 <i>Reactions with catalysts</i>	137

3.5	Conclusions for chapter 3	144
3.6	References for chapter 3	145
Chapter 4 - Results and discussion 3 : Synthesis and characterization of fluorinated lanthanide complexes		148
4.1	Introduction	148
	4.1.1 <i>Fluorinated ligands</i>	149
	4.1.2 <i>Excited state absorption (ESA)</i>	153
	4.1.3 <i>Ion-ion interactions</i>	154
	4.1.4 <i>Ion-ion interactions between chemically identical rare-earth ions: Upconversion and cooperative luminescence</i>	155
	4.1.5 <i>Ion-ion interaction between chemically identical rare-earth ions: Energy migration</i>	158
	4.1.6 <i>Ion-ion interaction between chemically identical rare-earth ions: Cross relaxation</i>	159
	4.1.7 <i>Ion-ion interactions between chemically different ions</i>	159
	4.1.8 <i>Overview of experimental work discussed in this chapter</i>	162
4.2	Preparations of phosphinic acids and fluorinated Er ³⁺ , Nd ³⁺ and Yb ³⁺ complexes	163
	4.2.1 <i>Route 1: Grignard chemistry to obtaining bis(pentafluorophenyl)phosphinic acid and bis[2,3,5,6-tetrafluoro-4(trifluoromethyl)phenyl]phosphinic acid</i>	164
	4.2.2 <i>Route 2: Organolithium method to obtaining phosphinic acids</i>	167
4.3	Preparation of Ln ³⁺ complexes	172
4.4	Chemical characteristics of Ln ³⁺ complexes	174
4.5	Morphology of these Ln ³⁺ complexes	179
	4.5.1 <i>Morphology of Er³⁺ complexes</i>	180
	4.5.2 <i>Morphology of Nd³⁺ complexes</i>	181
	4.5.3 <i>Morphology of Yb³⁺ complexes</i>	182
4.6	Spectroscopic characteristics of the ligands	183
4.7	Lifetimes of Er ³⁺ , Nd ³⁺ and Yb ³⁺ samples	186
4.8	Photoluminescence studies of Er ³⁺ phosphinate complexes	187
	4.8.1 <i>Effects of diluted Er³⁺ samples</i>	193

4.9	Photoluminescence studies of Nd ³⁺ phosphinate complexes	202
	4.9.1 <i>Effects of diluted Nd³⁺ samples</i>	212
4.10	Photoluminescence studies of Yb ³⁺ phosphinate complexes	218
	4.10.1 <i>Effects of diluted Yb³⁺ samples</i>	222
4.11	Conclusions for chapter 4	227
4.12	References for chapter 4	229
Chapter 5 – Experimental procedures and characterization data		234
5.1	General procedures	234
5.2	Preparation of Cs[Er(HFA) ₄]	236
5.3	Preparation of Cs[Nd(HFA) ₄]	237
5.4	Preparation of Cs[Yb(HFA) ₄]	238
5.5	Preparation of [Er(HFA) ₃ (H ₂ O) ₂] (Ref 3)	239
5.6	Preparation of deuterated 1,1,1,5,5,5-hexafluoroacetylacetone	240
5.7	Preparation of Cs[Er(HFA- <i>d</i>) ₄]	241
5.8	Preparation of Cs[Nd(HFA- <i>d</i>) ₄]	242
5.9	Preparation of Cs[Yb(HFA- <i>d</i>) ₄]	243
5.10	Attempted preparation of Cs[Er(pentafluorobenzoate) ₄]	244
5.11	Preparation of 3-(4-methoxybenzylidene)-1,1,1,5,5,5-hexafluoropentane-2,4-dione	245
5.12	Preparation of 3-[(4-methoxyphenyl)(pentafluorophenylsulfanyl)methyl]-1,1,1,5,5,5-hexafluoro-pentane-2,4-dione	246
5.13	Attempted preparation of Cs[Er(3-[(4-methoxyphenyl)(pentafluorophenylsulfanyl)methyl]-1,1,1,5,5,5-hexafluoro-pentane-2,4-dione) ₄]	247
5.14	Preparation of 1,1,1-trifluoro-3-phenylpropan-2-one	248
5.15	Attempt to prepare 1,1,1-trifluoro-3-pentafluorophenylpropan-2-one	249
5.16	Preparation of (<i>Z</i>)-1-Phenyl-2-pyrrolidiny-3,3,3-trifluoropropene	250
5.17	Preparation of benzyl(triphenyl)phosphonium chloride	251
5.18	Preparation of (pentafluorophenylmethyl)triphenylphosphonium bromide	251
5.19	Preparation of 4-(Trifluoroacetyl)morpholine	252
5.20	Preparation of 4-[2-phenyl-1-(trifluoromethyl)-vinyl]morpholine	253

5.21	Preparation of 4-[2-(pentafluorophenyl)-1-(trifluoromethyl)vinyl]morpholine	254
5.22	Preparation of 3-phenyl-pentane-2,4-dione	255
5.23	Reaction of acetylacetone with iodopentafluorobenzene	256
5.24	Preparation of tris(pentafluorophenyl)phosphine	257
5.25	Preparation of tri(pentafluorophenyl)phosphine oxide	258
5.26	Preparation of bis(pentafluorophenyl)phosphinic acid	259
5.27	Preparation of tris(2,3,5,6-tetrafluoro-4(trifluoromethyl)phenyl)phosphine	260
5.28	Preparation of tris(2,3,5,6-tetrafluoro-4(trifluoromethyl)phenyl)phosphine oxide	261
5.29	Preparation of bis[2,3,5,6-tetrafluoro-4(trifluoromethyl)phenyl]phosphinic acid	262
5.30	Preparation of (piperidinylamido)phosphoric dichloride	263
5.31	Reaction of bromopentafluorobenzene with (piperidinylamido)phosphoric dichloride	264
5.32	Reaction of 4-bromo-2,3,5,6-tetrafluorobenzotrifluoride with (piperidinylamido)phosphoric dichloride	267
5.33	Preparation of bis(pentafluorophenyl)phosphinic acid via hydrolysis of 1-[bis(pentafluorophenyl)phosphinoyl]piperidine	269
5.34	Preparation of nonafluorobiphenyl-4-yl(pentafluorophenyl)phosphinic acid	270
5.35	Preparation of bis(nonafluorobiphenyl-4-yl)phosphinic acid	271
5.36	Preparation of bis[2,3,5,6-tetrafluoro-4(trifluoromethyl)phenyl]phosphinic acid via hydrolysis of 1-[bis-(2,3,5,6-tetrafluoro-4-trifluoromethylphenyl)phosphinoyl]piperidine	272
5.37	Preparation of 1-[(2,3,5,6,3',6',2'',3'',5'',6''-decafluoro-4,5',4''-tris-trifluoromethyl[1,1';4',1'']terphenyl-2'-yl)-(2,3,5,6-tetrafluoro-4-trifluoromethyl-phenyl)]phosphinic acid	273
5.38	Preparation of erbium(III) bis(pentafluorophenyl)phosphinate	274
5.39	Preparation of erbium(III) bis(2,3,5,6-tetrafluoro-4(trifluoromethyl)phenyl)phosphinate	275
5.40	Preparation of erbium(III) (nonafluorobiphenyl-4-yl)(pentafluorophenyl)phosphinate	276

5.41	Preparation of erbium(III) bis(nonafluorobiphenyl-4-yl)phosphinate	277
5.42	Preparation of neodymium(III) bis(pentafluorophenyl)phosphinate	278
5.43	Preparation of neodymium(III) bis(2,3,5,6-tetrafluoro-4(trifluoromethyl)phenyl)phosphinate	279
5.44	Preparation of neodymium(III) (nonafluorobiphenyl-4-yl)(pentafluorophenyl)phosphinate	280
5.45	Preparation of neodymium(III) bis(nonafluorobiphenyl-4-yl)phosphinate	281
5.46	Preparation of ytterbium(III) bis(pentafluorophenyl)phosphinate	282
5.47	Preparation of ytterbium(III) bis(2,3,5,6-tetrafluoro-4(trifluoromethyl)phenyl)phosphinate	283
5.48	Preparation of ytterbium(III) (nonafluorobiphenyl-4-yl)(pentafluorophenyl)phosphinate	284
5.49	Preparation of ytterbium(III) bis(nonafluorobiphenyl-4-yl)phosphinate	285
5.50	Preparation of yttrium(III) bis(pentafluorophenyl)phosphinate	286
5.51	Preparation of yttrium(III) bis(2,3,5,6-tetrafluoro-4(trifluoromethyl)phenyl)phosphinate	287
5.52	Preparation of yttrium(III) (nonafluorobiphenyl-4-yl)(pentafluorophenyl)phosphinate	288
5.53	Preparation of yttrium(III) bis(nonafluorobiphenyl-4-yl)phosphinate	289
5.54	Preparation of erbium (50%) yttrium (50%)(III) bis(pentafluorophenyl)phosphinate	290
5.55	Preparation of erbium(III) diphenylphosphinate	291
5.56	Preparation of neodymium(III) diphenylphosphinate	292
5.57	Preparation of ytterbium(III) diphenylphosphinate	293
5.58	References for chapter 5	294
Chapter 6 – Conclusions		296
6.1	Conclusion	296
6.2	References for chapter 6	298
Abbreviations		299
Appendix		302

List of figures

Chapter 1

- Figure 1.1 : Poly(methyl methacrylate) (PMMA) polymer (1) and the fluorine-substituted phenyl methacrylates (2) prepared by Okamoto and co-workers 33
- Figure 1.2 : Poly(imides) – 6FDA/TFDB (3) prepared by Matsuura *et al* and PMDA/TFDB (4) 34
- Figure 1.3 : Crosslinkable fluorinated poly(aryl ether ketone)s synthesized by Ma *et al* (5) 35
- Figure 1.4 : 2,2,6,6-tetramethyl-3,5-heptane-dione (6) 1,1,5,5,5-hexafluoropentane-2,4-dione (7) and 1,1,1-trifluoro-pentane-2,4-dione (8) 36
- Figure 1.5 : Configuration of a three-level (left) and four-level laser (right) 38
- Figure 1.6 : Energy level diagram of the Ln^{3+} taken from Bünzli *et al* 39
- Figure 1.7 : (Right) shows the configurational coordinate diagram of a Ln^{3+} ion and (left) shows the configurational coordinate diagram of a d-transition metal ion for comparison 41
- Figure 1.8 : Emission spectrum of Er^{3+} , Nd^{3+} and Yb^{3+} in the near infrared region 44
- Figure 1.9 : Energy level diagram of NIR luminescent Ln^{3+} ions and high energy vibrational oscillators 46
- Figure 1.10 : Three steps for the indirect excitation or the sensitization process 48

Figure 1.11 : Scheme to sensitize Ln ³⁺ luminescence	50
Figure 1.12 : Structures of fluorescein (9) and eosin (10)	51
Figure 1.13 : Pyrene chromophore (11)	52
Figure 1.14 : Diagram of the deactivation processes between d-block and f-block metals	54
Figure 1.15 : { <i>fac</i> -Re ^I Cl(CO) ₃ } ₂ L-Ln ^{III} (12) synthesized by Pope <i>et al</i>	54
Figure 1.16 : Platinum complex with phenanthroline as a bridging ligand (13)	55
Figure 1.17 : Energy levels of Er ³⁺	57
Figure 1.18 : Energy levels of Nd ³⁺	58
Figure 1.19 : Energy levels of Yb ³⁺	59
Figure 1.20 : Experimental setup of photoluminescence experiments	60
Chapter 2	
Figure 2.1 : Chemical structure of HHFA (14) and HFA-D (15)	71
Figure 2.2 : Terphenyl-based ligands; non-deuterated (16) and partly deuterated (17)	74
Figure 2.3 : Triphenylene-functionalized ligand (18)	75
Figure 2.4 : Dinuclear complexes of the form [Ln(tta) ₃] ₂ (μ-BPTZ) (19) and mononuclear complexes of the form [Ln(tta) ₃ (H ₂ O) ₂] (20) prepared by Shavaleev <i>et al</i>	77

Figure 2.5 : Isotopes program and table	83
Figure 2.6 : Crystal structure of $[\text{Er}(\text{HFA})_3(\text{H}_2\text{O})_2]$ as determined from X-ray diffraction (XRD)	84
Figure 27 : Crystal structure of the anion, $[\text{Er}(\text{HFA})_4]^-$ as determined from X-ray diffraction (XRD) of the Cs^+ salt	85
Figure 2.8 : (a) Emission spectrum of $[\text{Er}(\text{HFA})_3(\text{H}_2\text{O})_2]$ and (b) shows the luminescence lifetime data and fit of $[\text{Er}(\text{HFA})_3(\text{H}_2\text{O})_2]$ when it had been hydrated	87
Figure 2.9 : (a) Emission spectrum of $\text{Cs}[\text{Er}(\text{HFA})_4]$ and (b) shows the luminescence lifetime data and fit of $\text{Cs}[\text{Er}(\text{HFA})_4]$	89
Figure 2.10 : (a) Emission spectrum of the 98% deuterated $\text{Cs}[\text{Er}(\text{HFA})_4]$ sample and (b) shows the corresponding luminescence lifetime data and fit	91
Figure 2.11 : (a) Emission spectrum of $\text{Cs}[\text{Nd}(\text{HFA})_4]$ and (b) shows the corresponding luminescence lifetime data and fit	96
Figure 2.12 : Powder X-ray diffraction data of $\text{Cs}[\text{Nd}(\text{HFA})_4]$ and $\text{Cs}[\text{Eu}(\text{HFA})_4]$	97
Figure 2.13 : (a) Emission spectrum of the 98% deuterated $\text{Cs}[\text{Nd}(\text{HFA}-d)_4]$ sample and (b) the corresponding luminescence lifetime data and fit	99
Figure 2.14 : Rate constant of the major lifetime component against % deuteration for the partially deuterated neodymium samples	101
Figure 2.15 : (a) Emission spectrum of $\text{Cs}[\text{Yb}(\text{HFA})_4]$ and (b) the corresponding luminescence lifetime data and fit	102

Figure 2.16 : (a) Emission spectrum of the 98% deuterated Cs[Yb(HFA-*d*)]₄ sample and (b) the corresponding luminescence lifetime data and fit 103

Chapter 3

Figure 3.1 : Common β-diketonates used for research 111

Figure 3.2 : Chemical structure of 2,4,6-tri(2-pyridyl)-1,3,5-triazine (TPTZ) (**22**) which is used as a neutral ligand 111

Figure 3.3 : Polyazine bridging ligands 2,2'-bipyrimidine (BPM) (**23**) and 2,3-bis(2-pyridyl)pyrazine (DPP) (**24**) 112

Figure 3.4 : Lanthanide complexes of the form Ln(HFA)₃BPM (**25**) (where Ln = Nd, Gd or Tb; HFA = 1,1,1,5,5,5-hexafluoroacetylacetone and BPM = 2,2'-bipyrimidine) 112

Figure 3.5 : A new collection of Ln³⁺ complexes comprising BPM and DPP as neutral bridging ligands and TTA as the β-diketonate 114

Figure 3.6 : Chemical structure of 8-hydroxyquinoline (**29**) 115

Figure 3.7 : Chemical structures of Er³⁺ benzoate and pentafluorobenzoate complexes with bipyridine (**32**) or H₂O (**33**) 120

Figure 3.8 : XRD chemical structure of [Er(C₆F₅CO₂)₃(H₂O)₅] 122

Figure 3.9 : (a) Emission spectrum of [Er(C₆F₅CO₂)₃(H₂O)₅] and (b) emission spectrum of the free pentafluorobenzoic acid 123

Figure 3.10 : Luminescence lifetime data and fit of [Er(C₆F₅CO₂)₃(H₂O)₅] 124

Figure 3.11 : (a) Absorption spectrum of pentafluorobenzoic acid and (b) excitation spectrum of [Er(C₆F₅CO₂)₃(H₂O)₅] at emission wavelength of 1540 nm 125

Figure 3.12 : Emission spectrum of the low melting solid which was obtained upon reaction of ligand 37 with Er ³⁺	128
Figure 3.13 : Chemical structure of 1,1,1,5,5,5-hexafluoro-3-pentafluorophenyl-pentane-2,4-dione (38)	129
Figure 3.14 : ¹⁹ F NMR of diketone 62	140
Figure 3.15 : ¹ H NMR of diketone 62	141
Chapter 4	
Figure 4.1 : Chemical structure of 3,4,5,6-tetrafluoro-2-nitrophenol (63)	149
Figure 4.2 : Chemical structure of tetrakis(pentafluorophenyl)imidodiphosphate (HF-tpip) (64)	151
Figure 4.3 : Energy level diagram of Er ³⁺ with possible upconversion routes, de-excitation pathways and radiative decay routes	156
Figure 4.4 : Chemical structure of 2-thenoyltrifluoroacetone (65)	158
Figure 4.5 : Perfluorodiphenylphosphinate ligand (66) used by Song <i>et al</i>	160
Figure 4.6 : The emission spectra of [(C ₆ F ₅) ₂ POO] ₃ Er (solid line) and [(C ₆ F ₅) ₂ POO] ₃ Er _{0.5} Yb _{0.5} (dotted line)	161
Figure 4.7 : Chemical structure of the four different phosphinic acids used for study in this chapter	163
Figure 4.8 : Chemical structure of phosphinamide dichloride (74)	167
Figure 4.9 : XRD chemical structure of phosphinamide 78	170

Figure 4.10 : Chemical structures of conjugate bases of phosphinic acids 66 , 67 , 68 and 69	171
Figure 4.11 : Chemical structure of diphenyl-phosphinic acid and its anion	172
Figure 4.12 : Powder X-ray diffraction data of $\text{Er}[(\text{C}_6\text{F}_5)_2\text{PO}_2]_3$ and $\text{Y}[(\text{C}_6\text{F}_5)_2\text{PO}_2]_3$	174
Figure 4.13 : Solid state ^{31}P NMR of $\text{Y}[(\text{C}_6\text{F}_5)_2\text{PO}_2]_3$	175
Figure 4.14 : Solid state ^{31}P NMR of $\text{Er}[(\text{C}_6\text{F}_5)_2\text{PO}_2]_3$	176
Figure 4.15 : Solid state ^{31}P NMR of $\text{Er}_{0.05}\text{Y}_{0.95}[(\text{C}_6\text{F}_5)_2\text{PO}_2]_3$	177
Figure 4.16 : EDX spectrum of $\text{Er}_{0.9}\text{Y}_{0.1}(\text{L-2})_3$	178
Figure 4.17 : Chelation at single Ln^{3+} centres (left) and formation of inter-lanthanide bridges (right)	179
Figure 4.18 : SEM image of (a) $\text{Er}_{0.3}\text{Y}_{0.7}(\text{L-1})_3$ (mag 50000 X), (b) $\text{Er}_{0.5}\text{Y}_{0.5}(\text{L-2})_3$ (mag 40000 X), (c) $\text{Er}_{0.9}\text{Y}_{0.1}(\text{L-3})_3$ (mag 100000 X) and (d) $\text{Er}_{0.7}\text{Y}_{0.3}(\text{L-4})_3$ (mag 40000 X)	180
Figure 4.19 : SEM image of (a) $\text{Nd}_{0.5}\text{Y}_{0.5}(\text{L-1})_3$ (mag 50000 X), (b) $\text{Nd}_{0.7}\text{Y}_{0.3}(\text{L-2})_3$ (mag 50000 X), (c) $\text{Nd}_{0.3}\text{Y}_{0.7}(\text{L-3})_3$ (mag 50000 X) and (d) $\text{Nd}_{0.7}\text{Y}_{0.3}(\text{L-4})_3$ (mag 50000 X)	181
Figure 4.20 : SEM image of (a) $\text{Yb}_1\text{Y}_0(\text{L-1})_3$ (mag 50000 X), (b) $\text{Yb}_{0.7}\text{Y}_{0.3}(\text{L-2})_3$ (mag 50000 X), (c) $\text{Yb}_{0.3}\text{Y}_{0.7}(\text{L-3})_3$ (mag 50000 X) and (d) $\text{Yb}_{0.1}\text{Y}_{0.9}(\text{L-4})_3$ (mag 50000 X)	182
Figure 4.21 : Ultraviolet-visible absorption of ligands; (a) L-1, (b) L-2, (c) L-3 and (d) L-4	183

Figure 4.22 : Emission spectra of ligands L-1 to L-4	185
Figure 4.23 : 750 nm lifetime luminescence data of ligand, L-4 at 410 nm excitation	186
Figure 4.24 : Emission spectra of 100% (a) Er(L-1) ₃ , (b) Er(L-2) ₃ , (c) Er(L-3) ₃ and (d) Er(L-4) ₃	188
Figure 4.25 : Excitation spectra of 100% (a) Er(L-1) ₃ , (b) Er(L-2) ₃ , (c) Er(L-3) ₃ and (d) Er(L-4) ₃	189
Figure 4.26 : Luminescence lifetime data and fit of 100% (a) Er(L-1) ₃ , (b) Er(L-2) ₃ , (c) Er(L-3) ₃ and (d) Er(L-4) ₃	190
Figure 4.27 : Luminescence lifetime data and fit for 100% Er(L-1) ₃ : (a) fitted by a stretched function and 100% Er(L-5) ₃ (b) fitted by a single exponential function	192
Figure 4.28 : Schematic diagram of the excitation pathway of Er ³⁺ at 520 nm	193
Figure 4.29 : Rise time data and fit of (a) Er(L-1) ₃ , (b) Er _{0.97} Y _{0.03} (L-2) ₃ , (c) Er _{0.5} Y _{0.5} (L-3) ₃ and (d) Er _{0.93} Y _{0.07} (L-4) ₃	194
Figure 4.30 : Er ³⁺ concentration v lifetime plots for (a) Er _x Y _{1-x} (L-1) ₃ , (b) Er _x Y _{1-x} (L-2) ₃ , (c) Er _x Y _{1-x} (L-3) ₃ and (d) Er _x Y _{1-x} (L-4) ₃	198
Figure 4.31 : Combined Er ³⁺ concentration v lifetime plots of all the different diluted Er ³⁺ samples	200
Figure 4.32 : Er ³⁺ concentration v lifetime plots of Er ³⁺ samples that have been kept for different periods of time	201

Figure 4.33 : Emission spectra of 100% (a) Nd(L-1) ₃ , (b) Nd(L-2) ₃ , (c) Nd(L-3) ₃ and (d) Nd(L-4) ₃	202
Figure 4.34 : Excitation spectra of 100% (a) Nd(L-1) ₃ , (b) Nd(L-2) ₃ , (c) Nd(L-3) ₃ and (d) Nd(L-4) ₃	204
Figure 4.35 : Luminescence lifetime data and fit of 100% (a) Nd(L-1) ₃ before truncation, (b) Nd(L-1) ₃ after truncation, (c) Nd(L-3) ₃ before truncation, (d) Nd(L-3) ₃ after truncation, (e) Nd(L-4) ₃ before truncation and (f) Nd(L-4) ₃ after truncation	206
Figure 4.36 : Luminescence lifetime data and fit of 100% Nd(L-2) ₃	207
Figure 4.37 : Luminescence lifetime data and fit of (a) Nd(L-4) ₃ ⁴ F _{3/2} → ⁴ I _{11/2} , (b) Nd(L-4) ₃ ⁴ F _{3/2} → ⁴ I _{9/2} , (c) Nd _{0.97} Y _{0.03} (L-3) ₃ ⁴ F _{3/2} → ⁴ I _{11/2} and (d) Nd _{0.97} Y _{0.03} (L-3) ₃ ⁴ F _{3/2} → ⁴ I _{9/2} transitions	209
Figure 4.38 : Luminescence lifetime data and fit for 100% (a) Nd(L-5) ₃ before any truncation and (b) after 30 points have been deleted	211
Figure 4.39 : Rise time data of Nd(L-1) ₃	212
Figure 4.40 : Nd ³⁺ concentration v lifetime plots for (a) Nd _x Y _{1-x} (L-1) ₃ , (b) Nd _x Y _{1-x} (L-2) ₃ , (c) Nd _x Y _{1-x} (L-3) ₃ and (d) Nd _x Y _{1-x} (L-4) ₃	214
Figure 4.41 : Combined Nd ³⁺ concentration v lifetime plots of all the different diluted Nd ³⁺ samples	216
Figure 4.42 : Emission spectra of 100% (a) Yb(L-2) ₃ , (b) Yb(L-3) ₃ and (c) Yb(L-4) ₃	218

Figure 4.43 : Excitation spectra of 100% (a) Yb(L-2)_3 , (b) Yb(L-3)_3 and (c) Yb(L-4)_3	219
Figure 4.44 : Luminescence lifetime data and fit of 100% (a) Yb(L-2)_3 , (b) Yb(L-3)_3 , (c) Yb(L-4)_3 and (d) Yb(L-5)_3	220
Figure 4.45 : Rise time data of $\text{Yb}_{0.9}\text{Y}_{0.1}(\text{L-2})_3$	222
Figure 4.46 : Yb^{3+} concentration v lifetime plots for (a) $\text{Yb}_x\text{Y}_{1-x}(\text{L-2})_3$, (b) $\text{Yb}_x\text{Y}_{1-x}(\text{L-3})_3$ and (c) $\text{Yb}_x\text{Y}_{1-x}(\text{L-4})_3$	224
Figure 4.47 : Combined Yb^{3+} concentration v lifetime plots of all the different diluted Yb^{3+} samples	226

List of tables

Chapter 1

Table 1.1 : Common presentation of L terms	42
--	----

Chapter 2

Table 2.1 : Lifetime measurements on Nd(HFA- <i>d</i>) ₃ performed in deuterated solvents	72
---	----

Table 2.2 : Lifetime data of various Nd ³⁺ salts in organic solvents	73
---	----

Table 2.3 : Lifetimes measured for the Ln ³⁺ complexes with non-deuterated and deuterated terphenyl-based ligands	75
--	----

Table 2.4 : Lifetimes of Ln ³⁺ complexes measured in DMSO- <i>h</i> ₆ and DMSO- <i>d</i> ₆	76
---	----

Table 2.5 : Lifetime data of Nd ³⁺ , Yb ³⁺ and Er ³⁺ mononuclear and dinuclear complexes	78
---	----

Table 2.6 : Lifetime table of [Er(HFA) ₃ (H ₂ O) ₂] for the ⁴ I _{13/2} → ⁴ I _{15/2} Transition	86
--	----

Table 2.7 : Lifetime table of Cs[Er(HFA)] ₄ and Cs[Er(HFA- <i>d</i>)] ₄ for the ⁴ I _{13/2} → ⁴ I _{15/2} transition	89
---	----

Table 2.8 : Luminescence decay data fitted with the minimum number of lifetime parameters	92
---	----

Table 2.9 : The calculated distribution of the nearest C–H oscillators and C–D oscillators for the partially deuterated samples at the different levels of deuteration	93
--	----

Table 2.10 : Measured percentage contributions by ‘forced fitting’	93
--	----

Table 2.11 : Lifetime data of Cs[Nd(HFA) ₄] and Cs[Nd(HFA- <i>d</i>) ₄] for the ${}^4F_{3/2} \longrightarrow {}^4I_{13/2}$ transition	95
Table 2.12 : Lifetimes of the partially deuterated Cs[Nd(HFA) ₄] samples for the ${}^4F_{3/2} \longrightarrow {}^4I_{13/2}$ transition	99
Table 2.13 : Lifetime data of Cs[Yb(HFA) ₄] and Cs[Yb(HFA- <i>d</i>) ₄] for the ${}^2F_{5/2} \longrightarrow {}^2F_{7/2}$ transition	102
Table 2.14 : Lifetimes of the Cs[Yb(HFA) ₄] partially deuterated samples	104
Chapter 3	
Table 3.1 : Lifetime and relative intensities of Er ³⁺ compounds with the different ligands	117
Table 3.2 : Results of the solid phase photoluminescence measurements at room temperature for tris Ln ³⁺ complexes	119
Table 3.3 : Summary of different conditions attempted for the preparation of 1,1,1,5,5,5-hexafluoro-3-phenyl-pentane-2,4-dione (43)	131
Table 3.4 : Different conditions for the reaction shown in scheme 3.8	136
Chapter 4	
Table 4.1 : Different Er ³⁺ and Yb ³⁺ complexes obtained by the two methods of recrystallization and a brief description of the physical appearance	150
Table 4.2 : Lifetime data of Er(F-tpip) ₃ and the non fluorinated analogue, Er(tpip) ₃	152
Table 4.3 : Lifetime and photoluminescence quantum yield of Ln ³⁺ compounds by Glover <i>et al</i>	153

Table 4.4 : Measured photoluminescence lifetimes and calculated quantum efficiencies of $[(C_6F_5)_2POO]_3Er$ and $[(C_6F_5)_2POO]_3Er_{0.5}Yb_{0.5}$	161
Table 4.5 : Lifetime table of $Er_xY_{1-x}(L-2)_3$ complexes prepared using methods A and B	173
Table 4.6 : Ultraviolet-visible absorption of ligands, L-1 to L-4 using ethanol as a solvent	184
Table 4.7 : Average lifetimes, β values and quantum yields of 100% $Er(L-1)_3$, $Er(L-2)_3$, $Er(L-3)_3$, $Er(L-4)_3$ and $Er(L-5)_3$	191
Table 4.8 : Rise times of the Er^{3+} samples	195
Table 4.9 : Average lifetimes, β values and quantum yields of diluted Er^{3+} samples	196
Table 4.10 : Average lifetime data for comparisons between ${}^4F_{3/2} \longrightarrow {}^4I_{11/2}$ and ${}^4F_{3/2} \longrightarrow {}^4I_{9/2}$ transitions	208
Table 4.11 : Average lifetimes, β values and quantum yields of 100% $Nd(L-1)_3$, $Nd(L-2)_3$, $Nd(L-3)_3$, $Nd(L-4)_3$ and $Nd(L-5)_3$	210
Table 4.12 : Average lifetimes, β values and quantum yields of diluted Nd^{3+} samples	213
Table 4.13 : Average lifetimes, β values and quantum yields of 100% $Yb(L-2)_3$, $Yb(L-3)_3$, $Yb(L-4)_3$ and $Yb(L-5)_3$	221
Table 4.14 : Average lifetimes, β values and quantum yields of diluted Yb^{3+} samples	223

List of schemes

Chapter 3

- Scheme 3.1 : Preparation of 3-[(4-methoxy phenyl)(pentafluorophenyl sulfanyl) methyl] -1,1,1,5,5,5-hexafluoro-pentane-2,4-dione) (**37**) 127
- Scheme 3.2 : Preparation of 1,1,1-trifluoro-3-phenylpropan-2-one (**41**) 130
- Scheme 3.3 : Attempt to prepare 1,1,1,5,5,5-hexafluoro-3-phenyl-pentane-2,4-dione (**43**) via Grignard chemistry 130
- Scheme 3.4 : Attempt to prepare 1,1,1-trifluoro-3-pentafluorophenyl-propan-2-one (**46**) 132
- Scheme 3.5 : Preparation of (Z)-1-phenyl-2-pyrrolidinyl-3,3,3-trifluoropropene (**49**) 133
- Scheme 3.6 : Attempt to prepare 1,1,1,5,5,5-hexafluoro-3-phenylpentane-2,4-dione (**43**) via enamine **49** 134
- Scheme 3.7 : Route to obtaining 4-(2-phenyl-1-trifluoromethyl-vinyl)-morpholine (**54**) or 4-[2-(pentafluorophenyl)-1-(trifluoromethyl-vinyl)-morpholine] (**55**) 135
- Scheme 3.8 : Attempted preparation of 1,1,1,5,5,5-hexafluoro-3-phenyl-pentane-2,4-dione (**43**) via enamine **54** 136
- Scheme 3.9 : Preparation of 3-phenyl-pentane-2,4-dione (**59**) 138
- Scheme 3.10 : Reaction of acetylacetone (**57**) with iodopentafluorobenzene (**60**) 139
- Scheme 3.11 : Reactions of HFA (**34**) with iodobenzene (**58**) 142

Scheme 3.12 : Reactions of HFA (**34**) with iodopentafluorobenzene (**60**) 142

Chapter 4

Scheme 4.1 : Route to preparing bis(pentafluorophenyl)phosphinic acid 165

Scheme 4.2 : Route to preparing 1-[bis-(2,3,5,6-tetrafluoro-4-trifluoromethyl-phenyl)-phosphinoyl]phosphinic acid 166

Scheme 4.3 : Organolithium method to obtaining phosphinic acids **66**, **68** and **69** 167

Scheme 4.4 : Organolithium method to obtaining Compounds **67** and **80** 169

List of charts

Chapter 3

Chart 3.1 : Structure of 8-hydroxyquinoline and its halogen substituted derivatives	116
Chart 3.2 : Structure of 8-hydroxyquinoline extended with amide substituents and its halogen substituted derivatives	118

List of publications

1. 'Non-radiative de-excitation mechanisms in long-lived Erbium(III) organic compounds $\text{Er}_x\text{Y}_{1-x}[(p\text{-CF}_3\text{-C}_6\text{F}_4)_2\text{PO}_2]_3$ ' Hernandez; I., Tan; R. H. C., Pearson; J., Wyatt; P. B. and Gillin; W. P., Submitted to the *Journal of Physical Chemistry B*, **2008** (Dec)
2. 'Erbium bis(pentafluorophenyl)phosphinate - a new hybrid material with unusually long-lived infrared luminescence' Zheng; Y., Pearson; J., Tan; R. H. C., Gillin; W. P. and Wyatt; P. B, *Journal of Material Science : Materials In Electronics*, 20, **2009**, 430
3. 'Evidence for erbium-erbium energy migration in erbium(III) bis(perfluoro-*p*-tolyl)phosphinate' Tan; R. H. C., Pearson; J., Zheng; Y., Gillin; W. P. and Wyatt; P. B., *Applied Physics Letters*, 92, **2008**, 103303
4. 'Near IR luminescent rare earth 3,4,5,6-tetrafluoro-2-nitrophenoxide complexes : Synthesis, X-ray crystallography and spectroscopy' Zheng; Y., Motevalli; M., Tan; R. H. C., Gillin; W. P. and Wyatt; P. W, *Polyhedron*, 27, **2008**, 1503
5. 'Quenching of IR Luminescence of Erbium, Neodymium, and Ytterbium β -diketonate Complexes by Ligand C-H and C-D Bonds' Tan; R. H. C, Motevalli; M., Abrahams; I., Wyatt; P. B. and Gillin W. P., *Journal of Physical Chemistry B*, 110, **2006**, 24476
6. 'Quenching of Er(III) luminescence by ligand C-H vibrations: Implications for the use of erbium complexes in telecommunications' Winkless; L., Tan; R. H. C., Zheng; Y., Motevalli; M., Wyatt; P. B. and Gillin; W. P., *Applied Physics Letters*, 89, **2006**, 111115

Chapter 1 - Introduction

1.1 General introduction

The role of telecommunications is increasing in today's society and has led to a dramatic growth in the importance of optoelectronics. Communication is the transfer of information from one point to another. A telecommunication system is required to convey the information such as radio signals in wireless applications and optical light pulses through glass-fibers over varying distances.^{1,2,3} With the introduction of high-quality optical fiber networks in the 1980's, long distance telecommunication has been achieved. Cable television, broad band internet surfing and telephone lines across the Atlantic Ocean are common applications that have benefited from optical networks. Traditional coaxial cables have been replaced by optical fibers for telecommunication over long distances. Although transmission speeds of over 1 Tbit/s can be achieved, these optical cables are susceptible to losses and intermittent amplification of the signals is necessary.

Even though modern optical fibers, which are made of glass, are extremely transparent, attenuation of the intensity of the optical pulse travelling along the fibers still occurs. Over vast distances, the light signal must be boosted back to a signal of a larger intensity and that is carried out with a repeater. In the late 1980s, David Payne and his team at the University of Southampton, United Kingdom reported the operation of the first optical amplifier for optical communication systems and since then, the optical fiber technology has seen tremendous success.⁴ Effectively, it is an optical fiber doped with erbium (Er^{3+}) ions and is known as the Erbium-Doped Fiber Amplifier (EDFA).

The expansion of the optical fiber network has been attributed to the development of optical amplifiers, particularly the erbium-doped fiber amplifier. Prior to the existence of optical amplifiers, the common way of coping with attenuation of light signals along a fiber was to use electronic regenerators along the line with the disadvantage that these regenerators are limited by the speed of their electronic components. These optical amplifiers, which are purely optical in nature, amplify signals without the need to first convert them into electrical signals, thus enabling

high bit rates.⁵ Optical amplifiers are often long and bulky, which is acceptable for telecommunications over long distances. However, for local fiber-to-home applications, it can be impractical and calls for a need to integrate optical amplifiers into optical devices; a technology known as integrated optics.⁶

In optical telecommunication systems, where light is used to transport information between different users, devices such as splitters, couplers, multiplexers and amplifiers are used. They can be readily made and integrated on one planar substrate.⁷ One essential component of a photonic integrated circuit is the planar optical waveguide, which consists of a high refractive index core guiding layer, sandwiched between two lower-index cladding layers.⁸ The optical signal, which travels in the guiding layer and confined in the transverse directions as a result of total internal reflection is subject to various losses. Optical losses in the waveguide, coupling losses or intrinsic intensity losses call for the integration of optical amplifiers with waveguides and other components in photonic integrated circuits. A photonic integrated circuit is also known as an integrated optical circuit and it integrates multiple photonic functions on a single chip. Some advantages of photonic integrated circuit include miniaturization, ability to integrate different electronic functions, power and cost efficiency. Optical amplification can be achieved by doping the guiding layer of an optical amplifier using lanthanide (Ln^{3+}) ions as the active element.²

In many cases, the integrated optics devices exploit organic polymeric materials as these polymers can be deposited easily on solid substrates like silicon wafers by spincoating from solution and patterns can be created with conventional lithographic techniques.⁹ The polymers have the advantage of being transparent over the telecommunications window.¹⁰ Moreover, high refractive index contrasts can be achieved with different polymers and this criterion is important as a high contrast will give a strong confinement of the light in the core of the waveguide. Furthermore, relatively sharp bends are possible without too large losses. It must also be mentioned that polymeric materials have similar refractive index to standard optical fibers and that facilitates coupling of optical signals to existing fibers with low coupling losses.⁷

Er^{3+} has an emission transition at around $1.5 \mu\text{m}$ and is therefore utilized in telecommunications systems, especially as optical amplifiers.¹¹ Other Ln^{3+} ions that are used for this purpose include praseodymium (Pr^{3+}) and neodymium (Nd^{3+}), which have optical transitions in the $1.3 \mu\text{m}$ window.¹² In integrated optics, these Ln^{3+} ions are incorporated in the devices and one way to do that is to solubilize or disperse the ions in organic polymers. Since these inorganic Ln^{3+} salts are insoluble in organic polymers, they have to be complexed to organic ligands to circumvent this problem.⁷

The objective of this research project is to design, synthesize and characterise novel organic ligands to be used to form Ln^{3+} complexes. In the next section, we shall look at the historical developments of the optical amplifier and then review some of the work that has been done in the area of polymer waveguides. Subsequently, some basic concepts of laser mechanisms and characteristics of Ln^{3+} will be discussed. We conclude this chapter by outlining the structure of this thesis.

1.2 History of optical amplifiers

In 1962, Geusic *et al*¹³ introduced the concept of a travelling wave optical amplifier and two years later in 1964, Snitzer and co-workers¹⁴ demonstrated a Nd^{3+} doped fiber amplifier at $1.06 \mu\text{m}$. The fiber of length 1 m, had a core of $10 \mu\text{m}$ with a 0.75 to 1.5 mm cladding. A year later in 1965, Snitzer demonstrated the first erbium-doped glass laser.¹⁵ Their systems consisted of 15 wt % Yb_2O_3 and 0.25 wt % Er_2O_3 dissolved in a glass base whose primary constituents are in the ratio of 75 wt % SiO_2 , 8 wt % Na_2O , 12 wt % K_2O and 5 wt % BaO . Rare-earth doped lasers in a small diameter crystal fiber form were investigated in the early 1970s by Stone and Burrus at Bell Telephone Laboratories as potential devices for fiber transmission systems.^{16,17,18} The $15 \mu\text{m}$ cores were doped with Nd^{3+} and surrounded with fused silica cladding. Lasing was achieved at $1.06 \mu\text{m}$ when pumped with a laser diode¹⁷ and an LED.¹⁸ The commercial fiber-optic transmission systems did not adopt $1.06 \mu\text{m}$ as a transmission wavelength and subsequently, these Nd^{3+} lasers were not utilised in modern telecommunications infrastructure. In 1983, Broer *et al*^{19,20} first demonstrated the rare-earth doping of

single-mode fibers and the fibers were fabricated using the modified chemical vapour deposition (MCVD) technique. Further improvements in the MCVD fabrication technique of single-mode fibers were achieved by Poole and his team at the University of Southampton, United Kingdom.²¹ In 1987, the teams at the University of Southampton and AT&T Bell Laboratories developed the erbium-doped single-mode fiber amplifiers for amplification of signals at 1.5 μm .^{22,23} Er^{3+} was utilised due to the fact that its transition at 1.5 μm was suitable as an amplifying medium for conventional telecommunication systems. Large frame lasers were used for the demonstrations by both of the teams; an argon laser-pumped dye laser operating at 650 nm for the team at Southampton and an argon laser operating at 514 nm for the group at AT&T Bell Laboratories. Their results featured high signal gains and attracted world wide interest. However, one major disadvantage is the large frame laser pumps. Nakazawa *et al*²⁴ rectified the problem by achieving optical gain characteristics of an erbium-doped silica fiber by pumping with a 1.48 μm InGaAsP high-power laser diode and this proliferated the use of erbium-doped fiber amplifiers for high-capacity undersea and terrestrial fiber-optic links and networks.

1.3 Polymer waveguides

Wavelength division multiplexing (WDM) technologies has been proliferated to a considerable extent. They provide a method to increase transmission capacities whilst using the existing optical fiber infrastructure.^{9,25} As such, the developments in this area will depend on cost reduction and optimizing the performance of critical waveguide devices. Since the 1990s, polymeric materials have attracted considerable attention due to their ease of fabrication, low cost and the capability for device integration.

Waveguiding is the phenomenon of total internal reflection of an optical beam within a relatively high refractive index material (core) embedded in another material with lower refractive index (cladding).⁷ As such, the optical beam is confined and guided through the core of a fiber. Channel waveguides have a different symmetry but the principles of waveguiding are the same. Polymer waveguides on a solid substrate are easily made by spincoating and standard

lithographic techniques.⁹ Both the core and cladding polymers are prepared in the same way. One advantage of polymer cores and cladding is to facilitate the easy tuning of the refractive index. This can be done using the large variety of available polymers or by chemical modifications of existing ones. Generally, the refractive index of polymers varies from 1.3 to 1.6, and that makes it possible to create high or low refractive index differences.²⁶ A high refractive index contrast will provide a strong confinement of light in the polymer core and consequently, relatively sharp bends are possible without too much loss. This ability to minimize the losses despite having sharp bends is important in the design of long structures in a small area.

In optical telecommunication, light is transmitted at Near-Infrared (NIR) wavelengths (1.5 μm , 1.4 μm and 1.3 μm) and silica is one of the most popular materials used in optical fibers. This is due to the transparency of silica fibers in the NIR region. However, these silica fibers have O–H groups and they induce strong absorption in the transmission window caused by the first overtone of the O–H vibration. Due to this reason, organic polymers have attracted much attention for optical device applications. Although they have high optical losses in the 1.0 – 1.6 μm region because of the presence of high C–H bond vibrational absorption, these bonds can be chemically modified by fluorination and deuteration.²⁷ By substituting hydrogen atoms with deuterium or halogen atoms, the absorption is reduced and will be shifted to longer wavelengths. Fluorinated polymers have low optical loss at the telecommunication wavelengths of 1.5 μm and 1.3 μm due to the reduction of the vibrational absorption overtone of the C–H bonds.^{9,28,29} For low-loss waveguides, it is also important to control the refractive index of the core and cladding. Imamura *et al*³⁰ controlled the refractive indices of their materials by monomer copolymerization and found that the refractive index of the polymer decreases as the fluorine content increases. At 1.52 μm , the refractive index can be controlled over the range 1.48 – 1.36.

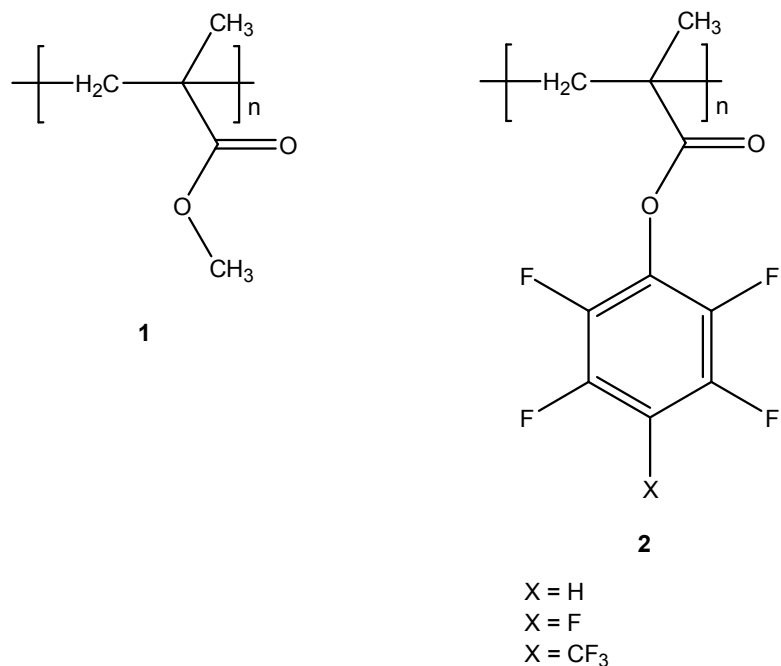


Figure 1.1 : Poly(methyl methacrylate) (PMMA) polymer (**1**) and the fluorine-substituted phenyl methacrylates (**2**) prepared by Okamoto and co-workers^{32,34}

Polymers such as poly(methyl methacrylate) (PMMA), (Figure 1.1, **1**) which is commercially available has high light transmittance and provides exceptional resistance to both chemical and weather corrosion.³¹ Additionally, their low manufacturing costs and easy processing make PMMA a valuable substitute for glass in modern optical device applications.³² However, some drawbacks of PMMA such as its relatively low glass transition temperature of around 100 °C and high water absorption have limited its utility for optoelectronic applications.³³ Okamoto and co-workers^{32,34} have prepared fluorine-substituted phenyl methacrylates to circumvent this problem. (Figure 1.1, **2**)

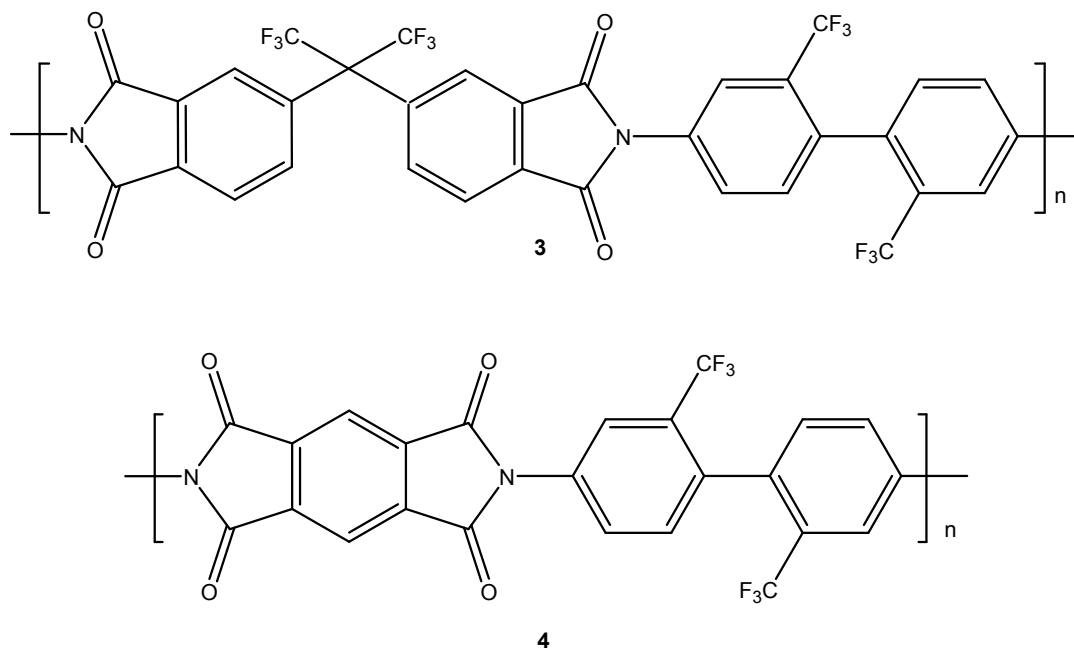


Figure 1.2 : Poly(imides) – 6FDA/TFDB (**3**) prepared by Matsuura *et al*³⁷ and PMDA/TFDB (**4**)

Poly(imides)^{28,35,36} are also common materials studied for optical waveguides due to their low losses in the NIR region, excellent mechanical properties and the ability to modify the fluorine content. The polyimide 6FDA/TFDB (Figure 1.2, **3**) prepared by Matsuura *et al*³⁷ has an optical loss of 0.3 dB/cm at 1.3 μm and the polyimide PMDA/TFDB (Figure 1.2, **4**) has a relatively high refractive index due to its low fluorine content. One disadvantage of poly(imides) is the low adhesion of these materials to various substrate but this can be rectified by the introduction of cross-linkable groups to the main polymer chain. The addition of cross-linkable groups also provides high thermal stability. Fluorinated poly(imides) can be prepared via a two-step method where the poly(imide) precursors, poly(amido acid)s were initially synthesized from ring-opening polymerization before they were subjected to thermal imidization.³⁸ They have advantages over PMMA polymers such as low moisture sensitivity, high glass transition temperatures (above 400 °C), greater optically transparency and high refractive index.^{39,40}

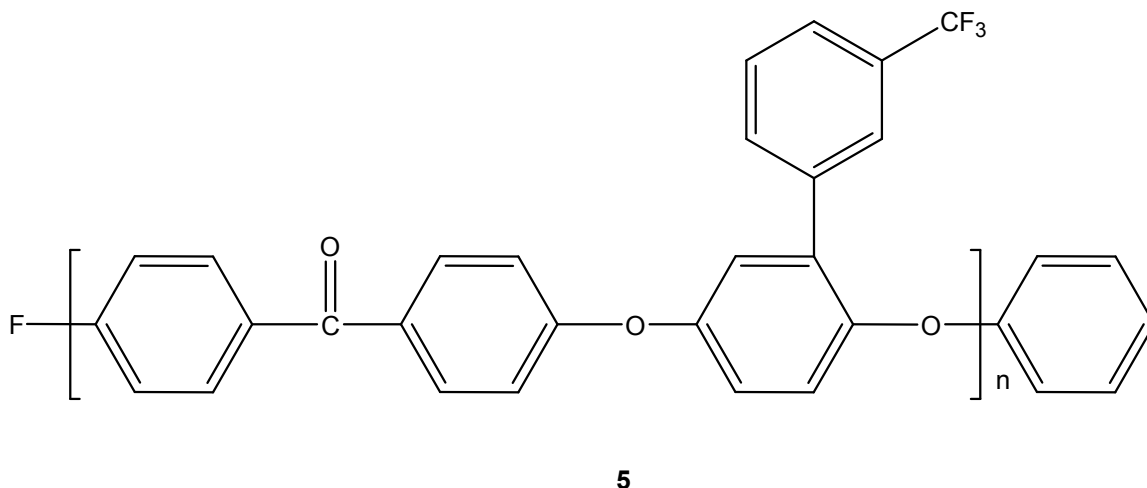


Figure 1.3 : Crosslinkable fluorinated poly(aryl ether ketone)s synthesized by Ma *et al*⁴¹ (**5**)

Ma *et al*⁴¹ synthesized a series of crosslinkable fluorinated poly(aryl ether ketone)s in a two step synthetic route (Figure 1.3). These crosslinked polymers offered highly thermal stability, high glass transition temperature and good solvent resistance. Due to the minimal optical absorptions at 1.3 μm and 1.5 μm , and lower birefringence, these polymers are potential candidates for optical materials.

1.4 Polymer waveguide doped with Ln³⁺ complexes

Integration of passive and active components is an important consideration in telecommunications and an efficient method of facilitating this is to use polymer-based waveguides as they allow easy patterning through standard lithography techniques. Polymers such as polyimides have been used for optical devices. However, these materials are insoluble in H₂O and that makes the incorporation of rare-earth ions difficult. Therefore, to avoid high technological cost such as ion implantation for the fabrication of waveguide amplifiers, the rare-earth ions have to be chelated by organic ligands. Chelation is the binding or complexation of ions with ligands that have two or more donor atoms. These ligands are organic in nature and can be bidentate or multidentate. Rare-earth chelates have been used in metal-organic chemical vapour deposition (MOCVD) to grow rare-earth doped semiconductor thin films to obtain rare-earth doped glass for optical amplifiers or

lasers.⁴² Polymers allow a certain concentration of guest molecules in their matrix and doped polymers can exhibit certain properties of the dopant. The limit to the amount of dopant that can be incorporated in such systems is determined by the solubility of the guest molecules in the host polymers. Beyond a certain concentration of guest molecules, the optical quality of material will be ruined.

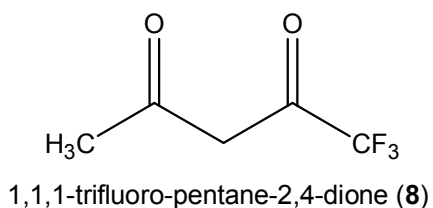
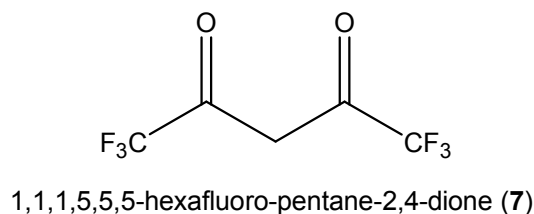
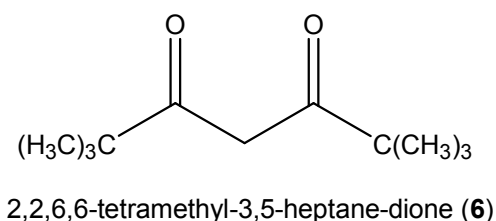


Figure 1.4 : 2,2,6,6-tetramethyl-3,5-heptane-dione (**6**), 1,1,1,5,5,5-hexafluoropentane-2,4-dione (**7**) and 1,1,1-trifluoro-pentane-2,4-dione (**8**)

Lin *et al*⁴³ reported on several optical polymers with Nd^{3+} complexes of 2,2,6,6-tetramethyl-3,5-heptane-dione (**6**), 1,1,1,5,5,5-hexafluoropentane-2,4-dione (**7**) and 1,1,1-trifluoro-pentane-2,4-dione (**8**) (Figure 1.4). The optical polymers used were PMMA, side-chained PMMA/disperse red 1 (PMMA/DR1), polystyrene, Ultem[®] (polyimide) and Ultradel[®] 9000 series (fluorinated polyimides). The best results were achieved with the Ultradel[®] 9000 series (fluorinated polyimides) and 1,1,1,5,5,5-hexafluoro-pentane-2,4-dione Nd^{3+} complexes. Their experiments also

demonstrate that it is possible to create low loss polymer optical devices by integrating organic rare-earth complexes into a polymer and pumping it with a low cost laser diode.

1.5 Optical amplification

Luminescence is the emission of light from an excited molecule. For a Ln^{3+} ion to luminesce, the electronically excited states must be populated and population at different excited states will give different emission lines. This promotion of electrons from the ground state to an excited state is called pumping. Photoluminescence is a process where a molecule gets excited onto a higher energy level via the absorption of light by the molecule.⁴⁴ Following excitation to an excited state, the molecule rapidly relaxes to a lower luminescent state and when the electrons interact with an incoming signal that matches the lasing level, amplification via stimulated emission occurs and energy in the form of light with the same phase and frequency as the incoming signal is emitted.⁴⁵ To achieve optical amplification, it is necessary to create population inversion, where the distribution of electrons is such that the population of the emissive state is greater than that of the ground state.¹ Three and four level laser systems will be presented in the following section.

1.6 Laser systems¹

Figure 1.5 shows the configuration of a three-level and four-level laser. In the three-level system, the electrons are excited to an excited state E_2 and they rapidly decay nonradiatively to level E_1 . As the lifetime of electrons in level E_1 is longer than those in level E_2 , over a period of time, the density of electrons in level E_1 increases above those in the ground state E_0 and population inversion takes place. Stimulated emission and amplification can then occur when an incoming signal interacts with the electrons in the emissive level E_1 . In the four-level system, level E_2 is populated in a similar way to the three-level laser and population inversion followed by amplification takes place between levels E_2 and E_1 . This is a more efficient system as electrons at level E_1 rapidly decays to their ground state, only to be re-excited to level E_3 and maintaining population inversion.

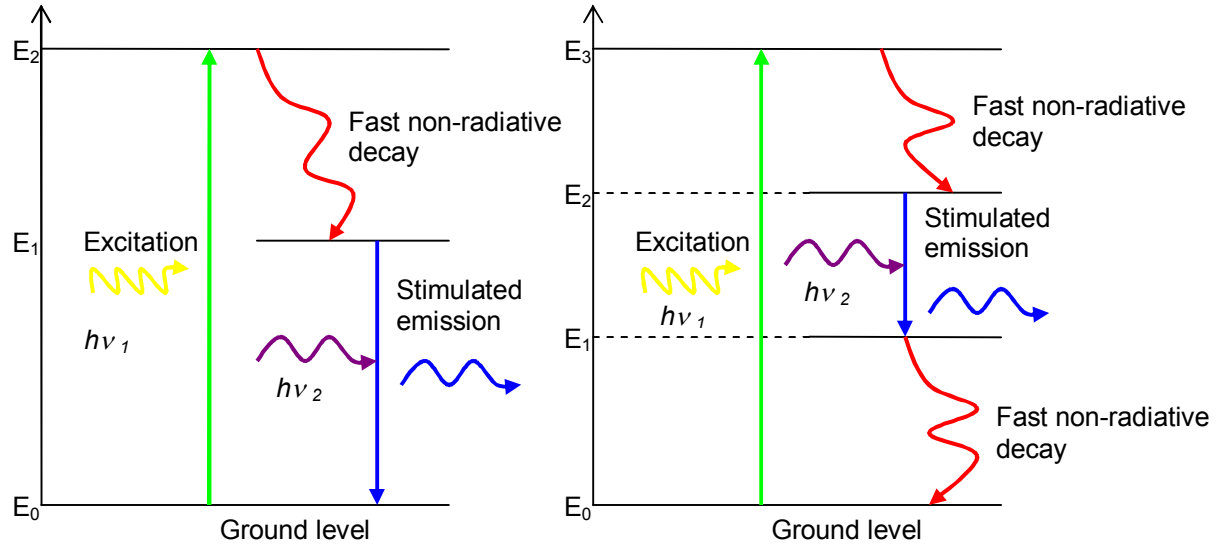


Figure 1.5 : Configuration of a three-level (left) and four-level laser (right)

1.7 Radiative and nonradiative recombination²

The electrons in the emissive states will discard their excitation energy and relax in two ways: radiatively and nonradiatively. When electrons relax radiatively, energy in the form of photons is released. Multiphonon relaxation or nonradiative recombination can rapidly depopulate the emissive level and energy is lost through heat or vibrations. The relationship between the radiative and non radiative lifetimes can be summarized by equation 1.

Equation 1
$$1/\tau = 1/\tau_r + 1/\tau_{nr}$$

From equation 1, τ is the total lifetime, τ_r is the radiative lifetime and τ_{nr} is the nonradiative lifetime. The reciprocals of the total lifetime ($1/\tau$), radiative lifetime ($1/\tau_r$) and nonradiative lifetime ($1/\tau_{nr}$) are known as the rate constants, k . Radiative lifetimes arise from the luminescence when an electron decays from its excited state to its ground state. To achieve a high level of population inversion and hence attain a long radiative lifetime suitable for use in optical amplification, it is essential to reduce the nonradiative processes from occurring.⁴⁶ There will be more

discussions on the nonradiative processes of Ln^{3+} complexes in section 1.11, when we look at the energy gap law.

1.8 Characteristics of lanthanides

Trivalent Ln^{3+} ions are luminescent.⁴⁶ Figure 1.6 shows the energy level diagram of the Ln^{3+} . They each have a different emitting level and consequently, their emission covers the entire electromagnetic spectrum from ultraviolet (UV) to the NIR. Gadolinium (Gd^{3+}), for example, emits in the UV while thulium (Tm^{3+}) has blue emission, terbium (Tb^{3+}) emits in the green and europium (Eu^{3+}) has a characteristic red emission.

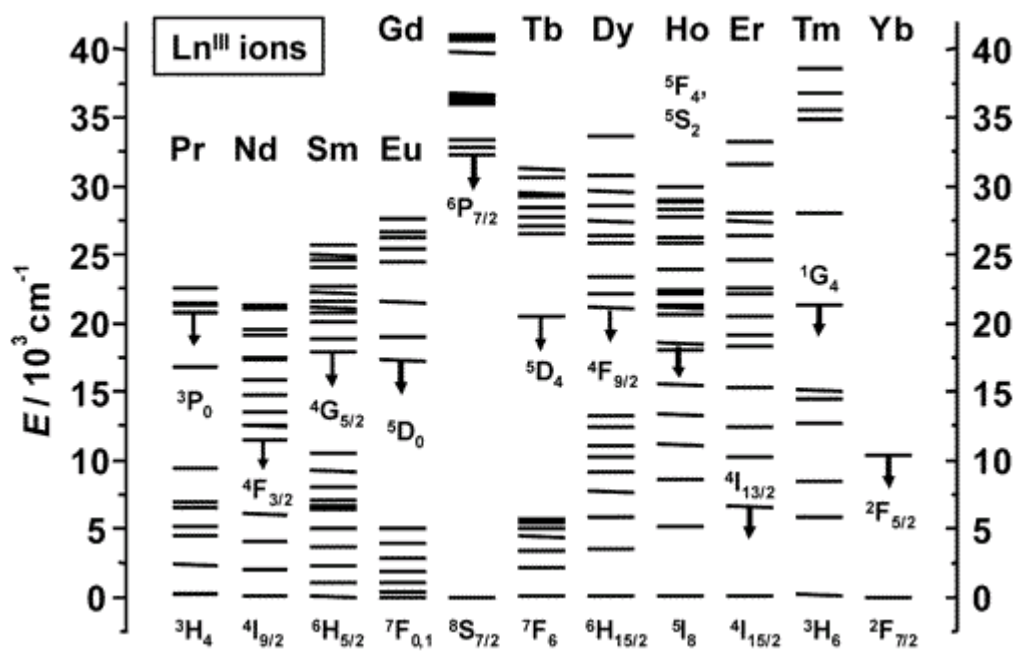


Figure 1.6 : Energy level diagram of the Ln^{3+} taken from Bünzli *et al*⁴⁸

Ln^{3+} ions are ideal for laser applications for various reasons. They are very stable under laser action because the luminescence originates from the internal transitions of an ion, without involving any physical or chemical bonds. Another reason is that these ions have long lifetimes in their excited state which is a criterion which facilitates laser action. The lanthanides, also known as the rare-earths, fit into the periodic table from atomic number 57 for lanthanum (La^{3+}) to

atomic number 71 for lutetium (Lu^{3+}). Except for Lu^{3+} , which is a d-block element, the rest of the elements in the family are f-block elements due to the filling of the 4f electron shell. These elements have a Xenon (Xe) core electronic configuration and n 4f electrons with n varying from 0 for La^{3+} to 14 for Lu^{3+} . The Xe core electronic configuration is $1s^2 2s^2 2p^6 3s^2 3p^6 3d^{10} 4s^2 4p^6 4d^{10} 5s^2 5p^6$. The three rare-earths being studied in this thesis can be expressed as follows; $\text{Er} = [\text{Xe}]4f^{12}6s^2$, $\text{Nd} = [\text{Xe}]4f^4 6s^2$ and $\text{Yb} = [\text{Xe}]4f^{14}6s^2$. Ionization of the Ln^{3+} involves the removal of two 6s electrons, and then either a 4f or a 5d electron to achieve a stable oxidation state of +3 ($\text{Er}^{3+} = [\text{Xe}]4f^{11}$, $\text{Nd}^{3+} = [\text{Xe}]4f^3$ and $\text{Yb}^{3+} = [\text{Xe}]4f^{13}$). The rare-earths can also be found in the divalent and tetravalent oxidation states, eg. europium (Eu^{2+}), samarium (Sm^{2+}) and cerium (Ce^{4+}).

Generally, each atom has a nucleus surrounded by shells of electrons which are progressively filled along the periodic table and these successive shells have increasing radii. However, for the Ln^{3+} series from atomic number 57, the lower energy 5s and 5p shells are both full and each subsequent electron is inserted into a 4f shell, resulting in a sudden contraction. Instead of having a larger radius than the 5s and 5p shells, the 4f shell actually contracts and is being encapsulated by them. This unique sequence of adding an additional electron to its 4f shell as the series progresses is called the lanthanide contraction and accounts for the optical characteristics of this family.⁴⁷ Since the electrons of the 4f shell are shielded by the complete 5s and 5p shells, the energies of the 4f electrons give rise to the special spectroscopic properties and are insensitive to the nature of the ligands surrounding a particular Ln^{3+} ion. The energy levels of the 4f-shell have equal parity which forbids electric dipole transitions, although in practice these are observable as relatively narrow bands with low extinction coefficients (typically $<3 \text{ m}^{-1} \text{ s}^{-1}$).⁴⁸ As a result of the insensitivity of the 4f electrons, the Stokes shifts are extremely small. The rearrangement of electrons in the 4f sub-shell does not lead to much change in the chemical bond lengths, relative to d-transition metal ions. Figure 1.7 (right) shows the configurational coordinate diagram of a Ln^{3+} ion and figure 1.7 (left) shows the configurational coordinate diagram of a d-transition metal ion for comparison.

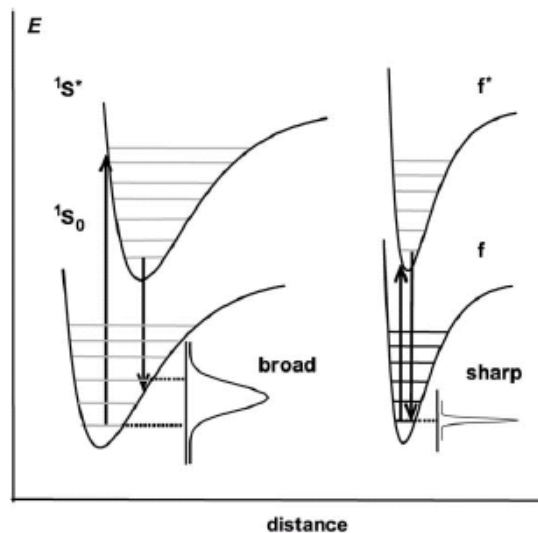


Figure 1.7 : (Right) shows the configurational coordinate diagram of a Ln^{3+} ion and (left) shows the configurational coordinate diagram of a d-transition metal ion for comparison

When a molecule is excited, the excited state potential energy curve is displaced with respect to the ground level curve. Vertical excitation following the Franck-Condon principle leads to vibrationally excited states. Similarly, the same rules hold for de-excitation and it results in sharp emissions for the Ln^{3+} ions, relative to the d-transition metal ions (Figure 1.7).⁴⁶

Energy levels within the rare-earth ions are classified using the terminology $^{(2S+1)}L_J$, where L is the total orbital angular momentum of the level and J the total angular momentum. The superscript S is the total spin multiplicity.

$$J = |L+S|, |L+S-1|, \dots, |L-S|.$$

Therefore for $L > S$, there is a $(2S+1)$ degeneracy and for $L < S$, there is a $(2L+1)$ degeneracy. The common presentation of L terms are given in table 1.1.

L	0	1	2	3	4	5	6
Standard Notation	S	P	D	F	G	H	I

Table 1.1 : Common presentation of L terms

Ln^{3+} luminescence in the NIR region has been of interest in recent years. Er^{3+} , Nd^{3+} and Yb^{3+} have unique properties for this purpose. Each rare-earth ion has its own specific energy levels which result in unique luminescence lines. Although transitions within these energy levels are strongly forbidden by the parity selection rules, the selection rules can be relaxed by stealing intensity from allowed transitions and it results in relatively weak optical absorption.⁴⁹ The reverse process of emission is also forbidden and results in long-lived excited states, up to milliseconds. The excited to ground state transitions of Er^{3+} , Nd^{3+} and Yb^{3+} at approximately 1.54 μm , 1.06 μm and 980 nm respectively are coincident to the commonly used wavelength in telecommunications and are often deployed in optoelectronics devices.⁴⁶

1.9 Electronic transitions of Ln^{3+} ions

Generally, the electronic transitions of Ln^{3+} can be classified under four main headings.

1. f-f transitions⁴⁶

The energy levels of the Ln^{3+} ions will split into many different energy levels and this is known as Stark splitting.⁴⁷ NIR emissions involve transitions between electrons in the 4f states which is made up of a number of different levels and before a 4f electron is excited to a higher lying orbital such as the 4d or 5g orbital, it can be excited within the different 4f levels. Splitting of the stark levels is dependent on the host and the various atomic interactions between the electrons create a permanent electric field known as the crystal or ligand field. The crystal or ligand field induces this Stark splitting.²

For the NIR emitting ions, these f-f transitions give rise to the emissions. These transitions involve a rearrangement of the electrons within the 4f sub-shell and as described in the previous section, they are polarity forbidden and give rise to weak intensities.

2. 4f-5d transitions⁵¹

These transitions correspond to the promotion of an electron from the 4f sub-shell into the 5d sub-shell and are allowed by the parity rule. It results in sizeable oscillator strengths with absorption coefficients in the range of $10^2 - 10^3 \text{ M}^{-1} \text{ cm}^{-1}$. The energy levels are governed by the environment around the metal because 5d orbitals interact directly with ligand orbitals.

3. Charge transfer transitions⁴⁶

Ligand-to-Metal (LMCT) and Metal-to-Ligand (MLCT) charge transfer transitions are allowed by Laporte's selection rule. For the Ln^{3+} , their energies are usually large and occur around the UV region of 40000 cm^{-1} . If the LMCT states lie at a high energy, energy can be transferred to the 4f states. However, when their energy level is close to the emitting level, the luminescence may be quenched.⁵⁰

4. Cooperative energy transfer²

The transitions that we have described so far concern isolated ions, where the distribution of the ions is even and the interionic distance is large. When the concentration of Ln^{3+} ions increases beyond a certain level, the interionic distance is reduced and this increases the probability of ion-ion coupling which leads to cooperative energy transfer. This phenomenon is concentration-dependent and competes directly with the light amplification process with the consequence of low emission quantum yields. In chapter 4, we shall study these effects in greater detail.

1.10 Ln³⁺ emission

Research on the NIR luminescence from Ln³⁺ ions is growing steadily and the primary reason is due to the increasing demand for optical amplifiers operating at wavelengths coincident with the telecommunications window.⁴⁸ Although Er³⁺ has several lines in both the visible and NIR region, the significant emission line is the $^4I_{13/2} \longrightarrow ^4I_{15/2}$ transition with transmission at around 1.54 μm .² Nd³⁺ displays NIR radiation in three spectral ranges: 0.87 – 0.92 μm , 1.06 – 1.09 μm and 1.32 – 1.39 μm due to the transitions, $^4F_{3/2} \longrightarrow ^4I_{9/2}$, $^4F_{3/2} \longrightarrow ^4I_{11/2}$ and $^4F_{3/2} \longrightarrow ^4I_{13/2}$, respectively.² Yb³⁺ possesses a simple electronic structure with the transition $^2F_{5/2} \longrightarrow ^2F_{7/2}$ accounting for emission from 0.96 – 1.03 μm .²

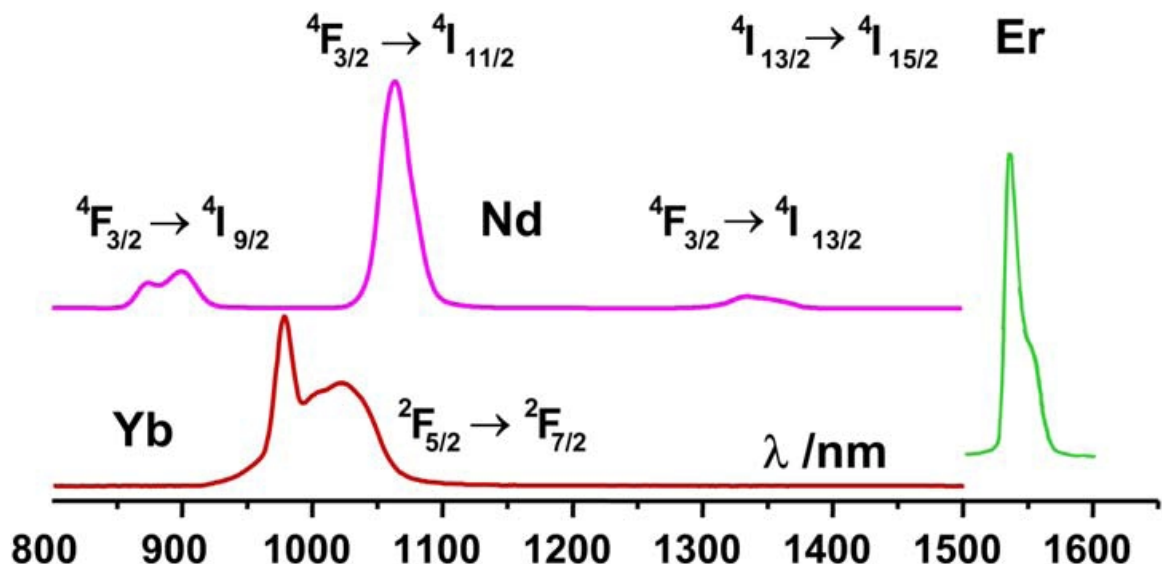


Figure 1.8 : Emission spectrum of Er³⁺, Nd³⁺ and Yb³⁺ in the near infrared region

Figure 1.8 shows the typical emission spectrum of Er³⁺, Nd³⁺ and Yb³⁺ in the NIR region. Er³⁺ and Yb³⁺ each displays a sharp emission peak while for Nd³⁺, there are three distinct features and the one with the highest intensity corresponds to the $^4F_{3/2} \longrightarrow ^4I_{11/2}$ transition with an emission wavelength of around 1.06 – 1.09 μm .

Since their luminescence is initiated from f-f transitions, the emission wavelength is not affected by surrounding hosts.⁵² NIR luminescence is prone to be vibrationally quenched by high energy oscillators such as C–H (2950 cm⁻¹) and O–H (3450 cm⁻¹) bonds usually present in organic ligands.^{53,54} They are also present in solvent molecules which may be coordinated directly to the ion to fulfil the high coordination number of Ln³⁺ ions.⁵⁴ One other pathway in which the luminescence can be quenched is through ion-ion interactions.^{2,47} This phenomenon is related to the ionic distance between adjacent Ln³⁺ ions and will be thoroughly discussed in chapter 4. Luminescence quenching leads to decreased intensity and shorter luminescence lifetimes, which limits any practical application of such complexes in useful devices.

Although these Ln³⁺ ions have varying natural luminescence lifetimes, τ_0 depending on the host material, τ_0 for Er³⁺, Nd³⁺ and Yb³⁺ are widely assumed to be 14 ms, 0.25 ms and 2.0 ms respectively.⁵⁵ We discussed earlier that Nd³⁺ has three transitions at 0.87 – 0.92 μm , 1.06 – 1.09 μm and 1.32 – 1.39 μm . It must be mentioned that the luminescence lifetimes for these three transitions are similar and that is due to the fact that these emissions occurs from the same excited level, ⁴F_{3/2}.

The quantum yield can be defined as the ratio of the number of photons emitted by the ions to the number of photons absorbed by the ligand/complex. The natural lifetimes (τ_0) are commonly used in equation 2 to measure the quantum yield, ϕ of Ln³⁺ complexes.⁵⁶

Equation 2

$$\phi = \frac{\tau_m}{\tau_0} \times 100 \%$$

where τ_m is the measured luminescence lifetime.

One method to prevent luminescence quenching and increase the quantum yield is to eliminate C–H and O–H oscillators near to the Ln³⁺ ion by introducing heavy atoms such as deuterium or fluorine.⁵⁷

Exclusion of H₂O molecules coordinated to the Ln³⁺ ions is another method to improve the luminescence lifetime.⁵⁸ This can be explained by the energy gap law.

1.11 The energy gap law

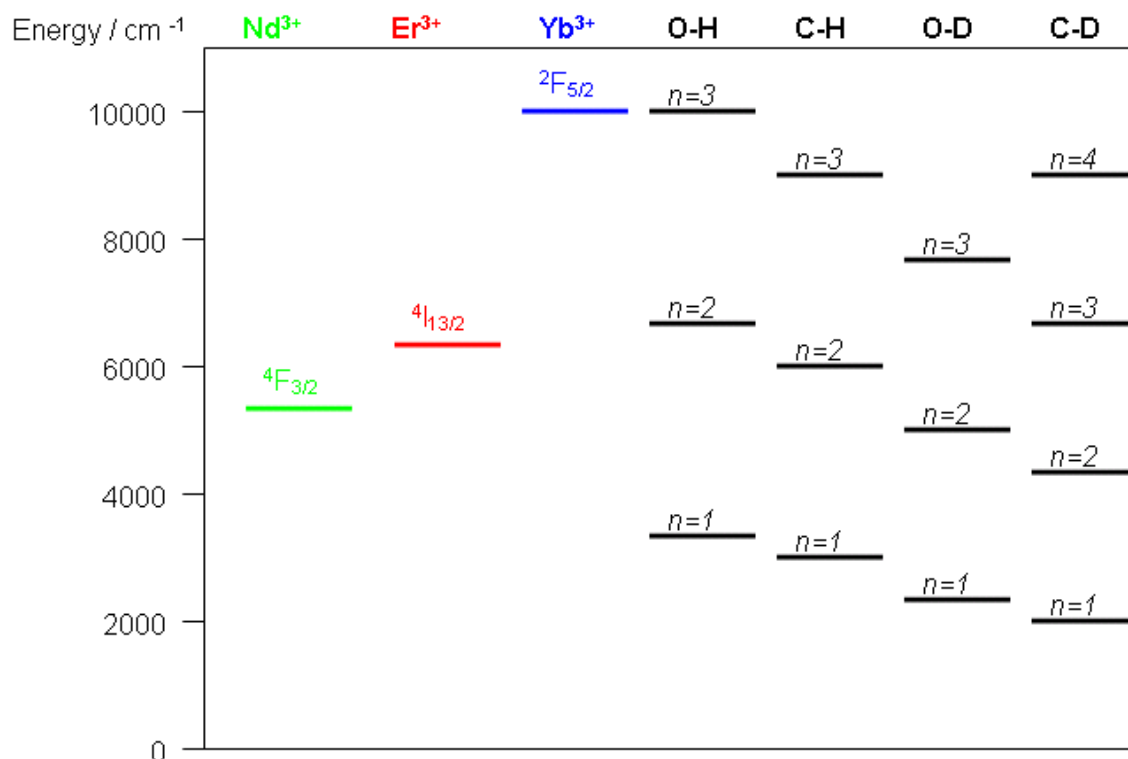


Figure 1.9 : Energy level diagram of NIR luminescent Ln³⁺ ions and high energy vibrational oscillators

Figure 1.9 shows the energy level diagram of the lowest luminescent state of the Ln³⁺ ions and common high vibrational energy bonds such as O–H, C–H, O–D and C–D. According to the energy gap law,^{59,60,61} quenching by vibrational energy is more effective when a smaller number of vibrational quanta are required to match the energy gap between the lowest luminescent state and the highest nonluminescent state. From figure 1.9, we can see that the O–H bond has the highest vibrational energy of 3450 cm⁻¹ and hence will be the most potent luminescent quencher followed by C–H, O–D and C–D bonds, with vibrational energies of 2950 cm⁻¹, 2500 cm⁻¹ and 2100 cm⁻¹, respectively.

We saw from the previous section that Er^{3+} has an energy gap of 6485 cm^{-1} , Nd^{3+} has an energy gap of 5400 cm^{-1} and Yb^{3+} has an energy gap of 9700 cm^{-1} . Since the three different ions have different energy gaps, their sensitivity towards the vibrational energy bonds varies with Yb^{3+} being the least sensitive followed by Er^{3+} and then Nd^{3+} .

1.12 Excitation of Ln^{3+} ions

We discussed earlier that Ln^{3+} ions have poor solubility which warrants the need for them to be complexed with organic ligands to facilitate fabrication. For optical amplification to take place, energy must be provided to bring the Ln^{3+} ions in their excited states and this process is normally referred to as pumping. In EDFAs, the energy is provided by an external laser diode at an absorption wavelength of Er^{3+} , typically $0.98 \mu\text{m}$ or $1.48 \mu\text{m}$.

One feature of the Ln^{3+} ions is that their emission properties are governed by the way their excited states can be populated. The electronic transitions of the trivalent Ln^{3+} ions involve a redistribution of electrons within the 4f sub-shell. Although electric dipole selection rules forbid such transitions, these rules are often relaxed by several mechanisms. One of these is the coupling with vibrational modes, where a molecular vibration changes the geometric arrangement around the metal ion and that has an effect on its symmetry. Other mechanisms such as J -mixing and the mixing with opposite-parity wavefunctions, such as 5d orbitals, ligand orbitals or charge transfer states have the potential to cause breakdown of the selection rules. Coupling between perturbing states and the 4f wavefunctions depends on the strength of interaction between the 4f orbitals and the complexing ligands. The mixing and the oscillator strengths of the f-f transitions are small and consequently, direct excitation of the Ln^{3+} ions produces low luminescence yields. Weissman *et al*⁶² discovered the effect of indirect excitation, which is also known as sensitization.

1.12.1 Direct excitation

To achieve optimal luminescent properties, the excited states of the ions must be populated and the nonradiative de-activation paths minimized. In optical amplification, laser light can be directly absorbed at the absorption wavelengths of the ions. Direct excitation of the Ln^{3+} ions is difficult because the optical transitions within the 4f subshells are parity forbidden and the optical cross-sections for the intra-4f transitions are small, typically 10^{-21} cm^2 for Er^{3+} .⁶³

1.12.2 Indirect excitation

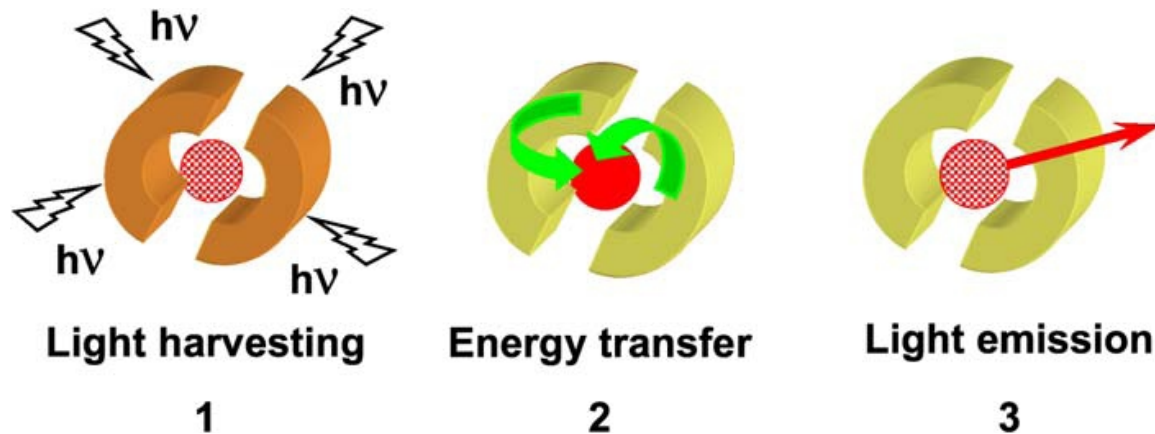


Figure 1.10 : Three steps for the indirect excitation or the sensitization process⁴⁶

To efficiently overcome the ion's intrinsically low extinction coefficient and also to increase the intensity of luminescence, the ions can be sensitized by incorporating into an organic complex, which absorbs and then transfers the excitation energy to the encapsulated Ln^{3+} ion, thus creating an antenna effect.⁶⁴ Indirect excitation or the sensitization process proceeds in three steps as shown in figure 1.10. Firstly, light is absorbed by the organic ligands of the emitting ion and then the excited energy is transferred onto the excited state of the Ln^{3+} ion.⁴⁶ Finally, light of the characteristic wavelength of the ion is emitted.

The organic ligands will also allow excitation at wavelengths where the Ln^{3+} ions do not exhibit a significant absorption.⁶⁵ For efficient energy transfer, the sensitizer needs to be in close proximity to the ion and the energy levels of sensitizer and Ln^{3+} ion should match. Intramolecular energy transfer from the organic chromophore to the intra-4f shell energy levels of the Ln^{3+} ions is the main contributing factor for the narrow line emissions.⁶⁶ For efficient energy transfer, there should be spectral overlap between the ligand (donor) and the Ln^{3+} (acceptor) states.⁶⁵

Energy transfer is depicted using a Jablonski diagram shown in figure 1.11. Firstly, light is absorbed by the sensitizing ligand, which is excited to the singlet excited state. From here, the energy can either be transferred directly to the Ln^{3+} ion (singlet energy transfer, ET_s), can convert to the triplet state in a process called intersystem crossing (ISC) or can decay to the ground state either by fluorescence or non-radiatively. Singlet energy transfer does not contribute significantly to the sensitization process.⁶⁷ Energy in the triplet state can transfer to the Ln^{3+} ion (ET_T) or decay to the ground state.⁶⁸ Generally, the most common route is for the energy to be transferred via the triplet state. This is because the intersystem crossing is enhanced by the nearby Ln^{3+} ions and also, energy transfer via the singlet state is not fast enough to compete with the fluorescence or the intersystem crossing process.

There are two ways for energy transfer to take place. In the Förster⁶⁹ mechanism of transfer, energy transfer is via dipolar or multipolar interactions between sensitizer (ligand) and acceptor (Ln^{3+} ion). An exchange mechanism known as the Dexter⁷⁰ mechanism can also take place. In the Dexter mechanism, orbital overlap is a prerequisite whereas in the Förster mechanism, the transfer is through space and is strongly dependant on the spectral overlap of the emission spectrum of the donor and the absorption spectrum of the acceptor. Förster energy transfer has been reported to take place over much longer distances whereas the Dexter mechanism is efficient at very small distances ($<10 \text{ \AA}$).⁷¹

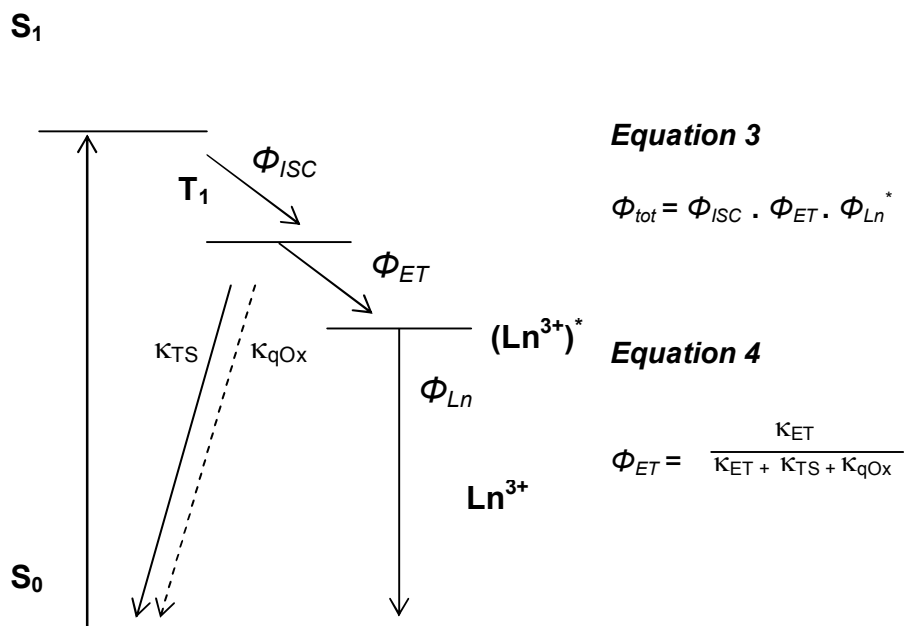


Figure 1.11 : Scheme to sensitize Ln^{3+} luminescence

Figure 1.11 shows the scheme in which to sensitize Ln^{3+} luminescence. The overall luminescence quantum yield (Φ_{tot}) is the product of the triplet yield (Φ_{ISC}), the energy transfer yield (Φ_{ET}) and the intrinsic luminescence quantum yield of the Ln^{3+} complex, (Φ_{Ln}^*). The energy transfer yield (Φ_{ET}) is determined by the rate of energy transfer (κ_{ET}), the deactivation of the triplet state by phosphorescence or nonradiative relaxation, (κ_{TS}), and by the rate of quenching of the donating triplet state by molecular oxygen, (κ_{qOx}).⁶⁸

One important phenomenon in sensitization of the Ln^{3+} ions is energy back transfer from the excited Ln^{3+} ion to the sensitizer. This effect will be prevalent in cases where the donating sensitizer level is too close to the accepting Ln^{3+} ion level and this makes thermally activated energy back transfer possible. For example, in the case of Tb^{3+} and Eu^{3+} , Latva *et al*⁷² demonstrated that the triplet state of a sensitizer should be at least $1,200 \text{ cm}^{-1}$ higher in energy than the accepting levels of the luminescent ions. Several strategies have been adopted to sensitize Ln^{3+} ions.

1.13 Sensitizing moieties

Researchers in this area have been focusing on developing antenna groups to circumvent the problem of poor absorption properties of the Ln^{3+} ions. The following presents some of the work that has been done.

1.13.1 Fluorescein derivatives

Werts *et al*⁶⁸ discussed the photophysical properties of Er^{3+} , Nd^{3+} and Yb^{3+} complexes with two sensitizer-modified diethylenetriaminepentaacetic acid (DTPA) derivatives. The sensitizing moieties derived from fluorescein and eosin are shown in figure 1.12.

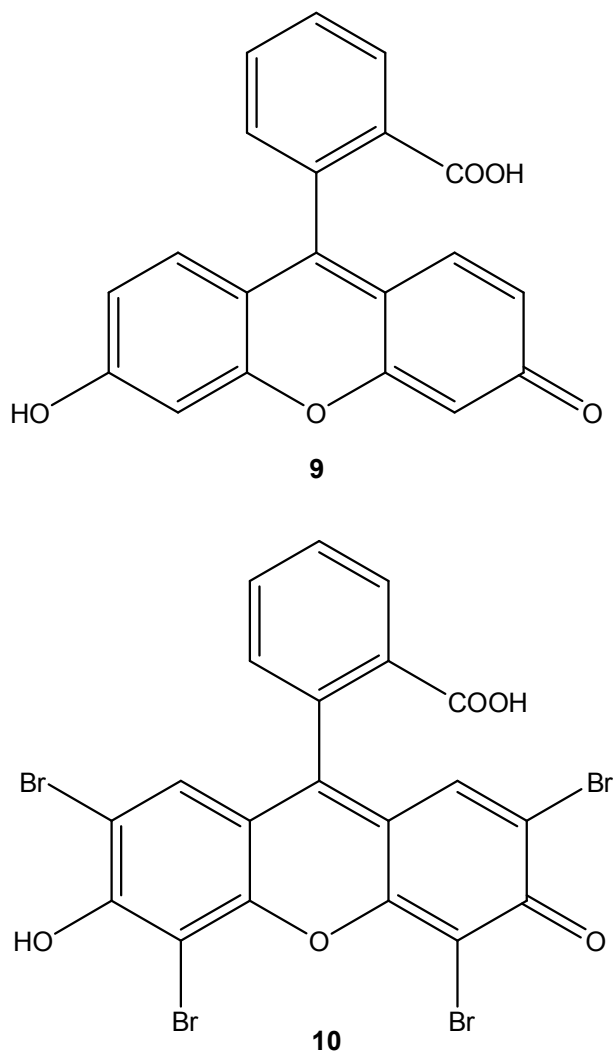
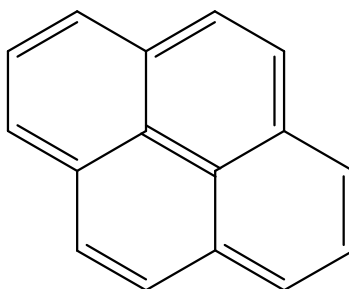


Figure 1.12 : Structures of fluorescein (9) and eosin (10)

Fluorescein is a dye that is widely used in biology as a green fluorescent probe. Its absorption maximum at around 488 nm makes it suitable for excitation with an argon laser. Sensitized emission of Nd^{3+} and Yb^{3+} were observed in H_2O and similarly, sensitized emission of Nd^{3+} , Yb^{3+} and Er^{3+} were observed in D_2O . Due to the enhanced intersystem crossing by the bromine atoms in eosin, it was found to be a more efficient sensitizer. It was also found that the energy transfer is slow, especially for Yb^{3+} , because the sensitized emission is strongly dependent on the oxygen concentration. Oxygen effectively quenches the triplet state of the dyes and this competes with the energy transfer to the emitting ions.

Fluorexon is another dye which is similar to fluorescein and has been reported to sensitize Nd^{3+} , Yb^{3+} and Er^{3+} upon excitation of the fluorexon with visible light.⁷³ This dye forms 1 : 1 complexes with Ln^{3+} ions and the photosensitization efficiency is very high due to the Ln^{3+} enhanced intersystem crossing in the sensitizing chromophore and rapid intracomplex energy transfer.

In a later paper, Werts *et al*⁷⁴ reported a Yb^{3+} complex based on a fluorexon derivative. The isothiocyanate function present in this complex makes reaction with amine functionalities in biological compounds possible. One great advantage of using this complex as a label is that visible light can be used to excite the complex and the Yb^{3+} luminescence which is long lived, allows the emitted light to be distinguished from the auto-fluorescence of biological systems.



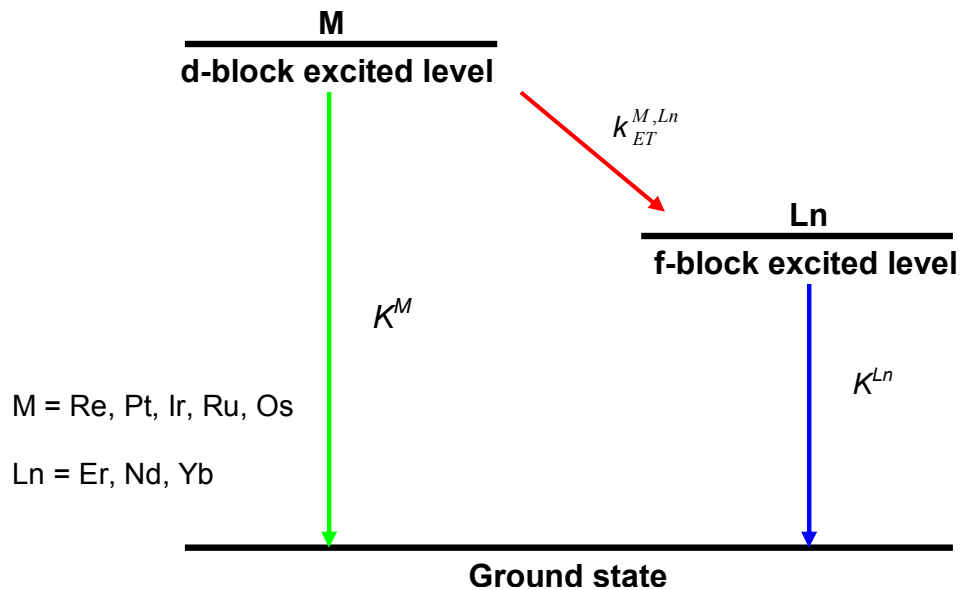
11

Figure 1.13 : Pyrene chromophore (11)

Pyrene chromophores (Figure 1.13) have also been shown to exhibit sensitization properties in Yb^{3+} and Nd^{3+} complexes.⁷⁵

1.13.2 Complexes of d-block metals

An efficient way of sensitizing Ln^{3+} ions is to take advantage of light absorbing properties of d-block transition metal complexes and then transferring energy to the emitting ions. Complexes of rhenium (Re), platinum (Pt), iridium (Ir), ruthenium (Ru) and osmium (Os) can be incorporated with Ln^{3+} complexes via bridging ligands such as bipyridines, phenanthroline and other aromatic chromophores for sensitized luminescence. Due to their stability and long-lived excited states with absorption bands spanning across the visible region, these d-block metal complexes can efficiently transfer the absorbed energy to the emissive Ln^{3+} ions. They may exhibit a metal-to-ligand charge-transfer (MLCT) based triplet excited state that closely matches the emitting state of Er^{3+} , Nd^{3+} and Yb^{3+} . The intense charge-transfer transitions, often mixed with d-d transitions, occur in the visible spectral range to efficiently collect photonic energy. Intersystem crossing, followed by multipolar d-4f energy transfer then lead to lanthanide-based NIR emission. Figure 1.14 shows the deactivation processes between d-block and f-block metals. The energy transfer process is similar to that of ligand–metal energy transfer.



- $k_{ET}^{M,Ln}$ - Energy transfer from the d-block metal (M) to the lanthanide (Ln)
- k^M - Intrinsic deactivation rate from the d-block metal to the ground state
- k^{Ln} - Intrinsic deactivation from the lanthanide to the ground state

Figure 1.14 : Diagram of the deactivation processes between d-block and f-block metals

Pope *et al*⁷⁶ synthesized kinetically stable complexes incorporating two Re(I) centres and one Ln³⁺ ion (Figure 1.15).

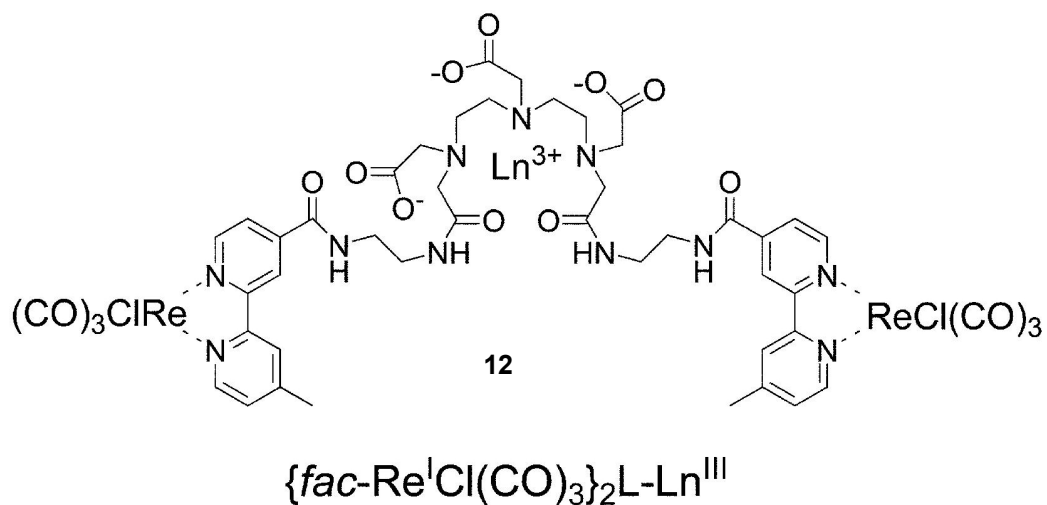


Figure 1.15 : $\{fac\text{-Re}^I\text{Cl}(\text{CO})_3\}_2\text{L-Ln}^{III}$ (**12**) synthesized by Pope *et al*⁷⁶

Figure 1.15 shows $\{fac-Re^1Cl(CO)_3\}_2L-Ln^{III}$ (where L = diethylenetriamine pentaacetic acid derived coordination environment and Ln = Nd, Er, Yb). These complexes displayed efficient sensitization of the Ln^{3+} ions by exciting at 337 nm. Lifetimes measured in CD_3OD were 512 ns, 540 ns and 8303 ns for Nd^{3+} , Er^{3+} and Yb^{3+} complexes respectively.

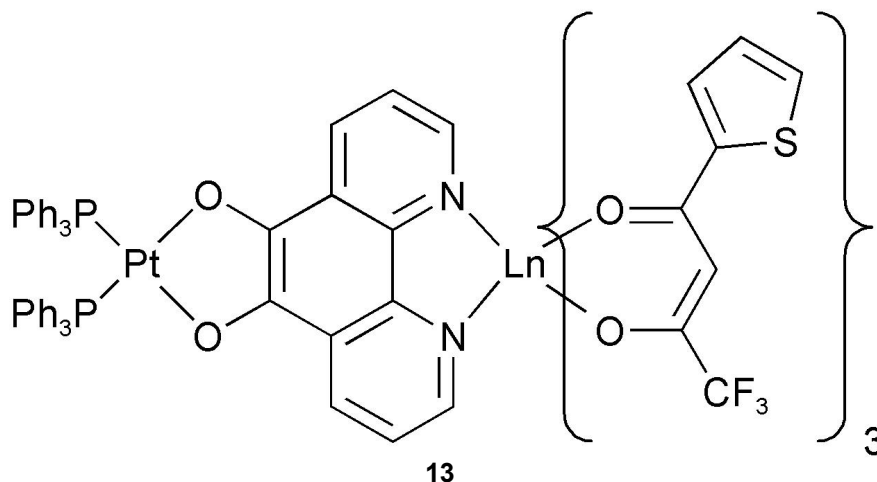


Figure 1.16 : Platinum complex with phenanthroline as a bridging ligand (**13**)

Shavaleev *et al*⁷⁷ demonstrated sensitization of Nd^{3+} , Er^{3+} and Yb^{3+} by attaching a platinum complex with phenanthroline as a bridging ligand (Figure 1.16). Lifetimes of 0.95 μs , 1.56 μs and 11 μs were obtained for Nd^{3+} , Er^{3+} and Yb^{3+} complexes respectively when the bimetallic complexes were excited at 520 nm.

Diplatinum complexes were also incorporated with Nd^{3+} and Yb^{3+} tris β -diketonates to sensitize luminescence.⁷⁸

1.14 Design of organic ligands

So far, we have seen that Ln^{3+} ions with organic molecules provide the possibility of enhancing the device quantum efficiency and obtaining spectrally narrow emissions. However, organic ligands have high vibrational bonds which affect the luminescence efficiencies of these Ln^{3+} complexes. Therefore, we can summarize that the design of organic ligands must achieve the following requirements:

1) Ligands must have a high absorption coefficient and provides an effective intersystem crossing from singlet to triplet states. The sensitizer needs to be excited in the near ultraviolet as the triplet energy should be sufficiently large to provide efficient energy transfer to the Ln^{3+} ions.⁶⁸

2) Ln^{3+} have a coordination number of 6 – 12 and therefore, it is necessary for the ligand to possess an adequate number of donor atoms to saturate the inner coordination sphere to prevent H_2O and solvent molecules from deactivating the excited states.

3) The ligands must also be free of any high energy bonds like O–H, C–H and N–H bonds. Anionic ligands bearing either oxygen or nitrogen donor atoms are preferred as the Ln^{3+} ions have chemical bonds with large electrostatic components.

4) High optical intensities are required for pumping and it is important that the organic complexes are thermally and photochemically stable.

5) Although many organic ligands absorb strongly in the UV, much emphasis has been placed on designing ligands which absorb in lower energies as visible light sources are cheaply and readily available.

1.15 Lifetime measurements

Lifetime measurements are performed using a technique known as photoluminescence, which will be described in section 1.16. Figure 1.17 shows the energy levels of Er^{3+} .⁴⁷

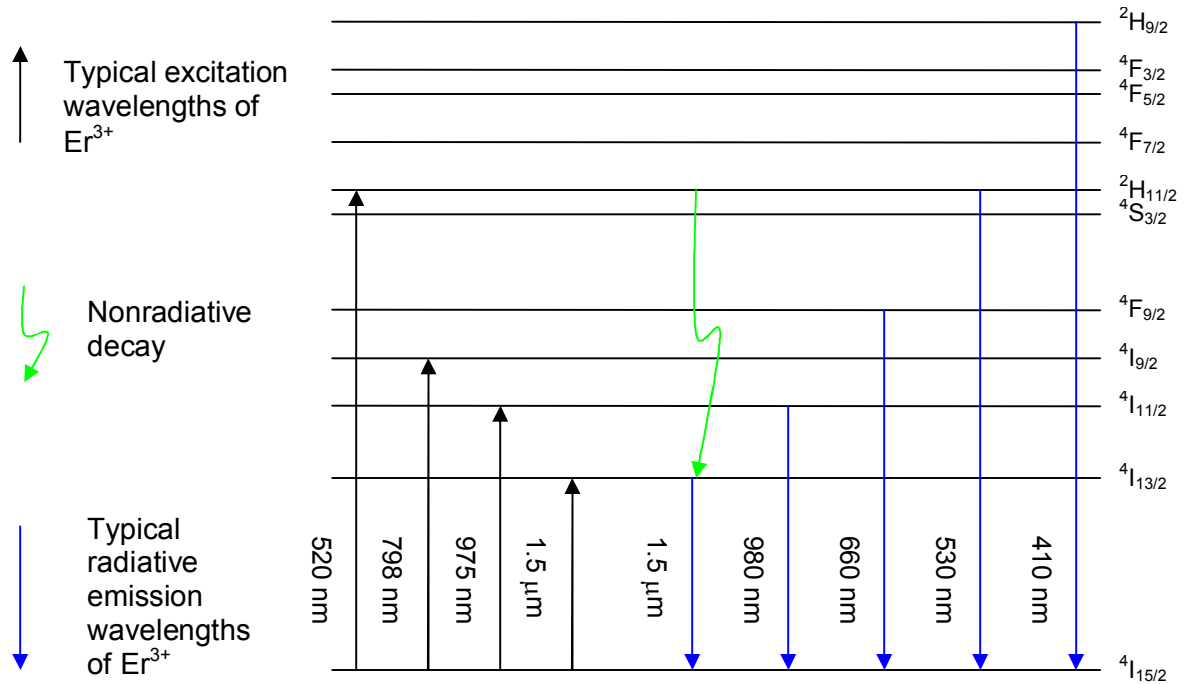


Figure 1.17 : Energy levels of Er^{3+}

For Er^{3+} samples, an excitation wavelength of 520 nm is used to provide direct excitation to the $^2\text{H}_{11/2}$ level, where the energy rapidly decays nonradiatively to the $^4\text{I}_{13/2}$ level.⁴⁷ The $^4\text{I}_{13/2} \rightarrow ^4\text{I}_{15/2}$ transition gives rise to emission at around 1.54 μm . Figure 1.18 shows the energy levels of Nd^{3+} .

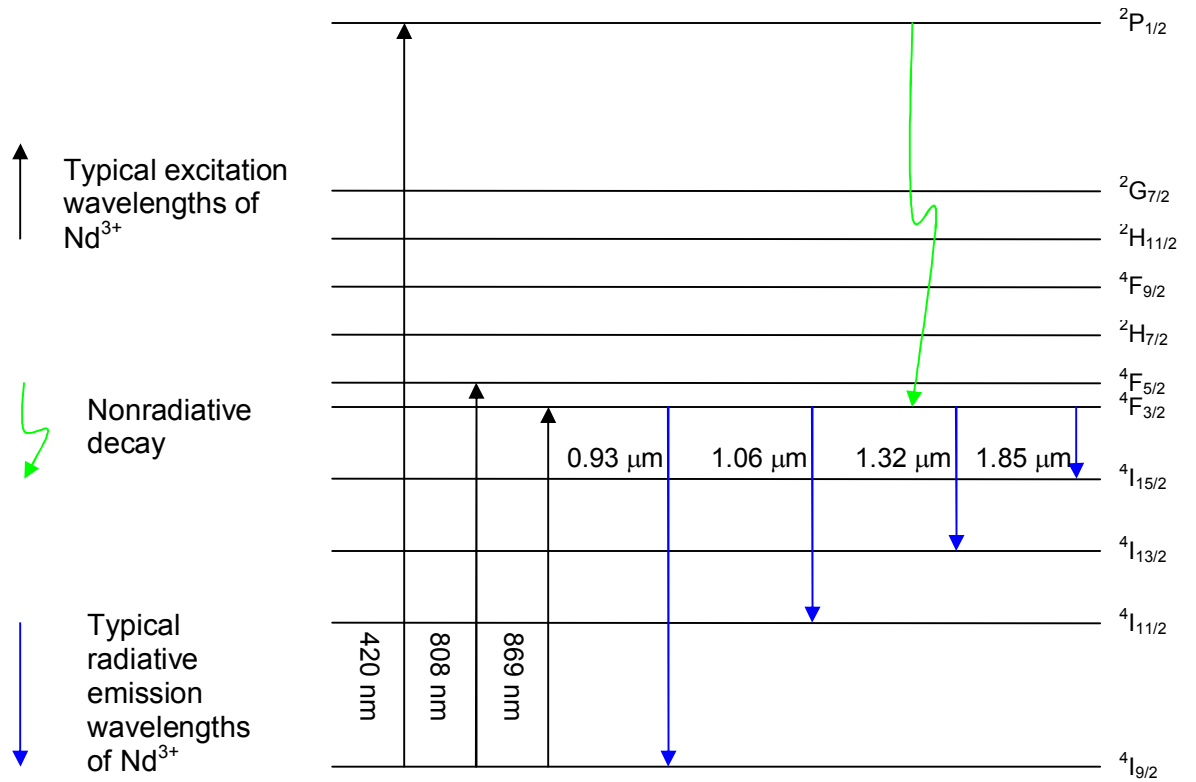


Figure 1.18 : Energy levels of Nd³⁺

For the Nd³⁺ samples, the excitation wavelength used is 420 nm to provide excitation to the ²P_{1/2} level before the energy relaxes to the ⁴F_{3/2} level, where NIR emissions take place. Figure 1.19 shows the energy levels of Yb³⁺.

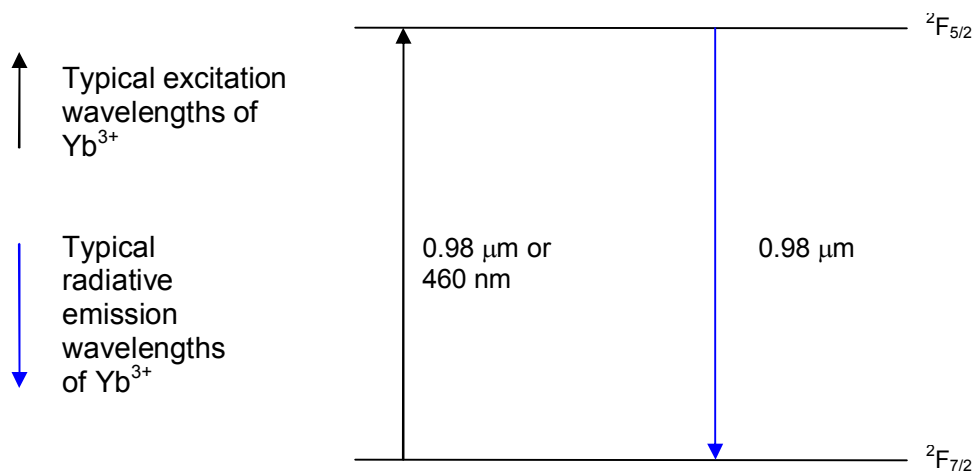


Figure 1.19 : Energy levels of Yb^{3+}

Yb^{3+} has only two energy levels⁴⁷ in the relevant range and the excited energy level, ${}^2F_{5/2}$ can be excited via either 460 nm or 960 nm.

1.16 Photoluminescence

Photoluminescence (PL) is a standard optical technique whereby a substance absorbs photons and then re-radiates them. Photo-excitation is normally carried out using a laser and the light incident on the sample promotes electrons to a higher energy level. At the higher energy state, the electrons will lose their energy through multiphonon relaxations before the formation of excitons. The recombination of the excitons allows us to obtain information such as the luminescence levels of a sample relative to the ground level and hence obtain the radiative decay lifetimes.

This thesis describes experiments that were normally performed on samples in powder form. A small quantity of the powder was placed inside a sample holder which was secured using a microscopic slide. The sample holder was then attached to a sample arm and placed inside a cryostat. In this thesis, the photoluminescence experiments were performed at room temperature.

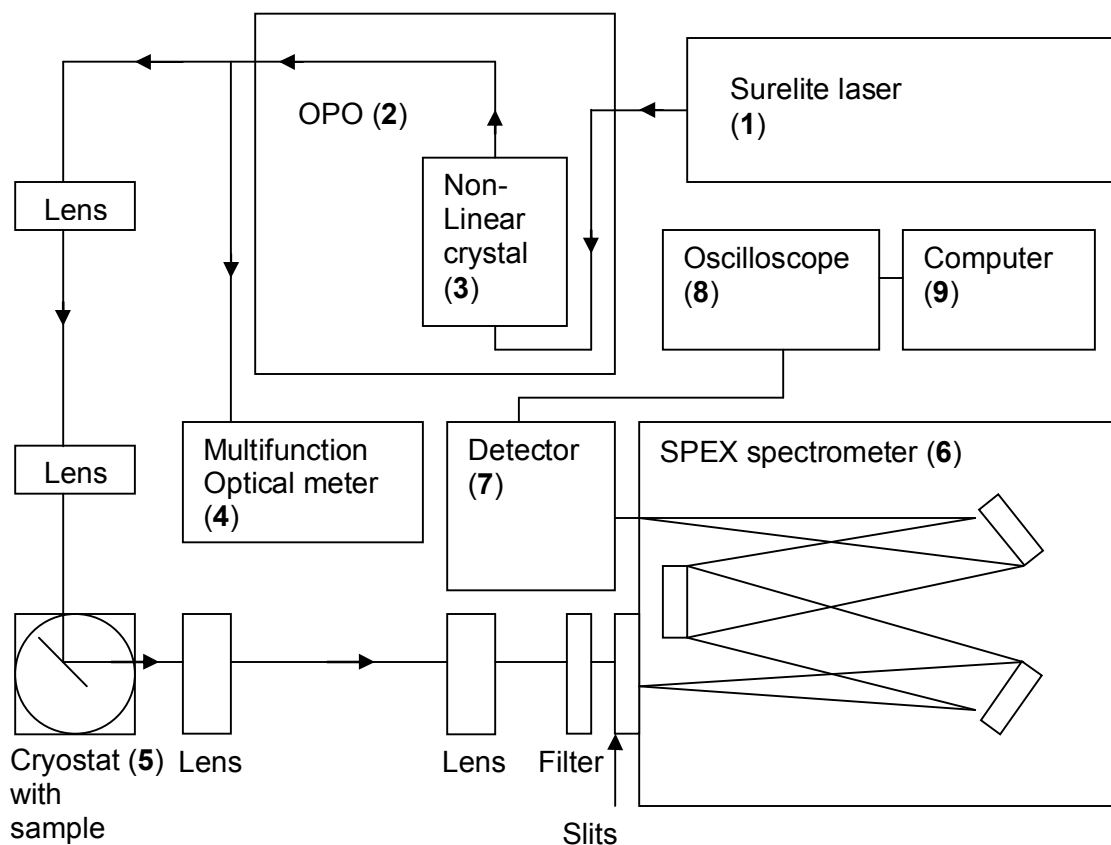


Figure 1.20 : Experimental setup of photoluminescence experiments

Figure 1.20 shows the experimental setup of our photoluminescence experiments. The Continuum Surelite (SLI-10) laser (1) generates laser light at the Nd:YAG (neodymium-doped yttrium aluminium garnet) fundamental wavelength of 1064 nm or its second (532 nm) or third (355 nm) harmonic by passing the fundamental beam through a second and second plus third harmonic generator. The 355 nm beam then go through the Panther optical parametric oscillator (OPO) (2), where coherent light between 410 nm and 2550 nm can be produced. Tuning the laser output at a specific wavelength is done using a computer controlled program. Similar to a laser, an OPO is a kind of laser resonator based on optical gain from parametric amplification in a nonlinear crystal (3). Optical parametric process involves a three photon interaction whereby one incoming pump photon splits into a pair of less energetic ones by means of a nonlinear optical interaction. In principle, the two resulting photons will not have the same energies and the higher

energy one is referred to as the signal and the other as the idler. Each of the OPO's three crystals must be phase matched at a specific angle for each wavelength and the angular position of the oscillator crystal determines the output wavelength. As such, the OPO allows a wide range of wavelengths to be accessed.

The laser line from the OPO is measured by using the Newport multifunction optical meter (model 1835-C) (4) and then it passes through a series of lenses which allow the beam to be focused onto the sample in the Oxford instrument cryostat (5). The photoluminescence is then collected and collimated by a lens before it is refocused using another lens and then filtered onto the adjustable entrance slits of the Jobin Yvon Horiba Triax 550 spectrometer (6). It is then dispersed using a 600 line/mm grating blazed at 1 μm before the selected wavelength is reflected onto the exit slits of the spectrometer. Usually, the exit slits are adjusted to be the same width as the entrance slits. A nitrogen cooled photomultiplier tube (PMT) (Photocool PC176TSCE005) (7) is then used to detect and multiply the signal collected from the spectrometer. The response from the PMT is then sent to an oscilloscope (LeCroy waverunner LT372) (8) and the collection of the photoluminescence spectra and lifetime data is facilitated by a connecting computer (9).

1.17 Outline of thesis

This thesis will present the work that has been done in the design, synthesis and characterisation of novel organic ligands to be used to form Ln^{3+} complexes. In this chapter, we have seen the work that has been done in the area of polymer waveguides and a basic grounding on light amplification and the characteristics of Ln^{3+} ions were also discussed. While this chapter has provided us with an overview of the work that has been done in the area of polymer waveguides and some basic concepts of laser systems and Ln^{3+} , further literature reviews in the area of Ln^{3+} complexes for optical devices will be discussed thoroughly in chapters 2, 3 and 4.

Consisting of six chapters, they can be classified under four main headings – introduction (Chapter 1), results and discussion (Chapters 2,3,4), experimental (Chapter 5) and conclusion (Chapter 6). In chapter 2, we discuss the effects of high vibrational bonds on Ln^{3+} ions by utilizing the 1,1,1,5,5,5-hexafluoroacetylacetone (HFA) ligand. Chapter 3 presents some of the attempts that we made to synthesize novel ligands and Ln^{3+} complexes without any high vibrational oscillators. In chapter 4, we discuss the preparation of new fluorinated Ln^{3+} complexes. By diluting these Ln^{3+} complexes with Y^{3+} , we have minimized the detrimental effects of ion-ion interactions and have produced unprecedented radiative lifetime results. Chapter 5 consists of all the experimental procedures and characterisation data. We will conclude in chapter 6 and highlight the future work that could be pursued.

1.18 References for chapter 1

1. Senior; J., *Optical fiber communication*, Prentice Hall, 2nd edition, London, **1992**
2. Desurvire; E., *Erbium-Doped Fiber Amplifiers – Principles and Applications*, John Wiley & Sons, Inc, New York, **1994**
3. Slooff; L. H., *PhD thesis – Utrecht University* ISBN: 90-393-2537-5, **2000**
4. Mears; R. J., Reekie; L., Jauncey; I. M. and Payne; D. N., *Electronic Letters*, 23, **1987**, 1026
5. Walker; G. R., Walker; N. G., Steele; R. C., Creaner; M. J. and Brain; M. C., *Journal of Lightwave Technology*, 9, **1991**, 182
6. Tsonev; L., *Optical Materials*, 30, **2008**, 892
7. Slooff; L. H., van Blaaderen; A., Polman; A., Hebbink; G. A., Klink; S. I., van Veggel; F. C. J. M., Reinhoudt; D. N. and Hofstraat; J. W., *Journal of Applied Physics*, 91, **2002**, 3955
8. Wang; H., Qian; G., Wang; Z. and Wang; M., *Spectrochimica Acta Part A*, 62, **2005**, 146
9. Ma; H., Jen; A. K-Y and Dalton; L. R., *Advance Materials*, 14, **2002**, 1339
10. Zhao; Y-G., Lu; W-K., Ma; Y., Kim; S-S., Ho; S. T. and Marks; T. J., *Applied Physics Letters*, 77, **2000**, 2961
11. Savio; R. L., Miritello; M., Piro; A. M., Priolo; F. and Lacona; F., *Applied Physics Letters*, 93, **2008**, 021919
12. Sun; L-N., Zhang; Y., Yu ; J-B., Peng; C-Y. and Zhang; H-J., *Journal of Photochemistry and Photobiology A: Chemistry*, 199, **2008**, 57

13. Geusic; J. E. and Scovil; H. E. D, *Bell Syst. Tech. J.* 41, **1962**, 1371
14. Koester; C. J. and Snitzer; E., *Applied Optics*, 3, **1964**, 1182
15. Snitzer; E. and Woodcock; R., *Applied Physics Letters*, 6, **1965**, 45
16. Stone; J. and Burrus; C. A., *Applied Physics Letters*, 23, **1973**, 388
17. Stone; J. and Burrus; C. A., *Applied Optics*, 13, **1974**, 1256
18. Stone; J., Burrus; C. A., Dentai; A. G. and Miller; B. I., *Applied Physics Letters*, 29, **1976**, 37
19. Hegarty; J., Broer; M. M., Golding; B., Simpson; J. R. and MacChesney; J. B., *Physical Review Letters*, 51, **1983**, 2033
20. Broer; M. M., Golding; B., Heammerle; W. H. and Simpson; J. R., *Physical Review B*, 33, **1986**, 4160
21. Poole; S. B., Payne; D. N. and Fermann; M. E., *Electronic Letters*, 21, **1985**, 737
22. Mears; R. J., Reekie; L., Jauncie; I. M. and Payne; D. N., *Electronic Letters*, 23, **1987**, 1026
23. Desurvire; E., Simpson; J. R. and Becker; P. C., *Optical Letters*, 12, **1987**, 888
24. Nakazawa; M., Kimura; Y. and Suzuki; K., *Applied Physics Letters*, 54, **1989**, 295
25. W. H. Wong and E. Y. B. Pun, *Applied Physics Letters*, 79, **2001**, 3576,

26. Eldada; L. and Shacklette; L. W., *IEEE Journal of Selected Topics in Quantum Electronics*, 6, **2000**, 54
27. Kaino; T., *Applied Physics Letters*, 48, **1986**, 757
28. X. Fei; J. Hu; H. Zhang; P. Sha; J. Piao; Z. Cui and D. Zhang, *Journal of Polymer Science Part A: Chemistry*, 45, **2007**, 5923,
29. Pitois; C., Vukmirovic; S. and Hult; A., *Macromolecules*, 32, **1999**, 2903
30. Imamura; S., Yoshimura; R and Izawa; T., *Electronics Letters*, 27, **1991**, 1342
31. Yuichi; K., Kazuo; K. and Koichi; N., *Journal of Applied Polymer Science*, 63, **1997**, 363
32. Zhou; D., Koike; Y. and Okamoto; Y., *Journal of Fluorine Chemistry*, 129, **2008**, 248
33. Braun; D. and Czewinski; W. K., *Macromolecules Chemistry*, 188, **1987**, 2389
34. Teng; H., Yang; L., Mikes; F., Koike; Y. and Okamoto; Y., *Polymers for Advanced Technologies*, 18, **2007**, 453
35. H. Gao; D. Wang; S. Guan; W. Jiang; Z. Jiang; W. Gao and D. Zhang, *Macromolecular Rapid Communications*, 28, **2007**, 252
36. Han; K., Jang; W-H. and Rhee; T. H., *Journal of Applied Polymer Science*, 77, **2000**, 2172
37. Matsuura; T., Ando; S., Sasaki; S. and Yamamoto; F., *Macromolecules*, 27, **1994**, 6665

38. Xie; S. X., Zhang; Z. J. and Wei; W., *Journal of the Korean Physical Society*, 51, **2007**, 1536
39. Kowalczyk; T. C, Kosc; T., Singer; K. D., Cahill; P. A., Seager; C. H., Meinhardt; M. B., Beuhler; A. J. and Wargowski; D. A., *Journal of Applied Physics*, 76, **1994**, 2505
40. Matsuura; T., Hasuda; Y., Nashi; S. and Yamada; N., *Macromolecules*, 24, **1991**, 5001
41. Ma; X., Lv; Z., Wang; D., Guan; S., Chen; C., Wang; G., Zhang; D. and Jiang; Z., *Journal of Photochemistry and Photobiology A : Chemistry*, 188, **2007**, 43
42. Tumminelli; R., Hakimi; F. and Haavisto; J., *Optical Letters*, 16, **1991**, 1098
43. Lin; S., Feuerstein; R. J. and Mickelson; A. R., *Journal of Applied Physics*, 79, **1996**, 2868
44. Kido; J., Okamoto; Y., *Chemical Reviews*, 102, **2002**, 2357
45. Wolbers; M. P. O., Van Veggel; F. C. J. M., Snellink-Ruel; B. H. M., Hofstraat; J. W., Geurts; F. A. J., and Reinhoudt; D. N., *Journal Chemical Society, Perkin Transactions 2*, **1998**, 2141
46. Bünzli; J-C. G., Comby; S., Chauvin; A-S. and Vandevyver; C. D. B., *Journal of Rare Earths*, 25, **2007**, 257
47. Becker; P. C., Olsson; N. A. and Simpson; J. R., *Erbium-Doped Fiber Amplifiers – Fundamentals and Technology*, Academic press, San Diego, **1999**
48. Bünzli; J-C. G., *Accounts of Chemical Research*, 39, **2006**, 53

49. Blasse; G. and Grabmaier; B. C., *Luminescent Materials*, Springer, Berlin, **1994**
50. Petoud; S., Bünzli; J-C. G., Glanzman; T., Piguet; C., Xiang; Q. and Thummel; R. P., *Journal of Luminescence*, 82, **1999**, 69
51. Dorenbos; P., *Journal of Luminescence*, 91, **2000**, 91
52. Hasegawa; Y., Wada; Y. and Yanagida; S., *Journal of Photochemistry and Photobiology C: Photochemistry Reviews*, 5, **2004**, 183
53. Bünzli; J-C. G. and Piguet; C., *Chemical Society Review*, 34, **2005**, 1048
54. Yanagida; S., Hasegawa; Y., Murakoshi; K., Wada; Y., Nakashima; N. and Yamanaka; T., *Coordination Chemistry Reviews*, 171, **1998**, 461
55. Klink; S. I., Grave; L., Reinhoudt; D. N., van Veggel; F. C. J. M., Werts; M. H. V., Geurts; F. A. J. and Hofstraat; J. W., *Journal Physical Chemistry A*, 104, **2000**, 5457 For erbium, another value (of 8 ms) was cited in the following literature - Magennis; S. W., Ferguson; A. J., Bryden; T., Jones; T. S., Beeby; A. and Samuel; I. D. W., *Synthetic Metals*, 138, **2003**, 463
56. Shavaleev; N. M., Pope; S. J. A., Bell; Z. R., Faulkner; S. and Ward; M. D., *Dalton Transactions*, **2003**, 808
57. Hasegawa; Y., Ohkubo; T., Sogabe; K., Kawamura; Y., Wada; Y., Nakashima; N. and Yanagida; S., *Angewandte Chemie International Edition*, 39, **2000**, 357
58. Ning; L., Italo; M. and Brivio; G. P., *Journal of Materials Chemistry*, 17, **2007**, 4464
59. Stein; G. and Wurzberg; E., *Journal of Chemical Physics*, 62, **1975**, 208

60. Haas; Y. and Stein; G., *Journal of Physical Chemistry*, 76, **1972**, 1093
61. Haas; Y., Stein; G. and Würzberg; E., *Journal of Chemical Physics*, 60, **1974**, 258
62. Weissman; S. I., *Journal of Chemical Physics*, 10, **1942**, 214
63. Kik; P. G., Polman; A., *Materials Science and Engineering B81*, **2001**, 3-8
64. Escribano; P., Julián-López; B., Planelles-Aragó; J., Cordoncillo; E., Viana; B. and Sanchez; C., *Journal of Materials Chemistry*, 18, **2008**, 23
65. Sun; L., Zhang; H., Meng; Q., Liu; F., Fu; L., Peng; C., Yu; J., Zheng; G., Wang; S., *Journal of Physical Chemistry, B*, 109, **2005**, 6174
66. Bowen; E. J., *Luminescence in Chemistry*, D. Van Nostrand Company Ltd, London, **1968**
67. Crosby; G. A., Whan; R. E., Alire; R. M., *Journal of Chemical Physics*, 34, **1961**, 743
68. Werts; M. H. V., Hofstraat; J. W., Geurts; F. A. J., Verhoeven; J. W., *Chemical Physics Letters*, 276, **1997**, 196
69. Förster; T., *Discussions of Faraday Society*, 27, **1959**, 7
70. Dexter; D. L., *Journal of Chemical Physics*, 21, **1953**, 836
71. Horrocks; W. D., Rhee; M- J., Snyder; A. P. and Sudnick; D. R., *Journal of American Chemical Society*, 102, **1980**, 3650
72. Latva; M, Takalo; H, Mukkala; V. M., Matachescu; C., Rodriguez-Ubis; J. C. and Kankare ; J., *Journal of Luminescence*, 75, **1997**, 149

73. Werts; M. H. V., Verhoeven; J. W. and Hofstraat; J. W., *Journal of Chemical Society, Perkin Transactions 2*, **2000**, 433
74. Werts; M. H. V., Woudenberg; R. H., Emmerink; P. G., van Gassel; R., Hofstraat; J. W. and Verhoeven; J. W., *Angewandte Chemie International Edition.*, 39, **2000**, 4542
75. Faulkner; S., Carrié; M-C., Pope; S. J. A., Squire; J., Beeby ; A. and Sammes ; P. G., *Dalton Transactions*, **2004**, 1405
76. Pope; S. J. A., Coe; B. J. and Faulkner; S., *Chemical Communications*, **2004**, 1550
77. Shavaleev; N. M., Moorcraft; L. P., Pope; S. J. A., Bell; Z. R., Faulkner; S. and Ward; M. D., *Chemical Communications*, **2003**, 1134
78. Xu; H., Shi; L., Ma; E., Zhang; L., Wei; Q. and Chen; Z., *Chemical Communications*, **2006**, 1601

Chapter 2 – Results and discussion 1 : The role of high energy oscillators in luminescence quenching

2.1 Introduction

Ln^{3+} ions such as Nd^{3+} , Er^{3+} and Yb^{3+} have remarkable optical properties such as high luminescence quantum efficiency and sharp emission lines with long decay lifetimes in the near infrared (NIR) region.^{1,2,3} Nd^{3+} is one of the most popular infrared luminescent materials for application in laser systems such as the common 1.06 μm laser.^{4,5} Yb^{3+} has an emission line at around 1 μm , which is transmitted efficiently through human tissues and can be deployed in diagnostic luminescent probes.^{5,6}

Er^{3+} has a transition line at about 1.5 μm and that wavelength is coincident with the low loss telecommunications window and hence is used as the active element in optical amplifiers.⁷ Erbium-Doped Fiber Amplifiers (EDFAs) and Erbium-Doped Waveguide Amplifiers (EDWAs) play a key role in long-distance optical communication and networking systems.⁸ These amplifiers have the potential for large optical gains and have the ability to integrate with other integrated optics components.⁹ Splitters, couplers, multiplexers and amplifiers can be integrated on one single planar substrate to enable efficient manipulation of optical signals.¹⁰ A basic element of integrated optics is the planar optical waveguide which consists of a high refractive index guiding core layer sandwiched between two lower-index cladding layers.¹⁰ Waveguiding is a process where optical signals travel in the guiding layer due to total internal reflection at the interface between the cladding and core.¹¹ Polymer optical waveguides doped with Er^{3+} are increasingly important due to the ease of fabrication using standard lithographic techniques, low cost and high packing density.¹²

Polymeric materials such as poly(methyl methacrylate) (PMMA) have been widely studied as hosts for rare-earth ions.^{13,14} However, due to the insolubility of the inorganic Ln^{3+} salts in polymeric hosts, organic ligands are used to encapsulate the emissive ions to improve their solubility properties. We saw in chapter 1 that the

high vibrational energy bonds such as C–H and O–H bonds can quench the luminescence of Ln^{3+} ions. In the following reviews, we discuss these effects by looking at the ligand systems deployed by the various research groups.

2.1.1 Effects of high vibrational energy bonds on Ln^{3+} ions

Conventional laser systems based on emission from Nd^{3+} in solution have been considered to be promising due to their ability to be cooled by circulation, which would enable the laser systems to work with high power and high pulse frequency.¹⁵ However, organic solvents contain many C–H bonds and de-excitation via vibrational excitation prevails. Heller *et al*^{16,17} employed the idea of using solvent molecules with low energy vibrations as a liquid matrix for Nd^{3+} and subsequently, led to the first successful utilization of inorganic aprotic solvents, SeOCl_2 and POCl_3 for enhanced luminescence of Nd^{3+} in a liquid matrix. Due to their reactivity and toxicity, these unconventional solvents are considered inappropriate for practical applications. In 1996, Hasegawa *et al*¹⁵ were the first to observe the luminescence of Nd^{3+} complexes in organic solvents. 1,1,1,5,5,5-Hexafluoroacetylacetonate (HHFA) was used to complex to Nd^{3+} and based on infrared spectroscopy, differential scanning calorimetry and elemental analysis, it was suggested that the Nd^{3+} complex should form a square-anti prism with eight coordinated oxygens of three HFA ligands and two molecules of H_2O of crystallization, giving the stoichiometry, $\text{Nd}(\text{HFA})_3 \cdot 2\text{H}_2\text{O}$. Elimination of H_2O and the replacement of C–H bond with C–D bond was done by treating $\text{Nd}(\text{HFA})_3 \cdot 2\text{H}_2\text{O}$ with methanol- d_1 and methanol- d_4 for deuteration by keto-enol equilibrium. Chemical structures of HHFA (**14**) and hexafluoroacetylacetonate- d_2 (**15**) are shown in figure 2.1.

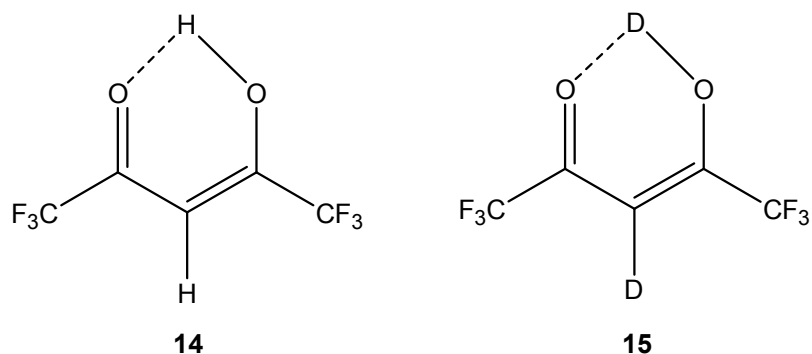


Figure 2.1 : Chemical structure of HHFA (**14**) and HFA-D (**15**)

Although the resulting Nd^{3+} complex could dissolve in various organic solvents such as methanol (CH_3OH), pyridine, acetone (CH_3COCH_3), dimethyl sulfoxide (DMSO), tetrahydrofuran (THF), dimethylformamide (DMF), diethyl ether (Et_2O) and acetic acid, it was found that $\text{Nd}(\text{HFA-}d)_3$ could dissolve with an extremely high concentration in acetone and this was the solvent of choice for optical measurements. A solution of $\text{Nd}(\text{HFA-}d)_3$ in acetone- d_6 showed typical Nd^{3+} emissions at 880 nm, 1062 nm and 1345 nm when the system was excited at 585 nm. The quantum yield of emission was determined to be of the order of 10^{-2} . In chapter 1 of this thesis, it was noted that the energy gap of Nd^{3+} at 5400 cm^{-1} is resonant with the 2nd harmonic of the O–H bond. No emission was observed in either non-deuterated acetone or deuterated acetone without careful dehydration of the complex; this demonstrates the potent quenching effect of H_2O molecules in the coordination sphere and the quantum yield of the system containing C–H or O–H bonds was estimated to be of the order of 10^{-5} .

In subsequent experiments, Hasegawa *et al*¹⁸ investigated the effects of the surrounding media in the quenching process. Lifetime measurements on $\text{Nd}(\text{HFA-}d)_3$, were performed in methanol- d_4 , acetone- d_6 , THF- d_8 , DMF- d_7 and DMSO- d_6 and the results are shown in table 2.1.

Solvent	Lifetime in μs
Methanol- d_4	0.70
Acetone- d_6	1.71
THF- d_8	2.33
DMF- d_7	2.86
DMSO- d_6	6.30

Table 2.1 : Lifetime measurements on $\text{Nd}(\text{HFA-}d)_3$ performed in deuterated solvents

Nd^{3+} has a usual coordination number of 8 - 10 and since the deuteration of the hydrated complex was done in methanol- d_4 , the remaining sites are likely to have been occupied by D_2O or CD_3OD molecules. Although O–D bonds are lower in energy than O–H bonds, quenching via D_2O molecules is efficient especially when

they are in the coordination sphere. The measured lifetime of Nd(HFA-*d*)₃ with two molecules of D₂O in its coordination sphere was the lowest in methanol-*d*₄ with a lifetime of 0.70 μs and highest in DMSO-*d*₆ with a lifetime of 6.30 μs. The dominant vibration of DMSO-*d*₆ ($\nu_{S=O} = 1060 \text{ cm}^{-1}$) is comparable with that of THF-*d*₈ ($\nu_{C-O-C} = 1070 \text{ cm}^{-1}$) and despite this similarity, the emission lifetime of the Nd³⁺ complex in DMSO-*d*₆ was found to be much higher than that in THF-*d*₈. When the lifetime measurements were done in DMSO-*d*₆, it was found that the DMSO-*d*₆ molecules had displaced D₂O in the coordination sphere, hence preventing nonradiative transmission to D₂O and achieving the highest emission efficiency. Similar lifetime experiments were also done in non-deuterated solvents. An improvement of four orders of magnitude in lifetimes was achieved for deuterated solvents compared to their non-deuterated equivalents and the fact that the same complex had different lifetimes in different solvents indicates that the surrounding medium has a role to play in luminescence quenching.

Beeby *et al*¹⁹ reported luminescent lifetimes of Nd³⁺ ions in a series of solvents such as H₂O, D₂O, methanol (CH₃OH), deuterated methanol (CH₃OD and CD₃OD), dimethyl sulfoxide (DMSO) and deuterated dimethyl sulfoxide (DMSO-*d*₆). Nd³⁺ salts used in the experiments were in the form of: acetate (OAc), nitrate (NO₃), chloride (Cl) and perchlorate (ClO₄). Lifetime results of the different salts in the different solvents are shown in table 2.2.

Salt/Solvent	H ₂ O	D ₂ O	CH ₃ OH	CH ₃ OD	CD ₃ OD	DMSO	DMSO- <i>d</i> ₆
Nd(NO ₃) ₃ ·6H ₂ O	29 ns	152 ns	70 ns	290 ns	476 ns	1700 ns	9020 ns
Nd(ClO ₄) ₃ ·xH ₂ O	30 ns	143 ns	43 ns	191 ns	385 ns	1726 ns	6200 ns
Nd(OAc) ₃ ·H ₂ O	41 ns	158 ns	131 ns	322 ns	517 ns	1148 ns	2329 ns
NdCl ₃	29 ns	147 ns	68 ns	245 ns	478 ns	1692 ns	7880 ns

Table 2.2 : Lifetime data of various Nd³⁺ salts in organic solvents

From table 2.2, it can be seen that deuteration of the solvent results in increased lifetimes by removing non radiative decay pathways coupled to the vibration of the

C–H and O–H bonds. Looking at the lifetimes for $\text{Nd}(\text{NO}_3)_3 \cdot 6\text{H}_2\text{O}$, measurements in CH_3OD demonstrated a lifetime of 290 ns, which is an improvement of >300% over measurements in CH_3OH , whereas the lifetime of 476 ns in CD_3OD is an improvement of ~64% over measurements in CH_3OD . The lifetimes measured in CH_3OH , CH_3OD and CD_3OD showed increments as the hydrogens are being replaced by deuteriums. From the results in table 2.2, we can confirm that O–H oscillators are more potent quenchers than C–H oscillators.

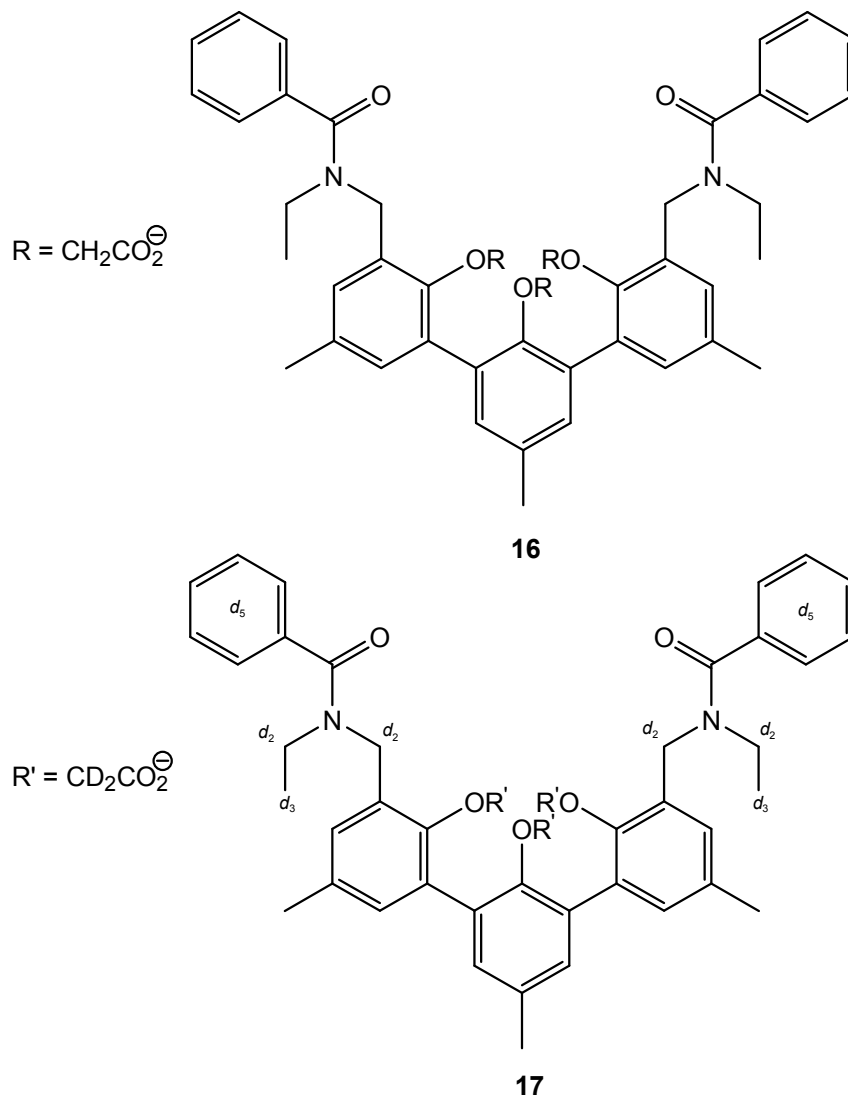


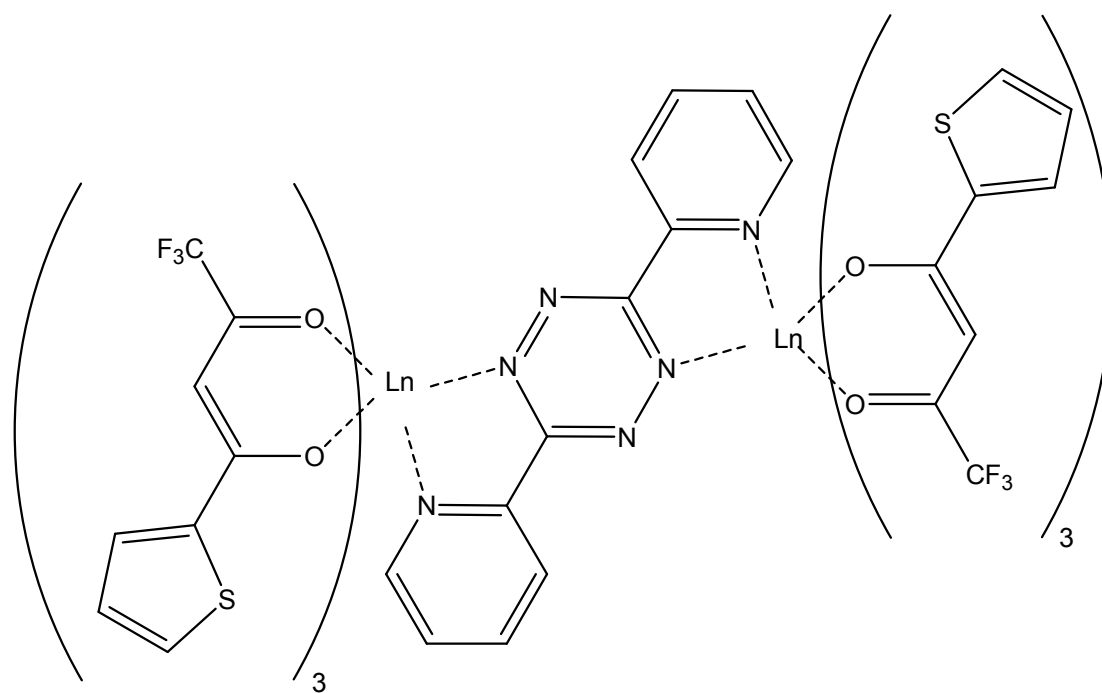
Figure 2.2 : Terphenyl-based ligands; non-deuterated (**16**) and partly deuterated (**17**)

Klink *et al*²¹ conducted luminescence studies of Nd³⁺, Er³⁺ and Yb³⁺ complexes with a polydentate ligand in dimethyl sulfoxide (DMSO-*h*₆) and deuterated dimethyl sulfoxide (DMSO-*d*₆). The triphenylene-functionalized ligand (Figure 2.3) used has eight oxygen donor atoms which encapsulate the Ln³⁺ ions and saturate the coordination sphere. By saturating the coordination sphere, solvent or H₂O molecules will not be coordinated and the quenching routes will be via the C–H bonds on the ligands and surrounding media.

Complex	Lifetime measured in DMSO-<i>h</i>₆	Lifetime measured in DMSO-<i>d</i>₆
(Yb)· 18	9.4 μs	18.6 μs
(Er)· 18	2.4 μs	3.4 μs
(Nd)· 18	1.4 μs	2.5 μs

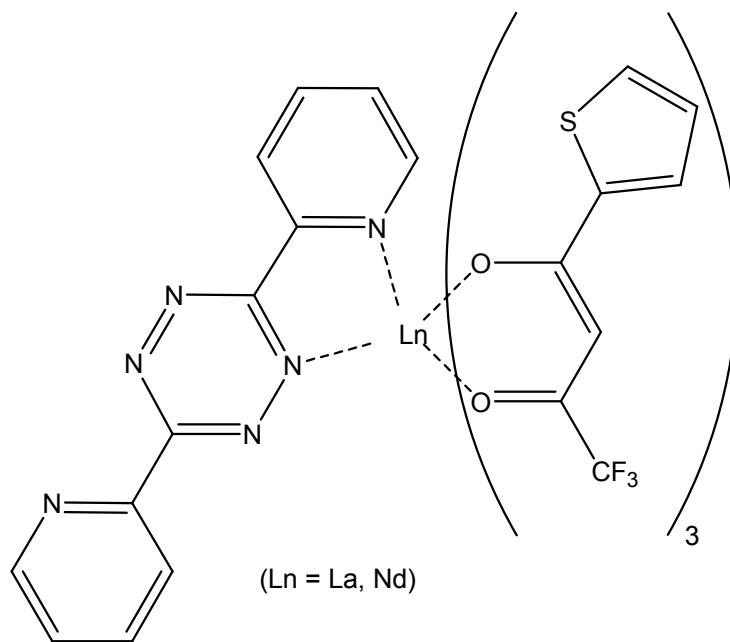
Table 2.4 : Lifetimes of Ln³⁺ complexes measured in DMSO-*h*₆ and DMSO-*d*₆

Table 2.4 shows the decay lifetime of the complexes measured in DMSO-*h*₆ and DMSO-*d*₆. Due to the lower vibrational energy of the C–D bond, decay lifetimes measured in DMSO-*d*₆ are significantly higher. Lifetime increments of about 80%, 42% and 100% were achieved for the Nd³⁺, Er³⁺ and Yb³⁺ complexes, respectively. C–H bonds of DMSO-*h*₆ have vibrational energy of 2950 cm⁻¹ and the number of vibrational quanta necessary to match the energy gaps are 1 - 2, 2 - 3 and 3 - 4 for Nd³⁺, Er³⁺ and Yb³⁺, respectively. C–D bonds have energy of 2100 cm⁻¹ and from figure 1.9 in chapter 1, it can be seen that more vibrational quanta are required to match the emissive states of the ions, rendering the de-excitation less effective. Natural radiative lifetimes of the ions have been measured and are found to be at least two orders of magnitude above the lifetimes measured in DMSO-*d*₆. This suggests that the high energy C–H bonds on the ligands limit the radiative lifetime and the surrounding medium may play a significant role as well.



(Ln = Gd, Er, Yb)

19



(Ln = La, Nd)

20

Figure 2.4 : Dinuclear complexes of the form $[\{Ln(tta)_3\}_2(\mu\text{-BPTZ})]$ (**19**) and mononuclear complexes of the form $[Ln(tta)_3(H_2O)_2]$ (**20**) prepared by Shavaleev *et al*²²

Mononuclear complexes of the form $[\text{Ln}(\text{tta})_3(\text{H}_2\text{O})_2]$ (where Ln = lanthanide ions: La, Nd, Gd, Er and Yb; tta = thenoyl(trifluoro)acetone) (Figure 2.4, **20**) and dinuclear complexes of the form $[\{\text{Ln}(\text{tta})_3\}_2(\mu\text{-BPTZ})]$ (where BPTZ = bis-bidentate bridging ligand 3,6-bis(2-pyridyl)tetrazine) (Figure 2.4, **19**) were synthesized by Shavaleev *et al.*²² One or two Ln^{3+} tris-diketonate units $\{\text{Ln}(\text{tta})_3\}$ are bound to the *N,N*-bidentate compartments of BPTZ for the mononuclear and dinuclear complexes, respectively. Larger Ln^{3+} such as La^{3+} and Nd^{3+} only give a mononuclear complex whereas smaller Ln^{3+} such as Gd^{3+} , Er^{3+} and Yb^{3+} give the dinuclear complex. Time-resolved luminescence studies on the complexes with Yb^{3+} , Nd^{3+} and Er^{3+} were conducted in the solid state and in dichloromethane (DCM) solution. The complexes can be sensitised by irradiation either at 337 nm into the tta-based transition, or at 520 nm into the BPTZ-centred transition and the lifetime data are presented in table 2.5.

	Lifetimes in μs		
	CH_2Cl_2 solution	CH_2Cl_2 solution	Solid
Complex / Excitation wavelength	λ_{exe} 337 nm	λ_{exe} 520 nm	λ_{exe} 337 nm
$[\text{Nd}(\text{tta})_3(\text{BPTZ})]$	0.76	0.78	1.25
$[\{\text{Yb}(\text{tta})_3\}_2(\mu\text{-BPTZ})]$	1.0, 13.3 *	14.5	14.1
$[\text{Yb}(\text{tta})_3(\text{H}_2\text{O})_2]$	0.85	–	–
$[\{\text{Er}(\text{tta})_3\}_2(\mu\text{-BPTZ})]$	0.15, 1.70 *	1.69	2.0
$[\text{Er}(\text{tta})_3(\text{H}_2\text{O})_2]$	0.20	–	–

* – Dual-exponential decay

Table 2.5 : Lifetime data of Nd^{3+} , Yb^{3+} and Er^{3+} mononuclear and dinuclear complexes

From table 2.5, we can see that all the emission lifetimes are in the microsecond domain and the detrimental effects of coordinated H_2O can be seen in $[\text{Yb}(\text{tta})_3(\text{H}_2\text{O})_2]$ and $[\text{Er}(\text{tta})_3(\text{H}_2\text{O})_2]$ where the lifetimes of 0.85 μs and 0.20 μs

respectively are in the submicrosecond region. O–H bonds have high vibrational energy and consequently, coordinated H₂O can quench luminescence effectively. For [Nd(tta)₃(BPTZ)], the lifetime of 1.25 μs performed in its solid state is longer than those conducted in CH₂Cl₂ solution with lifetimes of 0.76 μs (at λ_{exe} 337 nm) and 0.78 μs (at λ_{exe} 520 nm). The improvement can be ascribed to the absence of solvent-based quenching in the solid state. Comparing the lifetime results for [Nd(tta)₃(BPTZ)], [{Yb(tta)₃]₂(μ-BPTZ)] and [{Er(tta)₃]₂(μ-BPTZ)], the difference in the lifetimes measured in CH₂Cl₂ solution and in the solid-state is the least for [{Yb(tta)₃]₂(μ-BPTZ)], followed by [{Er(tta)₃]₂(μ-BPTZ)] and then [Nd(tta)₃(BPTZ)]. This is due to the fact that Yb³⁺ is much less sensitive than Nd³⁺ to quenching by C–H oscillators.

So far, we have seen the disadvantages posed by the presence of high energy oscillators on the Ln³⁺ ions. Luminescence lifetimes are significantly reduced by O–H and C–H bonds. Since Quochi *et al*²³ estimated the rate constant for quenching of Er³⁺ ions in an organic matrix, there has been very little quantitative work on the study of these oscillators. They based their studies on the assumption that the nonradiative decay could be modelled using a continuous medium approximation with a minimum distance, R_{min}, between the ions and the acceptors. This gave a simple expression for the nonradiative rate constant, k_{nr}, (Equation 5)

Equation 5

$$k_{nr} \cong \frac{\lambda_{em}^4}{(2\pi n)^4} \frac{k_r \langle \alpha_A \rangle_{Er}}{R_{min}^3}$$

Where

λ_{em} - Peak of the emission spectral window

n – Medium refractive index

k_r – Radiative decay rate constant

⟨α_A⟩_{Er} - Vibrational absorption averaged over the erbium spectral emission window

This model used by Quochi would naturally give an “average” deactivation rate constant and hence predict a single lifetime decay that would be proportional to the

strength of $\langle \alpha_A \rangle_{\text{Er}}$. Since $\langle \alpha_A \rangle_{\text{Er}}$ would be directly proportional to the average concentration of C–H oscillators in the material, as long as R_{min} remains unchanged, the lifetime will be single exponential and linearly proportional to the deuteration level.

2.1.2 Overview of experimental studies for chapter 2

While efforts are concentrated by various research groups on suppressing vibrational de-excitation by designing ligands without any high energy vibrations, the experimental work associated with this chapter is dedicated to the quantitative study of the effects of high energy vibrational oscillators on luminescence quenching. In order to conduct a systematic study on the effects of C–H bonds on the radiative lifetime of Ln^{3+} ions and to determine the spatial distance over which de-excitation can occur, the tris complex $[\text{Er}(\text{HFA})_3(\text{H}_2\text{O})_2]$ (HHFA = 1,1,1,5,5,5-hexafluoroacetylacetone) and tetrakis complexes $[\text{Cs}][\text{Ln}(\text{HFA})_4]$ (where Ln = Nd, Er and Yb) were used. HFA is chosen as a ligand because it has only one hydrogen atom. By deutrating these tetrakis samples, we are able to compare the benefits of having lower energy oscillators around the Ln^{3+} ions and partial deuteration of the Ln^{3+} complexes will allow us to determine the sensitivity of these ions to their surroundings.

2.2 Preparation of Ln^{3+} complexes

Preparation of Ln^{3+} complexes and deuteration of the HFA ligand will be described under experimental procedures in chapter 5. Two ways of preparing deuterated complexes were examined; the first involved deuteration of the HFA ligand according to literature procedures²⁴ before complexing it with Ln^{3+} ions while in the second method, non-deuterated Ln^{3+} complexes were subjected to H–D exchange using methanol- d_1 in the presence of HHFA.

Previously, it was reported by Hasegawa *et al*¹⁸ that $[\text{Nd}(\text{HFA}-d)_3(\text{D}_2\text{O})_2]$ can be prepared from $[\text{Nd}(\text{HFA}-h)_3(\text{H}_2\text{O})_2]$ and methanol- d_4 when they are kept in solution for 6 h. A similar method was adopted to deuterate $\text{Cs}[\text{Ln}(\text{HFA}-h)_4]$ (where Ln = Nd, Er, Yb). Methanol- d_1 (CH_3OH) (0.3 mL) was used instead of methanol- d_4

(CD₃OD) and after three days of keeping the complexes (0.03 mmol) in solution at 25 °C, the level of deuteration was determined by MALDI to be less than 20%. According to Ellinger, Duschner and Starke,²⁵ the presence of an acid promotes the exchange of hydrogen atoms with deuterium atoms of HHFA. A small quantity of the acidic HHFA free ligand (1 : 1.5 – molar ratio of free HHFA to metal complexes) was then added to the solution and after 24 h at 25 °C, deuteration levels of >90% were achieved. It was also found that adding the same molar concentration of trifluoroacetic acid instead of the HHFA ligand gave similar levels of deuteration. However, to prevent any other ligands from coordinating to the ions, HHFA was used in subsequent deuteration experiments.

Partially deuterated samples were prepared by dissolving Cs[Ln(HFA)₄] (0.03 mmol) in 0.30 mL of the desired composition mixture of CH₃OH and CH₃OD with 0.02 mmol of HHFA. The solutions were kept at 25 °C for 24 h and then rotary evaporated before drying in vacuo over P₂O₅.

For a deuteration level of 98% for Er³⁺, Nd³⁺ and Yb³⁺ complexes, it was calculated that the probability of each central Ln³⁺ (Er³⁺, Nd³⁺ and Yb³⁺) ion being surrounded by four deuterium atoms due to the HFA ligand is 92.2% and the probability of each central Ln³⁺ (Er³⁺, Nd³⁺ and Yb³⁺) ion being surrounded by three deuterium atoms and one hydrogen atom due to the HFA ligand is 7.5%. The probability of each central Ln³⁺ (Er³⁺, Nd³⁺ and Yb³⁺) ion being surrounded by two deuterium atoms and two hydrogen atoms due to the HFA ligand is 0.3%.

2.3 Determination of the deuteration levels

Mass spectroscopy is a technique which allows determination of mass/charge ratio of gas phase molecular ions. The intensity of the signals obtained for each value of *m/e* is representative of the relative abundance of the ion producing the signal. Mass spectra can be used to prove the identity of compounds and also to assist in establishing the structure of a new compound.

2.3.1 MALDI Mass Spectroscopy²⁶

Matrix-assisted laser desorption/ionization (MALDI) mass spectroscopy was the main technique used to obtain the mass spectrum of the prepared complexes. It is a soft ionization technique which facilitates the ionization of relatively involatile molecules, which tend to fragment when ionized by traditional methods such as electron impact. Measuring the deuterated samples using MALDI had the further advantage that samples could be presented in the solid state. Thus, any hydrogen-deuterium exchange with solvents used in electrospray mass spectrometry can be avoided. In MALDI, the ionization was triggered by a nitrogen-laser beam, with the material distributed evenly at one location on a metal MALDI plate. The laser was used to fire at the material in the MALDI spot, which absorbed the laser energy and ionization of the molecules took place.

2.3.2 Determination of the deuteration levels of complexes

Deuteration levels were estimated by simulating the mass spectra using a program called 'isotopes', written by James E. Redman²⁷ in 2005. The relative intensity and m/e ratio values can be determined for a particular molecule by changing the relative abundance table and entering the molecular formula in the main program. Theoretical values for a molecule with any specific deuteration level can be obtained (Figure 2.5).

To vary the level of deuteration from the isotopes table. Top value is for hydrogen and bottom is for deuterium

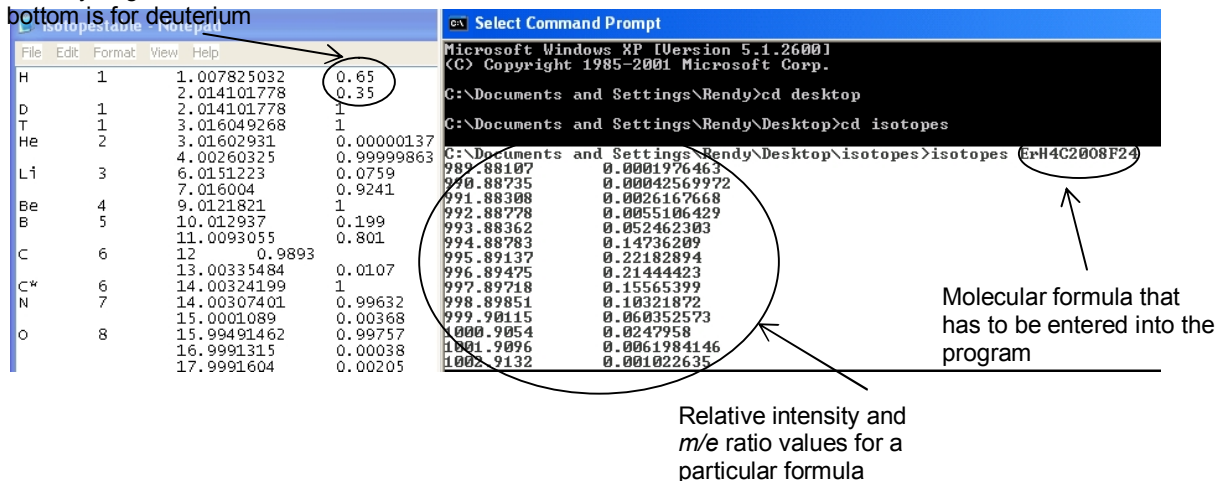


Figure 2.5 : Isotopes program and table

The left of figure 2.5 is the isotopes relative abundance table which allows the user to change the theoretical levels of deuteration. The molecular formula is then entered into the main isotopes program to determine the relative intensity and m/e ratio values, which are then compared with the empirical mass spectrum.

2.4 Lifetime measurements

Photoluminescence from the complexes was excited using ~7 ns pulses from a Continuum Panther optical parametric oscillator (OPO) pumped with a Surelite I laser. Lifetime measurements were all taken at room temperature. For Er^{3+} , an excitation wavelength of 520 nm was chosen to provide direct excitation into $^2\text{H}_{11/2}$ level of the Er^{3+} ion which rapidly decays to the $^4\text{I}_{13/2}$ level with a measured decay time of the order of 25 ns. For the Nd^{3+} and Yb^{3+} excitation, wavelengths of 420 nm and 460 nm were used, respectively. The luminescence was dispersed in a Triax 550 spectrometer and detected using a Hamamatsu R5509-72 infrared photomultiplier tube.

2.5 Crystal structure of Er³⁺ complexes

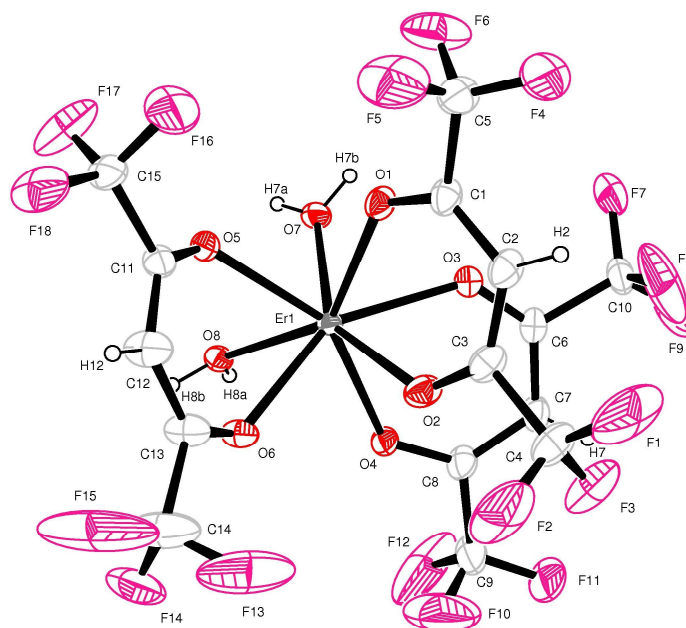


Figure 2.6 : Crystal structure of [Er(HFA)₃(H₂O)₂] as determined from X-ray diffraction (XRD)

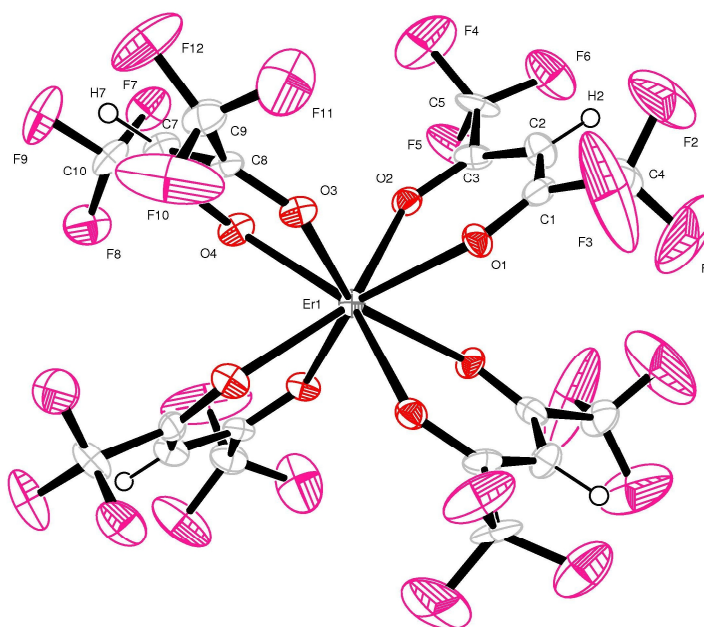


Figure 2.7 : Crystal structure of the anion, $[\text{Er}(\text{HFA})_4]^-$ as determined from X-ray diffraction (XRD) of the Cs^+ salt

Figure 2.6 shows the crystal structure of $[\text{Er}(\text{HFA})_3(\text{H}_2\text{O})_2]$ and figure 2.7 shows the anion $[\text{Er}(\text{HFA})_4]^-$ in the Cs^+ salt as determined from X-ray diffraction (XRD). It was determined from XRD data for the Er^{3+} tetrakis complex that the hydrogen atom on each ligand is $\sim 4.7 \text{ \AA}$ away from the Er^{3+} ion and hydrogen atoms on neighbouring ligands are at a distance of greater than 6.9 \AA . For the Er^{3+} tris complex, it was determined that each hydrogen atom due to H_2O being coordinated with the central Er^{3+} ion is only $\sim 2.9 \text{ \AA}$ away from each Er^{3+} ion. Hydrogen atoms on the next nearest neighbour H_2O molecules are slightly closer to a neighbouring Er^{3+} ion ($\sim 3.6 \text{ \AA}$) than the hydrogen atoms on its own coordinating HFA ligands ($\sim 4.6 \text{ \AA}$).

2.6 Effects of coordinated H₂O

Table 2.6 presents the lifetime data of the Er³⁺ tris complexes.

Entry	Compound	Lifetime	Peak emission wavelength
1.	[Er(HFA) ₃ (H ₂ O) ₂]	0.13 μs 17.3%	1530 nm
		1.83 μs 82.7%	
2.	[Er(HFA) ₃ (H ₂ O) ₂] after 2 months at room temperature in a sample vial	0.10 μs 87.5%	1530 nm
		0.57 μs 12.5%	
3.	[Er(HFA) ₃ (H ₂ O) ₂] hydrated	0.10 μs 100%	1530 nm
4.	[Er(HFA) ₃ (H ₂ O) ₂] hydrated then sublimed	0.91 μs 87%	1530 nm
		0.30 μs 13%	
		1.66 μs 18.8%	

Table 2.6 : Lifetime table of [Er(HFA)₃(H₂O)₂] for the ${}^4I_{13/2} \longrightarrow {}^4I_{15/2}$ transition

Er³⁺ has an emission line at around 1.5 μm and this is due to the f-f transition ${}^4I_{13/2} \longrightarrow {}^4I_{15/2}$ which corresponds to an energy gap of 6485 cm⁻¹. The emitting level of Er³⁺ ions at ${}^4I_{13/2}$ is resonant with the 2nd vibrational energy level of a C-H bond and 2nd vibrational energy level of an O-H bond.

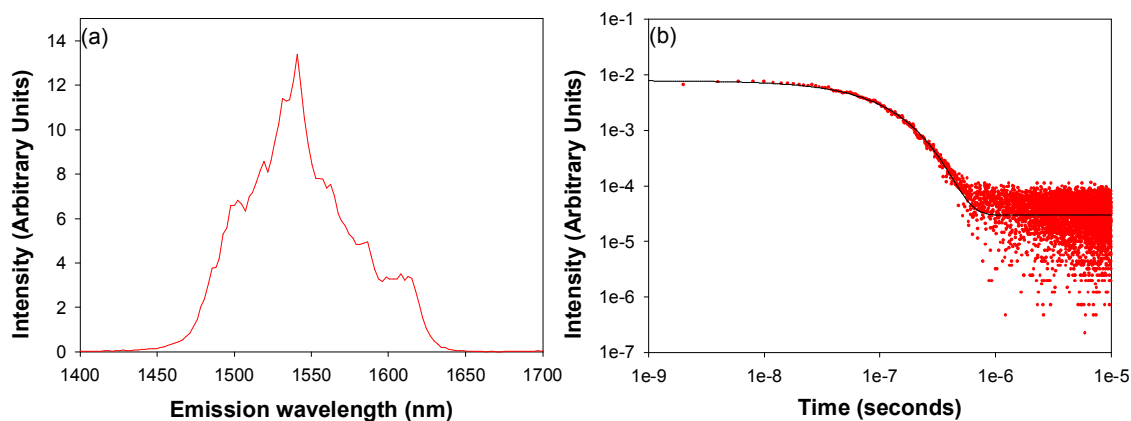


Figure 2.8 : (a) Emission spectrum of $[\text{Er}(\text{HFA})_3(\text{H}_2\text{O})_2]$ and (b) shows the luminescence lifetime data and fit of $[\text{Er}(\text{HFA})_3(\text{H}_2\text{O})_2]$ when it had been hydrated

Figure 2.8 (a) shows the emission spectrum of $[\text{Er}(\text{HFA})_3(\text{H}_2\text{O})_2]$ and figure 2.8 (b) shows the luminescence lifetime data and fit of $[\text{Er}(\text{HFA})_3(\text{H}_2\text{O})_2]$ when it has been hydrated. (Table 2.6, Entry 3) It must be mentioned that the emission spectrum of all the samples in table 2.6 are similar.

From table 2.6, $[\text{Er}(\text{HFA})_3(\text{H}_2\text{O})_2]$ exhibited two lifetime components of $0.13 \mu\text{s}$ and $1.83 \mu\text{s}$. The long lifetime component of $1.83 \mu\text{s}$ is probably due to the majority (82.7%) of Er^{3+} ions in an anhydrous environment ($[\text{Er}(\text{HFA})_3]$) and the short lifetime component suggests that there is a minority (17.3%) of Er^{3+} ions in a hydrous environment ($[\text{Er}(\text{HFA})_3(\text{H}_2\text{O})_2]$). Although a majority of the ions are in an anhydrous environment, their radiative lifetimes may be quenched by the surrounding hydrogen atoms. The lifetime of an Er^{3+} HFA tetrakis complex, $\text{Cs}[\text{Er}(\text{HFA})_4]$ was measured to be $1.80 \mu\text{s}$ and initially, it was thought that the long lifetime component was due to some tetrakis complex being formed but after leaving the same sample for two months at room temperature and at atmospheric pressure, the sample was measured again and two lifetime components were observed (Table 2.6, Entry 2); a majority (87.5%) of short lifetime component ($0.10 \mu\text{s}$) and a minority (12.5%) of long lifetime component ($0.57 \mu\text{s}$). It was then assumed that the short lifetime component of $0.10 \mu\text{s}$ is due to the majority of Er^{3+} ions in a totally hydrous environment ($[\text{Er}(\text{HFA})_3(\text{H}_2\text{O})_2]$) and the long lifetime

component of 0.57 μs was probably due to the minority of Er^{3+} ions in an anhydrous environment ($[\text{Er}(\text{HFA})_3]$), being affected by the hydrogen atoms of the H_2O molecules coordinated to the hydrated species. Within two months, moisture from the atmosphere might have interacted with the compound and is indicative that $[\text{Er}(\text{HFA})_3(\text{H}_2\text{O})_2]$ is hygroscopic. The argument for some tetrakis species being formed is then not valid.

Since the results have indicated that some of the Er^{3+} ions are in an anhydrous environment, 20 mg of the sample ($[\text{Er}(\text{HFA})_3(\text{H}_2\text{O})_2]$) was left in the presence of H_2O in a sealed beaker for two days at room temperature to deliberately hydrate the complex. Photoluminescence measurements produced a single lifetime component of 0.10 μs and this led us to confirm that the short lifetime component in entry 2 was due to Er^{3+} ions in a totally hydrated environment ($[\text{Er}(\text{HFA})_3(\text{H}_2\text{O})_2]$). This is consistent with the findings of Nail *et al*²² with a measured lifetime of 0.20 μs for $[\text{Er}(\text{tta})_3(\text{H}_2\text{O})_2]$ (tta = thenoyl(trifluoro)acetone), where two molecules of H_2O are directly coordinated to the ion.

In a deliberate attempt to remove as much H_2O from the hydrated sample as possible, $[\text{Er}(\text{HFA})_3(\text{H}_2\text{O})_2]$ was sublimed in a Kurt Lesker organic sublimation system under vacuum. Shortly after sublimation, photoluminescence measurements produced two lifetime components of 0.91 μs (87%) and 0.30 μs (13%) (Table 2.6, Entry 4). The fact that the lifetimes remained in the submicrosecond region suggests that H_2O was not completely removed from the sample and we can therefore conclude that H_2O being in the coordination sphere could not be easily removed.

Having seen the detrimental effects of H_2O being present in the coordination sphere, we proceed to study tetrakis complexes where no solvent molecules are coordinated.

2.7 Luminescence of Er³⁺ tetrakis HFA complexes

Table 2.7 shows the lifetimes of the Er³⁺ tetrakis HFA complexes. From infrared spectroscopy, these samples were found to be anhydrous.

Entry	Compound	Lifetime	Peak emission wavelength
1.	Cs[Er(HFA)] ₄	1.80 μs 100%	1530 nm
2.	Cs[Er(HFA- <i>d</i>)] ₄ 98% deuterated	11 μs 96%	1530 nm
		100 μs 4%	

Table 2.7 : Lifetime table of Cs[Er(HFA)]₄ and Cs[Er(HFA-*d*)]₄ for the ⁴I_{13/2} → ⁴I_{15/2} transition

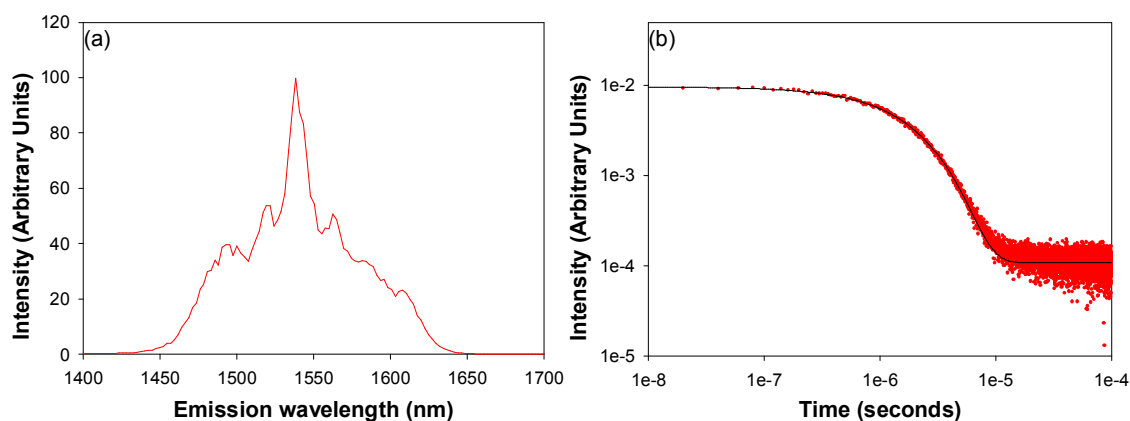


Figure 2.9 : (a) Emission spectrum of Cs[Er(HFA)]₄ and (b) shows the luminescence lifetime data and fit of Cs[Er(HFA)]₄

Figure 2.9 (a) shows the emission spectrum of Cs[Er(HFA)]₄ and figure 2.9 (b) shows the luminescence lifetime data and fit of Cs[Er(HFA)]₄.

From table 2.7, Cs[Er(HFA)]₄ has a single exponential lifetime of 1.80 μs and that is due to the Er³⁺ ions being in identical local environments. Each Er³⁺ ion is surrounded by four hydrogen atoms from the ligand and from the XRD data, each is determined to be ~4.7 Å away from the Er³⁺ ion.

For a 98% deuterated sample, most of the C–H bonds on the HFA ligand will be replaced by C–D bonds with the effect of the vibrational energy being lowered from 2950 cm^{-1} to 2100 cm^{-1} . Hence, more quanta of energy are involved in luminescence quenching and this reduces the possibility of nonradiative transitions. The emitting level at $^4I_{13/2}$ of $\text{Cs}[\text{Er}(\text{HFA}-d)_4]$ is resonant with the 3rd harmonic of a C–D bond, rendering the luminescence quenching less effective. Two different lifetimes were recorded for $\text{Cs}[\text{Er}(\text{HFA}-d)_4]$.

As a result of deuteration, the lifetime has increased by an order of magnitude, from $1.80\text{ }\mu\text{s}$ to about $11\text{ }\mu\text{s}$. The 4% component of $100\text{ }\mu\text{s}$ for the $[\text{Er}(\text{HFA}-d)_4]^-$ anion was probably due to some of the Er^{3+} ions in an environment with only a relatively weak nonradiative transition process occurring which implies that for a deuteration level of 98%, 4% of the Er^{3+} ions will be in sites where the nearest ~ 160 hydrogen sites are all fully deuterated. It corresponds to a sphere radius of $\sim 20\text{ \AA}$ around the Er^{3+} ion and is approximately equivalent to each of the forty next nearest $[\text{Er}(\text{HFA})_4]^-$ anions being fully deuterated. 4% of the Er^{3+} ions are not affected by the more distant C–H oscillators which give rise to the longer lifetime component. The next nearest hydrogen atom was probably too far away to have any significant effect on nonradiative transitions and the relatively short lived $11\text{ }\mu\text{s}$ component suggests that 96% of Er^{3+} ions are in sites where the neighbouring hydrogen atoms have an effect on luminescence quenching. It can therefore be deduced that the Er^{3+} ions are sensitive to hydrogen atoms in their coordination sphere and any presence of hydrogen atoms within a specific radius of the Er^{3+} ions will also play a significant role in nonradiative transitions.

While deuteration of the HFA ligand has been demonstrated to increase the luminescence lifetimes, the sensitivity of Er^{3+} ions to quenching by nonradiative processes is still unclear. In order to quantify the extent of quenching by C–H bonds on the Er^{3+} ions, partially deuterated Er^{3+} samples $\text{Cs}[\text{Er}(\text{HFA})_4]$ were prepared to study the effect of gradually removing C–H oscillators.

2.7.1 Partially deuterated Er^{3+} samples

Nine $\text{Cs}[\text{Er}(\text{HFA})]_4$ samples, with deuteration levels of 0%, 30%, 47%, 58%, 87%, 90%, 94% and 98%, were prepared. All deuteration levels were confirmed using MALDI mass spectroscopy and have an error of $\pm 2\%$. The luminescence decay data were fitted with the minimum number of lifetime parameters and they are presented in table 2.8.

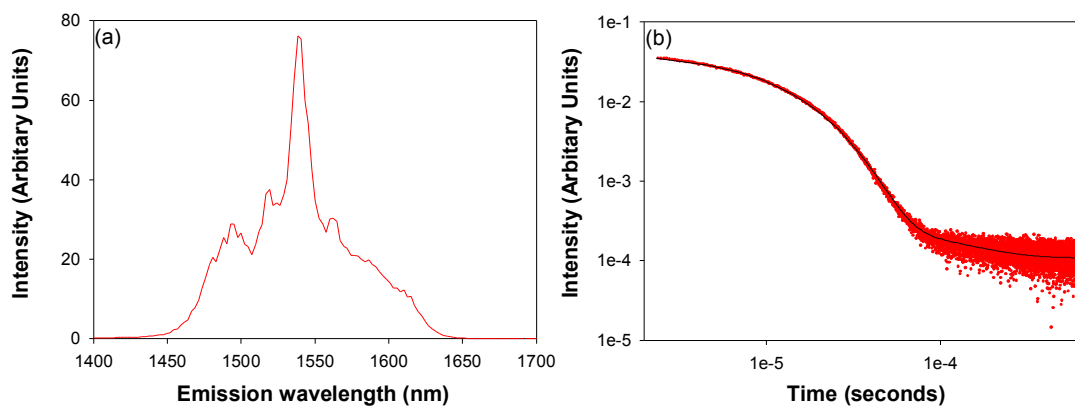


Figure 2.10 : (a) Emission spectrum of the 98% deuterated $\text{Cs}[\text{Er}(\text{HFA})]_4$ sample and (b) shows the corresponding luminescence lifetime data and fit

Figure 2.10 (a) shows the emission spectrum of the 98% deuterated $\text{Cs}[\text{Er}(\text{HFA})]_4$ sample and figure 2.10 (b) shows the corresponding luminescence lifetime data and fit.

Deuteration level (%)	Lifetime component 1, τ_1 (μs)	Percentage contribution from component 1	Lifetime component 2, τ_2 (μs)	Percentage contribution from component 2	Lifetime component 3, τ_3 (μs)	Percentage contribution from component 3
0	1.8	100	-	-	-	-
30	1.8	37	3.0	55	10	8
47	2.4	46	5.5	54	-	-
58	2.5	31	6.0	68	-	-
81	3.3	17	8.4	83	-	-
87	3.7	11	9.5	89	-	-
90	3.5	10	10	90	-	-
94	3.6	6	10.6	94	-	-
98	11	96	106	4	-	-

Table 2.8 : Luminescence decay data fitted with the minimum number of lifetime parameters

From table 2.8, it can be seen that only the 0% deuterated sample has a single lifetime component and as previously discussed, that is due to all the ions being in identical environments. The 30% deuterated sample can be fitted using three lifetime components and the remaining partial deuterated samples each need only two lifetime components. The symbols τ_1 , τ_2 and (where applicable) τ_3 have been used to denote the components in order of increasing size.

Based on the assumption that the measured lifetime of 1.80 μs is solely due to the contributions by only the nearest C–H oscillators, the rate constant, k for each C–H oscillator is calculated to be $\sim 140,000 \text{ s}^{-1}$. Using this rate constant for a single nearest C–H oscillator, the predicted lifetimes for anions having between 1 (d_3) and 4 (d_0) nearest hydrogen atoms were calculated to be as follows: 1.80 μs for d_0 , 2.40 μs for d_1 , 3.60 μs for d_2 and 7.20 μs for d_3 . Comparing table 2.8 with the predicted lifetimes for each of the partially deuterated samples, it can be seen that the fastest lifetime component (τ_1 in table 2.8) observed corresponds to the predicted lifetime due to four nearest C–H oscillators (30% deuteration), three

nearest C–H oscillators (47% and 58%) and two nearest C–H oscillators (81%, 87%, 90% and 94%).

For each partially deuterated sample, the distribution of the nearest C–H oscillators was calculated and presented in table 2.9.

	Deuteration %						
No of C–H bonds	30%	47%	58%	81%	87%	90%	94%
4	24%	9%	3%	0%	0%	0%	0%
3	41%	29%	18%	3%	1%	0%	0%
2	26%	37%	36%	15%	8%	6%	3%
1	8%	21%	32%	41%	34%	31%	22%
0	1%	4%	11%	41%	57%	63%	75%

Table 2.9 : The calculated distribution of the nearest C–H oscillators and C–D oscillators for the partially deuterated samples at the different levels of deuteration

	Deuteration %						
No. of C–H bonds	30%	47%	58%	81%	87%	90%	94%
4	34%	9%	0%	0%	0%	0%	0%
3	32%	16%	20%	0%	0%	0%	0%
2	24%	48%	35%	18%	7%	7%	4%
1	10%	27%	45%	48%	37%	24%	12%
0	0%	0%	0%	34%	56%	69%	84%

Table 2.10 : Measured percentage contributions by ‘forced fitting’

From table 2.8, it can be observed that even for deuteration levels >81%, the calculated lifetime of 3.60 μ s which corresponds to the anion $[\text{Er}(\text{HFA})_4\text{-d}_2]^-$ can be measured. This suggest that for Er^{3+} ions, providing there are at least two C–H oscillators in its nearest neighbour positions, it is these nearest neighbour C–H

oscillators which dominate the quenching. Once there is only one C–H oscillator in its nearest neighbour, the contribution of more distant C–H oscillators becomes more significant. For all the samples, except in the case of the 30% deuterated sample, the lifetimes could be adequately fitted with a dual exponential fit, which suggests that there is not a unique solution to the deconvolution of the various lifetime components and this approach gives the “best-fit” with the minimum number of fitting parameters.

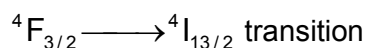
Using the measured value of 11 μs for $[\text{Er}(\text{HFA})_4\text{-}d_4]^-$ and the predicted values for $d_0 - d_3$, we then tried to force fit the decay data. We have used a five exponential fit and constrained the lifetimes to the predicted values and allowing free fitting of the prefactors. Fitting the data then gave the % contribution due to each component and shown in table 2.10. Reasonable fits were obtained and the percentage contribution is shown in table 2.10. Comparing tables 2.9 and 2.10, it can be seen that the calculated and measured percentage contributions are in fairly good agreement. This shows that for Er^{3+} ions, the main quenching pathway is dominated by its nearest neighbour and the next nearest neighbour will only play a significant role when there is only one C–H oscillator in the nearest neighbour.

2.8 Luminescence of Nd³⁺ complexes

Table 2.11 presents the lifetime data of Cs[Nd(HFA)₄] and Cs[Nd(HFA-*d*)₄].

Entry	Compound	Lifetime	Peak emission wavelength
1.	Cs[Nd(HFA) ₄]	1.65 μs 92%	1340 nm
		0.40 μs 8%	
2.	Cs[Nd(HFA) ₄] hydrated	0.17 μs 96%	1340 nm
		1.02 μs 4%	
3.	Cs[Nd(HFA- <i>d</i>) ₄]	4.20 μs 96%	1340 nm
		0.70 μs 4%	

Table 2.11 : Lifetime data of Cs[Nd(HFA)₄] and Cs[Nd(HFA-*d*)₄] for the



Nd³⁺ has three possible emissions at 930 nm, 1064 nm and 1340 nm corresponding to ${}^4F_{3/2} \longrightarrow {}^4I_{9/2}$, ${}^4F_{3/2} \longrightarrow {}^4I_{11/2}$ and ${}^4F_{3/2} \longrightarrow {}^4I_{13/2}$ transitions, respectively. The radiative lifetimes measured for all three transitions were similar and only the ${}^4F_{3/2} \longrightarrow {}^4I_{13/2}$ transition lifetimes are presented. The emitting level of Nd³⁺ ions at ${}^4F_{3/2}$ has an energy gap of 5400 cm⁻¹ and is resonant with the second vibrationally excited energy level of a C–H bond and second excited energy level of an O–H bond.

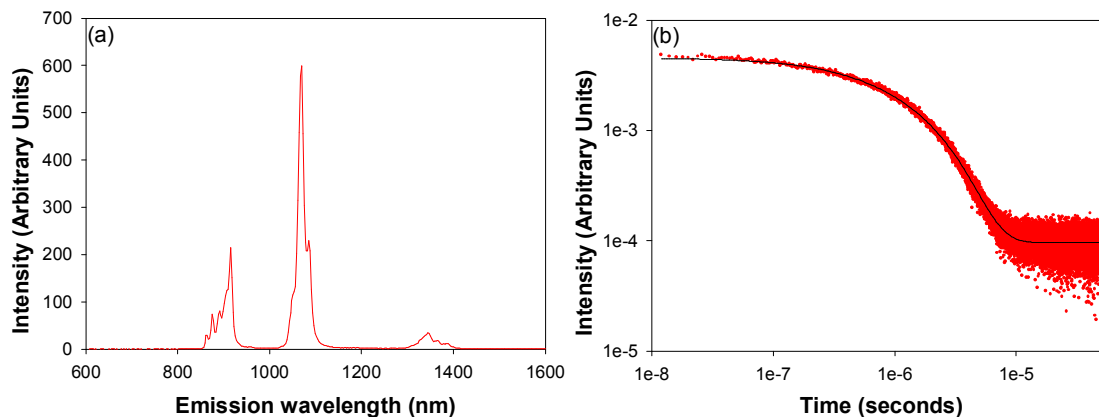


Figure 2.11 : (a) Emission spectrum of Cs[Nd(HFA)₄] and (b) shows the corresponding luminescence lifetime data and fit

Figure 2.11 (a) shows the emission spectrum of Cs[Nd(HFA)₄] and figure 2.11 (b) shows the corresponding luminescence lifetime data and fit.

From table 2.11 (Entry 1), it can be seen the [Nd(HFA)₄]⁻ anion exhibited two lifetime components of 1.65 μs (92%) and 0.40 μs (8%). The long lifetime component of 1.65 μs (92%) was due to the Nd³⁺ ions in an anhydrous environment, surrounded only by four bidentate HFA ligands. The short lifetime component of 0.40 μs (8%) seems to suggest that H₂O molecules might have coordinated with the Nd³⁺ ions, forming Cs[Nd(HFA)₄(H₂O)]. Nd³⁺ has a larger radius than Er³⁺ and hence there is more space for solvent coordination.²⁸ Previous studies have indicated that Nd³⁺ ions have a coordination number that varies from 8 to 10, depending on the nature of the ligands and Cs[Nd(HFA)₄(H₂O)] and Cs[Nd(HFA)₄] have been described in the literature.¹⁸ Cs[Nd(HFA)₄H₂O] has been studied by single crystal X-ray diffraction.²⁹ Our Cs[Nd(HFA)₄] sample has been studied by powder X-ray diffraction and was compared with the calculated data of Cs[Eu(HFA)₄].³⁰

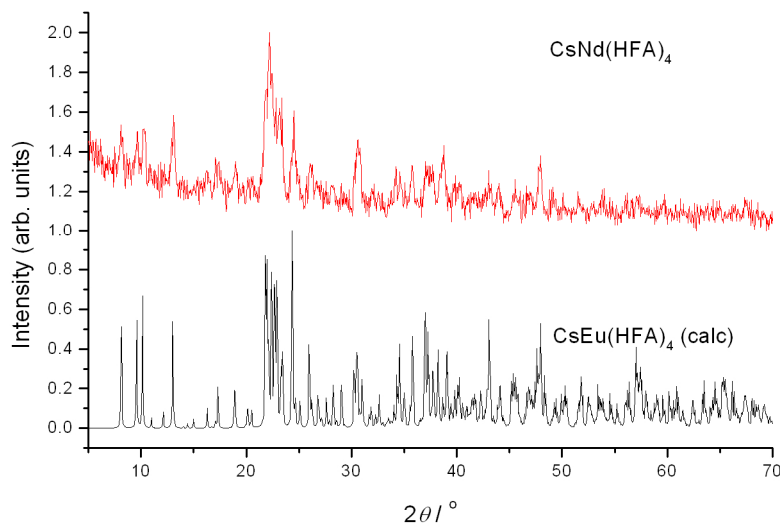


Figure 2.12 : Powder X-ray diffraction data of Cs[Nd(HFA)₄] and Cs[Eu(HFA)₄]

From figure 2.12, we can confirm that Cs[Nd(HFA)₄] and Cs[Eu(HFA)₄] are isostructural. The wavelength of the radiation was 1.5418 Å.

A small portion of Cs[Nd(HFA)₄] (20 mg) was left overnight at room temperature in a sealed vessel that was saturated with water vapour. Following this, the lifetimes measured were 0.17 μs (96%) and 1.02 μs (4%) (Table 2.11, Entry 2). The short lived component of 0.17 μs suggests that 96% of Nd³⁺ ions are hydrated and the 1.02 μs component is probably due to some anhydrous species. However, the lifetime of 1.02 μs, which is relatively shorter than the pre-hydrated sample with a lifetime of 1.65 μs can be due to the fact that in the hydrated sample, there are more hydrogen atoms in the neighbouring sites which play a significant role in luminescence quenching.

Photoluminescence measurements on a sample of Cs[Nd(HFA-*d*)₄] (60% deuterated) exhibited a relatively short lifetime component of 0.61 μs (4.6%) which might suggest that it was partly hydrated. Sublimation on the sample was carried out in an attempt to remove any coordinated H₂O. Following that, photoluminescence measurement revealed the presence of a 0.51 μs (8%) component in the sublimed sample and is indicative that dehydration did not take

place. Similar to Er^{3+} , it can be concluded that H_2O in the coordination sphere of a Nd^{3+} ion cannot be easily removed and this is consistent with the findings by Danford *et al.*²⁹

By deuterating the Nd^{3+} tetrakis HFA complex, the C–H bonds of the HFA ligand are replaced by the lower vibrational energy C–D bonds, so minimizing the vibrational quenching effects. Photoluminescence measurements of a 98% deuterated $\text{Cs}[\text{Nd}(\text{HFA-}d)_4]$ produced two lifetime components of 4.20 μs (96%) and 0.70 μs (4%) (Table 2.11, Entry 3). The long lifetime component of 4.20 μs seems to suggest that 96% of the Nd^{3+} ions are in an anhydrous environment, surrounded only by four bidentate HFA-*d* ligands ($\text{Cs}[\text{Nd}(\text{HFA-}d)_4]$). The short lifetime component of 0.70 μs (4%) suggests that H_2O molecules from the atmosphere might have coordinated with a minority of the Nd^{3+} ions, giving $\text{Cs}[\text{Nd}(\text{HFA-}d)_4(\text{H}_2\text{O})]$.

For 98% deuteration, it was calculated that 92.2% of Nd^{3+} ions are coordinated with fully deuterated HFA ligands. However, the lifetime of 4.20 μs is only a minor improvement compared with the non-deuterated analogue which exhibited a lifetime of 1.65 μs . Earlier in the discussion, we also saw how the 1.65 μs component is reduced to 1.02 μs as a consequence of hydration. Therefore, it seems to suggest that the Nd^{3+} ions might be sensitive to more distant C–H oscillators than Er^{3+} ions are. By partial deuterating the samples, we are able to determine specifically the role of the next nearest C–H oscillators.

2.8.1 Partially deuterated Nd^{3+} samples

Six samples with deuteration levels of 0%, 49%, 59%, 60%, 85% and 98% were studied. For all of these samples, a dual-exponential fit is required and the lifetimes are given in table 2.12.

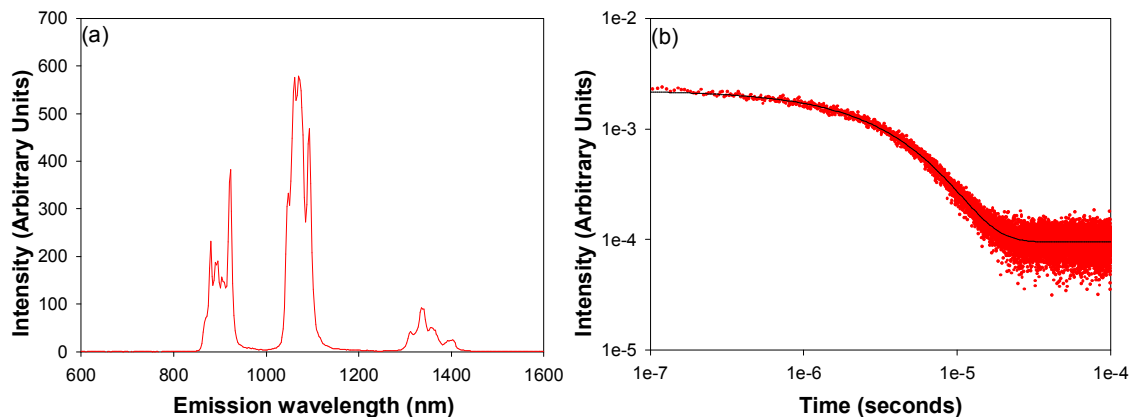
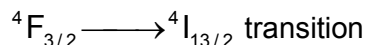


Figure 2.13 : (a) Emission spectrum of the 98% deuterated Cs[Nd(HFA-*d*)₄] sample and (b) the corresponding luminescence lifetime data and fit

Figure 2.13 (a) shows the emission spectrum of the 98% deuterated Cs[Nd(HFA-*d*)₄] sample and figure 2.13 (b) shows the corresponding luminescence lifetime data and fit.

Level of deuteration (%)	Lifetime component 1, τ_1 (μ s)	Percentage contribution from component 1	Lifetime component 2, τ_2 (μ s)	Percentage contribution from component 2
0	0.40	8	1.65	92
49	0.30	1	2.40	99
59	0.30	3	2.60	97
60	0.50	3	2.70	97
85	0.60	2	3.60	98
98	0.70	4	4.20	96

Table 2.12 : Lifetimes of the partially deuterated Cs[Nd(HFA)₄] samples for the



It can be observed from table 2.12 that lifetime component 1, τ_1 is very fast ($<1 \mu$ s) and the percentage contribution is not more than 8%. From the earlier discussion,

submicrosecond lifetimes can be attributed to the presence of some hydrated ions.²² For the anhydrous species, it can be concluded from table 2.12 and previous discussion that the lifetime of Nd^{3+} in a $[\text{Nd}(\text{HFA})_4]^-$ anion is 1.65 μs . If this lifetime is solely due to the nearest C–H oscillators on the ligands coordinated to the Nd^{3+} , the rate constant for each C–H oscillator is calculated to be $\sim 151,515 \text{ s}^{-1}$. This would give a prediction of 2.20 μs for d_1 , 3.30 μs for d_2 and 6.60 μs for d_3 . Note that the predicted lifetime for d_3 is longer than the measured lifetime for 98% deuterated $[\text{Nd}(\text{HFA})_4]^-$. Moreover, we were not able to fit the luminescence data using the predicted lifetime values. Therefore it seems to suggest that for Nd^{3+} ions, either the more distant C–H oscillators or nearest neighbouring C–D oscillators play a significant role in quenching the luminescent state of Nd^{3+} ions. The calculated rate constant of $151,515 \text{ s}^{-1}$ per neighbouring C–H group is not valid if the lifetime is affected by other oscillators as well.

From chapter 1, it was discussed that Nd^{3+} is more sensitive than Er^{3+} to C–H and C–D bonds due to the lower energy gap of the ion.

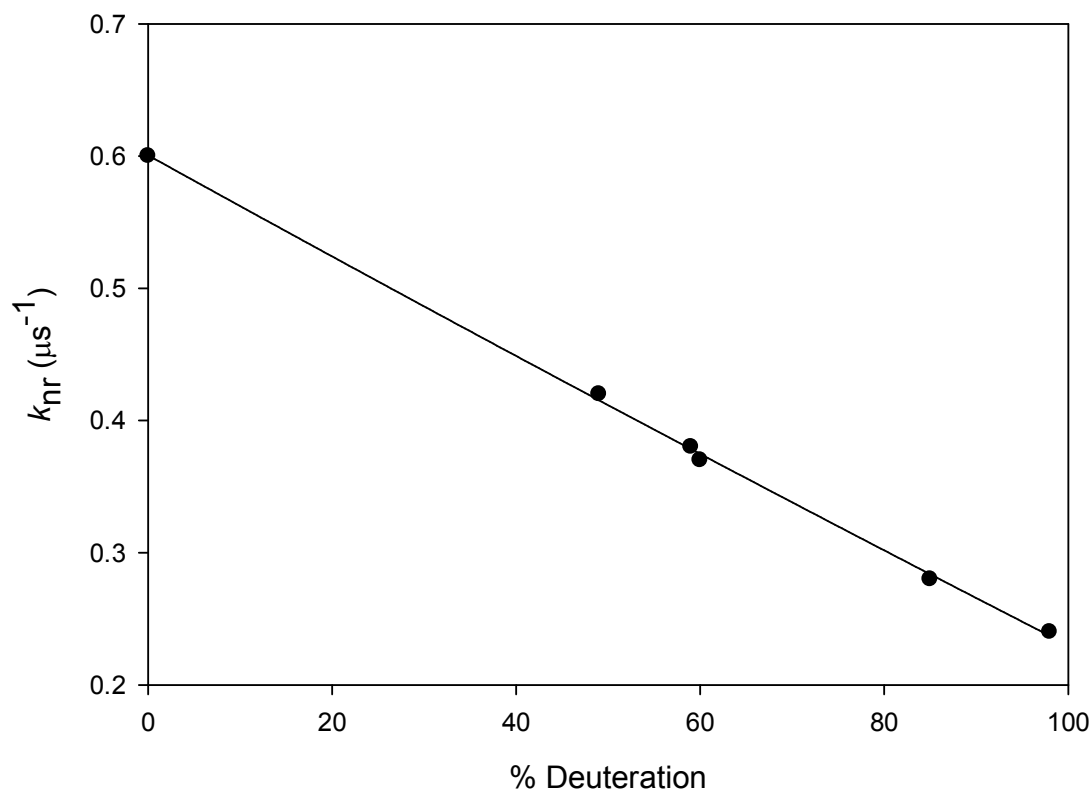


Figure 2.14 : Rate constant of the major lifetime component against % deuteration for the partially deuterated neodymium samples

In figure 2.14, the rate constant obtained from the major lifetime component is plotted against % deuteration. It can be seen that the data fit a straight line, which is consistent with the continuous medium approximation model used by Quochi *et al.*²³ Increased sensitivity to the effect of more distant C–H oscillators or the sensitivity to C–D oscillators in the nearest neighbour positions is probably the cause of this linear dependence.

Unlike Er^{3+} , Nd^{3+} cannot be fitted with a model based on a discrete nearest neighbour C–H bonds. This implies that more distant C–H bonds may be having an effect. Quochi's²³ model is based on this assumption. Therefore, we tested our data against that model and got our results shown in figure 2.14.

2.9 Luminescence of Yb³⁺ complexes

Yb³⁺ has a simple energy level scheme consisting of only two accessible levels, the ²F_{7/2} ground state and the ²F_{5/2} excited state which corresponds to an energy gap of around 9700 cm⁻¹. The emitting level of Yb³⁺ ions at ²F_{5/2} is resonant with the 3rd vibrational energy level of a C–H bond.

Entry	Compound	Lifetime	Peak emission wavelength
1.	Cs[Yb(HFA)] ₄	22.6 μs 100%	1032 nm
2.	Cs[Yb(HFA-d)] ₄	289 μs 100%	1032 nm

Table 2.13 : Lifetime data of Cs[Yb(HFA)]₄ and Cs[Yb(HFA-d)]₄ for the ²F_{5/2} → ²F_{7/2} transition

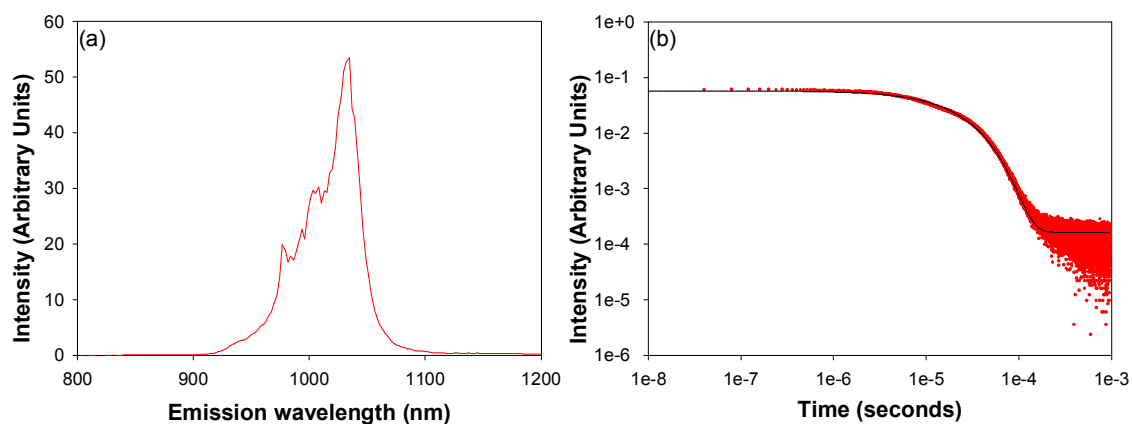


Figure 2.15 : (a) Emission spectrum of Cs[Yb(HFA)]₄ and (b) the corresponding luminescence lifetime data and fit

Figure 2.15 (a) shows the emission spectrum of Cs[Yb(HFA)]₄ and figure 2.15 (b) shows the corresponding luminescence lifetime data and fit.

From infrared spectroscopy data, these samples were found to be anhydrous and do not contain O–H or O–D bonds.

From table 2.13 (Entry 1), the $[\text{Yb}(\text{HFA})_4]^-$ anion exhibited a single lifetime component of 22.6 μs . The fact that it only exhibited a single lifetime component seems to suggest that all the Yb^{3+} ions were in identical environments.

Due to the relatively large energy gap (as compared to 6485 cm^{-1} of Er^{3+} ion and 5400 cm^{-1} of Nd^{3+} ions), the effects of the C–H bonds were reduced. Deuterating the tetrakis complex increased the vibrational energy level that best matched the electronic energy of the excited ion from the 3rd to 4th, which further suppressed the probability of nonradiative transitions.

The lifetime of a 98% deuterated $[\text{Yb}(\text{HFA-}d)_4]^-$ is 289 μs (Table 2.13, Entry 2) which is much greater than that observed for Er^{3+} and Nd^{3+} . This suggests that Yb^{3+} ions are less sensitive to the nearest neighbouring C-H oscillators than Er^{3+} ions. In order to support this argument, partially deuterated Yb^{3+} samples were prepared and studied.

2.9.1 Partially deuterated Yb^{3+} samples

For $\text{Cs}[\text{Yb}(\text{HFA-}d)_4]$, six samples were prepared with deuteration levels of 0%, 32%, 53%, 66%, 86% and 98%. For each sample the lifetime could be fitted with a single exponential lifetime and is shown in table 2.14.

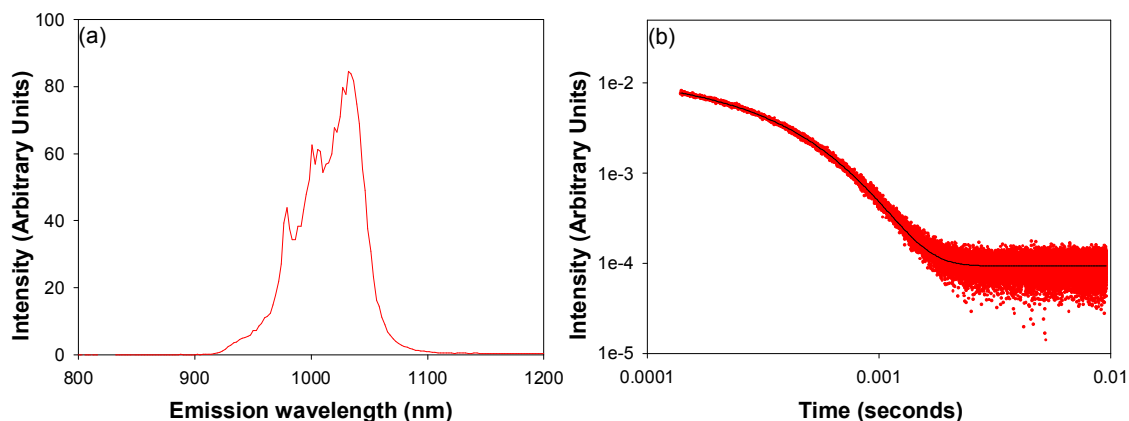


Figure 2.16 : (a) Emission spectrum of the 98% deuterated $\text{Cs}[\text{Yb}(\text{HFA-}d)_4]$ sample and (b) the corresponding luminescence lifetime data and fit

Figure 2.16 (a) shows the emission spectrum of the 98% deuterated Cs[Yb(HFA-*d*)]₄ sample and figure 2.16 (b) shows the corresponding luminescence lifetime data and fit.

Entry	% Deuteration	Lifetime
1	0%	22.6 μs
2	32%	33.7 μs
3	53%	47.4 μs
4	66%	65.5 μs
5	86%	130.4 μs
6	98%	289 μs

Table 2.14 : Lifetimes of the Cs[Yb(HFA)]₄ partially deuterated samples

Unlike Er³⁺, these Yb³⁺ samples demonstrated a single exponential decay, which suggests that they are not dominated by the number of C–H oscillators in the nearest neighbour sites in the way Er³⁺ is. However, the increase in the lifetimes with increasing deuteration levels does show that C–H oscillators are definitely the dominant quenching mechanism. As the deuteration levels increase, the C–H bonds are increasingly being replaced by C–D bonds and that has the effect of minimizing the luminescence quenching pathways. It is presently unclear why Yb³⁺ shows only single-exponential decay for all samples. However, due to the fact that the energy gap for the transition in Yb³⁺ ions is much bigger than for either of the other ions and is resonant with the 3rd vibrational energy level of the C–H bond, it is likely that the dominant Yb³⁺ de-excitation may be energy transfer to more than one C–H oscillator.

2.10 Conclusions for chapter 2

We have observed an improvement in the luminescence lifetimes of Ln³⁺ complexes as a consequence of excluding H₂O or solvent molecules in the coordination sphere and then by deuteration of the HFA ligand. O–H bonds have the highest vibrational energy of 3450 cm⁻¹ and we saw that luminescence lifetimes are most effectively quenched for the Er³⁺ tris complexes when H₂O molecules are coordinated. From the XRD data, we found that the hydrogen atoms from the coordinated H₂O molecules are ~2.9 Å away from the Er³⁺ ion. Comparing this lifetime with the tetrakis Er³⁺ complex, Cs[Er(HFA)]₄, where the nearest hydrogen atom of the HFA ligand is ~4.7 Å away from the ion, the lifetime is increased to 1.80 μs. We also found that in the tris complex, the hydrogen atoms on the next nearest neighbour H₂O molecules are slightly closer to a neighbouring Er³⁺ ion (~3.6 Å) than the hydrogen atoms on its own coordinating ligands (~4.6 Å), thus making the presence of any H₂O more efficient in luminescence quenching.

A greater than two orders of magnitude increase in luminescence lifetime is observed for Er³⁺ and Yb³⁺ complexes while Nd³⁺ demonstrated an improvement of over 150% upon deuteration. Each C–H bond has a vibrational quantum of 2950 cm⁻¹ and the number of harmonics, *n* to match the energy gap is largest for Yb³⁺ (*n* = 3 - 4), followed by Er³⁺ (*n* = 2 - 3) and smallest for Nd³⁺ (*n* = 1 - 2). The effect of nonradiative emission by a lower energy C–D bond (2100 cm⁻¹) is less dramatic as higher harmonics are required to match the emitting levels. For 98% deuteration, we achieved a maximum lifetime of 100 μs for Er³⁺, 4.20 μs for Nd³⁺ and 289 μs for Yb³⁺. Contrary to the findings of Hebbink *et al*²⁰, who determined that hydrogen ~6 Å away has no significant quenching effects, we found that any hydrogen within ~20 Å away will effectively quench the luminescence lifetime. Our results have shown that any hydrogen in the sample will drastically quench the luminescence and even when the hydrogen is ~20 Å away, the obtained lifetime of 100 μs lifetime is not sufficient to develop useful telecommunication devices. Therefore, fully halogenated molecules are required.

We have shown from the partially deuterated Er³⁺ samples that the rapid luminescence quenching is strongly dependent on the immediate local

environment with only a secondary effect due to more distant C–H oscillators. This contradicts the continuous medium approximation model adopted by Quochi *et al.*²³ For Nd³⁺ and Yb³⁺ ions, we observed single exponential decay for the anhydrous ions at all deuteration levels and the rate constant for quenching was found to vary linearly with deuteration levels.

Now that we have seen the detrimental effects of high energy oscillators towards luminescence quenching, the next two chapters will focus on ligands without any high energy bonds.

2.11 References for chapter 2

1. Bünzli; J-C. G. and Piguet; C., *Chemical Society Reviews*, 34, **2005**, 1048
2. Hasegawa; Y., Wada; Y. and Yanagida; S., *Journal of Photochemistry and Photobiology C: Photochemistry Reviews*, 5, **2004**, 183
3. Wolbers; M. P. O., Van Veggel; F. C. J. M., Snellink-Ruel; B. H. M., Hofstraat; J. W., Geurts; F. A. J. and Reinhoudt; D. N., *Journal of the Chemical Society, Perkin Transactions 2*, **1998**, 2141
4. Yanagida; S., Hasegawa; Y., Murakoshi; K., Wada; Y., Nakashima; N. and Yamanaka; T., *Coordination Chemistry Reviews*, 171, **1998**, 461
5. Sun; L., Zhang; H., Meng; Q., Liu; F., Fu; L., Peng; C., Yu; J., Zheng; G. and Wang; S., *Journal of Physical Chemistry B*, 109, **2005**, 6174
6. Beeby; A., Dickins; R. S., Faulkner; S., Parker; D. and Gareth Williams; J. A., *Chemical Communications*, **1997**, 1401
7. Slooff; L. H., Van Blaaderen; A., Polman; A., Hebbink; G. A., Klink; S. I., Van Veggel; F. C. J. M., Reinhoudt; D. N. and Hofstraat; J. W., *Journal of Applied Physics*, 91, **2002**, 3955
8. Miniscalco; W. J., *Journal of Lightwave Technology*, 9, **1991**, 234
9. Baker; C. C., Heikenfeld; J., Yu; Z. and Steckl; A. J., *Applied Physics Letters*, 84, **2004**, 1462
10. Bünzli; J-C. G., Comby; S., Chauvin; A-S. and Vandevyver; C. D. B., *Journal of Rare Earths*, 25, **2007**, 257
11. Comby; S. and Bünzli; J-C. G., *Handbook on the Physics and Chemistry of Rare Earths*, 37, **2007**

12. Zhang; X. Z., Zhang; D. M., Mu; S. K., Zhang; D. and Chen; C., *Applied Physics B*, 86, **2007**, 677
13. Liang; H., Zhang; Z., Chen; B., Zhang; Q. and Ming; H., *Materials Chemistry and Physics*, 86, **2004**, 430
14. Zheng; Z., Liang; H., Ming; H., Zhang; Q. and Xie; J., *Optics Communication*, 233, **2004**, 149
15. Hasegawa; Y., Murakoshi; K., Wada; Y., Yanagida; S., Kim; J-H., Nakashima; N. and Yamanaka; T., *Chemical Physics Letters*, 248, **1996**, 8
16. Heller; A., *Journal of the American Chemical Society*, 88, **1966**, 2058
17. Heller; A., *Applied Physics Letters*, 9, **1966**, 106
18. Hasegawa; Y., Kimura; Y., Murakoshi; K., Wada; Y., Kim; J-H., Nakashima; N., Yamanaka; T. and Yanagida; S., *Journal of Physical Chemistry*, **1996**, 10201
19. Beeby; A. and Faulkner; S., *Chemical Physics Letters*, 266, **1997**, 116
20. Hebbink; G. A., Reinhoudt; D. N. and Van Veggel; F. C. J. M., *European Journal of Organic Chemistry*, **2001**, 4101
21. Klink; S. I., Grave; L., Reinhoudt; D. N., Van Veggel; F. C. J. M., Werts; M. H. V., Geurts; F. A. J. and Hofstraat; J. W., *Journal Physical Chemistry A*, 104, **2000**, 5457
22. Shavaleev; N. M., Pope; S. J. A., Bell; Z. R., Faulkner; S. and Ward; M. D., *Dalton Transactions*, **2003**, 808

23. Quochi; F., Orru; R., Cordella; F., Mura; A., Bongiovanni; G., Artzzu; F., Deplano; P., Mercuri; M. L., Pilia; L. and Serpe; A., *Journal of Applied Physics*, 99, **2006**, 053520
24. Ogoshi; H. and Nakamoto; K., *Journal of Chemical Physics*, 45, **1996**, 3113
25. Ellinger; M., Duschner; H. and Starke; K., *Journal of Inorganic and Nuclear Chemistry*, 40, **1978**, 1063
26. Redman; E., <http://textonly.kombyonyx.com/sequence.htm>, last accessed June 2006
27. Wyatt; M. F., *EPSRC National Mass Spectrometry Service Centre Application Notes*, Swansea University, 5, **2008**
28. Wolbers; M. P. O., Van Veggel; F. C. J. M., Hofstraat; J. W., Geurts; F. A. J. and Reinhoudt; D. N., *Journal of the Chemical Society, Perkin Transactions 2*, **1997**, 2275
29. Danford; M. D., Burns; J. H., Higgins; C. E., Stokely Jr; J. R. and Baldwin; W. H., *Inorganic Chemistry*, 9, **1970**, 1953
30. Burns; J. H. and Danford M. D., *Inorganic Chemistry*, 8, **1969**, 1780

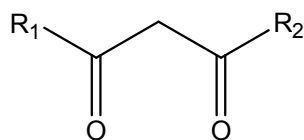
Chapter 3 - Results and discussion 2 : Attempted preparation of fluorinated complexes

3.1 Introduction

Ln^{3+} ions are often deployed as the amplifying medium in photonics applications. Recently, the development of integrated planar waveguide optical amplifiers has provided an advantage for efficient high speed communication systems of large capacity optical communication, information storage and processing.¹ The growing demand for these NIR amplifiers is a consequence of low fabrication cost and their sharp emission lines.² Luminescent transitions from trivalent Ln^{3+} ions which arise from 4f orbitals are forbidden on symmetry grounds and leads to poor absorption cross sections and long-lived excited states. A requirement for optical amplification is to have long excited state lifetimes, which makes it easier to obtain population inversion.³ Population of the emitting levels of the Ln^{3+} ions can be achieved by light-harvesting ligands, which act as antenna chromophores that sensitize the ions by intramolecular energy transfer. However, ligands often contain high energy C–H and O–H bonds which effectively quench the excited states nonradiatively, leading to decreased luminescence intensity and shorter excited state lifetimes. Ln^{3+} ions such as Er^{3+} , Nd^{3+} and Yb^{3+} have a coordination number of 8 - 10 and it is widely assumed that in an unsaturated structure, the coordination sphere is readily occupied by H_2O or solvent molecules. H_2O molecules have been demonstrated to be potent quenchers.⁴ Several strategies have been employed to saturate the coordination sphere in an effort to prevent nonradiative de-excitation via coordinated high vibrational energy solvent molecules.

One of the ways to eliminate the coordination of H_2O molecules in the coordination sphere of a Ln^{3+} ion is to utilize a neutral ligand to fulfill the high coordination number. β -Diketonate Ln^{3+} complexes are extensively studied. An electrically neutral complex is produced when three β -diketonate ligands are coordinated to a trivalent Ln^{3+} ion. Common β -diketonates extensively researched include dibenzoylmethane (DBM), 1-benzoylacetone (BA), thenoyl-trifluoroacetone (TTA) and 4,4,4-trifluoro-1-phenyl-1,3-butanedione (BTFA) and they differ from each other by the end groups at either end of the five membered carbon chain

(Figure 3.1). These β -diketonate Ln^{3+} complexes are susceptible to solvent coordination to fulfill the high coordination number of Ln^{3+} ions and therefore, neutral ligands are used to prevent the coordination of high vibrational energy solvent molecules. Moreover, these neutral ligands have the advantage of modifying the luminescent properties and contributing to the overall stability of the resulting complexes.⁵

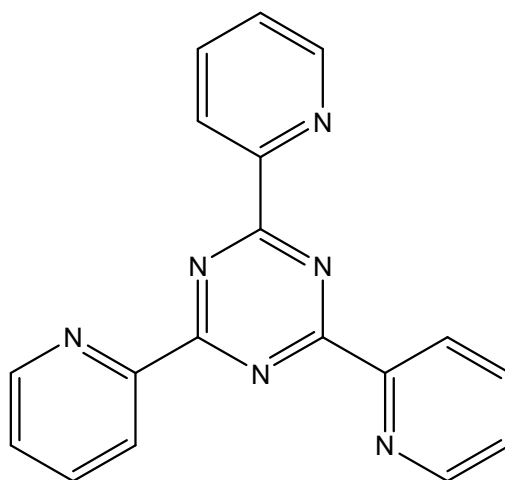


21

DBM - $\text{R}_1 = \text{R}_2 = \text{C}_6\text{H}_5$
 BA - $\text{R}_1 = \text{C}_6\text{H}_5$, $\text{R}_2 = \text{CH}_3$
 TTA - $\text{R}_1 = \text{C}_4\text{H}_3\text{S}$, $\text{R}_2 = \text{CF}_3$
 BTFA - $\text{R}_1 = \text{C}_6\text{H}_5$, $\text{R}_2 = \text{CF}_3$

Figure 3.1 : Common β -diketonates used for research

De Silva *et al*⁶ prepared and characterized Er^{3+} , Eu^{3+} and Tb^{3+} β -diketonate complexes with 2,4,6-tri(2-pyridyl)-1,3,5-triazine (TPTZ) (Figure 3.2) as a tridentate neutral ligand.



22

Figure 3.2 : Chemical structure of 2,4,6-tri(2-pyridyl)-1,3,5-triazine (TPTZ) (**22**) which is used as a neutral ligand

The neutral ligand, TPTZ (**22**), is first introduced to the metal chlorides before the introduction of the β -diketonates. For each of these complexes, the metal ion is situated in a coordination sphere comprising of six oxygen atoms of the β -diketonate ligands and three nitrogen atoms of the TPTZ ligand. TPTZ ligands are bulky and thus saturate the coordination sphere of these complexes. Essentially, the congested chemical environment protects the Ln^{3+} ion from any substantial interactions with potential luminescence-quenching solvent molecules with the advantage of increased luminescence efficiency.

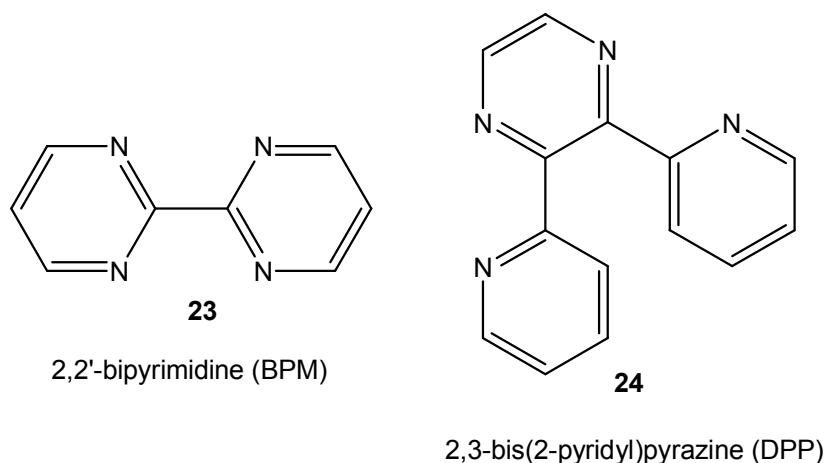
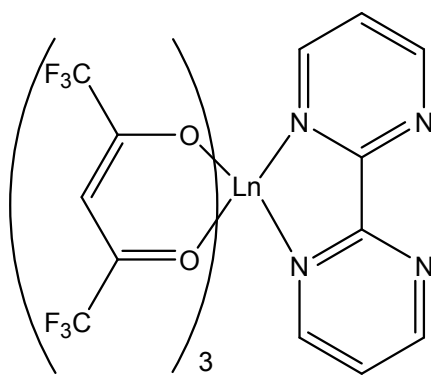


Figure 3.3 : Polyazine bridging ligands 2,2'-bipyrimidine (BPM) (**23**) and 2,3-bis(2-pyridyl)pyrazine (DPP) (**24**)

Recently, polyazine bridging ligands such as 2,2'-bipyrimidine (BPM) (Figure 3.3, **23**) and 2,3-bis(2-pyridyl)pyrazine (DPP) (Figure 3.3, **24**) have been widely used to link metal ions through the donating nitrogen atoms.^{7,8} BPM is a planar heterocycle and is of particular interest as a neutral ligand due to their ability to form facile supramolecular complexes through their four equivalent nitrogen atoms which bind to two metal centers. The DPP bridging ligand binds to two metal centers through a pyridyl and a pyrazine nitrogen. Fratini *et al*⁹ characterized Ln^{3+} complexes of the form $\text{Ln}(\text{HFA})_3\text{BPM}$ (**25**) (where $\text{Ln} = \text{Nd, Gd or Tb}$; $\text{HFA} = 1,1,1,5,5,5$ -hexafluoroacetylacetonone and $\text{BPM} = 2,2'$ -bipyrimidine) (Figure 3.4).



25

Figure 3.4 : Lanthanide complexes of the form $\text{Ln}(\text{HFA})_3\text{BPM}$ (**25**) (where Ln = Nd, Gd or Tb; HFA = 1,1,1,5,5,5-hexafluoroacetylacetonate and BPM = 2,2'-bipyrimidine)

A new collection of Ln^{3+} complexes comprising BPM and DPP as neutral bridging ligands and TTA as the β -diketonate has also been synthesized by Sultan *et al.*⁷ (Figure 3.5)

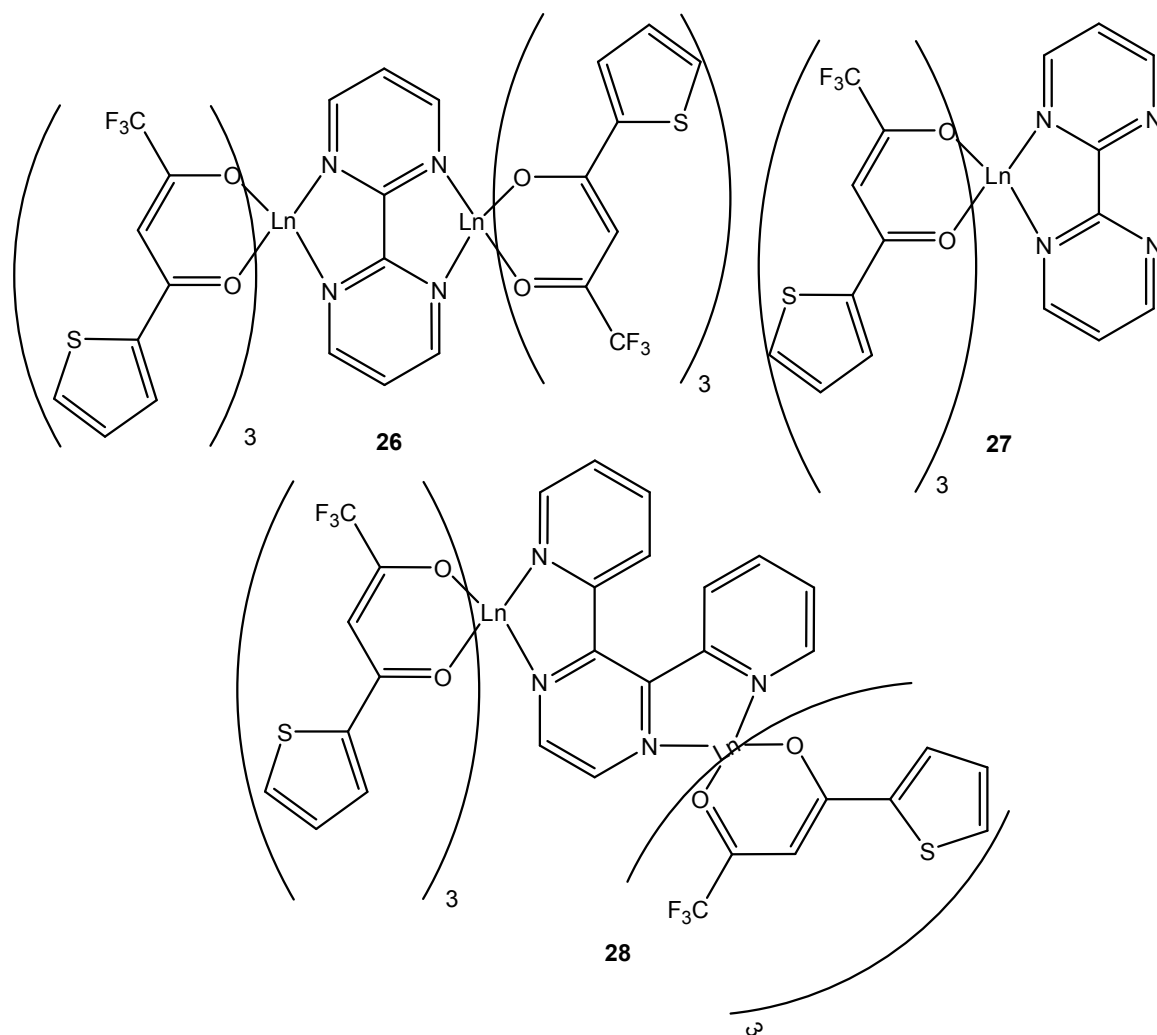
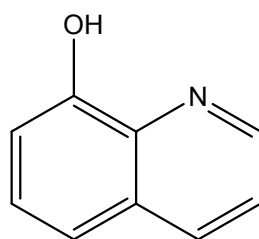


Figure 3.5 : A new collection of Ln³⁺ complexes comprising BPM and DPP as neutral bridging ligands and TTA as the β-diketonate

The complexes shown in figure 3.5 are chemically saturated and H₂O and solvent molecules are prevented from coordinating to the ions.

NIR emitting Ln³⁺ chelates of quinolinates such as 8-hydroxyquinoline have been perceived to be promising candidates for active components in NIR optical devices.^{10,11} Since the observation of erbium(III) tris(8-hydroxyquinolate) (ErQ)-based organic light-emitting diodes displaying luminescence at 1.53 μm,^{12,13} there has been a spectacular rise in the incorporation of the ligand in Ln³⁺ complexes. Its

popularity is also due to the intense green electroluminescence from tris (8-hydroxyquinolato)-aluminum(III) (AlQ) where it is utilized as the active component in organic light-emitting diodes.¹⁰ Figure 3.6 shows the structure of 8-hydroxyquinoline and the ligand can be chelated to metals via the quinolate oxygen and the nitrogen atom.

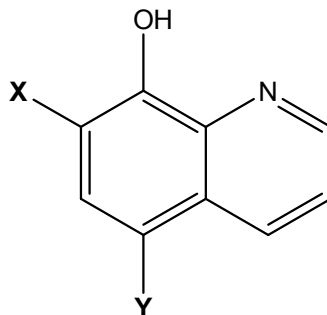


29

Figure 3.6 : Chemical structure of 8-hydroxyquinoline (**29**)

Depending on the reaction conditions, it has been assumed that 8-hydroxyquinoline (Figure 3.6, **29**) with Ln^{3+} tend to form tris complexes (1 : 3 metal-to-ligand ratio),^{14,15} tetrakis complexes (1 : 4 metal-to-ligand ratio)¹⁶ or trimeric complexes (3 : 8 metal-to-ligand ratio).¹⁶ Photoluminescence measurements of erbium tris(8-hydroxyquinoline) revealed lifetimes in the region of 0.2 μs for the powder, 0.4 μs for the thin film blend, 0.9 μs for the evaporated film and 2 μs in dimethyl sulfoxide ($\text{DMSO-}d_6$), which imply quantum yields that range from 0.002 to 0.03%.¹⁷

Van Deun *et al*¹⁰ synthesized a family of halogen substituted 8-hydroxyquinoline derivatives (**30**) shown in chart 3.1.



30

Ligand	Name	X	Y
30a	8-quinolinol	H	H
30b	5-chloro-8-quinolinol	H	Cl
30c	5,7-dichloro-8-quinolinol	Cl	Cl
30d	5,7-dibromo-8-quinolinol	Br	Br
30e	5,7-diiodo-8-quinolinol	I	I

Chart 3.1 : Structure of 8-hydroxyquinoline and its halogen substituted derivatives

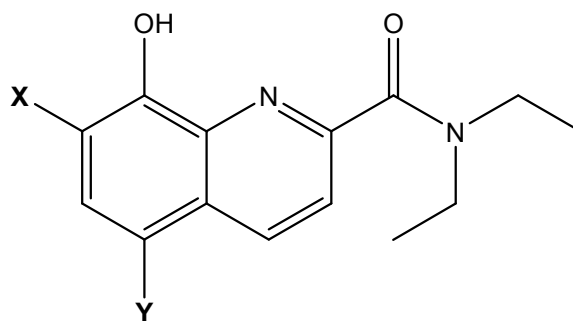
To fulfill the coordination number, H₂O molecules are coordinated to these complexes and in the tetrakis species, sodium (Na) is used as the counter ion. Table 3.1 shows the overview of lifetime and relative intensities of Er³⁺ compounds with the different ligands. These measurements were conducted at room temperature in DMSO-*d*₆.

Entry	Structure	Lifetime in μs	Relative luminescence intensity
1	$\text{Na}[\text{Er}(\text{30c})_4] \cdot 1/2\text{H}_2\text{O}$	2.3	1.54
2	$[\text{Er}(\text{30c})_3]_2 \cdot 2\text{H}_2\text{O}$	2.2	1.45
3	$\text{Na}[\text{Er}(\text{30b})_4] \cdot \text{H}_2\text{O}$	1.6	1.22
4	$\text{Na}[\text{Er}(\text{30a})_4] \cdot 1/2\text{H}_2\text{O}$	1.5	1.00
5	$\text{Na}[\text{Er}_3(\text{30a})_8\text{Cl}(\text{OH}) \cdot 2\text{H}_2\text{O}$	1.6	1.08

Table 3.1 : Lifetime and relative intensities of Er^{3+} compounds with the different ligands

In table 3.1, the luminescence intensity of the Er^{3+} tetrakis complex with unsubstituted 8-hydroxyquinoline has been set to 1.00. Comparing entries 1, 3 and 4 in table 3.1, it can be deduced that halogen substitution increases the lifetimes and luminescence intensity. One efficient quencher of luminescence is the aromatic C–H stretching vibration which occurs at $\sim 3060 \text{ cm}^{-1}$ and is resonant with the second harmonic of the emitting level of the Er^{3+} ion. When the aromatic proton is replaced by a heavy atom, it significantly lowered the stretching frequency with the effect of increasing the number of harmonics required to match the emitting level. This is known as the heavy atom effect.¹⁵ Although an increment of lifetimes can be observed with halogen substituted 8-hydroxyquinoline, the metal ions were not completely protected from the intrusion of H_2O molecules. This implies that the H_2O molecules are probably in the crystal lattice and hence these complexes demonstrated lifetimes in the region of 1 - 2 μs .

Albrecht *et al*¹¹ originated an idea to extend the coordination site of 8-hydroxyquinoline by attachment of amide substituents in the 2-position (Chart 3.2). By doing so, an additional coordination site is introduced on the ligand and the metal is shielded against the coordination of H_2O or solvent molecules to obtain 3 : 1 tris complexes.



31

Ligand	X	Y
31a	H	H
31b	H	Br
31c	Br	Br

Chart 3.2 : Structure of 8-hydroxyquinoline extended with amide substituents and its halogen substituted derivatives

Elemental analysis confirmed the formation of Er³⁺ tris complexes, except for Er³⁺ complexed with ligand 31b, where analytically pure complexes could not be obtained. Mass spectroscopy showed peaks corresponding to tris species for Er³⁺ complexes with the three ligands. From the X-ray data of Er(31a)₃, ligand 31a acts as a tridentate ligand coordinating to the metal by the quinolate oxygen, nitrogen atom and the amide oxygen and hence leading to coordination number nine at the Er³⁺ ion. The three different ligands were also complexed to Nd³⁺ and Yb³⁺ and the lifetime data are presented in table 3.2.

Ligand(L)		NdL ₃	ErL ₃	YbL ₃
31a	Q (%)	0.14(2)	0.012(1)	0.56(5)
	$\tau/\mu\text{s}$	0.39(1)	1.15(2)	11.10(1)
31b	Q (%)	0.23(4) [^]	*	0.60(6)
	$\tau/\mu\text{s}$	0.69(2) [^]	*	10.50(1)
31c	Q (%)	0.40(2)	0.033(5)	1.40(15)
	$\tau/\mu\text{s}$	1.57(1)	4.05(5)	20.60(2)

Q – Quantum yield

τ – Lifetime

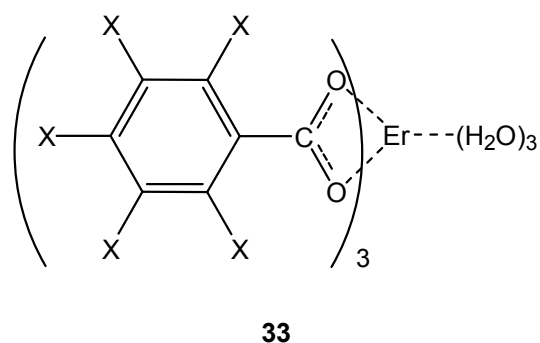
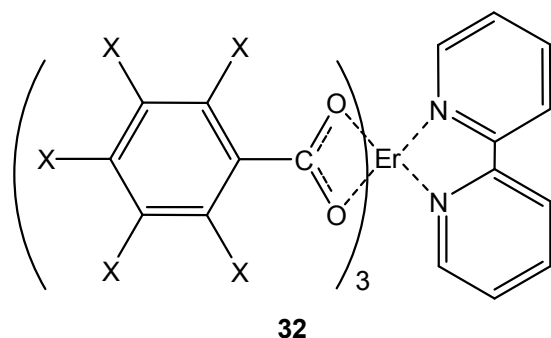
* – No correct analysis

[^] – Analysis showed eight H₂O molecules per complex

Table 3.2 : Results of the solid phase photoluminescence measurements at room temperature for tris Ln³⁺ complexes

For the Nd³⁺ complexes, the quantum yield, Q increases progressively in the series Nd(31a)₃ < Nd(31b)₃ < Nd(31c)₃. The presence of two bromine atoms has resulted in an improvement by a factor of ~2.9. Comparatively, there is a four-fold increase in the lifetime, pointing to a decrease in the non-radiative de-activation processes. Similar results were obtained for the Er³⁺ complexes where the quantum yields increase in the series Er(31a)₃ < Er(31b)₃ < Er(31c)₃ by an almost identical factor of ~2.8 while the lifetimes increase about 3.5-fold. Due to the large energy gap and therefore less sensitivity towards high energy oscillators, the largest quantum yield was obtained for Yb(31c)₃. There was no substantial improvement when a single bromine atom was introduced and the overall 2.5-fold enhancement can be attributed to the addition of a second bromine atom.

Fluorine plays a strategic role in modern optics.¹⁸ The C–F bond has a much lower vibrational energy of ~1200 cm⁻¹ as compared to ~2950 cm⁻¹ of a C–H bond and ~3450 cm⁻¹ of a O–H bond. Thus, fluorinated Ln³⁺ complexes are gaining interest amongst research groups. Chapter 4 will introduce more fluorinated Ln³⁺ complexes.



Benzoate - X=H

Pentafluorobenzoate - X=F

Figure 3.7 : Chemical structures of Er^{3+} benzoate and pentafluorobenzoate complexes with bipyridine (**32**) or H_2O (**33**)

Roh *et al*¹⁹ investigated Er^{3+} complexes based on benzoate and pentafluorobenzoate ligands. These sensitizing bidentate ligands form 3 : 1 complexes and either three molecules of H_2O or a molecule of bipyridine was coordinated to fulfil the coordination number of Er^{3+} (Figure 3.7). The authors synthesized these complexes through the ligand-exchange reaction using ErCl_3 where the potassium salts of the ligands were obtained before reacting them with ErCl_3 to form the Er^{3+} complexes (**32** and **33**). Upon excitation at 488 nm, the complexes with a molecule of bipyridine exhibited stronger near IR emission bands than those with three molecules of H_2O . Er^{3+} complexes with pentafluorobenzoate ligands also showed much stronger near IR emission than those with benzoate ligands. This can be attributed to the lower vibrational energy C–F bond.

3.1.1 Outline of chapter

In chapter 2, we saw the effects of deuteration and removing hydrogen atoms from near the Ln^{3+} ion. From the preceding reviews, we saw that oxygen atoms are good donors which can be coordinated to the Ln^{3+} ions. One important requirement of achieving high luminescence quantum efficiency is by the exclusion of solvent molecules as well as the removal of high vibrational energy oscillators.

In this chapter, we discuss our attempts to prepared 4 : 1 Er^{3+} complexes with pentafluorobenzoate ligands. Following that, we discuss our preparation and attempt to form Er^{3+} complexes with a novel ligand, 3-[(4-methoxy phenyl)(pentafluorophenylsulfanyl) methyl] -1,1,1,5,5,5-hexafluoro-pentane-2,4-dione). In the final part of this chapter, we discuss our efforts to synthesize 1,1,1,5,5,5-hexafluoro-3-(pentafluorophenyl)-pentane-2,4-dione.

3.2 Attempt to prepare Cs[Er(pentafluorobenzoate)₄]

As discussed in section 3.1, Roh *et al*¹⁹ investigated Er³⁺ complexes based on pentafluorobenzoate ligands. They prepared 3 : 1 Er³⁺ complexes where H₂O or bipyridine is utilised to fulfil the high coordination number of Er³⁺.

In this section, we discuss our attempt to prepare 4 : 1 complexes of pentafluorobenzoate with Er³⁺. Chapter 5 provides the preparation procedures and the characterisation data for the product of the reaction between pentafluorobenzoic acid and erbium(III) chloride. Figure 3.8 shows the crystal structure of the resulting complex. It can be seen that 3 : 1 complexes were formed and five H₂O molecules were coordinated. This is consistent with the findings of Roh *et al*¹⁹ where 3 : 1 complexes were obtained. Even though caesium carbonate was used in the reaction to stabilize the overall charge, we were not able to form the desired saturated 4 : 1 tetrakis complexes. The IR spectrum of this complex shows a O–H stretching band centred at around 3425 cm⁻¹, which is consistent with the presence of H₂O molecules. The C=O stretching band of the carboxylate ligand can be observed at around 1589 cm⁻¹. The C=C and C–F bands can be seen at 1412 cm⁻¹ and 1003 cm⁻¹, respectively.

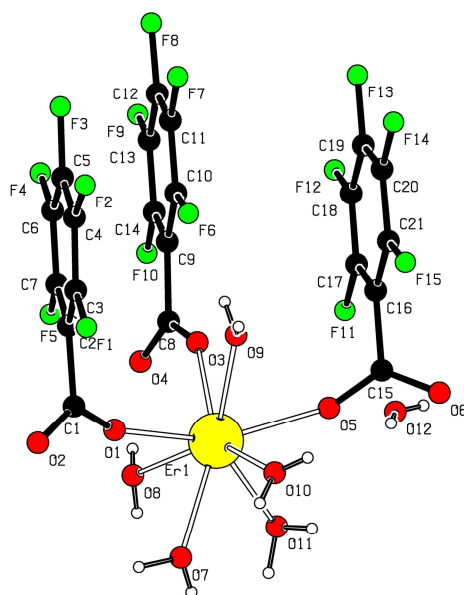


Figure 3.8 : XRD chemical structure of [Er(C₆F₅CO₂)₃(H₂O)₅]

Figure 3.9 (a) and figure 3.9 (b) show the emission spectra of the Er^{3+} complex and pentafluorobenzoic acid, respectively. They were both excited at 520 nm and the spectrum was obtained using a 850 nm long pass filter and thus, the short wavelength part of the band was truncated.

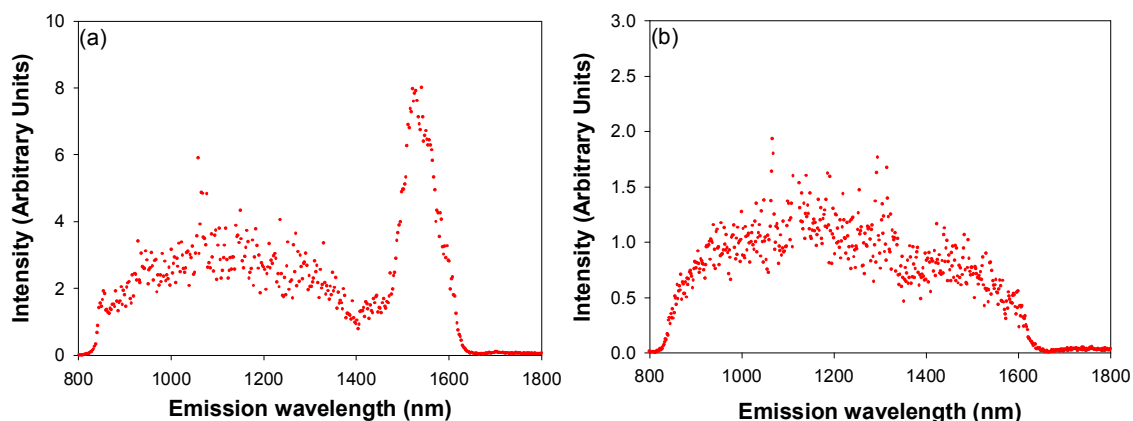


Figure 3.9 : (a) Emission spectrum of $[\text{Er}(\text{C}_6\text{F}_5\text{CO}_2)_3(\text{H}_2\text{O})_5]$ and (b) emission spectrum of the free pentafluorobenzoic acid

Comparing figures 3.9 (a) and 3.9 (b), we can attribute the broad feature seen from about 800 nm to 1600 nm in figure 3.9 (a) to the ligand emission. In figure 3.9 (a), we can see the distinct features of Er^{3+} , centred at around 1.5 μm . The peak of the emission is at 1540 nm.

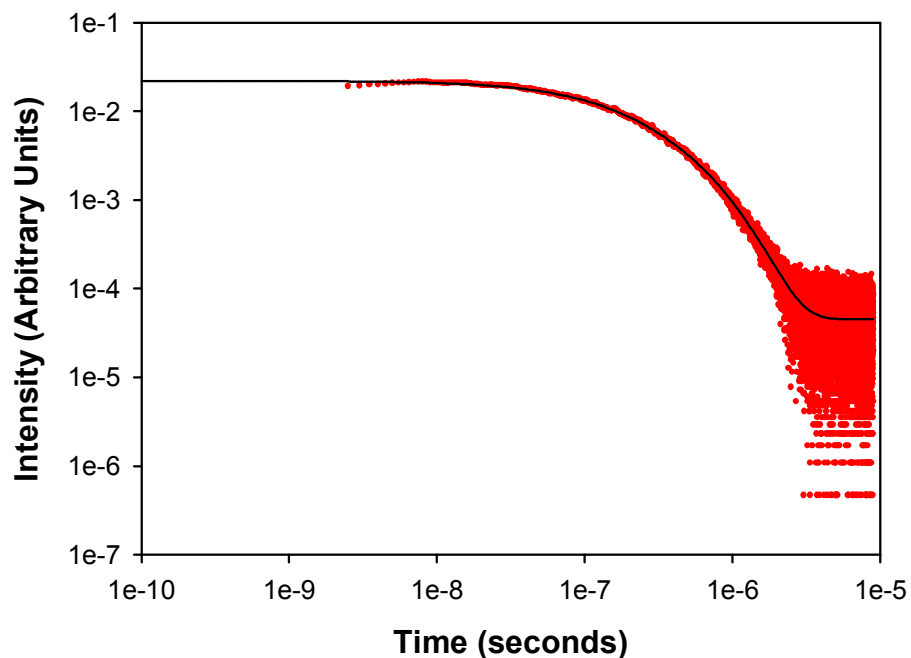


Figure 3.10 : Luminescence lifetime data and fit of $[\text{Er}(\text{C}_6\text{F}_5\text{CO}_2)_3(\text{H}_2\text{O})_5]$

The luminescence lifetime data and fit of $[\text{Er}(\text{C}_6\text{F}_5\text{CO}_2)_3(\text{H}_2\text{O})_5]$ is shown in figure 3.10. Lifetimes of 105 ns (37.8%), 265 ns (44.3%) and 567 ns (17.9%) were obtained. These lifetimes are consistent with those that we saw for $[\text{Er}(\text{HFA})_3(\text{H}_2\text{O})_2]$ in section 2.6 of chapter 2 (Table 2.6), where we attribute lifetimes in the ns region to H_2O molecules in the coordination sphere of the Ln^{3+} ions.

Figure 3.11 (a) shows the absorption spectrum of pentafluorobenzoic acid and figure 3.11 (b) shows the excitation spectrum of the Er^{3+} complex at the emission wavelength of 1540 nm.

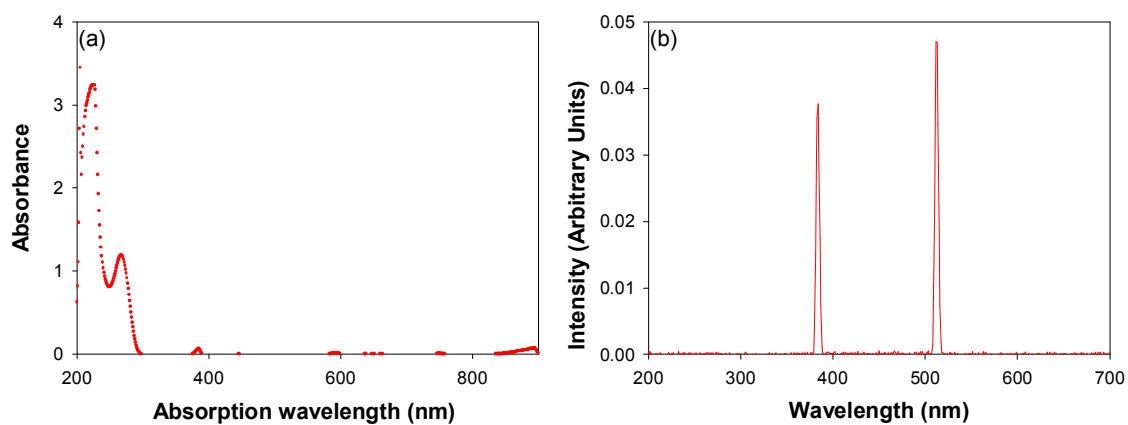
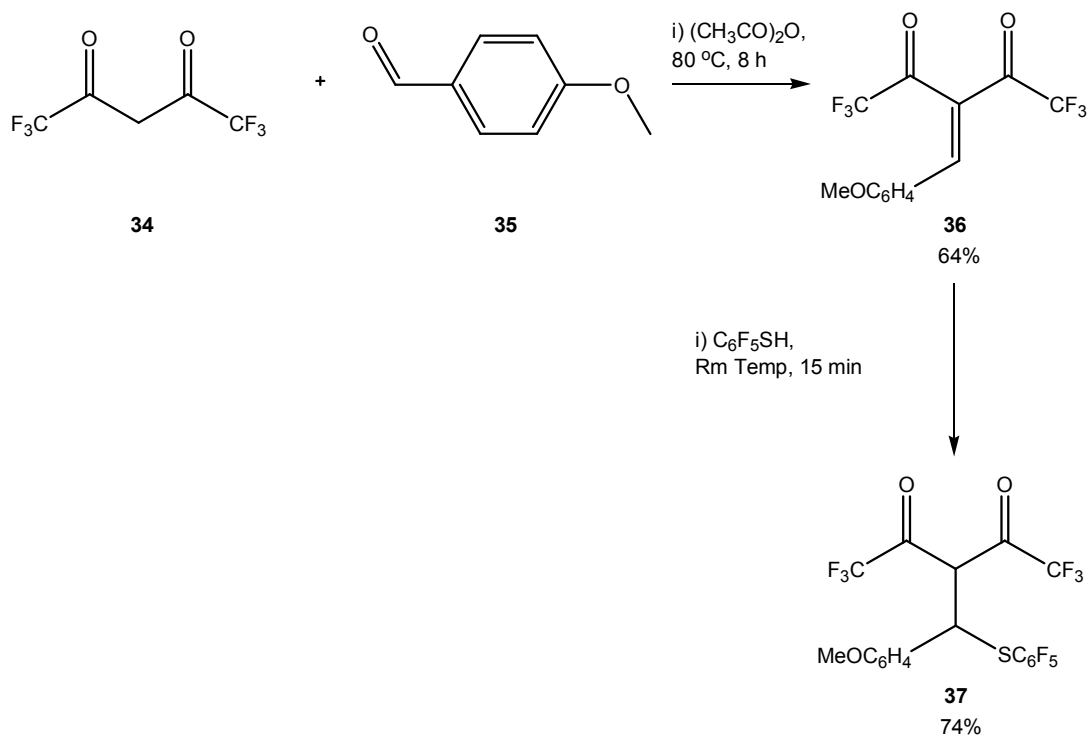


Figure 3.11 : (a) Absorption spectrum of pentafluorobenzoic acid and (b) excitation spectrum of [Er(C₆F₅CO₂)₃(H₂O)₅] at emission wavelength of 1540 nm

Comparing figures 3.11 (a) and 3.11 (b), we can conclude that there is no sensitisation from the ligand to the Er³⁺. The concentration of the sample used for the absorption measurement was $4.717 \times 10^{-4} \text{ mol L}^{-1}$ and absorbance peaks are at 224 nm and 267 nm. The extinction coefficients are $6873 \text{ L mol}^{-1} \text{ cm}^{-1}$ and $2519 \text{ L mol}^{-1} \text{ cm}^{-1}$ for 224 nm and 267 nm, respectively.

3.3 Attempted preparation of Cs[Er(3-[(4-methoxy phenyl) (pentafluorophenylsulfanyl)methyl] -1,1,1,5,5,5-hexafluoro-pentane-2,4-dione)₄]

We saw from chapter 1 that β -diketonates are thermodynamically and kinetically stable ligands which form robust Ln^{3+} complexes through their donor oxygen atoms. From chapter 2, we studied Ln^{3+} complexes of 1,1,1,5,5,5-hexafluoroacetylacetone (HFA) and found that for the tetrakis complexes, the hydrogen atom is ~ 4.7 Å away from the central ion and that has limited the radiative lifetime for use in optical devices. Deuteration has improved the radiative lifetime and for a 98% deuterated $\text{Cs}[\text{Er}(\text{HFA-}d)]_4$ sample, about two magnitude orders of increase was observed. In this section, we synthesized a novel β -diketonate potential ligand and attempted to complex it to Er^{3+} . Full synthetic procedures²⁰ and characterization data are presented in chapter 5. Heating a 1 : 1 mixture of HFA (**34**) and 4-methoxybenzaldehyde (**35**) in acetic anhydride at 80 °C for 8 h according to the literature²⁰ gave the condensation product (**36**) in 64% yield (Scheme 3.1).



Scheme 3.1 : Preparation of 3-[(4-methoxy phenyl)(pentafluorophenylsulfanyl) methyl] -1,1,1,5,5,5-hexafluoro-pentane-2,4-dione (**37**)

Diketone **36** underwent conjugate addition when heated with pentafluorothiophenol (Scheme 3.1), to yield the adduct **37**; this process is analogous to the addition of thiophenol which has been reported in the literature.²⁰

Ligand **37** was obtained as a white solid with a yield of 74%. The formation of 3-[(4-methoxy phenyl)(pentafluorophenylsulfanyl) methyl] -1,1,1,5,5,5-hexafluoro-pentane-2,4-dione (**37**) was confirmed by elemental analysis. Electrospray mass spectroscopy was also done on ligand **37** but the expected molecular ion could not be observed and there was a large peak at 208 *m/z* corresponding to hexafluoropentanedione. It is likely that the ligand is unstable and breaks apart during the ionization process. Nevertheless, an attempt was made to form the Er^{3+} complex. The attempted preparation resulted in a yellow low melting solid, which had moderate solubility in common organic solvents like MeOH. Electrospray mass spectroscopy again did not reveal any peaks corresponding to the initial ligand **37**.

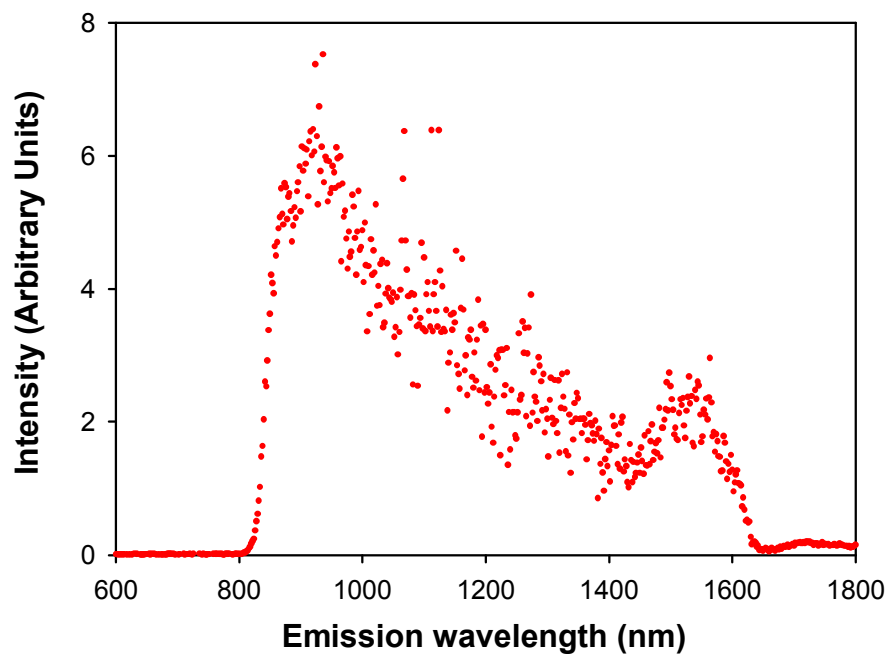


Figure 3.12 : Emission spectrum of the low melting solid which was obtained upon reaction of ligand **37** with Er^{3+}

Figure 3.12 shows the emission spectra of the low melting solid. It was excited at 520 nm and the spectrum was obtained using a 850 nm long pass filter and thus, the short wavelength part of the band was truncated. It has a broad feature from 800 nm to 1600 nm and from the spectrum, we were unable to conclude the presence of Er^{3+} in our sample.

3.4 Attempted preparation of 1,1,1,5,5,5-hexafluoro-3-pentafluorophenyl-pentane-2,4-dione

Since the beginning of this thesis, the advantages of fluorination have been thoroughly discussed. In pursuit of obtaining potentially suitable fluorinated ligands, we have attempted several ways of synthesizing 1,1,1,5,5,5-hexafluoro-3-pentafluorophenyl-pentane-2,4-dione (**38**) shown in figure 3.13. The three main approaches are through the Grignard reaction, the Wittig reaction and the catalytic arylation of 1,3-diketones.

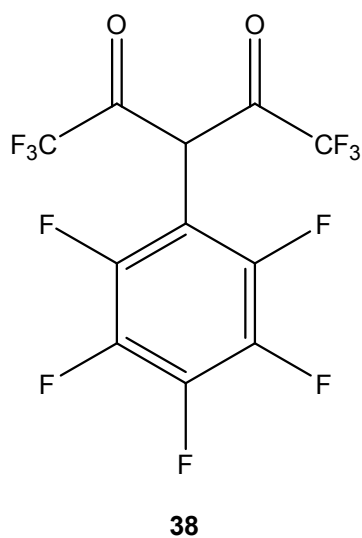
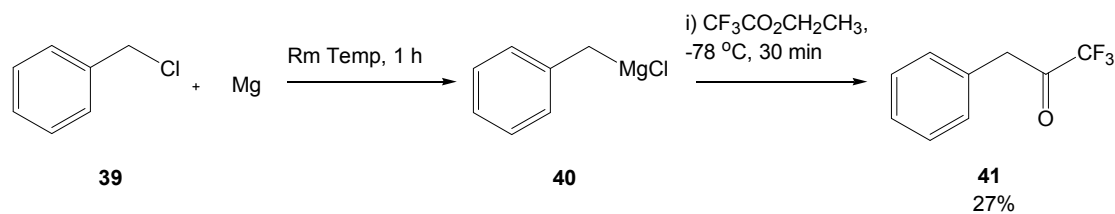


Figure 3.13 : Chemical structure of 1,1,1,5,5,5-hexafluoro-3-pentafluorophenyl-pentane-2,4-dione (**38**)

In the following sections, we shall discuss the attempts to prepare diketone **38**. Full synthetic procedures and characterization of synthetic intermediates will be presented in chapter 5. For each of the different approaches, some model studies were performed using non-fluorinated precursors.

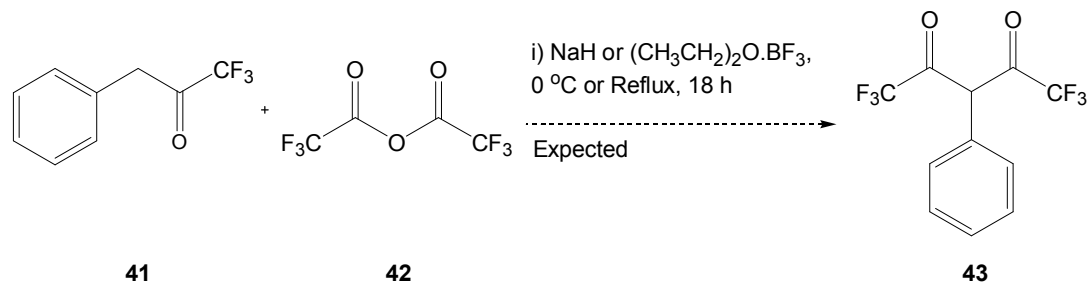
3.4.1. Grignard reaction

Our Grignard approach involved two main steps. Firstly, the Grignard reaction was carried out to obtain 1,1,1-trifluoro-3-phenylpropan-2-one (**41**) (Scheme 3.2). Following that, Claisen condensation was performed in an attempt to obtain 1,1,1,5,5,5-hexafluoro-3-phenyl-pentane-2,4-dione (**43**). The expected reaction pathway is shown in scheme 3.3.



Scheme 3.2 : Preparation of 1,1,1-trifluoro-3-phenylpropan-2-one (**41**)

Scheme 3.2 was carried out by analogy to Felix *et al*²¹ and full details of the preparation can be found in chapter 5. We obtained ketone **41** in 27% yield and our boiling point of 80 °C at approximately 15 mmHg is consistent with Herkes *et al*²², where boiling point of 66 °C at 16 mmHg was reported. From our ¹H NMR data, we saw a peak at δ_{H} 4 and this corresponds to the hydrogens on the saturated α carbon. A multiplet from δ_{H} 7.2 – 7.4 is attributed to the phenyl group. Carbonyl stretching at 1759 cm^{-1} can be observed from our IR spectroscopy data.



Scheme 3.3 : Attempt to prepare 1,1,1,5,5,5-hexafluoro-3-phenyl-pentane-2,4-dione (**43**) via Grignard chemistry

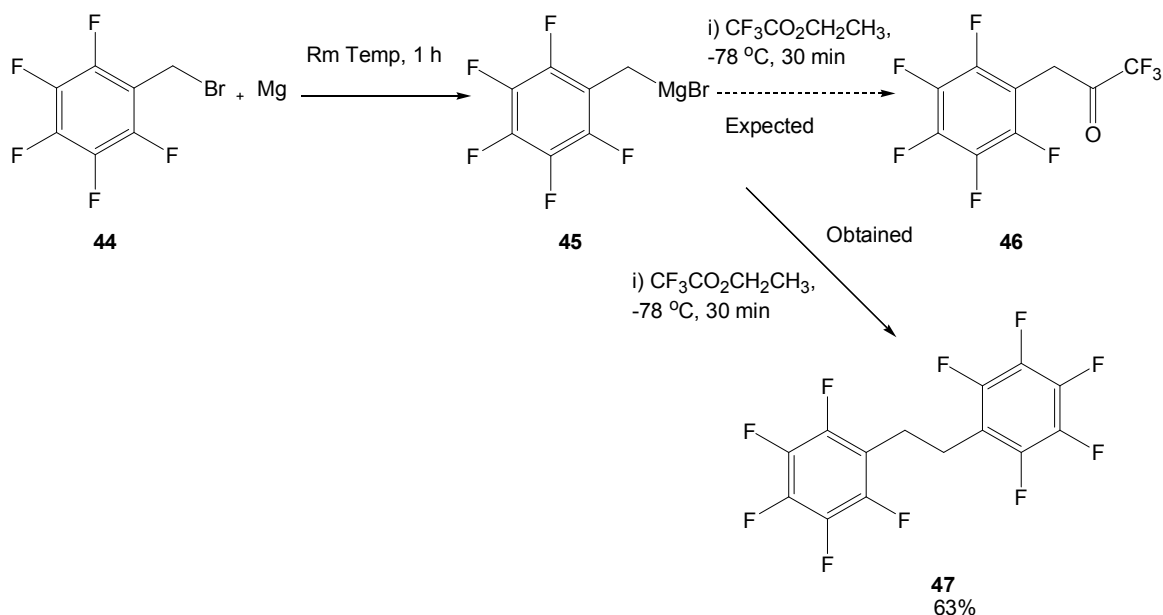
For the second step of the reaction shown in scheme 3.3, the main reagents used were ketone **41** and trifluoroacetic anhydride (**42**). However, for some of the experiments, sodium hydride (NaH) was used as a base while in other cases, the Lewis acid, boron trifluoride diethyl etherate was used instead. THF and DCM were the two different solvents used. There were also variations in the temperature and time. Table 3.3 shows a summary of the different conditions.

Entry	Base / Acid	Solvent	Temperature	Time
1	NaH (Base)	THF	Reflux	18 h
2	NaH (Base)	THF	0 °C	18 h
3	(CH ₃ CH ₂) ₂ O·BF ₃ (Acid)	DCM	Reflux	18 h
4	(CH ₃ CH ₂) ₂ O·BF ₃ (Acid)	DCM	0 °C	18 h

Table 3.3 : Summary of different conditions attempted for the preparation of 1,1,1,5,5,5-hexafluoro-3-phenyl-pentane-2,4-dione (**43**)

For entries 1 & 2 in table 3.3, the reaction mixture was neutralized with HCl at the end of the reaction time. The crude product was then extracted into Et₂O. For entries 3 & 4, the reaction mixture was neutralized with sodium acetate before being extracted into DCM. In all the experiments upon extraction, the organic layers were dried using MgSO₄ before evaporation to obtain the crude product. Distillation was done on the crude product and in all cases, the ¹H NMR spectrum revealed the unreacted starting material, ketone **41**. We suspect that the electron withdrawing CF₃ groups on compounds **41** and **42** have provided some resistance to the formation of the desired diketone **43**.

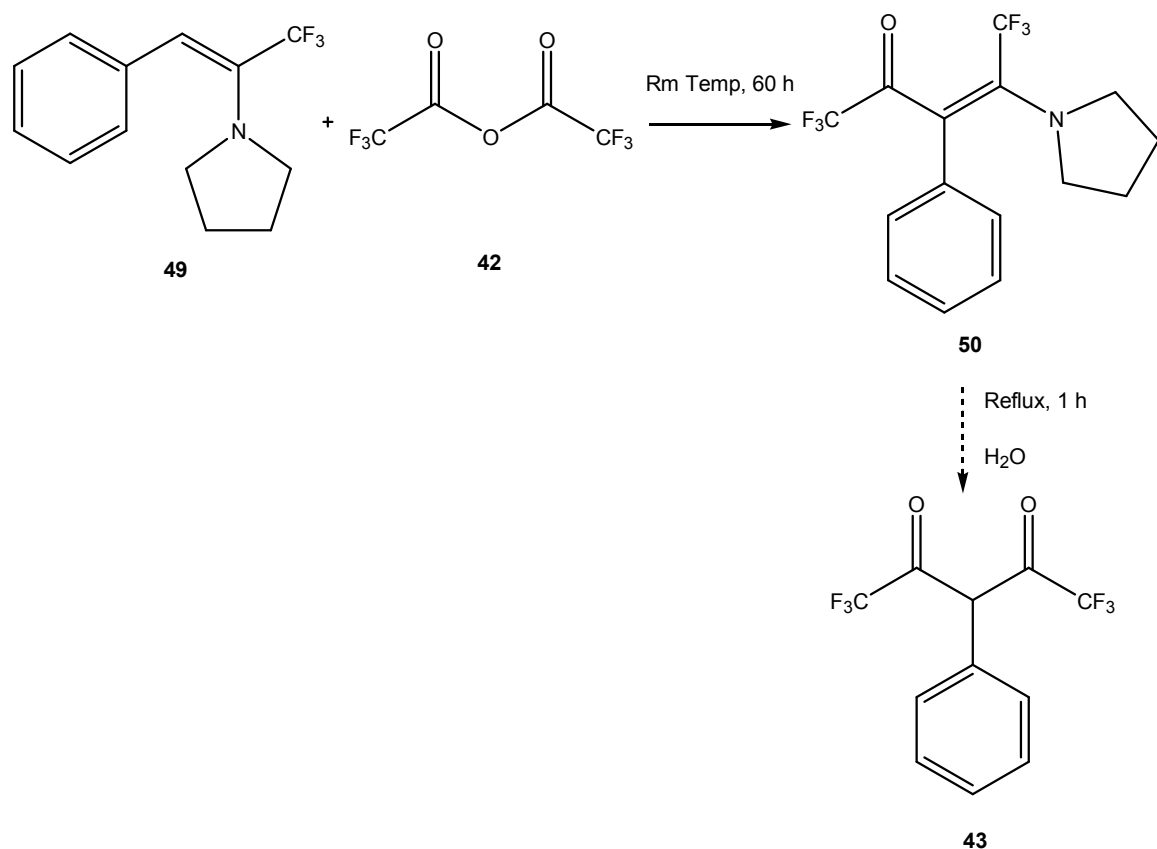
Despite the unsuccessful attempts to synthesize the diketone **43** via the above described method, we proceeded to attempt to synthesize the fluorinated analogue, 1,1,1-trifluoro-3-pentafluorophenyl-propan-2-one (**46**). The methods and conditions used were similar to scheme 3.2 but this time, pentafluorobenzyl bromide (**44**) was used to prepare the Grignard reagent instead of benzyl chloride (**39**) (Scheme 3.4).



Scheme 3.4 : Attempt to prepare 1,1,1-trifluoro-3-pentafluorophenyl-propan-2-one (**46**)

Scheme 3.4 was carried out with similar conditions to scheme 3.2. A solid product was isolated but its IR spectrum showed no C=O stretch, thus ruling out the ketone **46**. Its ¹H NMR spectrum showed a singlet at δ_H 3.0, which is consistent to the literature value for the bibenzyl derivative (**47**).²³ Two melting points were reported in the literature.^{23,24} We obtained a melting point of in the range of 102 – 105 °C and is identical with that (107 – 108 °C) reported by Birchall *et al.*²⁴ Krafczyk and co. reported a melting point of 90 °C.²³

Other methods were then attempted to synthesize diketone **38**. With the availability of ketone **41**, we went on to synthesize enamine (**49**) (Scheme 3.5).



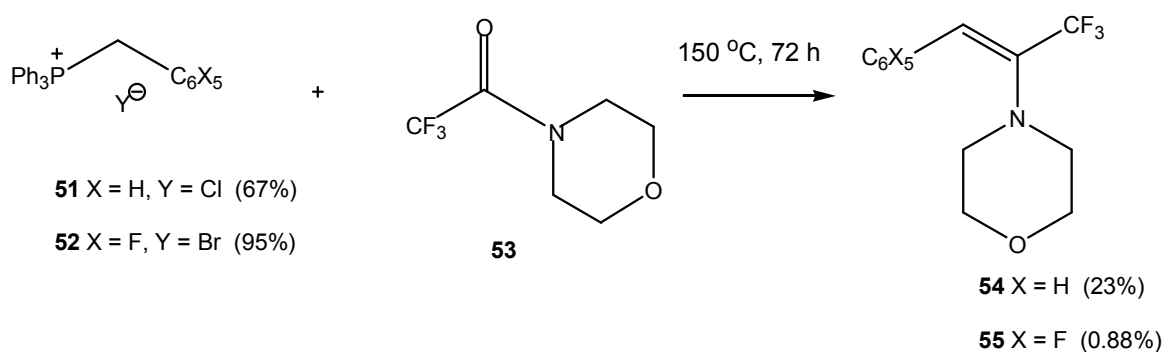
Scheme 3.6 : Attempt to prepare 1,1,1,5,5,5-hexafluoro-3-phenylpentane-2,4-dione (**43**) via enamine **49**

Enamine **49** was left to stir with trifluoroacetic anhydride in DCM for 60 h at room temperature. Dilute hydrochloric acid was then added and the reaction was left to stir for 1 h. It was then extracted into Et₂O and dried using MgSO₄. The organic layer was then evaporated to give a yellow liquid. To test for the formation of the β-diketone **43**, the yellow liquid was treated with copper(II) acetate. There were no signs of copper salt formation which suggests that we did not obtain the desired β-diketone **43**.

3.4.2 Wittig reaction

The starting materials for the Wittig reactions were the phosphonium salts **51** and **52** (Scheme 3.7). Phosphonium chloride **51** was prepared according to literature

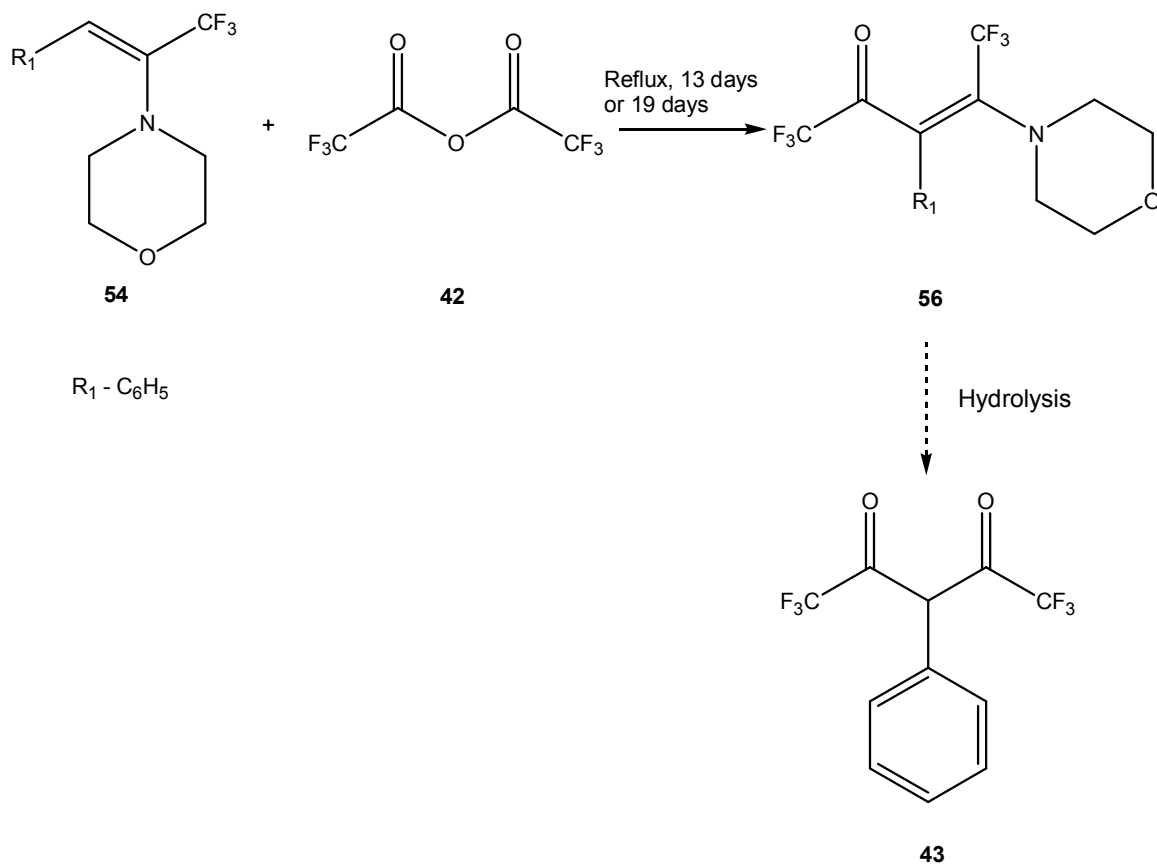
procedures²⁵ with slight modifications; we used toluene instead of the reported THF as a solvent. Phosphonium bromide **52** was prepared using the procedures used by Filler and Heffern.²⁷ Amide **53** was prepared by analogy to Joullie *et al.*²⁸ Chapter 5 provides the full synthetic procedures and characterization data.



Scheme 3.7 : Route to obtaining 4-(2-phenyl-1-trifluoromethyl-vinyl)-morpholine (**54**) or 4-[2-(pentafluorophenyl)-1-(trifluoromethyl-vinyl)-morpholine] (**55**)

The Wittig reactions of trifluoroacetamide **53** with the ylids derived from phosphonium salts **51** and **52**, gave the respective enamines **54** and **55** (Scheme 3.7). Enamine **54** had been previously prepared in this way by Bégué *et al.*²⁹ Enamine **55** is a new compound which has been fully characterized (Chapter 5). For enamine **54**, the ¹H NMR revealed a 5.2 : 1 ratio of the *Z* : *E* isomers. The *Z* isomer has a chemical shift of δ_{H} 6.5, while the *E* isomer has a chemical shift of δ_{H} 6.2.

Upon obtaining enamines **54** and **55**, the next step of the reaction involved trifluoroacetylation with trifluoroacetic anhydride (**42**), e.g. to give ketone **56**. It was then expected that hydrolysis of the enamine function in ketone **56** would give us the desired diketone **43** (Scheme 3.8).



Scheme 3.8 : Attempted preparation of 1,1,1,5,5-hexafluoro-3-phenyl-pentane-2,4-dione (**43**) via enamine **54**

Two different conditions were performed for the reaction shown in scheme 3.8 and presented in table 3.4.

Entry	Solvent	Total time of reaction	Reaction temperature	Mole ratio of Compound 54 to Compound 42
1	Dichloromethane	19 days	40 °C	1 : 2
2	Chloroform	13 days	60 °C	1 : 10

Table 3.4 : Different conditions for the reaction shown in scheme 8

For entry 1 in table 3.4, the reaction was monitored daily by either ^1H NMR or thin layer chromatography (ratio – 70 : 5 petrol : Et_2O) and each time, it was found that

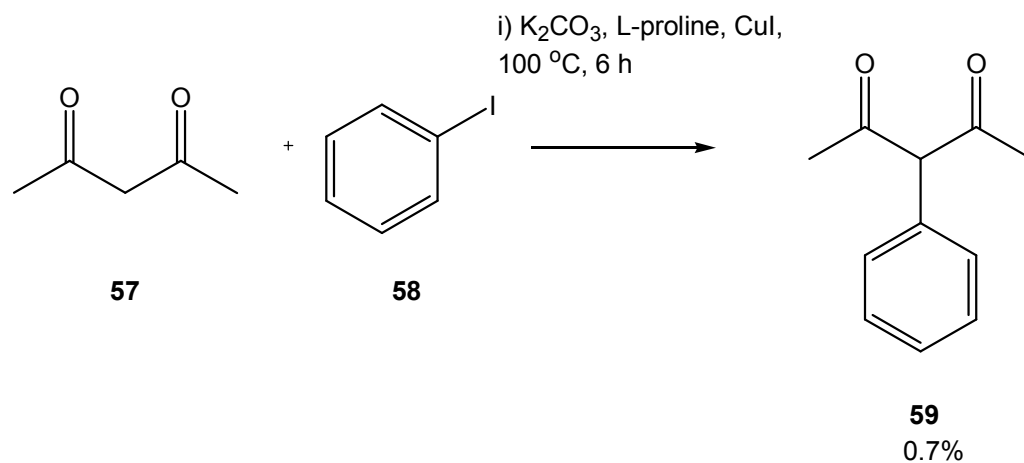
the starting material (enamine **54**) was present. On day seven of the reaction, about 50 mg of 4-dimethylaminopyridine was added as a catalyst. Subsequent tests still revealed the presence of starting material.

For entry 2 in table 3.4, the reaction started without any solvent and similarly to entry 1, the reaction was monitored daily by ^1H NMR and thin layer chromatography. The presence of enamine **54** was detected each time. A week after the start of the reaction, chloroform (CHCl_3) was added as a solvent. The following tests still revealed the presence of enamine **54**. On day twelfth of the reaction, 0.5 mL of boron trifluoride diethyl ether was added as a catalyst. The reaction was then left to reflux for another day and the ^1H NMR again showed the presence of starting material (enamine **54**). Again, this can be attributed to the electron withdrawing CF_3 groups which resisted the formation of the desired diketone **43**. No reactions were attempted with the fluorinated enamine **55**.

The reaction described above (Scheme 3.8) was similar to that in scheme 3.6. The presence of the starting material, enamine **54** after a maximum of 19 days suggests that the presence of the oxygen atom in enamine **54** reduced the nucleophilicity, hence rendering the compound unreactive, relative to enamine **49**. For reactions with enamine **49** (Scheme 3.6), TLC showed the total consumption of starting material (enamine **49**) after 60 h.

3.4.3 Reactions with catalysts

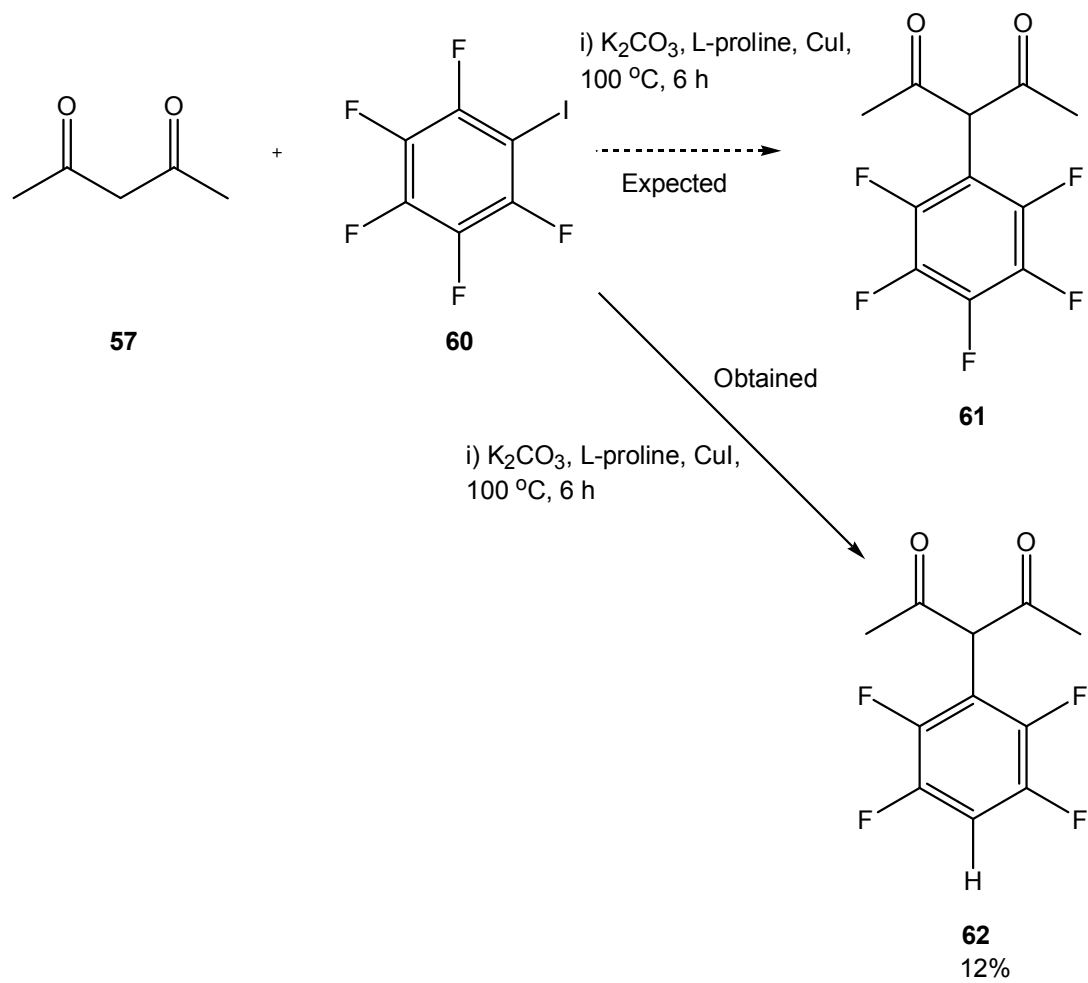
Jiang *et al.*³⁰ carried out arylation reactions on β -diketones using aryl iodides in the presence of K_2CO_3 , L-proline and copper iodide (Scheme 3.9). Firstly, we repeated this work to obtain 3-phenyl-pentane-2,4-dione (**59**) and the characterization data (Chapter 5) matched those obtained by Barton *et al.*³¹



Scheme 3.9 : Preparation of 3-phenyl-pentane-2,4-dione (**59**)

The low yield of 0.7% obtained for our diketone **59** was due to the fact that distillation was done to purify the compound.

We then proceeded to react acetylacetone (**57**) with iodopentafluorobenzene (**60**) under the same conditions (Scheme 3.10). We expected to obtain 3-pentafluorophenyl-pentane-2,4-dione (**61**) but ^{19}F NMR (Figure 3.14), 1H NMR (Figure 3.15) and mass spectroscopy confirmed that 3-(2,3,5,6-tetrafluoro-phenyl)-pentane-2,4-dione (**62**) was obtained in 12% yield.



Scheme 3.10 : Reaction of acetylacetone (**57**) with iodopentafluorobenzene (**60**)

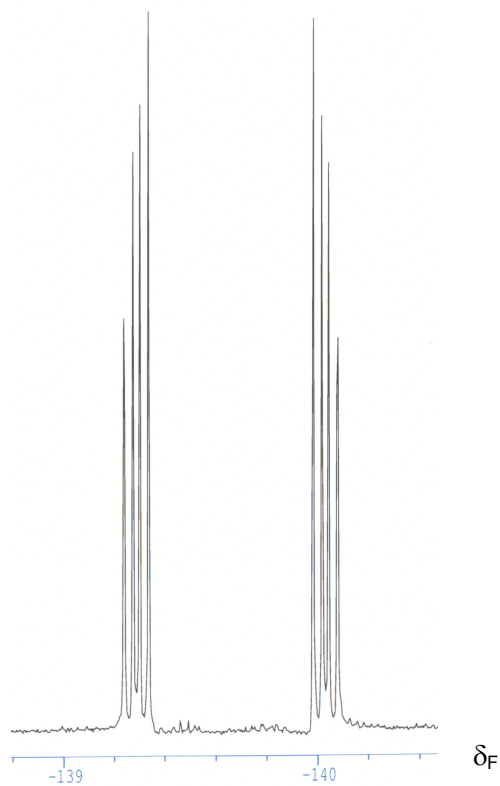


Figure 3.14 : ^{19}F NMR of diketone **62**

From the ^{19}F NMR spectrum shown in figure 3.14, the peaks are symmetrical and give an AA'BB' pattern consistent with the lack of fluorine at the 1- and 4-positions.

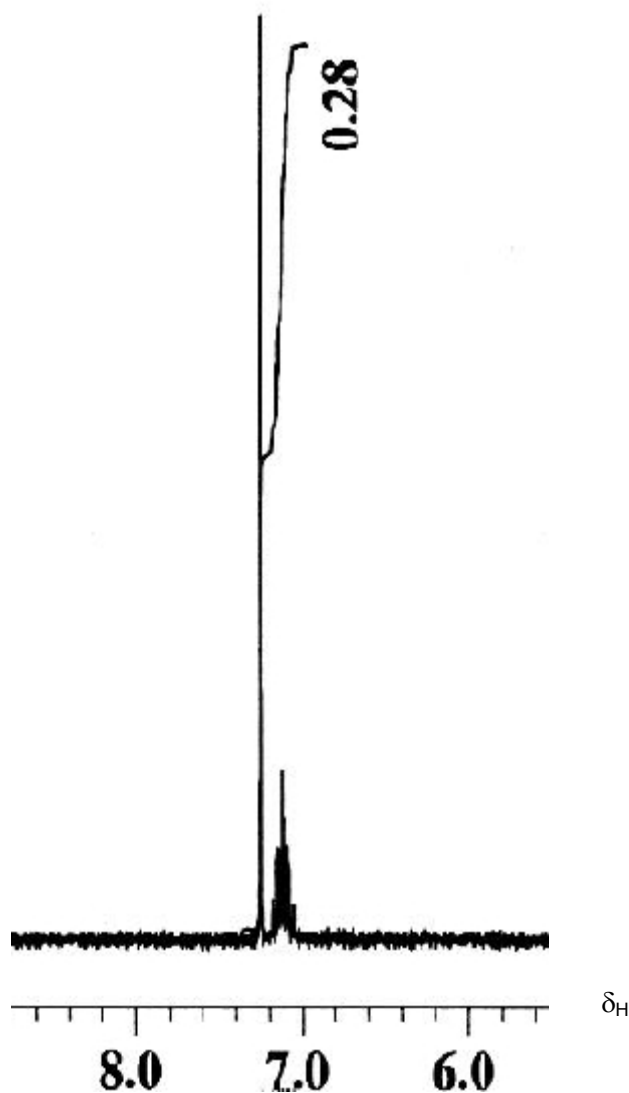
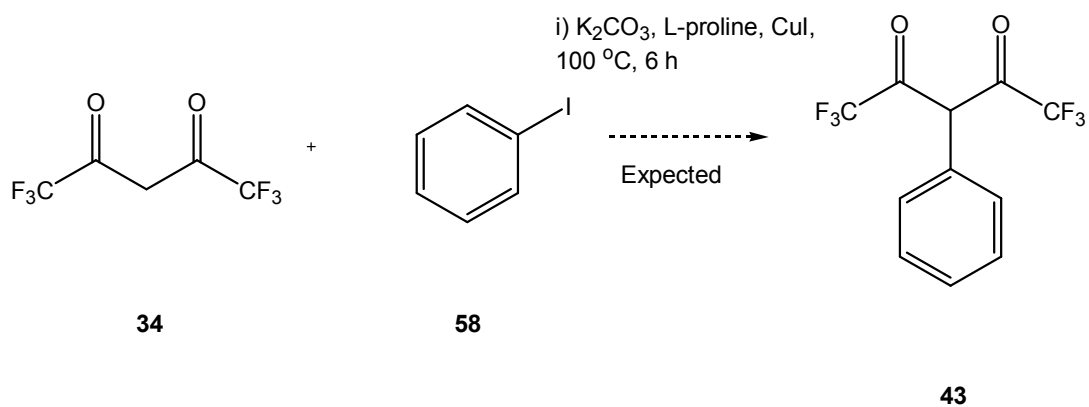


Figure 3.15 : ^1H NMR of diketone **62**

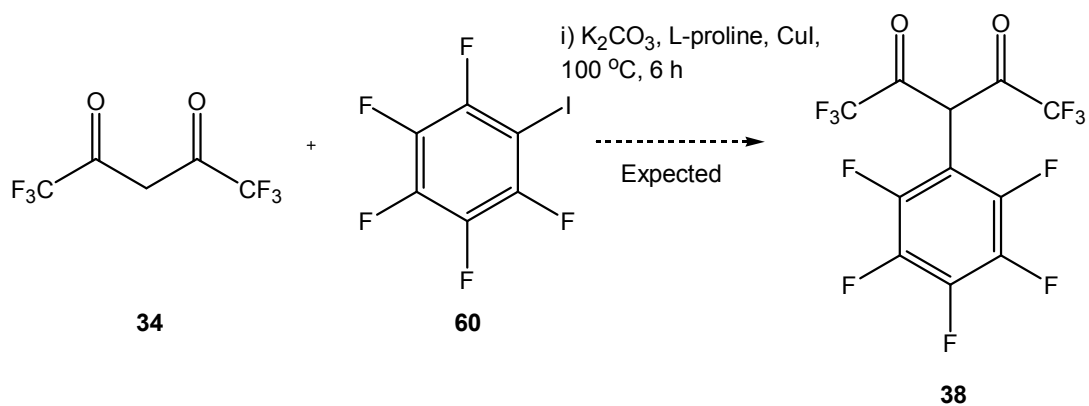
From the ^1H NMR spectrum in figure 3.15, a multiplet centred around δ_{H} 7.1 confirmed the presence of an aromatic proton. The sharp singlet peak at around δ_{H} 7.3 is due to the presence of residue CHCl_3 (solvent used for ^1H NMR – CDCl_3). The IR data revealed strong $\text{C}=\text{O}$ stretching at 1738 cm^{-1} and $\text{C}=\text{C}$ stretching at 1495 cm^{-1} . Strong $\text{C}-\text{H}$ stretching was also observed at 2986 cm^{-1} . Chapter 5 presents the full preparation procedures and the characterization data.

We adopted the same methodology in an attempt to obtain compound **43** (Scheme 3.11).



Scheme 3.11 : Reactions of HFA (**34**) with iodobenzene (**58**)

The attempted reaction of HFA (**34**) and iodobenzene (**58**) under similar conditions resulted in the isolation of a pink liquid. The IR and ^1H NMR spectra of this material showed that it was unreacted iodobenzene (**58**).



Scheme 3.12 : Reactions of HFA (**34**) with iodopentafluorobenzene (**60**)

We also attempted reactions with compound **34** and compound **60** under similar conditions (Scheme 3.12). ^{19}F NMR of the resultant yellow solid showed the loss of

the fluorinated ring and the desired compound **38** was not obtained. For the diketone **34**, we suspect that the presence of two powerfully electron-withdrawing trifluoromethyl groups reduced the ability to undergo arylation reactions.

3.5 Conclusions for chapter 3

We have shown that pentafluorobenzoate ligands are not likely to form 4 : 1 tetrakis complexes with Er^{3+} in an aqueous environment. In our experiments, we obtained erbium(III) pentafluorobenzoate pentahydrate, which was characterised by single crystal X-ray diffraction.

We have prepared and characterized a novel β -diketone, 3-[(4-methoxyphenyl) (pentafluorophenylsulfanyl) methyl] -1,1,1,5,5,5-hexafluoro-pentane-2,4-dione). However, we were unable to characterize any erbium complexes derived from this potential ligand.

Three pathways were attempted to prepare 1,1,1,5,5,5-hexafluoro-3-pentafluorophenyl-pentane-2,4-dione. Our attempts via Grignard chemistry, Wittig chemistry and some experiments involving catalytic arylation of diketones were unsuccessful and this was attributed to the electron withdrawing nature of the CF_3 groups which provided resistance to the formation of the desired compounds. We observed an unexpected reductive defluorination, specifically at position 4, in the copper catalyzed arylation of 2,5-pentanedione by iodopentafluorobenzene.

3.6 References for chapter 3

1. Kim; H. K., Oh; J. B., Baek; N. S., Roh; S., Nah; M. and Kim; Y. H., *Bulletin of the Korean Chemical Society*, 26, **2005**, 201
2. Mancino; G., Ferguson; A. J., Beeby; A., Long; N. J. and Jones; T. S., *Journal of the American Chemical Society*, **2005**, 524
3. Hofstraat; J. W., Oude Wolbers; M. P., van Veggel; F. C. J. M., Reinhoudt; D. N., Werts; M. H. V. and Verhoeven; J. W., *Journal of Fluorescence*, 8, **1998**, 301
4. Artizzu; F., Deplano; P., Marchiò; L., Mercuri; M. L., Pilia; L., Serpe; A., Quochi; F., Orrù; R., Cordella; F., Meinardi; F., Tubino; R., Mura; A. and Bongiovanni; G., *Inorganic Chemistry*, 44, **2005**, 840
5. Bellusci; A., Barberio; G., Crispini; A., Ghedini; M., Deda; M. L. and Pucci; D., *Inorganic Chemistry*, 44, **2005**, 1818
6. De Silva; C. R., Maeyer; J. R., Dawson; A. and Zheng; Z., *Polyhedron*, 26, **2007**, 1229
7. Sultan; R. , Gadamsetti; K. and Swavey; S., *Inorganica Chimica Acta*, 359, **2006**, 1233
8. Jang; H., Shin; C., Jung; B., Kim; D., Shim; H. and Do; Y., *European Journal of Inorganic Chemistry*, **2006**, 718
9. Fratini; A., Richards; G., Larder; E. and Swavey; S., *Inorganic Chemistry*, 47, **2008**, 1030
10. Deun; R. V., Fias; P., Nockemann; P., Schepers; A., Parac-Vogt; T. N., Hecke; K. V., Meervelt; L. V. and Binnemans; K., *Inorganic Chemistry*, 43, **2004**, 8461

11. Albrecht; M., Osetska; O., Klankermayer; J., Frohlich; R., Gumy; F. and Bünzli; J.-C. B., *Chemical Communications*, **2007**, 1834
12. Curry; R. J. and Gillin; W. P., *Applied Physics Letters*, **75**, **1999**, 1380
13. Curry; R. J., Gillin; W. P., Knights; A. P. and Gwilliam; R., *Optical Materials* **17**, **2001**, 161
14. Blyth; R. I. R., Thompson; J., Zou; Y., Fink; R., Umbach; E., Gigli; G. and Cingolani; R., *Synthetic Metals*, **139**, **2003**, 207
15. Deun; R. V., Fias; P., Driesen; K., Binnemans; K. and Gorller-Walrand; C., *Physical Chemistry Chemical Physics*, **5**, **2003**, 2754
16. Tochiyama; O. and Freiser; H., *Analytical Chemistry*, **53**, **1981**, 874
17. Magennis; S. W., Ferguson; A. J., Bryden; T., Jones; T. S., Beeby; A. and Samuel; I. D. W., *Synthetic Metals*, **138**, **2003**, 463
18. Lucas; J., Smektala; F. and Adam; J. L., *Journal of fluorine chemistry*, **114**, **2002**, 113
19. Roh; S-G., Oh; J. B., Nah; M-K., Baek; N. S., Lee; Y. and Kim; H. K., *Bulletin of the Korean Chemical Society*, **25**, **2004**, 1503
20. Zhu; S. Z., Xu; B. and Zhang; J., *Journal of Fluorine Chemistry* **74**, **1995**, 167
21. Felix; C., Laurent; A. and Mison; P., *Journal of Fluorine Chemistry*, **70**, **1995**, 71
22. Herkes; F. E. and Burton; D. J., *Journal of Organic Chemistry*, **32**, **1967**, 1311

23. Krafczyk; R., Thönnessen; H., Jones; P. G. and Schmutzler; R., *Journal of Fluorine Chemistry*, 83, **1997**, 159
24. Birchall; J. M. and Haszeldine; R. N., *Journal of Chemical Society*, **1961**, 3719
25. Bégué; J-P., Bonnet-Delpon; D., Bouvet; D and Rock. M. H., *Journal of Chemical Society, Perkin Transactions*, 1, **1998**, 1797
26. Linde; C., Koliaï; N., Norrby; P-O. and Åkermark; B., *Chemistry – A European Journal*, 8, **2002**, 2568
27. Filler; R. and Heffern; E. W., *Journal of Organic Chemistry*, 32, **1967**, 3249
28. Joullie; M. M., *Journal of American Chemical Society*, 77, **1955**, 6662
29. Bégué; J-P. and Mesureur ; D, *Synthesis*, 4, **1989**, 309
30. Jiang; Y., Wu; N., Wu; H. and He; M., *Synlett*, 18, **2005**, 2731
31. Barton; D. H. R., Blazejewski; J-C, Charpiot; B., Finet; J-P. and Motherwell; W. B., *Journal of Chemical Society Perkin Transactions 1*, **1985**, 2667

Chapter 4 - Results and discussion 3 : Synthesis and characterization of fluorinated lanthanide complexes

4.1 Introduction

Optical telecommunication technology is gaining significant interest with rare-earth (Nd^{3+} , Er^{3+} and Yb^{3+}) doped lasers and amplifiers being basic components in integrated optics. Fabrication of high resolution integrated devices has the advantages of cost and size reductions.¹ Polymeric materials such as poly(methyl methacrylate) (PMMA) and doped glasses have been widely studied as hosts for rare-earth ions.^{2,3} However, inorganic rare-earth salts are insoluble in polymeric hosts and organic ligands are used to encapsulate the emissive ions to enhance their solubility. Rare-earth doped glasses which possess high chemical durability and thermal stability are ideal candidates for optoelectronics applications.⁴ Chalcogenide glasses,⁵ heavy metal oxide glasses and tellurite glasses are considered to be promising hosts due to their transparency over a wide range of wavelengths in the infrared region, high refractive index, low phonon energy and ease of fabrication.^{4,6} Despite the vast attention that has been focused on waveguide design and pump wavelength to increase the amplifier efficiency, control of loss mechanisms such as vibrational quenching, excited state absorption (ESA) and ion-ion interactions between the same rare-earth ions also has a significant role to play in the advancement of these devices.

Vibrational quenching has been discussed in chapter 3 where we saw how the near infrared (NIR) radiation of emissive ions is prone to be quenched by high energy oscillators such as C–H (2950 cm^{-1}) and O–H (3450 cm^{-1}) bonds usually present in organic ligands. These high energy bonds are also present in solvent molecules which may be coordinated directly to the ion to fulfil the high coordination number of lanthanide (Ln^{3+}) ions. Luminescence quenching leads to decreased intensity and shorter luminescence lifetimes, which in turn limits any practical application of such complexes in useful telecommunication devices. Consequently, there has been an recent interest in designing and synthesizing ligands which keeps out solvent molecules from the coordination sphere and identifying effective ligands without any high vibrational bonds. In the following

section, we shall review some organic ligands without any O–H and C–H bonds before we discuss the other loss mechanisms. It must be mentioned that as of now, there are very few reports of ion-ion interaction effects in organic materials and vibrational quenching is the primary loss mechanism that has been observed in organic materials. On the other hand, there has been a vast amount of literature on excited state absorption and ion-ion interactions in glasses and inorganic hosts.

4.1.1 Fluorinated ligands

Zheng *et al*⁷ synthesized and characterised Er³⁺ and Yb³⁺ complexes with 3,4,5,6-tetrafluoro-2-nitrophenoxide (L⁻), which can be easily prepared by hydrolysis of commercially available pentafluoronitrobenzene.⁸ Figure 4.1 shows the chemical structure of 3,4,5,6-tetrafluoro-2-nitrophenol. These ligands have the advantage of not containing any hydrogen as well as having a chromophore for photosensitization by absorbing visible light.

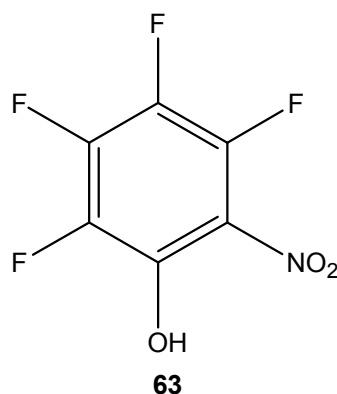


Figure 4.1 : Chemical structure of 3,4,5,6-tetrafluoro-2-nitrophenol (**63**)

The metal complexes were prepared by dissolving the perfluorinated ligand and caesium carbonate (Cs₂CO₃) in MeCN at room temperature. An aqueous solution of the metal chloride (ErCl₃·6H₂O or YbCl₃·6H₂O) was then added dropwise before the mixture was evaporated to dryness and the residue was extracted into Et₂O. Upon filtration and concentration of the organic layer, the residue was recrystallized. Two different methods were used for the recrystallization. Method **1** involved an Et₂O-hexane mixture while method **2** adopted the process of

recrystallization by layering of Et₂O-pentane or Et₂O-carbon tetrachloride mixtures. Table 4.1 tabulates the different complexes obtained by the two methods of recrystallization and a brief description of their physical appearance.

Entry	Stoichiometry of complexes	Method of recrystallization	Physcial appearance
1	Cs ₂ Er(o-O ₂ N-C ₆ F ₄ -O) ₅	Method 1	Orange blocks
2	Cs ₂ (Et ₂ O)Er(o-O ₂ N-C ₆ F ₄ -O) ₅	Method 2	Yellow blades
3	Cs ₂ (Et ₂ O) _{0.5} Yb(o-O ₂ N-C ₆ F ₄ -O) ₅	Method 1	Orange prisms
4	Cs ₂ (Et ₂ O) _{0.5} Yb(o-O ₂ N-C ₆ F ₄ -O) ₅	Method 2	Orange blocks

Table 4.1 : Different Er³⁺ and Yb³⁺ complexes obtained by the two methods of recrystallization and a brief description of the physical appearance

From X-ray crystallography, each metal is bound to five aryloxide ligands, of which three are monodentate; the remaining two ligands are additionally coordinated to the rare earth through one oxygen atom of the nitro group, making them bidentate and hence giving a coordination number of seven. The method of recrystallization has minimal effects on the lifetimes. One other important observation from the X-ray data is that the etherates (Table 4.1; Entries 2, 3 & 4) do not have any solvent molecules coordinated to the metals. The Er³⁺ complexes produced lifetimes of 20.2 μs and 22.9 μs for entries 1 and 2, respectively. A majority (92%) component of 142 μs and a minority (8%) component of 351 μs were obtained for the Yb³⁺ complex. Comparing these lifetimes with those studied in chapter 2, where a lifetime of 1.8 μs was obtained for the anion [Er(HFA)₄]⁻ (HFA = 1,1,1,5,5,5-hexafluoroacetylacetonate) and 22.6 μs for the anion [Yb(HFA)₄]⁻, an improvement of over an order of magnitude has been achieved. This can be attributed to the absence of hydrogen atoms from the immediate environs of the Er³⁺ ion. As noted previously in chapter 2, it is very difficult to remove all traces of hydrogen-containing solvents from these materials and any C–H oscillators within 20 Å can limit the lifetimes to <100 μs.

The advantages of fluorination were also demonstrated by Mancino *et al*⁹ who synthesized a new bidentate chelating ligand, tetrapentafluorophenylimidodiphosphate (HF-tpip) (Figure 4.2).

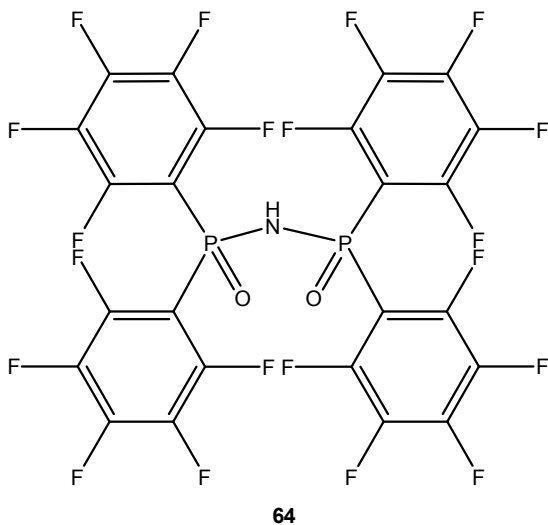


Figure 4.2 : Chemical structure of tetrakis(pentafluorophenyl)imidodiphosphate (HF-tpip) (**64**)

This ligand is hydrophobic in nature, this ligand does not have any high energy oscillators and can encapsulate the metal. By analogy to Magennis *et al*¹⁰, compound **64** was prepared by first synthesizing the appropriate phosphine precursor, $(C_6F_5)_2PCl$, followed by coupling to hexamethyldisilazane. Upon formation of the potassium salt of the ligand (KF-tpip), the tris metal complex, $Er(F-tpip)_3$ was formed and purified by vacuum sublimation between 260 and 280 °C at 10^{-6} mBar. Time resolved photoluminescence measurements were carried out on the $Er(F-tpip)_3$ complex as a powder, a 500 nm evaporated thin film on quartz and in deuterated chloroform ($CDCl_3$) solution. Lifetime data and photoluminescence quantum yield of $Er(F-tpip)_3$ and the non fluorinated analogue, $Er(tpip)_3$ is presented in table 4.2. Note that the photoluminescence quantum yield is calculated with respect to the average radiative lifetime (8 ms) of the Er^{3+} ion.¹¹

Sample type and complex	Lifetime component 1, τ_1 (μs)	Lifetime component 2, τ_2 (μs)	Photoluminescence Quantum yield
Powder			
Er(tpip) ₃	6.0 (77%)	1.5 (23%)	0.05%
Er(F-tpip) ₃	164 (95%)	46 (5%)	1.8%
CDCl₃ solution			
Er(tpip) ₃	5.0 (87%)	2.4 (13%)	0.06%
Er(F-tpip) ₃	145 (27%)	28 (73%)	0.4%
500 nm film			
Er(tpip) ₃	4.8 (84%)	1.0 (16%)	0.04%
Er(F-tpip) ₃	224 (92%)	27 (8%)	1.71%

Table 4.2 : Lifetime data of Er(F-tpip)₃ and the non fluorinated analogue, Er(tpip)₃

Evident from table 4.2, the lifetimes are significantly longer in the perfluorinated complex relative to those of the nonfluorinated analogue. On average, a 10-fold increase in lifetime in solution, a 30-fold increase for the powder and a 50-fold increase for the evaporated thin films were observed.

In a more recent paper, Glover *et al*¹² obtained NIR-emitting Er³⁺, Nd³⁺ and Yb³⁺ complexes with the F-tpip ligand (**64**).

Sample type and complex	Lifetime τ (μs)	Photoluminescence Quantum yield
Powder		
Er(F-tpip) ₃	316	2.26%
Nd(F-tpip) ₃	46	18.4%
Yb(F-tpip) ₃	582	29.1%
CD₃CN solution		
Er(F-tpip) ₃	741	5.29%
Nd(F-tpip) ₃	44	17.6%
Yb(F-tpip) ₃	1111	55.55%

Table 4.3 : Lifetime and photoluminescence quantum yield of Ln³⁺ compounds by Glover *et al*¹²

The observed NIR lifetimes presented in table 4.3 represent unprecedented values for Er³⁺, Nd³⁺ and Yb³⁺ coordination compounds in solution and solid state. The advantages of fluorination are evident from the measured lifetimes of the non fluorinated (tpip) analogue complexes in solid state, where lifetimes of 2.3 μs , 1.2 μs and 17.8 μs were obtained for Er³⁺, Nd³⁺ and Yb³⁺, respectively.¹³ Lifetime increases were seen for the Er³⁺ and Yb³⁺ samples when the measurements were done in solution and according to the authors, this was due to crystal lattice vibration or cross relaxation mechanisms operational in solid state.

The preceding reports have provided significant evidence of the need to remove any high vibrational oscillators in close proximity to the primary and secondary sphere of Ln³⁺ ions in order to prevent luminescence quenching. Next, we shall look at other mechanisms that might present other luminescence quenching pathways for NIR emitting ions.

4.1.2 Excited state absorption (ESA)

Excited state absorption (ESA) is a loss mechanism whereby an excited ion in its metastable state is excited to a higher level via the absorption of a pump or signal

photon. In the case of Er^{3+} , an ion in the metastable $^4I_{13/2}$ level is excited to a higher energy level such as the $^4I_{9/2}$ level and even if the ion ultimately returns to the $^4I_{13/2}$ level, a photon will be lost either to heat or through spontaneous emission at an unwanted wavelength. It was first reported by Brown *et al*¹⁴ in 1969 where ESA was observed by pairs of Er^{3+} ions in crystalline strontium fluoride. A few years later in 1972, Johnson *et al*¹⁵ utilised the effect of ESA to produce visible emission from infrared radiation in rare-earth doped crystals. Since then, this process has been exploited and became known as upconversion. Upconversion is a feature of ion-ion interactions and will be reviewed in the next section.

4.1.3 Ion-ion interactions

One characteristic of rare-earth ions that affects the efficiency of these materials is their susceptibility to interact with each other (ion-ion interactions). Ion-ion interactions, which are due to multipolar interactions between neighbouring ions, can involve either ions of the same rare-earth or between different species. In the former case, a loss mechanism is constituted which increases non-radiative decay channels or luminescence from unwanted transitions.^{16,17} Ion-ion interactions of this nature are dependent on concentration and are manifested in the form of upconversion, energy migration and cross relaxation. Upconversion is unique among the ion-ion interaction effects in that it is the only effect that can be observed and measured empirically.

At low rare-earth concentrations, and provided that the ions are evenly distributed, the large interionic distances will be large and any interactions will be prevented. However, when the concentration is increased beyond a certain level, the distribution may become uneven and the reduction of interionic distance leads to ion-ion coupling.¹⁸ Although integrated optics has led to cost and space optimization, the reduced length of optical amplifiers requires doping with a high concentration of rare-earth ions and that has the disadvantage of promoting these loss mechanisms.¹⁹

When there are high concentrations of emitting rare-earth ions, ion-ion interactions lead to concentration quenching. Concentration quenching relates to energy

transfer between Ln^{3+} ions and when the concentration of ions goes beyond a certain level, it is no longer valid to assume that each ion behaves independently of its neighbours. The possibility of energy transfer, which occurs via phonon-mediated interactions can have a negative impact on amplifiers when the upper state of an amplifying transition is being depleted by excitation energy.²⁰

In Er^{3+} -doped laser glasses, such a concentration effect is known as clustering. It arises because silica, for example, has a lack of nonbridging oxygen groups which are important for the solubility and incorporation of Ln^{3+} ions. Consequently, these Ln^{3+} ions tend to aggregate and lead to undesirable effects that reduce the amplifier performance.²¹ Significant success has been achieved to alleviate clustering by the addition of P_2O_5 and aluminium oxide (Al_2O_3) to silica.^{22,23,24} According to Arai *et al*²⁵ the effect of aluminium is to produce solvation shells for Nd^{3+} ions to insert themselves, thus mitigating the clustering effects. There are several other reports on concentration quenching in glasses.^{26,27}

Contrary to the case for the same rare-earth ions, the interactions between different rare-earth ions is not a loss mechanism but is employed in novel pumping schemes whereby excitation is transferred from one species to another and that allows a wider selection of pump sources to be used.¹⁷ We shall now look at the effects of ion-ion interactions between the same rare-earth ions before proceeding to discuss ion-ion interactions between different species.

4.1.4 Ion-ion interactions between chemically identical rare-earth ions: Upconversion and cooperative luminescence

Upconversion is a form of ion-ion interaction whereby two ions in the excited state are able to emit a luminescence photon of a higher energy.¹⁶ Due to the fact that this concentration-dependent phenomenon requires two interacting ions in the metastable state, it only becomes important at high excitation wavelengths. Usually in the case of Er^{3+} , ions in the $^4\text{I}_{13/2}$ emitting level have a long radiative lifetime of >10 ms which allows ample time for the neighbouring ions in the same state to interact and transfer energy through the absorption of a pump or signal photon. It has the effect of promoting ion 1 onto a higher energy state which gives

rise to emission at ~500 nm and simultaneously, deactivates ion 2 nonradiatively to its $^4I_{15/2}$ ground state. This anti-Stokes process, which constitutes a loss mechanism at the NIR region, is made possible by the mechanism of excited state absorption which involves the absorption of photons from ions in the excited states.

The process of upconversion can take several routes and the emitting wavelengths can be of different values, depending on the number of excitation steps, the excitation wavelength and intermediate nonradiative relaxations of the acceptor ions.¹⁸ Figure 4.3 shows the energy level diagram of Er^{3+} with possible upconversion routes, de-excitation pathways and radiative decay routes.

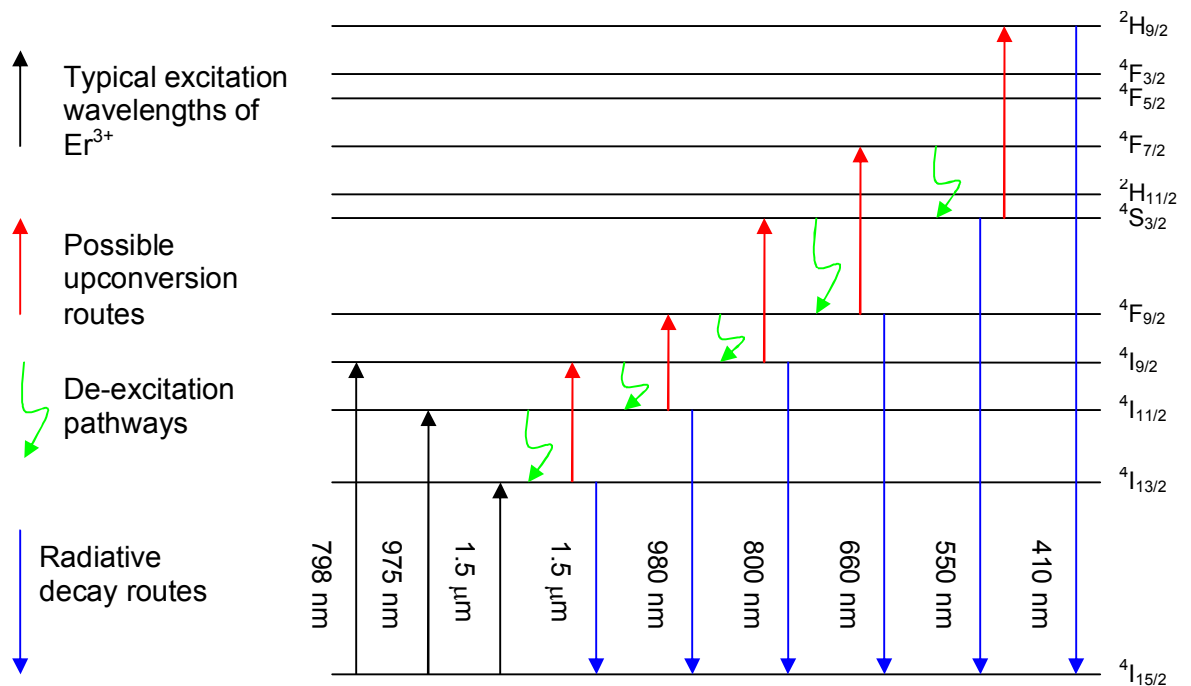


Figure 4.3 : Energy level diagram of Er^{3+} with possible upconversion routes, de-excitation pathways and radiative decay routes

While figure 4.3 presents a general view of the possible upconversion routes that Er^{3+} ions can take, it must be mentioned that all these transitions are not simultaneously observed in any host material.¹⁸ In the literature, many routes for

upconversion have been proposed. For example, Van der Ziel *et al*²⁸ illustrated that at 1.5 μm excitation of Er^{3+} doped yttrium fluoride crystals, the ions were initially pumped to the $^4\text{I}_{13/2}$ emitting level where excited state absorption takes place and the ions get excited to the $^4\text{I}_{9/2}$ level. From there, some ions decay nonradiatively to the $^4\text{I}_{11/2}$ level and the other ions were further excited into the $^4\text{S}_{3/2}$ level and decay from that level gives green emission (550 nm). From the $^4\text{S}_{3/2}$ level, some ions decay nonradiatively to the $^4\text{F}_{9/2}$ level and decay from that level gives rise to red emission (660 nm). Excited state absorption to the $^2\text{H}_{9/2}$ level may happen from the $^4\text{S}_{3/2}$ level and that provides a 410 nm emission.

Whitley *et al*²⁹ were the first to demonstrate room temperature lasing at 546 nm on the $^4\text{S}_{3/2} \longrightarrow ^4\text{I}_{15/2}$ transition of Er^{3+} in a zirconium fluoride glass host. The green output power of 23 mW has been achieved by pumping a 2.4 m length of the Er^{3+} doped fibre with 780 mW of power at a wavelength of 801 nm. Other similar observations were made by Mita *et al*³⁰ for Er^{3+} -doped silica glass fibers and for fibers and bulk material of calcium metaphosphate glass.

Xiao *et al*³¹ reported on strong ultraviolet and visible frequency (399 – 585 nm) upconversion in Nd^{3+} implantation single crystalline silicon at the excitation wavelengths of 625, 650, 675 and 700 nm.

Cooperative luminescence is a special type of upconversion reported for Yb^{3+} ions. Two interacting ions in the excited state return to the ground state simultaneously and emit one shorter wavelength photon with an energy that corresponds to the total energies of the interacting ions.³² Luminescence at around 500 nm has been detected under NIR excitation in Yb^{3+} -doped borosilicate, aluminosilicate and phosphate glasses. Cooperative luminescence, which is caused by clustering in glass hosts, relies on Coulombic interaction between ions and has a strong dependence on interionic distances.^{33,34}

4.1.5 Ion-ion interaction between chemically identical rare-earth ions: Energy migration

In energy migration, an Er^{3+} ion for example, in the metastable state can interact with a nearby ion in the ground state with the effect of promoting this second ion to the $^4I_{13/2}$ level.³⁵ While this does not quench luminescence by itself, it enhances the probability of quenching by allowing the energy to finally migrate onto a site where more rapid nonradiative decay can take place. This constitutes a loss mechanism as the probability of nonradiative decay is increased with each successive transfer.

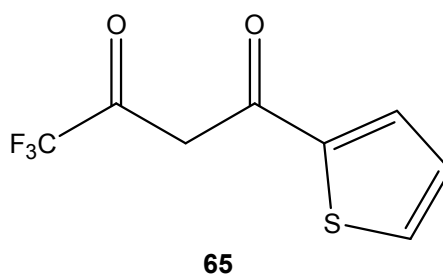


Figure 4.4 : Chemical structure of 2-thenoyltrifluoroacetone (**65**)

A novel tetranuclear Nd^{3+} complex was synthesized by Qiu *et al.*³⁶ In this study, the ligand 2-thenoyltrifluoroacetone (HTTA) (Figure 4.4) was used and the molar ratio of Nd^{3+} ion to ligand is 1 : 2.5. Ln^{3+} complexes with β -diketonates such as HTTA and HHFA are well documented and the majority of these complexes are monometallic.^{37,38} The crystal structure of the resulting tetranuclear complex revealed that the four Nd^{3+} ions are coordinated by ten ligands. By comparison with mononuclear complexes even with bulky ligands to prevent any solvent coordination, the Nd^{3+} ions in the tetranuclear structure are more closely wrapped in the molecule and therefore, shielded more efficiently from the surrounding environment to improve the luminescence. For the same Nd^{3+} ion concentration, the average distance between molecules of tetranuclear complex is about 1.583 times of the mononuclear one and the cross-relaxation or excitation energy migration rate of the tetranuclear complex is 1/16 times of the mononuclear one. Considering the fact that concentration quenching is a function of ion-ion distance, this is a useful way for increasing the concentration to obtain population inversion for lasing or optical amplification.

4.1.6 Ion-ion interaction between chemically identical rare-earth ions: Cross relaxation

Concentration quenching was also demonstrated in the experiments conducted by Orignac *et al*³⁹ with Nd³⁺-doped sol-gel planar waveguides. For Nd³⁺ samples, this occurs in the form of cross relaxation. An excited ion in the metastable ⁴F_{3/2} state can interact with a nearby ion in the ⁴I_{9/2} ground state with the effect of transferring part of the energy to the second ion and leaving both in the intermediate ⁴I_{15/2} state. As there are some intermediate levels lying between the intermediate ⁴I_{15/2} state and the ⁴I_{9/2} ground state with small energy gaps, both ions quickly decay nonradiatively to the ground state. Cross relaxation is less prevalent in Er³⁺ samples as they have no energy levels between the ⁴I_{13/2} metastable state and the ⁴I_{15/2} ground state which prevents any energy transfer between an excited ion and one in the ground state.¹⁶

Sol-gel chemistry coupled with spin-coating technique is a good method for producing rare-earth doped planar waveguides for integrated optics. High doping levels of rare-earth is required for integrated optics but this quenches the fluorescent emission and reduces the performance of the amplifier. A decrease in fluorescence lifetime is a manifestation of this effect. The Nd³⁺ concentration in the sol-gel was varied from 0.1 to 5 atom %. Phosphorus pentoxide (P₂O₅) was also dissolved in the sol for the Nd³⁺ samples as it has been known that codoping with phosphorus prevents, to a certain extent, the Nd³⁺ ions from clustering.²⁵

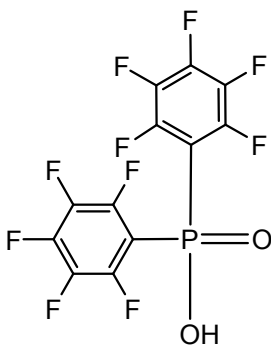
From Orignac's experiments, it was observed that the fluorescence lifetime decreases with Nd³⁺ concentration and a maximum fluorescence lifetime of 375 μs was reached for the 0.1 atomic % of Nd³⁺ sample, which is largely sufficient for laser or amplification purposes.³⁹

4.1.7 Ion-ion interactions between chemically different ions

Ion-ion interactions between two different rare-earth ions can be employed in novel pumping schemes whereby excitation is provided to one ion and then transferred to another.¹⁷ Examples of such mechanism are the Er/Yb codoping schemes

frequently employed in polymer waveguide amplifiers.^{2,40,41} One feature of organic ligands is that they can act as light-harvesting antennae to sensitize the Ln³⁺ ions via intramolecular energy transfer process. However, the maximum absorption bands of organic ligands are usually in the ultraviolet or visible region and consequently, sensitization of the Er³⁺ ions cannot utilize the cheap commercial semiconductor laser diode emitting at 980 nm as the excitation source. Co-doping with Yb³⁺ ions enhances the excitation efficiency as the absorption cross section of Yb³⁺ at 980 nm is approximately ten times higher than Er³⁺. In the past decade, a considerable amount of work has been done by researchers on co-doping Er³⁺ glasses with Yb³⁺ and very little work has been done on organic materials.^{15,42}

Recently, Song *et al*⁴³ reported on the Er³⁺ and Er-Yb complexes with perfluorodiphenylphosphinate ligands (Figure 4.5). General procedures for the preparation of the complexes involved a one pot process where the tris-(pentafluorophenyl)phosphine oxide is refluxed for 6 h with the Ln³⁺ chloride hydrates in a water-ethanol mixture (molar ratio of metal to ligand – 1 : 3). Upon cooling, the precipitate was separated by centrifugation and washed with ethanol several times. The photoluminescence quantum efficiency obtained for the Er³⁺ complex, [(C₆F₅)₂POO]₃Er and the Er-Yb complex, [(C₆F₅)₂POO]₃Er_{0.5}Yb_{0.5}, was 50 times and 175 times respectively, higher than Er³⁺ organic complexes with hydrogen-containing ligands.



66

Figure 4.5 : Perfluorodiphenylphosphinate ligand (**66**) used by Song *et al*⁴³

Sample	$\tau_1/\mu\text{s}$	$\tau_2/\mu\text{s}$	$\eta(\%)$
$[(\text{C}_6\text{F}_5)_2\text{POO}]_3\text{Er}$	13 (11%)	336 (89%)	0.98
$[(\text{C}_6\text{F}_5)_2\text{POO}]_3\text{Er}_{0.5}\text{Yb}_{0.5}$	19 (2%)	748 (98%)	3.5

Table 4.4 : Measured photoluminescence lifetimes and calculated quantum efficiencies of $[(\text{C}_6\text{F}_5)_2\text{POO}]_3\text{Er}$ and $[(\text{C}_6\text{F}_5)_2\text{POO}]_3\text{Er}_{0.5}\text{Yb}_{0.5}$

From table 4.4, the effect of fluorination is notable for the complexes and at 336 μs for $[(\text{C}_6\text{F}_5)_2\text{POO}]_3\text{Er}$, the lifetime is longer than those achieved by Mancino *et al*⁹ as discussed previously. Figure 4.6 shows the emission spectra of $[(\text{C}_6\text{F}_5)_2\text{POO}]_3\text{Er}$ (solid line) and $[(\text{C}_6\text{F}_5)_2\text{POO}]_3\text{Er}_{0.5}\text{Yb}_{0.5}$ (dotted line) excited at 978 nm. The intensity of the emission band of $[(\text{C}_6\text{F}_5)_2\text{POO}]_3\text{Er}_{0.5}\text{Yb}_{0.5}$ is much stronger than that of $[(\text{C}_6\text{F}_5)_2\text{POO}]_3\text{Er}$ which indicates that Er^{3+} is sensitized efficiently by Yb^{3+} . Lifetimes of 748 μs and 19 μs were achieved for $[(\text{C}_6\text{F}_5)_2\text{POO}]_3\text{Er}_{0.5}\text{Yb}_{0.5}$ which might also suggest that in this system, the Er-Er ionic distance is greater than those of $[(\text{C}_6\text{F}_5)_2\text{POO}]_3\text{Er}$ and that has the effect of suppressing concentration quenching.

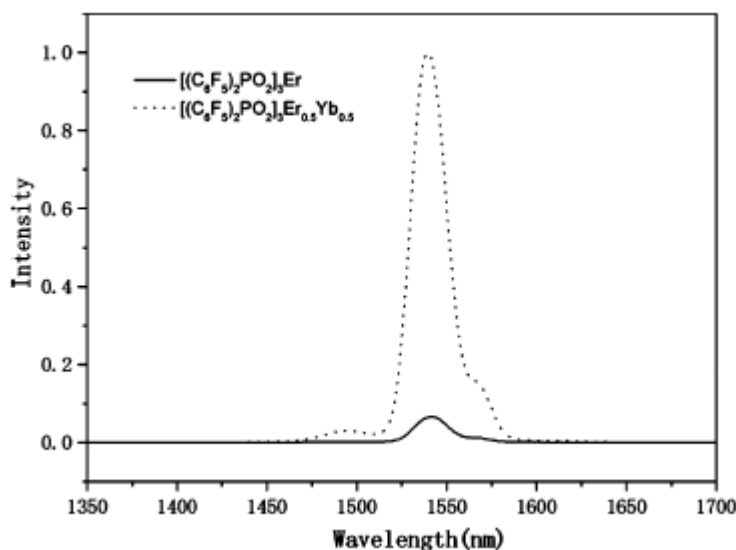


Figure 4.6 : The emission spectra of $[(\text{C}_6\text{F}_5)_2\text{POO}]_3\text{Er}$ (solid line) and $[(\text{C}_6\text{F}_5)_2\text{POO}]_3\text{Er}_{0.5}\text{Yb}_{0.5}$ (dotted line)

The process of sensitization of Er^{3+} by Yb^{3+} can be described as follows: the pump energy is absorbed by Yb^{3+} and energy transfer from the energy level ${}^2\text{F}_{5/2}$ of Yb^{3+} to the ${}^4\text{I}_{11/2}$ level of Er^{3+} takes place. This is followed by a rapid nonradiative relaxation to the ${}^4\text{I}_{13/2}$ level of Er^{3+} and finally results in the near infrared emission at 1535 nm attributed to the ${}^4\text{I}_{13/2} \longrightarrow {}^4\text{I}_{15/2}$ transition.

4.1.8 Overview of experimental work discussed in this chapter

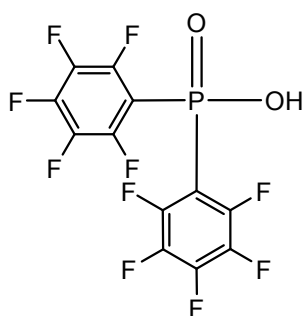
From the discussions presented, we have seen the advantages of fluorination on increasing the photoluminescence quantum yield. This chapter will examine four different fluorinated diarylphosphinate ligands and their complexes with Er^{3+} , Nd^{3+} and Yb^{3+} . The absence of high vibrational energy bonds such as O–H, C–H and N–H will suppress any luminescence quenching via high energy bonds.

We also saw from the literature review at the start of this chapter that ion-ion interactions have a major role in luminescence quenching which is prevalent in glass hosts and fibers. The tendency of Ln^{3+} ions to interact with each other is related to the interionic distance and has the potential to reduce the luminescence efficiency. Concentration quenching can be suppressed by keeping the luminescence centres apart and in this chapter, we seek to provide an insight into this phenomenon by keeping the luminescent centres apart in organic hosts. This is achieved by diluting the organic Er^{3+} , Nd^{3+} and Yb^{3+} complexes with Y^{3+} and measuring the luminescence lifetimes with increasing concentrations of NIR emitting Er^{3+} , Nd^{3+} and Yb^{3+} ions.

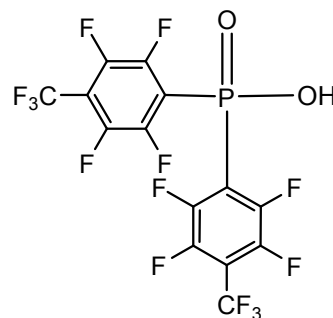
4.2 Preparations of phosphinic acids and fluorinated Er³⁺, Nd³⁺ and Yb³⁺ complexes

Full descriptions of the preparation and characterisation of fluorinated phosphinic acids and their Er³⁺, Nd³⁺ and Yb³⁺ complexes are provided in chapter 5.

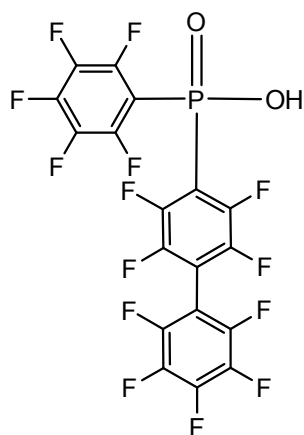
Figure 4.7 shows the four different types of new fluorinated phosphinic acids used for our study in this chapter.



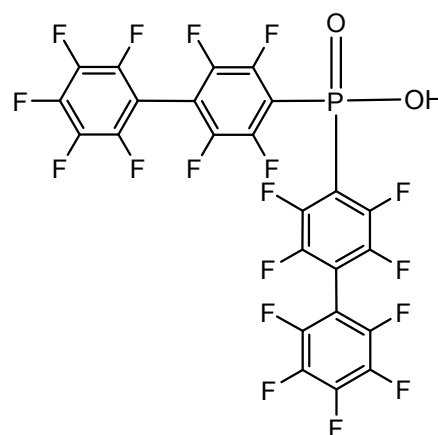
Bis(pentafluorophenyl)phosphinic acid
(66)



Bis[2,3,5,6-tetrafluoro-4-(trifluoromethyl)phenyl]
phosphinic acid (67)



Nonafluorobiphenyl-4-yl
(pentafluorophenyl)phosphinic acid
(68)



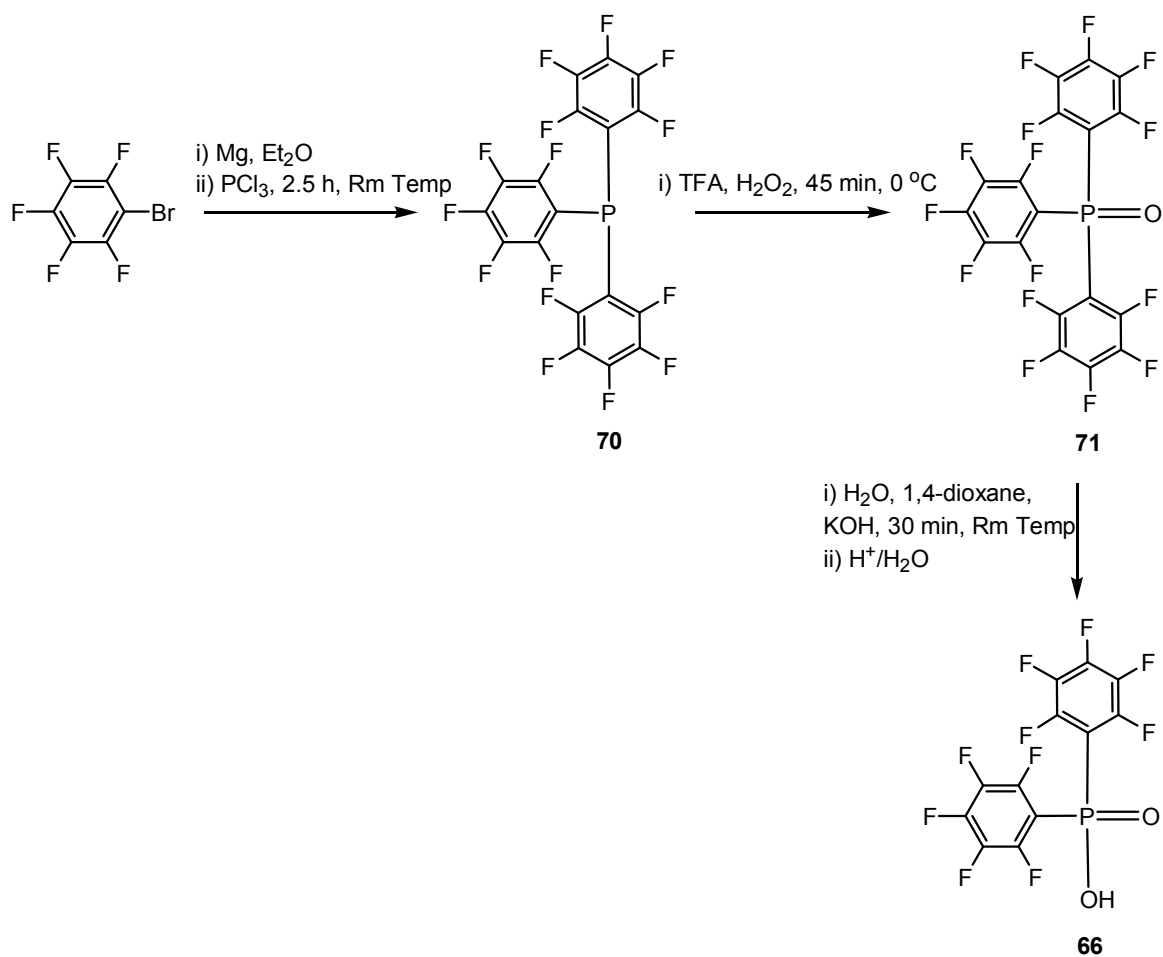
Bis(nonafluorobiphenyl-4-yl)phosphinic acid
(69)

Figure 4.7 : Chemical structure of the four different phosphinic acids used for study in this chapter

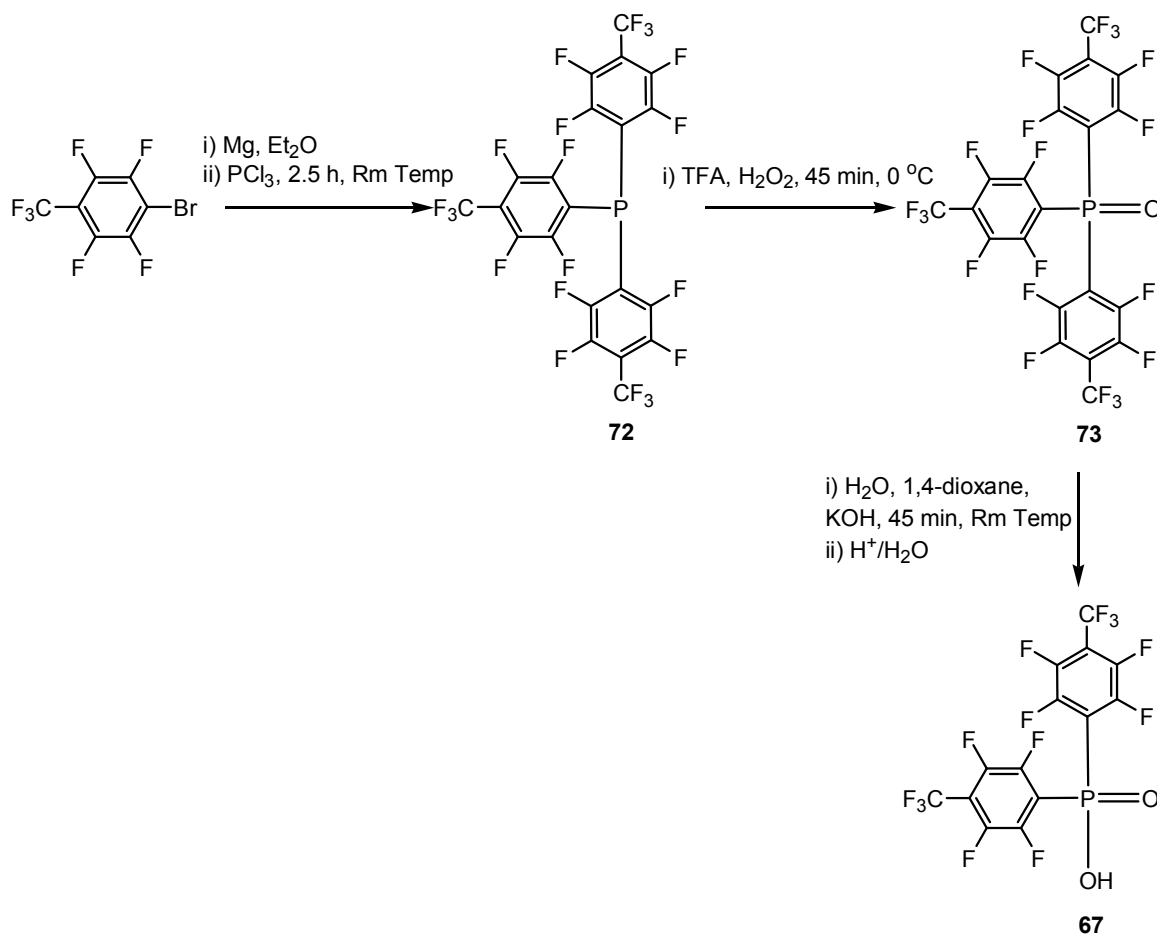
Grignard chemistry and organolithium methods were used to obtain phosphinic acids **66** and **67** whereas the biphenyl derived phosphinic acids **68** and **69** were prepared by the organolithium method.

4.2.1 Route 1: Grignard chemistry to obtaining bis(pentafluorophenyl)phosphinic acid and bis[2,3,5,6-tetrafluoro-4(trifluoromethyl)phenyl]phosphinic acid

Schemes 4.1 and 4.2 show the Grignard chemistry route to obtaining bis(pentafluorophenyl)phosphinic acid (**66**) and bis[2,3,5,6-tetrafluoro-4(trifluoromethyl)phenyl]phosphinic acid (**67**), respectively. This was carried out by analogy to Oliver *et al.*⁴⁴ In the oxidation step, they suspended their phosphine **70** in H₂O and H₂O₂ and heat was used in the process until the excess H₂O₂ had decomposed. For our oxidation process, which was first carried out by Jem Pearson⁴⁵, we monitored our reaction by TLC to ensure the complete consumption of the starting material (**70**). Also they prepared the oxonium salt (C₁₂H₃F₁₀PO₃) before obtaining the phosphinic acid **66** while we hydrolysed our phosphine oxide (**71**) to get the same compound.



Scheme 4.1 : Route to preparing bis(pentafluorophenyl)phosphinic acid



Scheme 4.2 : Route to preparing 1-[bis-(2,3,5,6-tetrafluoro-4-trifluoromethylphenyl)-phosphinoyl]phosphinic acid

Schemes 4.1 and 4.2 are similar with the difference being the halide used to form the Grignard reagent. Upon forming the Grignard reagent, it was then added to a solution of PCl₃ to form the phosphines **70** and **72**. Oxidation to the phosphine oxides **71** and **73** followed by hydrolysis was carried out to obtain phosphinic acids **66** and **67**.

4.2.2 Route 2: Organolithium method to obtaining phosphinic acids

Full synthetic procedures and characterisation are described in chapter 5.

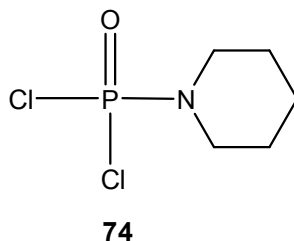
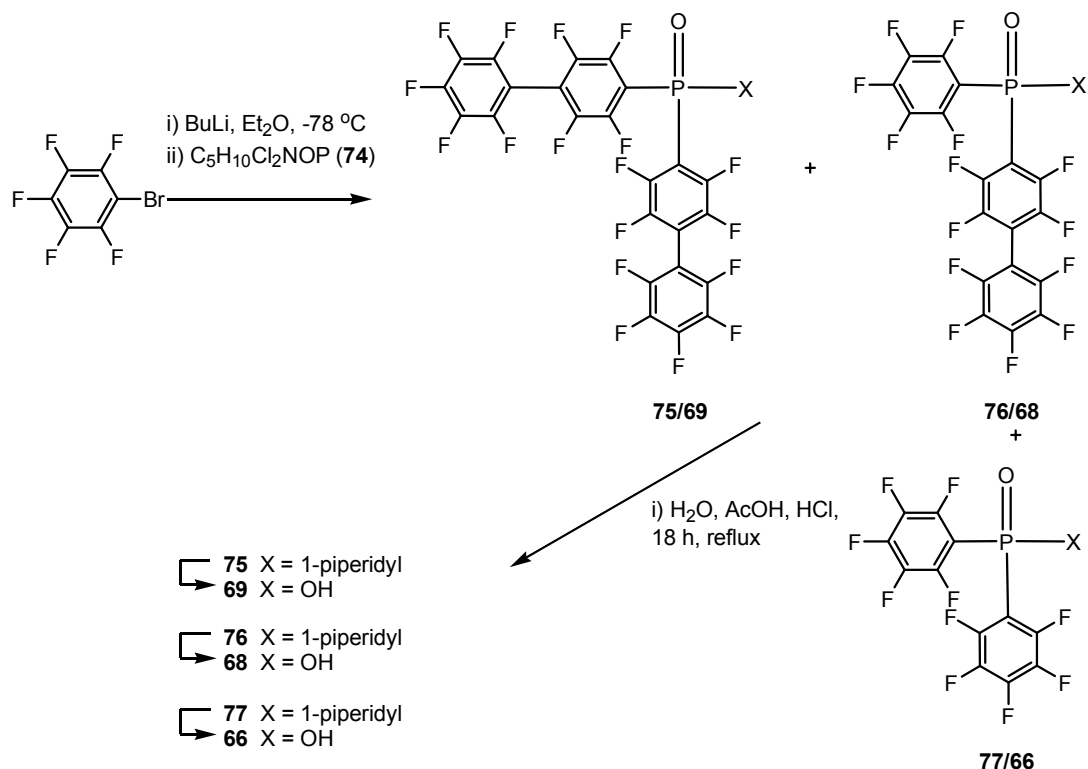


Figure 4.8 : Chemical structure of phosphinamide dichloride (**74**)



Scheme 4.3 : Organolithium method to obtaining phosphinic acids **66**, **68** and **69**

The organolithium method shown in scheme 4.3 was used to obtain phosphinic acids **66**, **68** and **69**. It is a two stage process which involves the synthesis of phosphinamide derivatives (**75**, **76** and **77**) before hydrolysis to obtain the acids.

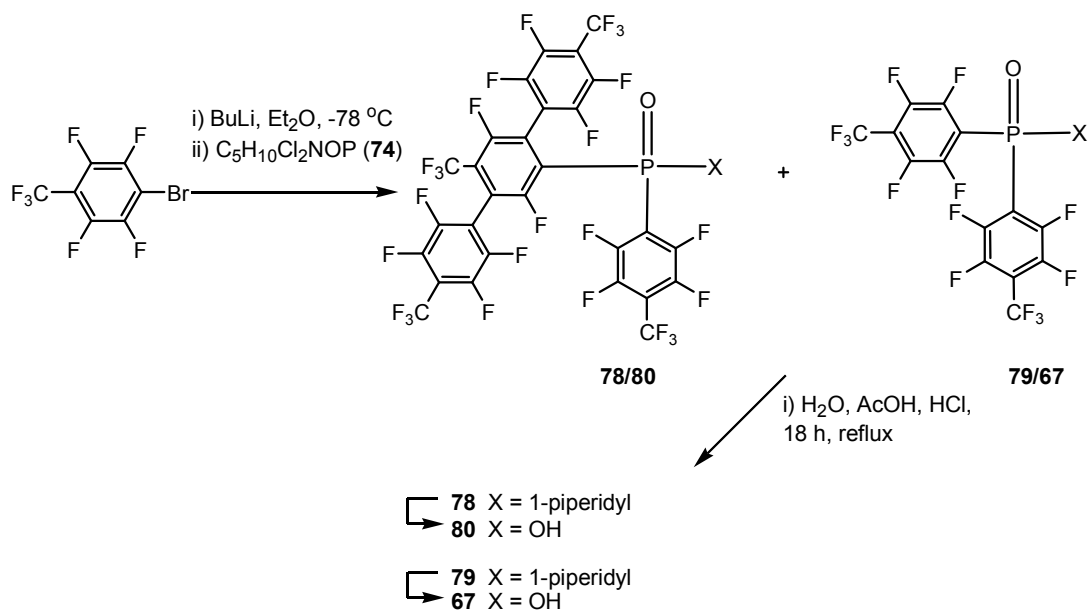
Use of the precursor, phosphinamide dichloride (**74**)⁴⁶ (Figure 4.8) allows controlled introduction of two perfluoroaryl groups at the phosphorus (V) centre.

The initial intention was to synthesize bis(pentafluorophenyl)phosphinic acid (**66**) using a more direct route via hydrolysis of the intermediate, 1-[bis(pentafluorophenyl) phosphinoyl]piperidine (**77**). Formerly, our three-step approach which involves Grignard chemistry to obtain phosphinic acids **66** and **67** was inefficient as one perfluoroaryl group has to be removed by hydrolysis after oxidation. By utilizing this organolithium method, the oxidation step is not required as the phosphorus is already in the correct oxidation state and therefore one step is eliminated.

Bromopentafluorobenzene was subjected to bromine-lithium exchange in Et₂O at -78 °C followed by reaction with the dichloride **74**. The crude organic product was obtained in the form of white foam which was subjected to chromatography. Thin layer chromatography (TLC) (DCM) revealed three different spots with R_f values of 0.2, 0.4 and 0.6. A series of peaks were observed from the ³¹P NMR spectrum of the crude sample and after flash chromatography, three products were isolated. Characterisation by ³¹P NMR and ¹⁹F NMR revealed three distinct products.

From ¹H NMR, ³¹P NMR, ¹⁹F NMR and mass spectroscopy data, the three isolated compounds can be confirmed as phosphinamides **75**, **76** and **77**. Compound **75** was found to be the most polar and compound **77** was the least. Hydrolysis was done to obtain the corresponding phosphinic acids, compounds **69**, **68** and **66**, which were confirmed by ¹H NMR, ³¹P NMR, ¹⁹F NMR and mass spectroscopy.

A similar approach was examined in an attempt to obtain bis(2,3,5,6-tetrafluoro-4(trifluoromethyl)phenyl)phosphinic acid (**67**) by a direct approach.



Scheme 4.4 : Organolithium method to obtaining Compounds **67** and **80**

Upon solvent extraction with Et₂O and H₂O, the light yellow solid crude product was tested. Thin layer chromatography (TLC) (DCM) revealed two spots with R_f values of 0.1 and 0.3. A series of peaks were observed from the ³¹P NMR spectrum of the crude sample and after flash chromatography, two products were isolated. Characterisation by ³¹P NMR and ¹⁹F NMR revealed two distinct products.

From ¹H NMR, ³¹P NMR, ¹⁹F NMR and mass spectroscopy data, the two isolated compounds can be confirmed as phosphinamides **78** and **79**. From the TLC, compound **78** was more polar than compound **79**. Hydrolysis was done to obtain the corresponding phosphinic acids, compounds **80** and **67** which were confirmed by ¹H NMR, ³¹P NMR, ¹⁹F NMR and mass spectroscopy. X-ray crystallography was also done to confirm the structure of phosphinamide **78** (Figure 4.9).

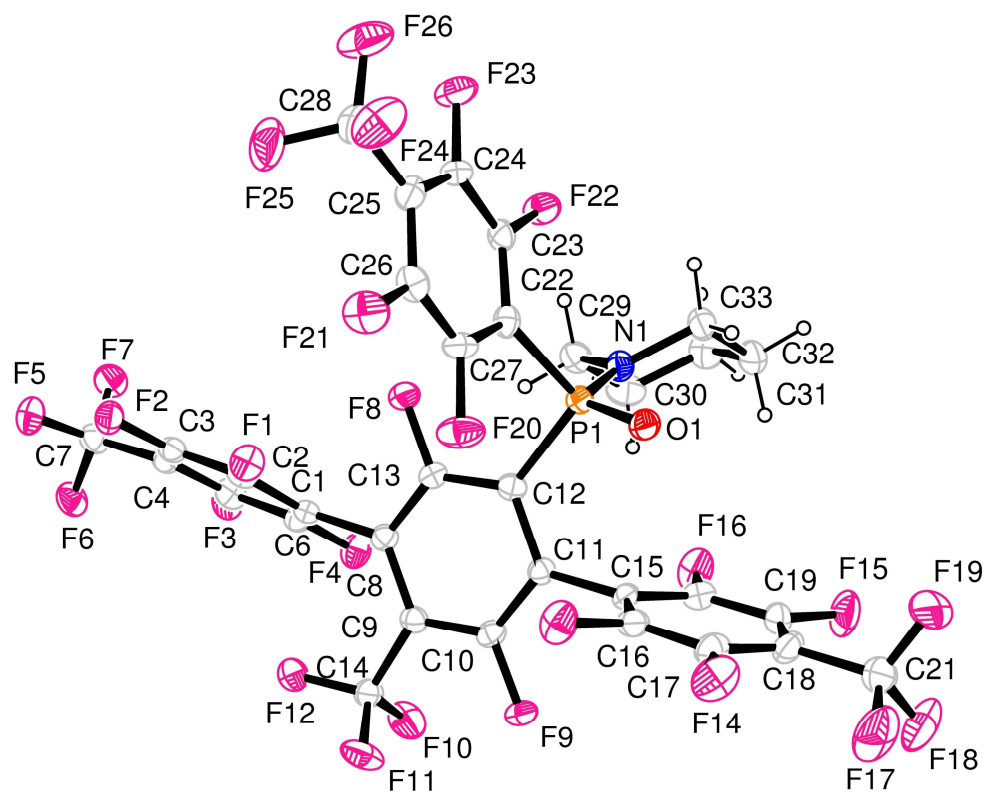
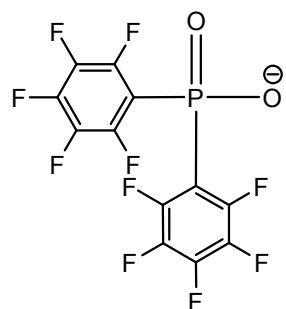
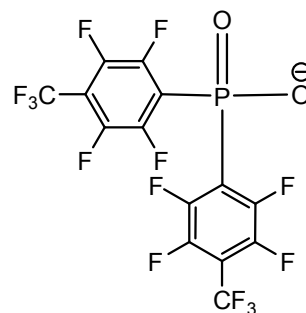


Figure 4.9 : XRD chemical structure of phosphinamide **78**

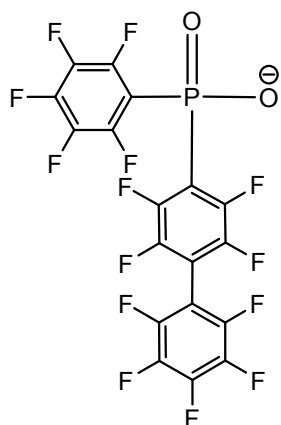
Phosphinic acids **66**, **67**, **68** and **69** (Figure 4.7) were converted into their Er^{3+} , Nd^{3+} and Yb^{3+} salts. Compound **80** did not form Er^{3+} , Nd^{3+} and Yb^{3+} complexes using the methods that will be described in section 4.3.



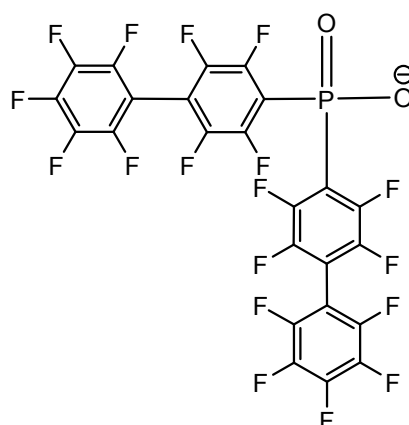
Bis(pentafluorophenyl)phosphinate
(L-1)⁻



Bis[tetrafluoro-4(trifluoromethyl)phenyl]
phosphinate (L-2)⁻



(Nonafluorobiphenyl-4-yl)(pentafluorophenyl)
phosphate (L-3)⁻



Bis(nonafluorobiphenyl-4-yl)
phosphinate (L-4)⁻

Figure 4.10 : Chemical structures of conjugate bases of phosphinic acids

66, 67, 68 and 69

The fluorinated ligands shown in figure 4.10 do not have any high vibrational C–H and O–H bonds which have been discussed in chapter 2 to be potent in luminescence quenching. To enable us to compare the advantages of fluorination, the Er³⁺, Nd³⁺ and Yb³⁺ salts of commercially available diphenylphosphinic acid (Figure 4.11) were prepared.

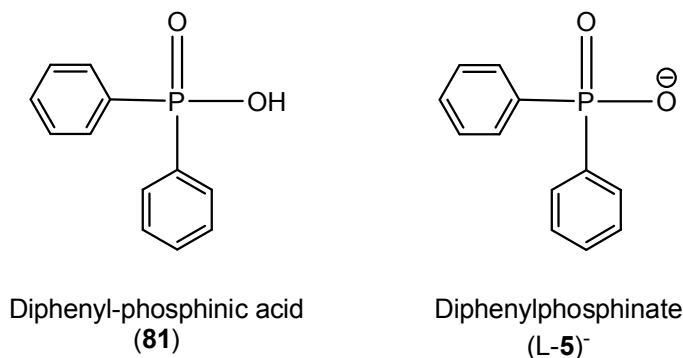


Figure 4.11 : Chemical structure of diphenyl-phosphinic acid and its anion

Ligand L-5 is similar to ligand L-1 in that there are two phenyl rings attached to phosphorus and the difference is that the phenyl rings on ligand L-1 are fully fluorinated whereas the ones on ligand L-5 are not. Dunstan and co.⁴⁷ were the first to prepare Ln³⁺ complexes with ligand L-5.

4.3 Preparation of Ln³⁺ complexes

Two methods were adopted for preparing the Er³⁺, Nd³⁺ and Yb³⁺ diarylphosphinate complexes. In the first method (Method **A**), the lanthanide chloride was dissolved in H₂O in a sample vial before pure H₂O was layered above the solution. Then, the required ligand which was dissolved in a 1 : 1 ratio mixture of MeOH and Et₂O was added slowly into the vial. A layer of precipitation was formed instantly at the interface between the aqueous layer and the ligand layer and the samples were kept at room temperature. The layer of precipitate grew over time and after about three days, it sunk to the bottom of the vial. The precipitate was then filtered off and washed in turn with H₂O, MeOH and Et₂O. In the second method (Method **B**), only MeOH was used for dissolving the metal chlorides and ligands. Upon mixing the metal solution and ligand solution, the mixture appeared homogenous. However, a thin layer of precipitate could be observed at the bottom of the sample vial after leaving it overnight. The precipitate was very fine and difficult to filter. A centrifuge was therefore used to facilitate separation of the solid samples. As in the first method, the samples were washed with H₂O, MeOH and Et₂O.

In sections 4.8, 4.9 and 4.10, we shall discuss Er^{3+} , Nd^{3+} and Yb^{3+} samples that were diluted with Y^{3+} . Preparation of the diluted samples was done in a similar way as described above. Stock solutions of the respective metal chlorides were prepared and the calculated volume of each stock solution was mixed to obtain the necessary dilutions. All samples that will be discussed later in this chapter were dried at a temperature of $\sim 150\text{ }^\circ\text{C}$ for ten days in a pistol under vacuum (1 mmHg) with P_2O_5 . In subsequent sections, the diluted samples are presented in the form, $\text{Ln}_x\text{Y}_{1-x}(\text{L-1} - \text{L-4})_3$, where Ln is either Er, Nd or Yb and x is the mole fraction of Ln^{3+} .

To determine if there were any differences in the photoluminescence lifetimes between samples prepared using methods **A** and **B**, a selection of diluted Er^{3+} complexes, $\text{Er}_x\text{Y}_{1-x}(\text{L-2})_3$ were prepared and the lifetimes are presented in table 4.5. These samples were prepared and left at room temperature for three days before they were filtered off and washed.

Sample	Method A	Method B
100% Er	179 μs	222 μs
97% Er	187 μs	192 μs
93% Er	230 μs	237 μs
70% Er	496 μs	427 μs

Table 4.5 : Lifetime table of $\text{Er}_x\text{Y}_{1-x}(\text{L-2})_3$ complexes prepared using methods **A** and **B**

From table 4.5, we can conclude that the lifetimes between complexes prepared using method **A** and **B** were very similar.

In the subsequent discussions on Er^{3+} , Nd^{3+} and Yb^{3+} samples, error bars were presented in the lifetime plots. The errors on the lifetimes were deduced by measuring the lifetimes of duplicated samples which were synthesized from the same stock solution. These duplicated samples have varying lifetimes and the root mean square of all the errors was found to be 15%. Hence, the lifetimes presented in sections 4.8, 4.9 and 4.10 will have an error of $\pm 15\%$.

4.4 Chemical characteristics of Ln³⁺ complexes

The Ln³⁺ samples have very limited solubility in common solvents, including H₂O, MeOH, Et₂O, DMSO and CH₃COCH₃ and this has prevented us from obtaining single crystals suitable for X-ray diffraction. However, MALDI mass spectra could be obtained by using solid state grinding to disperse the compounds in a pentafluorobenzoic acid matrix and showed the expected isotope patterns for ions of the type [ML₄]⁻ and [M₂L₅]⁺.

For our diluted samples, MALDI mass spectroscopy has detected the species [ErYL₅]⁺, (where M = 0.5 Er and 0.5 Y and L = L-1) and that has provided us with evidence that these samples are mixed to the atomic levels. From our powder X-ray analysis, we determined that the Er³⁺ and Y³⁺ complexes are isostructural. Figure 4.12 shows the powder X-ray diffraction data of Er[(C₆F₅)₂PO₂]₃ and Y[(C₆F₅)₂PO₂]₃. The wavelength of the radiation was 1.5418 Å.

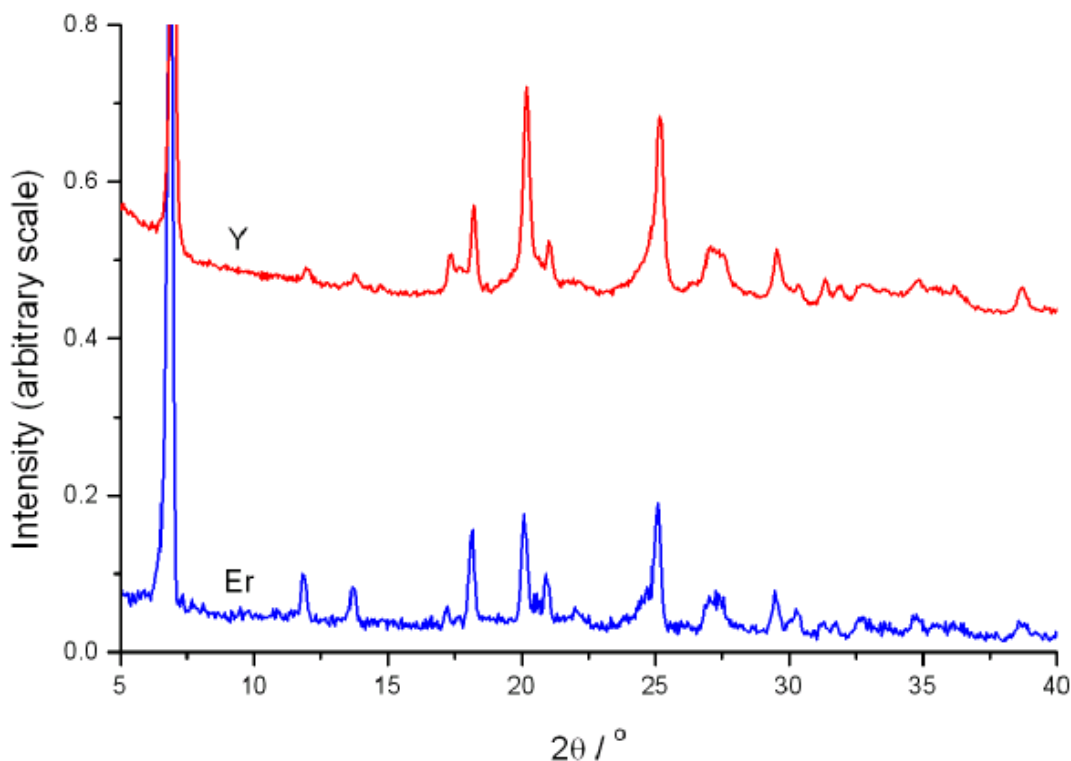


Figure 4.12 : Powder X-ray diffraction data of Er[(C₆F₅)₂PO₂]₃ and Y[(C₆F₅)₂PO₂]₃

Solid state ^{31}P NMR was done on $\text{Y}[(\text{C}_6\text{F}_5)_2\text{PO}_2]_3$ and the spectrum shown in figure 4.13 revealed the expected single phosphorous environment.

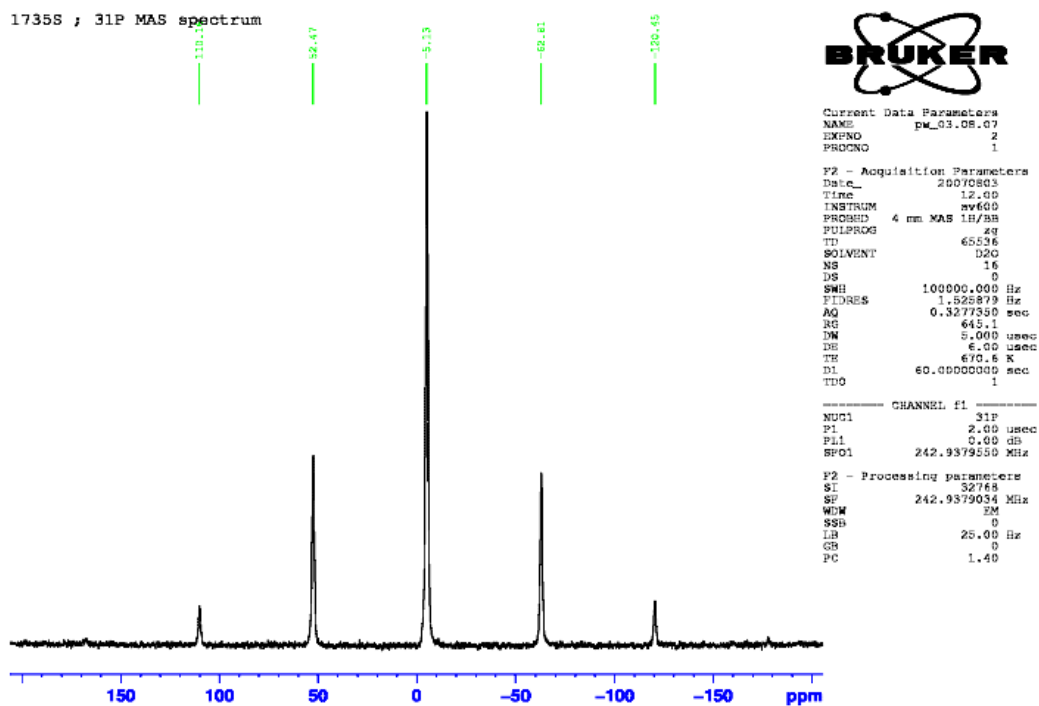


Figure 4.13 : Solid state ^{31}P NMR of $\text{Y}[(\text{C}_6\text{F}_5)_2\text{PO}_2]_3$

Figure 4.14 shows the solid state ^{31}P NMR of $\text{Er}[(\text{C}_6\text{F}_5)_2\text{PO}_2]_3$ and due to the paramagnetic nature of Er^{3+} , the NMR signals are broad.

RT 200 100% Er ; ^{31}P MAS spectrum @ 14000Hz

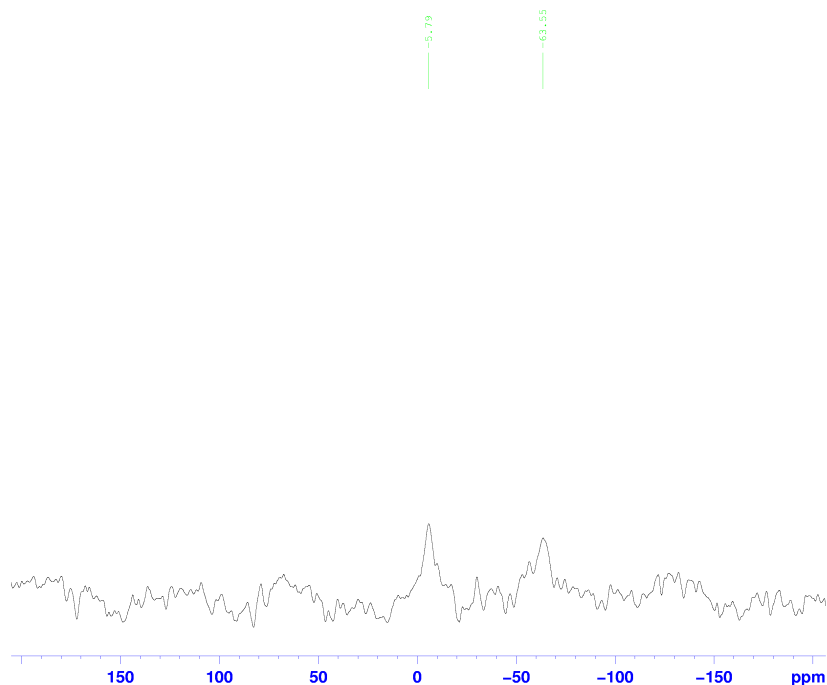


Figure 4.14 : Solid state ^{31}P NMR of $\text{Er}[(\text{C}_6\text{F}_5)_2\text{PO}_2]_3$

Figure 4.15 shows the solid state ^{31}P NMR of $\text{Er}_{0.05}\text{Y}_{0.95}[(\text{C}_6\text{F}_5)_2\text{PO}_2]_3$. The spectrum is similar to that of $\text{Y}[(\text{C}_6\text{F}_5)_2\text{PO}_2]_3$ shown in figure 4.13 whereby only a single phosphorous environment can be seen. This also provides further evidence that the diluted samples are mixed to the atomic levels.

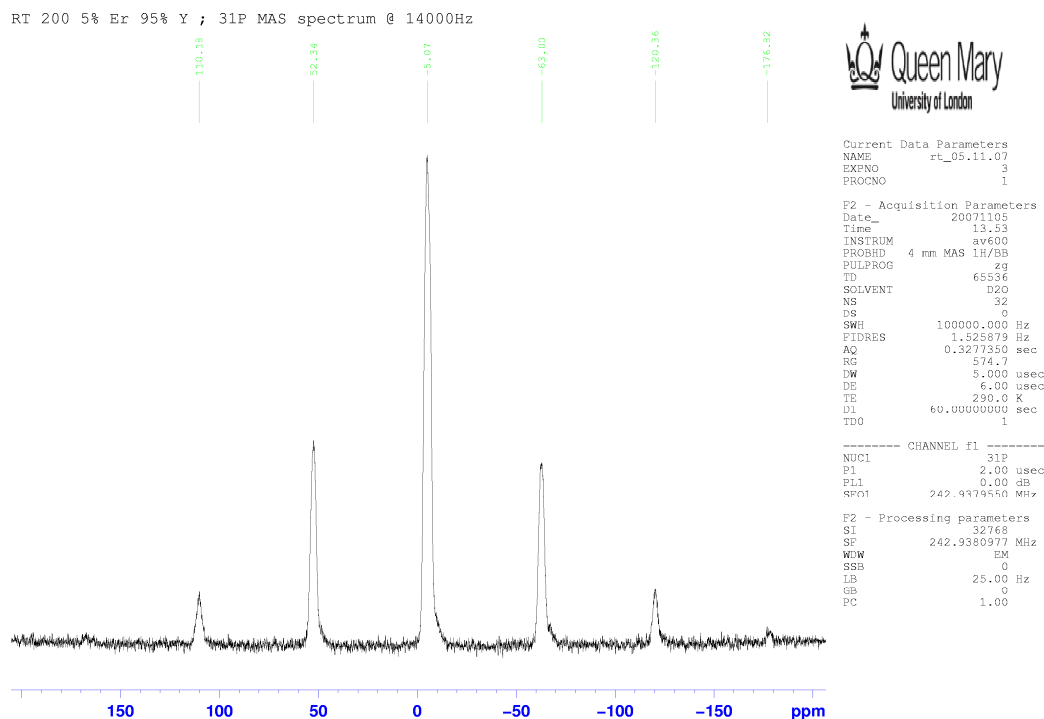


Figure 4.15 : Solid state ^{31}P NMR of $\text{Er}_{0.05}\text{Y}_{0.95}[(\text{C}_6\text{F}_5)_2\text{PO}_2]_3$

Energy dispersive X-ray (EDX) spectroscopy is a method that was attempted to determine the elemental composition of these diluted Ln^{3+} samples. It is a type of spectroscopy and it involves the investigations of a sample through interactions between electromagnetic radiation and matter. This technique utilizes X-rays that are emitted from the sample during bombardment of the sample by the electron beam. When the sample is bombarded by the electron beam, electrons are ejected from the atoms on the surface of the sample. A resulting electron vacancy is then filled by an electron from a shell of higher energy and an X-ray is emitted to balance the energy difference between the two electrons. The EDX detector then measures the number of emitted X-rays versus their energy, which is characteristic of the element from which the X-ray was emitted. The X-rays being emitted by the matter in response to the interactions with the charged particles are then analyzed. However, the detected X-ray energy of phosphorus was similar to that of yttrium and this posed some difficulties for the facility to differentiate the two different elements accurately. Since our diluted samples contain both elements, we were not able to obtain conclusive results. Figure 4.16 shows the resultant EDX

spectrum of $\text{Er}_{0.9}\text{Y}_{0.1}(\text{L-2})_3$. This spectrum was obtained using Oxford instruments INCA detector. The chamber vacuum was at around 8×10^{-6} torr and the voltage of electron beam was at 10 kV. It can be seen from figure 4.16 that the peaks corresponding to phosphorus (P) and yttrium (Y) are close together.

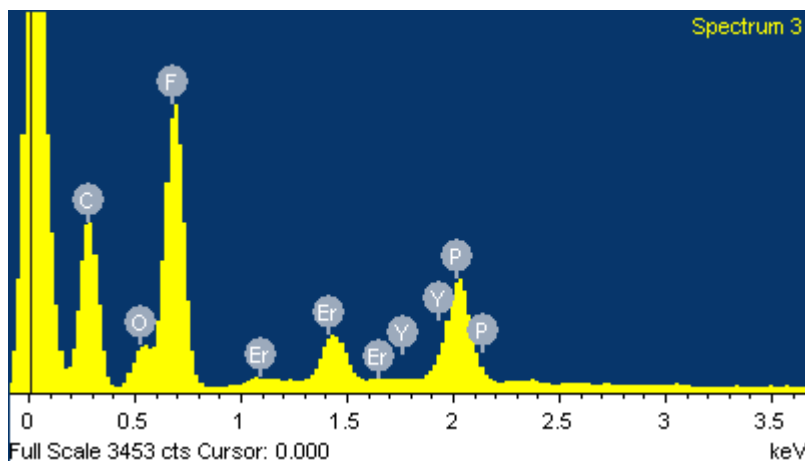


Figure 4.16 : EDX spectrum of $\text{Er}_{0.9}\text{Y}_{0.1}(\text{L-2})_3$

Recently, similar Er^{3+} iminodiphosphinates, $\{[(\text{C}_6\text{F}_5)_2\text{P}(\text{O})]_2\text{N}\}_3\text{Er}$ and its non-fluorinated analogue, $\{[(\text{C}_6\text{H}_5)_2\text{P}(\text{O})]_2\text{N}\}_3\text{Er}$ have been characterized by single X-ray diffraction and is shown to adopt molecular structures in which each Er^{3+} ion is coordinated by six oxygen atoms from three bulky bidentate ligands.^{12,13} The phosphinate ligands (L-1 – L-5) resemble the iminodiphosphinates in the sense that they provide a screen of aromatic rings and a single negative charge delocalized over the two oxygen donor groups on each ligand molecule, but the closeness of the oxygen atoms in the phosphinates favours the formation of inter-lanthanide bridges rather than chelation at single Ln^{3+} centres (Figure 4.17).

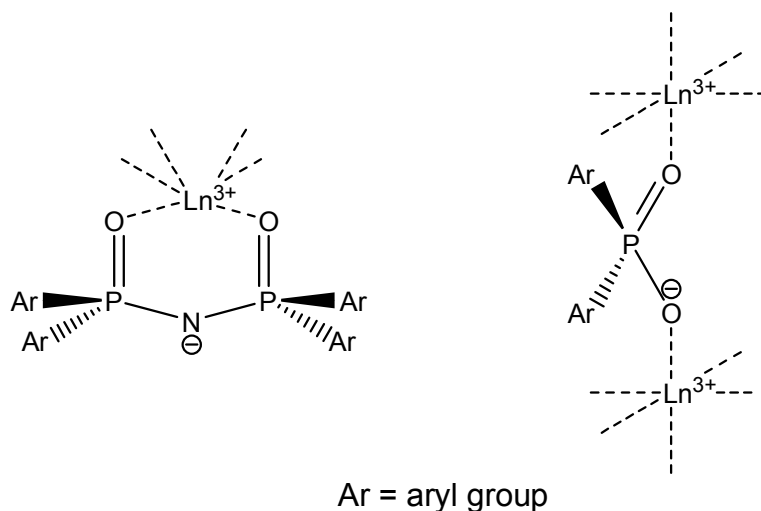


Figure 4.17 : Chelation at single Ln³⁺ centres (left) and formation of inter-lanthanide bridges (right)

Song *et al*⁴³ have suggested that metal complexes of the form, R₂POO (R = alkyl, alkoxy and aryl) are likely to be polymeric, involving bridging –O–P–O– groups and based on the low solubility of our Er³⁺, Nd³⁺ and Yb³⁺ complexes and high melting points (>300 °C), it is very likely that our complexes are coordination polymers.

4.5 Morphology of these Ln³⁺ complexes

Figures 4.18, 4.19, 4.20 show the scanning electron microscopy (SEM) images of Er³⁺, Nd³⁺ and Yb³⁺ phosphinates, respectively. The images within each family of complexes are identical and only representative images are shown. To obtain these images, each sample was individually applied over a sticky carbon tape and then carbon coated. The SEM was done on the Oxford Instrument Inspect F.

4.5.1 Morphology of Er^{3+} complexes

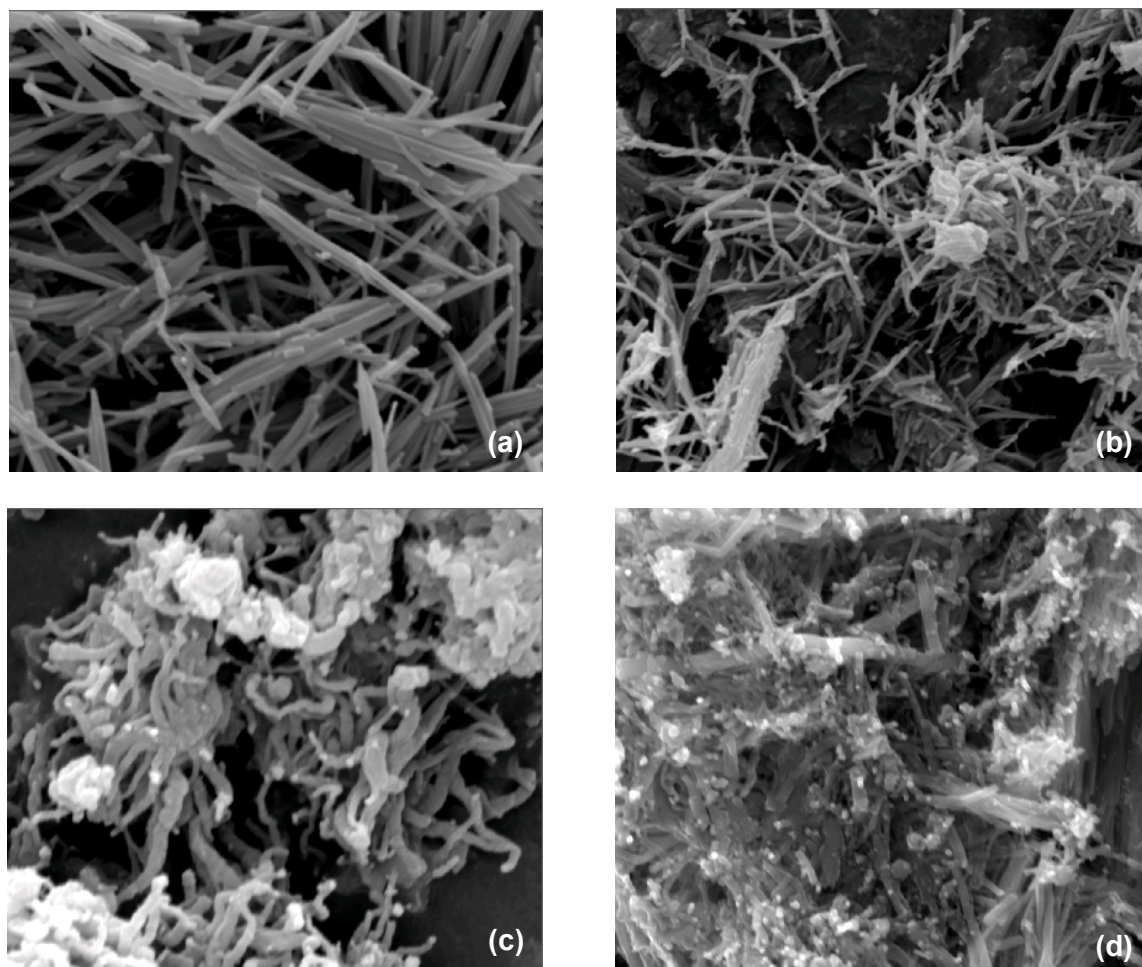


Figure 4.18 : SEM image of (a) $Er_{0.3}Y_{0.7}(L-1)_3$ (mag 50000 X),
(b) $Er_{0.5}Y_{0.5}(L-2)_3$ (mag 40000 X), (c) $Er_{0.9}Y_{0.1}(L-3)_3$ (mag 100000 X)
and (d) $Er_{0.7}Y_{0.3}(L-4)_3$ (mag 40000 X)

Figure 4.18 shows the SEM images of the Er^{3+} complexes. The image of $Er_{0.3}Y_{0.7}(L-1)_3$ was magnified 50000 X (a), $Er_{0.5}Y_{0.5}(L-2)_3$ was magnified 40000 X (b), $Er_{0.9}Y_{0.1}(L-3)_3$ was magnified 100000 X (c) and $Er_{0.7}Y_{0.3}(L-4)_3$ was magnified 40000 X (d). The average diameter for $Er_{0.3}Y_{0.7}(L-1)_3$ and $Er_{0.7}Y_{0.3}(L-4)_3$ is about 150 nm and for $Er_{0.5}Y_{0.5}(L-2)_3$ and $Er_{0.9}Y_{0.1}(L-3)_3$, it is about 80 nm. This is consistent with the findings of Song *et al*⁴³, where dimensions of between 50 – 200 nm were reported for their phosphinate complexes. From the images, it

can be seen that $\text{Er}_{0.3}\text{Y}_{0.7}(\text{L-1})_3$ have distinct rod-like characteristics whereas the other samples have a tendency to lump together.

4.5.2 Morphology of Nd^{3+} complexes

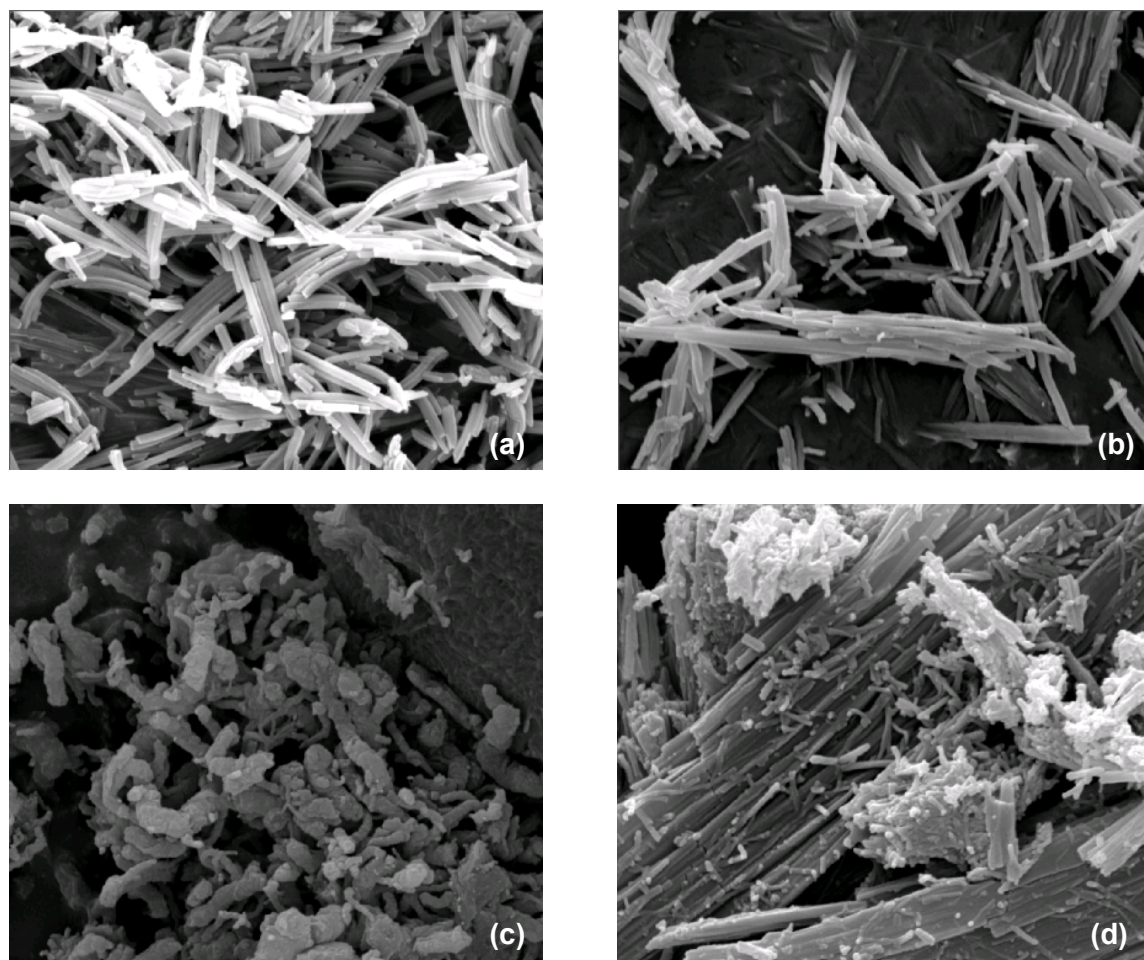


Figure 4.19 : SEM image of (a) $\text{Nd}_{0.5}\text{Y}_{0.5}(\text{L-1})_3$ (mag 50000 X),
(b) $\text{Nd}_{0.7}\text{Y}_{0.3}(\text{L-2})_3$ (mag 50000 X), (c) $\text{Nd}_{0.3}\text{Y}_{0.7}(\text{L-3})_3$ (mag 50000 X)
and (d) $\text{Nd}_{0.7}\text{Y}_{0.3}(\text{L-4})_3$ (mag 50000 X)

Figure 4.19 shows the SEM images of the Nd^{3+} complexes. All the samples shown in figure 4.19 were magnified 50000 X. The average diameter for $\text{Nd}_{0.5}\text{Y}_{0.5}(\text{L-1})_3$, $\text{Nd}_{0.7}\text{Y}_{0.3}(\text{L-2})_3$ and $\text{Nd}_{0.7}\text{Y}_{0.3}(\text{L-4})_3$ is about 110 nm and for $\text{Nd}_{0.3}\text{Y}_{0.7}(\text{L-3})_3$, the particles are too bulky for us to determine any reasonable dimensions. From the

images, it can be seen that $\text{Nd}_{0.5}\text{Y}_{0.5}(\text{L-1})_3$ and $\text{Nd}_{0.7}\text{Y}_{0.3}(\text{L-2})_3$ have distinct rod-like characteristics whereas the other samples have a tendency to form blocks.

4.5.3 Morphology of Yb^{3+} complexes

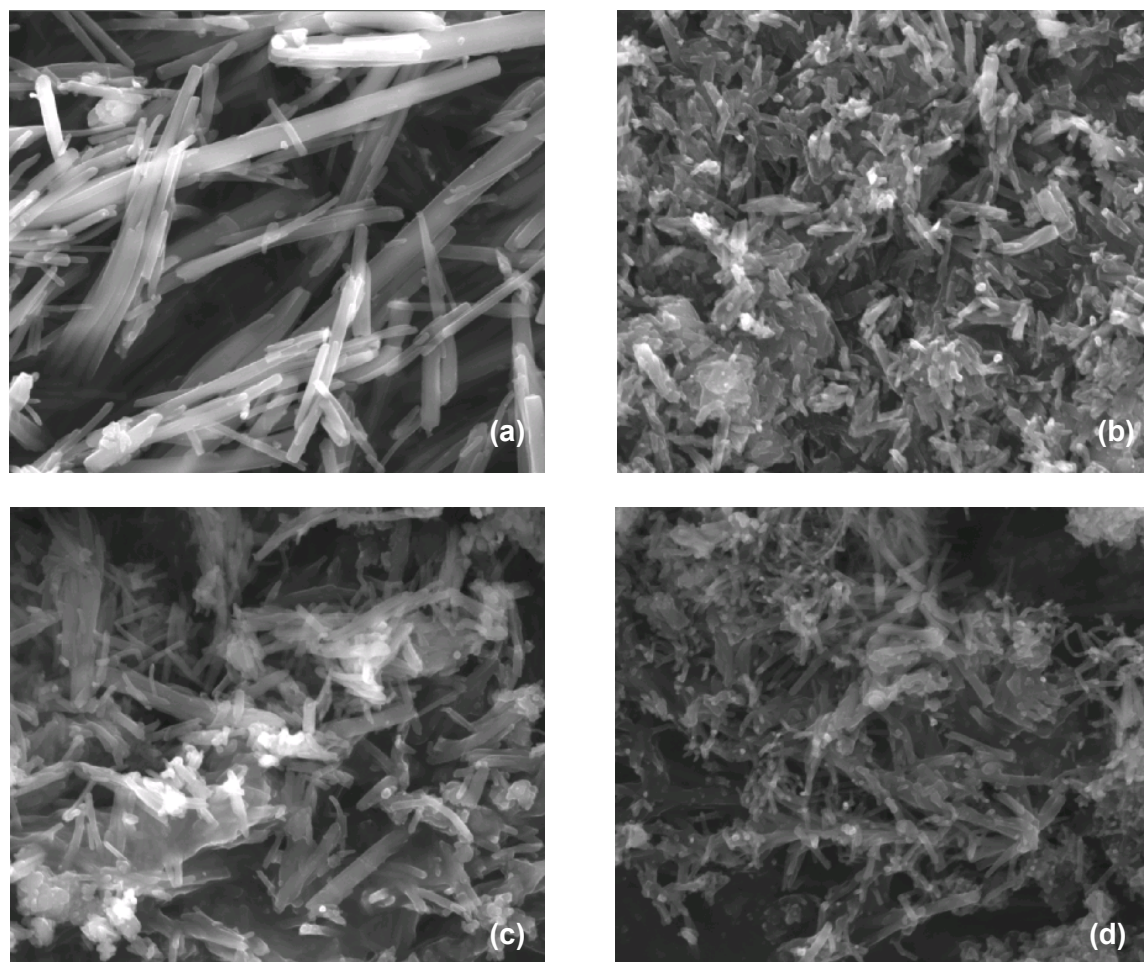


Figure 4.20 : SEM image of (a) $\text{Yb}_1\text{Y}_0(\text{L-1})_3$ (mag 50000 X),
(b) $\text{Yb}_{0.7}\text{Y}_{0.3}(\text{L-2})_3$ (mag 50000 X), (c) $\text{Yb}_{0.3}\text{Y}_{0.7}(\text{L-3})_3$ (mag 50000 X)
and (d) $\text{Yb}_{0.1}\text{Y}_{0.9}(\text{L-4})_3$ (mag 50000 X)

Figure 4.20 shows the SEM images of the Yb^{3+} complexes. All the samples shown in figure 4.20 were magnified 50000 X. The average diameter for $\text{Yb}_{0.7}\text{Y}_{0.3}(\text{L-2})_3$, $\text{Yb}_{0.3}\text{Y}_{0.7}(\text{L-3})_3$ and $\text{Yb}_{0.1}\text{Y}_{0.9}(\text{L-4})_3$ is about 110 nm and for $\text{Yb}_1\text{Y}_0(\text{L-1})_3$, the average size was determined to be about 150 nm. From the images, it can be seen that

$\text{Yb}_1\text{Y}_0(\text{L-1})_3$ have distinct rod-like characteristics whereas the other samples have a tendency to form blocks.

4.6 Spectroscopic characteristics of the ligands

The lifetime measurements and emission spectra of the Ln^{3+} complexes will be discussed in sections 4.8, 4.9 and 4.10 for Er^{3+} , Nd^{3+} and Yb^{3+} , respectively. When the lifetime measurements were done, it was observed that a very fast process at around 700 nm was detected. Absorption spectra of these ligands were obtained and it was found that they absorbed strongly in the ultra-violet (Figure 4.21).

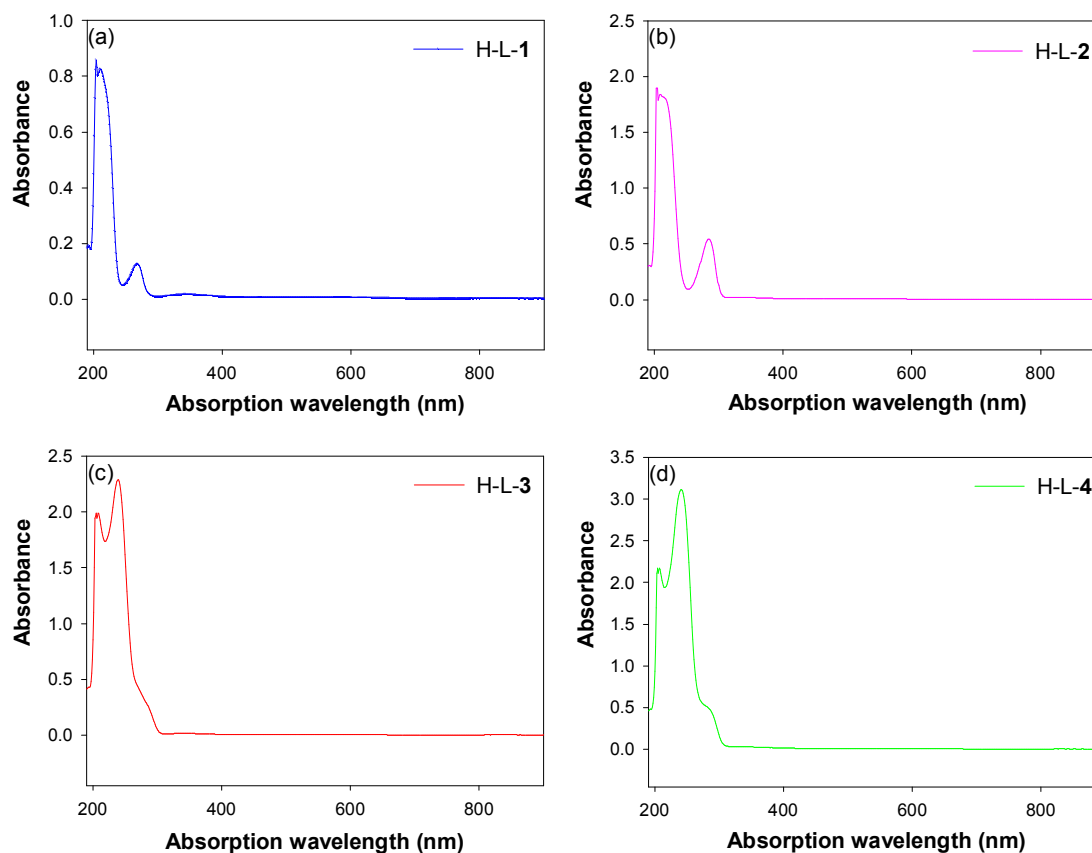


Figure 4.21 : Ultraviolet-visible absorption of ligands; (a) L-1, (b) L-2, (c) L-3 and (d) L-4

Figure 4.21 shows the absorption spectra of the ligands, L-1 to L-4. The absorption data was collected in solution using ethanol as a solvent and the results are presented in table 4.6.

Entry	Ligand	Concentration (mol L ⁻¹)	Peak absorbing wavelengths (nm)	Extinction coefficients (L mol ⁻¹ cm ⁻¹)
1	L-1	6.1 x 10 ⁻⁵	204	14082
			268	2066
2	L-2	1.22 x 10 ⁻⁴	209	15082
			285	4451
3	L-3	6.1 x 10 ⁻⁵	208	32574
			239	37557
4	L-4	1.83 x 10 ⁻⁴	208	11858
			241	17033

Table 4.6 : Ultraviolet-visible absorption of ligands, L-1 to L-4 using ethanol as a solvent

From the absorption spectra, it can be observed that the main absorption is in the ultraviolet region from 190 nm – 300 nm. No absorption can be observed in the visible region of the spectrum. Excitation spectra of the Er³⁺, Nd³⁺ and Yb³⁺ complexes will be presented in the following sections and that will enable us to determine if there is any energy transfer from the ligands to the luminescent ions.

These ligands were then excited at 410 nm to obtain the emission spectra. Figure 4.22 shows the emission spectrum of each ligand.

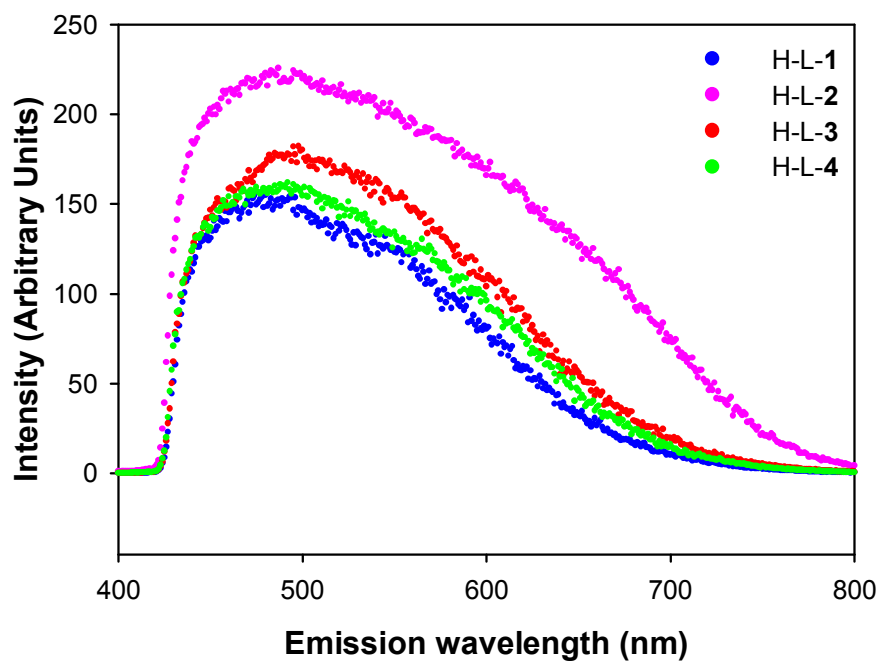


Figure 4.22 : Emission spectra of ligands L-1 to L-4

Note that the emission spectrum was obtained using a 435 nm long pass filter and thus, the short wavelength part of the band was truncated. From figure 4.22, it can be seen that the shape of the emission curves for all ligands are similar with the peak at around 500 nm. Luminescence data of each ligand at various wavelengths were collected and were found to be identical. Figure 4.23 shows the 750 nm lifetime luminescence data of ligand, L-4 at 410 nm excitation.

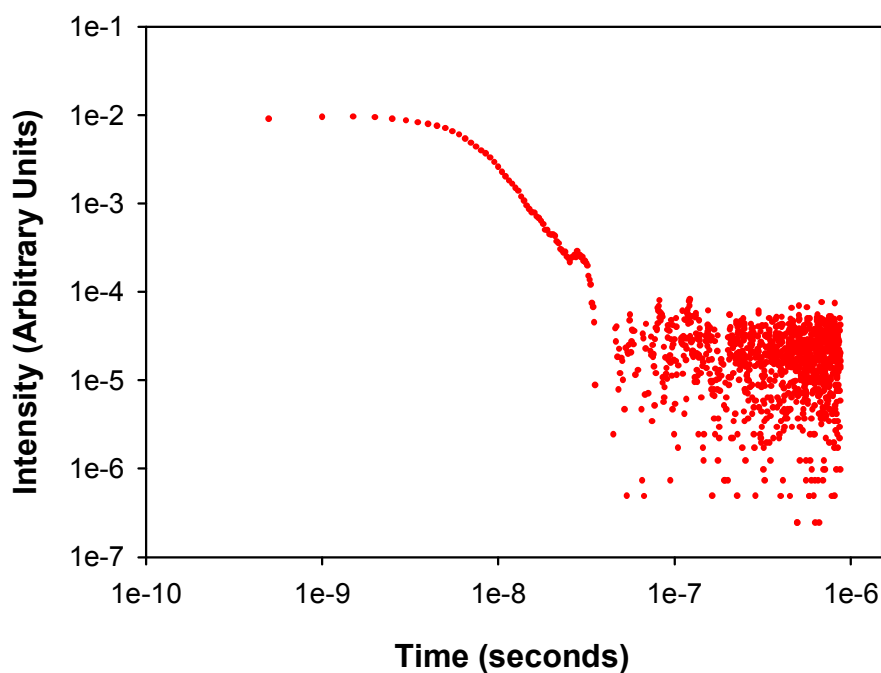


Figure 4.23 : 750 nm lifetime luminescence data of ligand, L-4 at 410 nm excitation

Figure 4.23 shows that the decay is very fast, in the order of ~ 10 ns. It must be mentioned that no reasonable fits could be achieved for all the collected luminescence lifetime data of the ligands.

4.7 Lifetimes of Er^{3+} , Nd^{3+} and Yb^{3+} samples

The luminescence lifetime data of the fluorinated complexes of the form $\text{Ln}(\text{L-1} - \text{L-4})_3$ (where $\text{Ln} = \text{Er}^{3+}$, Nd^{3+} and Yb^{3+}) cannot be fitted with a single exponential decay, but could be fitted with a stretched exponential decay according to equation 6. In this equation, I_0 is the offset intensity, I_1 is the initial intensity, τ is the lifetime and β is the stretching function.

Equation 6
$$I = I_0 + I_1 \exp\left(-\left(t / \tau\right)^\beta\right)$$

This is an empirical fit that is widely used to fit non-exponential decay processes and although there is no well defined physical significance to the fit, it is frequently

used to describe a superposition of exponential relaxation times.⁴⁸ From equation 6, an average lifetime can be calculated using equation 7. In equation 7, Γ is a gamma function.

Equation 7
$$\langle \tau \rangle = \frac{\tau}{\beta} \Gamma\left(\frac{1}{\beta}\right)$$

This stretched exponential function is widely used where there are a range of lifetimes for the emitting sites and there is energy exchange between the sites. The average lifetimes of the Er^{3+} , Nd^{3+} and Yb^{3+} complexes can be calculated using equation 7. Our samples are finely divided and the results are compatible with the Er^{3+} , Nd^{3+} and Yb^{3+} ions near the surface being quenched by the presence of C–H or O–H oscillators at those surfaces and energy migration from the bulk to these quenched sites occurring through ion-ion interactions. None of the samples measured show any active high energy vibrational modes at $>2500 \text{ cm}^{-1}$ that would be observed if C–H or O–H bonds were present.

4.8 Photoluminescence studies of Er^{3+} phosphinate complexes

Figure 4.24 (a), (b), (c) and (d) shows the emission spectra of Er(L-1)_3 , Er(L-2)_3 , Er(L-3)_3 and Er(L-4)_3 , respectively. These 100% Er^{3+} samples were excited at 520 nm at 300 K. Er^{3+} has an emission line centred around 1550 nm and that is attributed to the ${}^4I_{13/2} \longrightarrow {}^4I_{15/2}$ transition.²⁰ Due to Stark^{20,49} splitting of the energy levels, emission was observed at various wavelengths around this region.

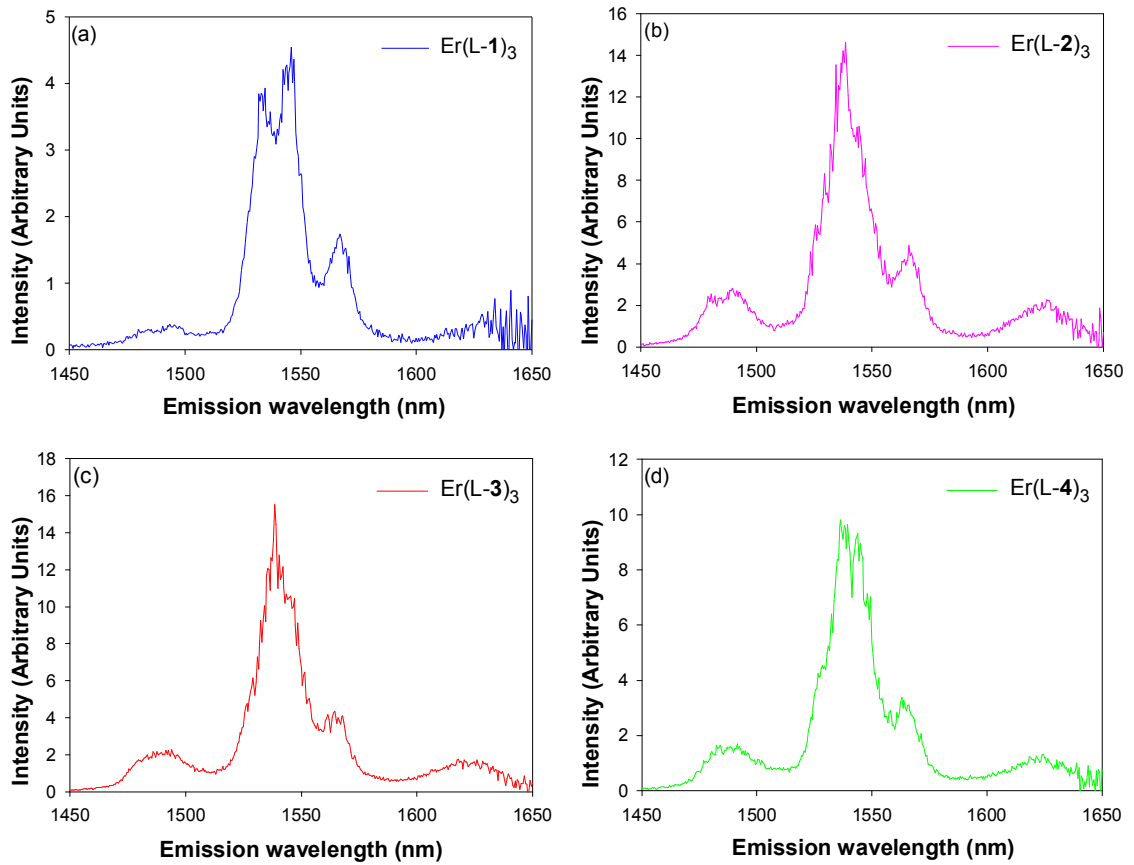


Figure 4.24 : Emission spectra of 100% (a) Er(L-1)_3 , (b) Er(L-2)_3 , (c) Er(L-3)_3 and (d) Er(L-4)_3

For the Er(L-1)_3 sample (Figure 4.24 (a)), the main peak was split into two with the one of a higher intensity emission centred at 1546 nm and the other at 1535 nm. A smaller peak at 1567 nm can also be observed. The main peak of the Er(L-2)_3 sample was centred at 1538 nm with other peaks at 1545 nm and 1566 nm. The Er(L-3)_3 sample has a main peak at 1538 nm together with peaks of lower intensity at 1543 nm and 1565 nm. Similar to the emission spectrum of the Er(L-1)_3 sample, the main feature of the Er(L-4)_3 sample was split into two with the higher intensity peak occurring at 1537 nm and another at 1544 nm. A peak of smaller intensity can be observed at 1563 nm.

Changes in the peak positions and the splitting of the emission peaks are a consequence of the symmetry of their surrounding hosts. Dieke⁴⁹ has shown that

the free Er^{3+} ions at the ${}^4I_{13/2}$ energy level will split into seven Stark components. Since each ligand is different, the emission spectrum for each sample obtained is different as the position of the energy levels of Er^{3+} may vary with the field surrounding the ion due to Stark²⁰ splitting. As these spectra were collected at room temperature, the presence of phonon interactions will contribute to the overall shape of the emission spectra.

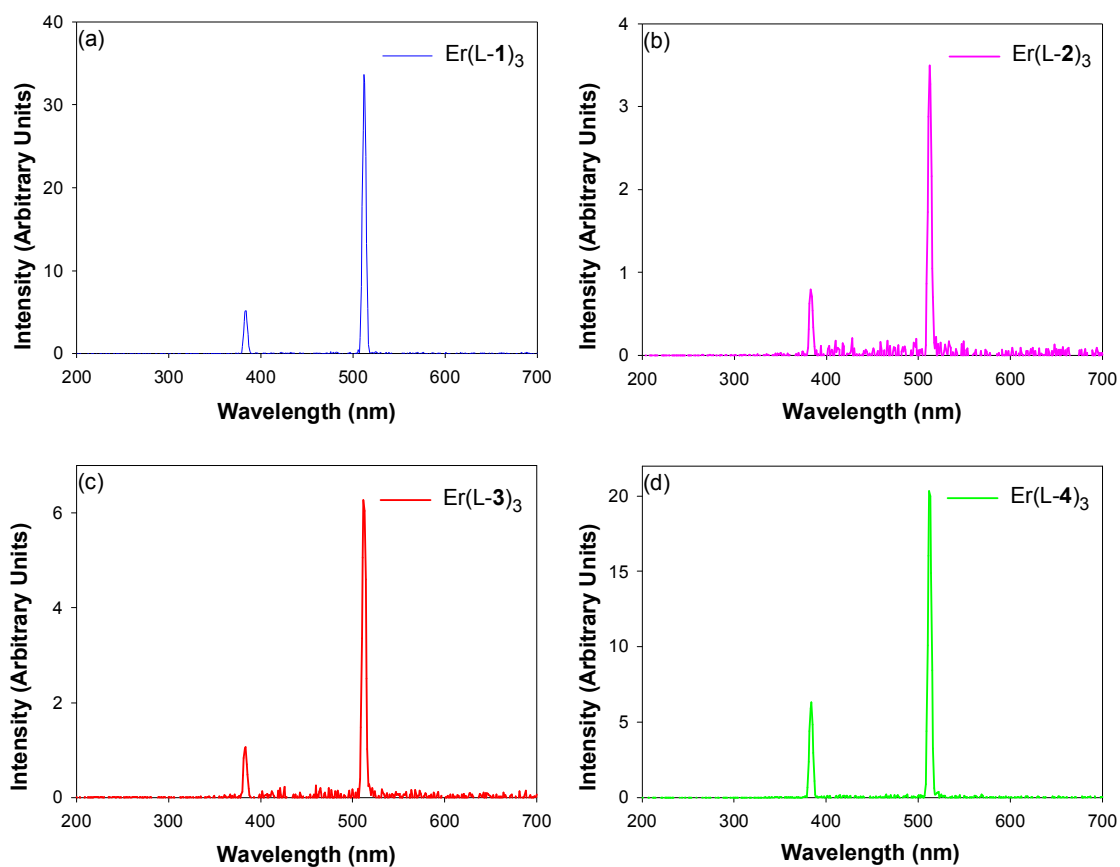


Figure 4.25 : Excitation spectra of 100% (a) Er(L-1)_3 , (b) Er(L-2)_3 , (c) Er(L-3)_3 and (d) Er(L-4)_3

Figure 4.25 (a), (b), (c) and (d) shows the excitation spectra at the peak emission wavelength of ~ 1540 nm of 100% Er(L-1)_3 , Er(L-2)_3 , Er(L-3)_3 and Er(L-4)_3 , respectively. All the spectra looked similar with peaks at 384 nm and 512 nm. The stronger peak at 512 nm is attributed to the ${}^2H_{11/2} \longrightarrow {}^4I_{15/2}$ transition whereas

the weaker peak is attributed to the ${}^4G_{11/2} \longrightarrow {}^4I_{15/2}$ transition.²⁰ Recall from section 4.6 where we saw that the absorption of the ligands are in the UV region from 190 nm to 300 nm. Thus, we can conclude from the relatively flat UV region of the excitation spectra that no measurable energy transfer from the ligands to the Er^{3+} ions took place.

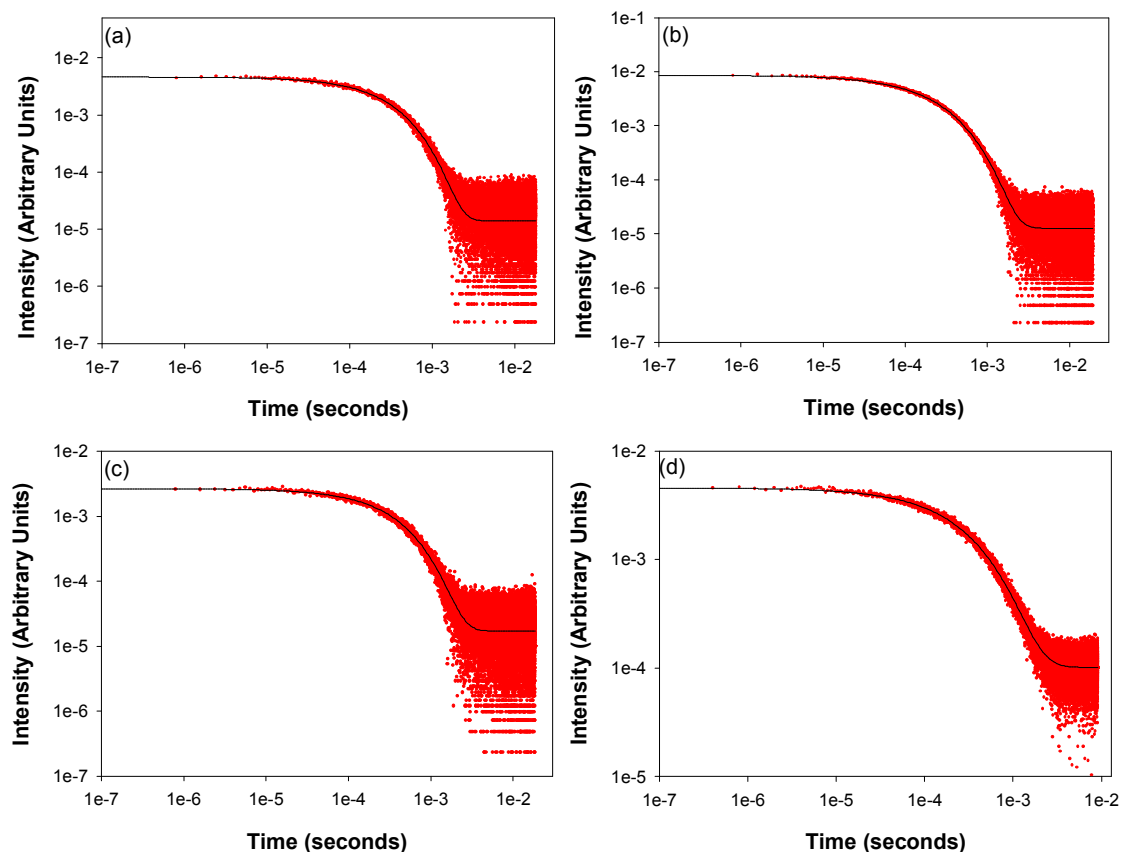


Figure 4.26 : Luminescence lifetime data and fit of 100% (a) $\text{Er}(\text{L-1})_3$, (b) $\text{Er}(\text{L-2})_3$, (c) $\text{Er}(\text{L-3})_3$ and (d) $\text{Er}(\text{L-4})_3$

Figure 4.26 (a), (b), (c) and (d) shows the luminescence lifetime data and fit of 100% $\text{Er}(\text{L-1})_3$, $\text{Er}(\text{L-2})_3$, $\text{Er}(\text{L-3})_3$ and $\text{Er}(\text{L-4})_3$, respectively. All the Er^{3+} samples can be fitted with a stretched function and the average lifetimes, β values and quantum yields are presented in table 4.7. The average lifetimes have an error of $\pm 15\%$.

Entry	Complex	Average lifetime	η (%)	β value	Peak emission
1	Er(L-1) ₃	295 μ s	3.7	0.87	1546 nm
2	Er(L-2) ₃	222 μ s	2.8	0.78	1538 nm
3	Er(L-3) ₃	363 μ s	4.5	0.86	1538 nm
4	Er(L-4) ₃	343 μ s	4.3	0.79	1537 nm
5	Er(L-5) ₃	5.3 μ s	0.07	1	1538 nm

Table 4.7 : Average lifetimes, β values and quantum yields of 100% Er(L-1)₃, Er(L-2)₃, Er(L-3)₃, Er(L-4)₃ and Er(L-5)₃

From table 4.7, it can be seen that the average lifetimes of the 100% Er³⁺ fluorinated complexes are in the same region of between 222 μ s – 363 μ s. Song *et al*⁴³ achieved lifetimes of 336 μ s (89%) and 13 μ s (11%) for 100% Er(L-1)₃. Recall from our earlier work that Cs[Er(HFA)]₄ samples has a single exponential lifetime of 1.8 μ s and for a 98% deuterated Cs[Er(HFA-d)]₄ sample, lifetimes of 11 μ s (96%) and 100 μ s (4%) were achieved. For the 100 μ s component, the nearest hydrogen atom is >20 Å away from the metal ion. Comparing the average lifetimes of entries 1 - 4 in table 4.7 with those of the HFA samples, we can see significant improvements with having low vibrational energy bonds in the environs of the emitting ion.

To compare the detrimental effects of high vibrational oscillators such as C–H bonds, Er(L-5)₃ was measured and found to have a single exponential lifetime of 5.3 μ s. This short lifetime can be attributed to nonradiative decay pathways through the high vibrational C–H bonds.

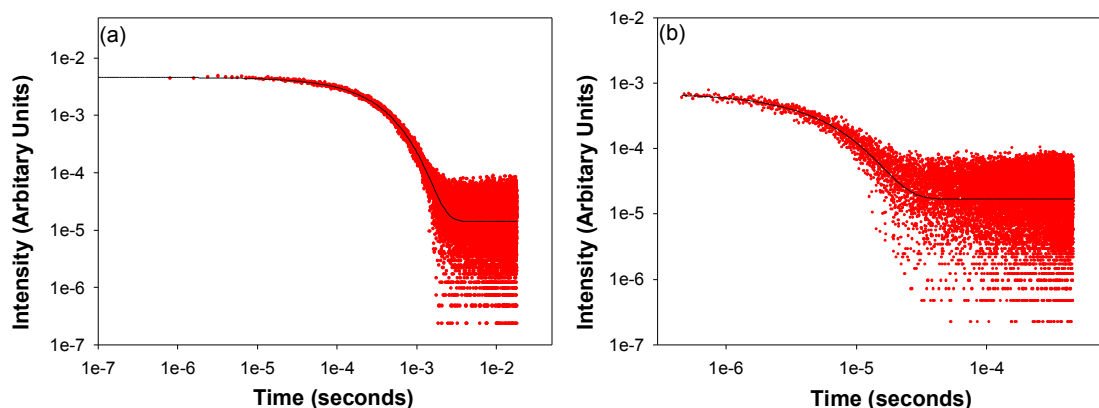


Figure 4.27 : Luminescence lifetime data and fit for 100% Er(L-1)₃: (a) fitted by a stretched function and 100% Er(L-5)₃ (b) fitted by a single exponential function

Figure 4.27 (a) and (b) shows the luminescence lifetime data and fit for 100% Er(L-1)₃ by a stretched function and 100% Er(L-5)₃ by a single exponential function, respectively. The single exponential fit indicates that all the Er³⁺ ions are in equivalent sites from the perspective of luminescence quenching and the lifetime is similar to that seen for solid $\{[(C_6H_5)_2P(O)]_2N\}_3Er$, where a lifetime of 2.3 μs was obtained.¹³ Removal of high energy vibrational oscillators has improved the lifetimes by about two orders of magnitude. C–F bonds have energy of 1200 cm^{-1} and the emitting level of Er³⁺ at ⁴I_{13/2} is resonant with the 6th harmonic of a C–F bond and from the energy gap law, it renders any high vibrational quenching less effective.

The average lifetimes shown in table 4.7 are also similar to those obtained for $\{[(C_6F_5)_2P(O)]_2N\}_3Er$, where a lifetime of 316 μs was obtained.¹² Assuming a natural lifetime of 8 ms,¹¹ these Er³⁺ phosphinates demonstrate quantum yields ($\eta\%$) of 3.7%, 2.8%, 4.5% and 4.3% for Er(L-1)₃, Er(L-2)₃, Er(L-3)₃ and Er(L-4)₃, respectively. Although the long average lifetimes can be attributed to the exclusion of solvent molecules by the bulky ligands, the low quantum yields suggest that other quenching mechanisms are still present. The β values obtained for these samples were below unity and that suggests that there is a distribution of lifetimes, which is indicative of ion-ion interactions. Earlier, we discussed that Ln³⁺ complexes have the tendency to interact with each other and that leads to lower

quantum yields. The only way to prevent this from occurring is to keep the luminescent centres apart and in the following section, we do this by diluting the Er^{3+} complexes with Y^{3+} . Y^{3+} has approximately the same ionic radius as Er^{3+} but is optically inert.

4.8.1 Effects of diluted Er^{3+} samples

Ten Er^{3+} samples were diluted with Y^{3+} with Er^{3+} concentrations varying from 10% to 100%. These samples are presented in the form, $\text{Er}_x\text{Y}_{1-x}(\text{L-1} - \text{L-4})_3$, where x is the mole fraction of Er^{3+} . Each of these samples is excited at 520 nm to provide direct excitation into the ${}^2\text{H}_{11/2}$ level of the Er^{3+} ion which rapidly decays to the ${}^4\text{I}_{13/2}$ level (Figure 4.28).

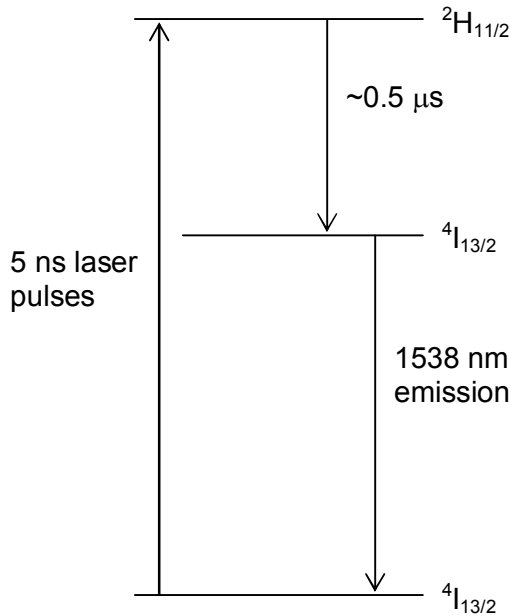


Figure 4.28 : Schematic diagram of the excitation pathway of Er^{3+} at 520 nm

The rise time, which is defined as the time taken for the excitation energy to decay from the ${}^2\text{H}_{11/2}$ level to the ${}^4\text{I}_{13/2}$ level can be measured by fitting the measured data using equation 8. The rise times of the Er^{3+} samples are presented in table 4.8. Figure 4.29 (a), (b), (c) and (d) shows the measured rise time data and fit of $\text{Er}(\text{L-1})_3$, $\text{Er}_{0.97}\text{Y}_{0.03}(\text{L-2})_3$, $\text{Er}_{0.5}\text{Y}_{0.5}(\text{L-3})_3$ and $\text{Er}_{0.93}\text{Y}_{0.07}(\text{L-4})_3$, respectively. It must be noted that the rise time of the $\text{Er}_{0.1}\text{Y}_{0.9}(\text{L-1})_3$ sample cannot be fitted.

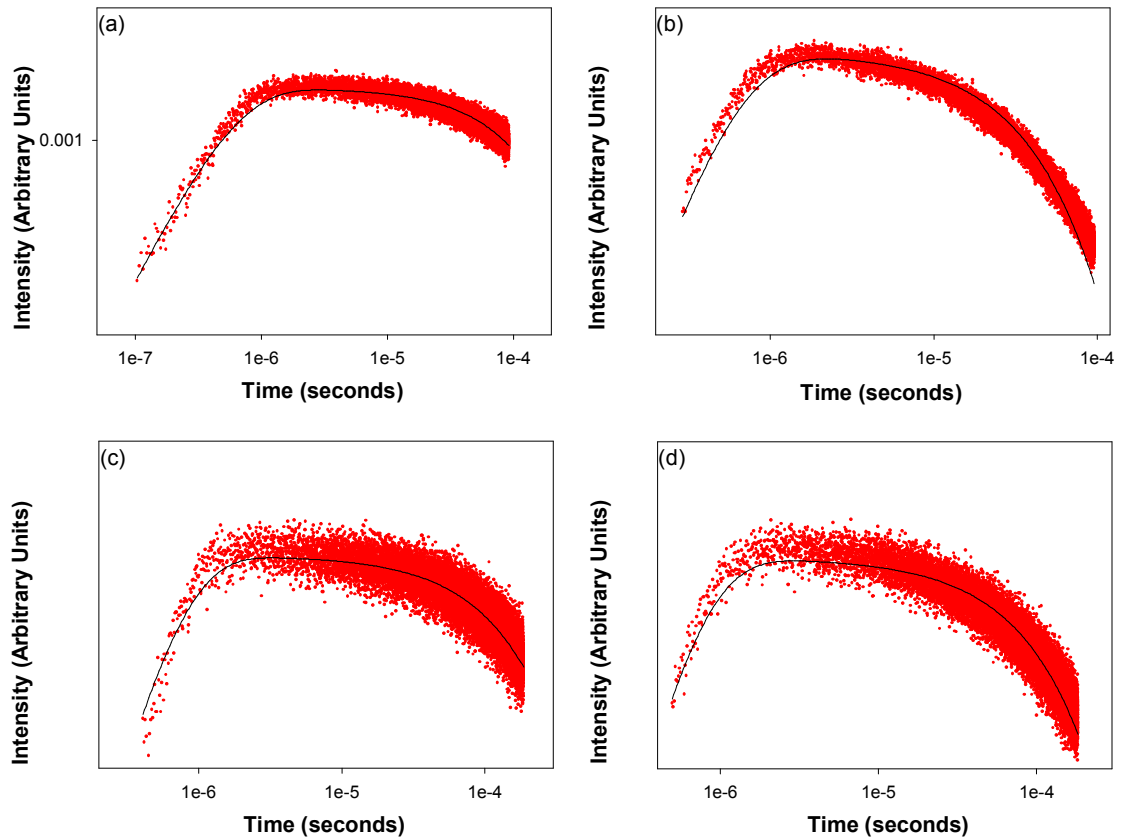


Figure 4.29 : Rise time data and fit of (a) $\text{Er}(\text{L-1})_3$, (b) $\text{Er}_{0.97}\text{Y}_{0.03}(\text{L-2})_3$,
(c) $\text{Er}_{0.5}\text{Y}_{0.5}(\text{L-3})_3$ and (d) $\text{Er}_{0.93}\text{Y}_{0.07}(\text{L-4})_3$

Equation 8

$$f = y_0 + a(1 - e^{-bt})(e^{-ct})$$

Equation 8 is a multiplication of an exponential rise to maximum function and a single exponential decay function. In equation 8, y_0 is the initial offset, a is related to the intensity of the laser pulse, b is the inverse rise time of the measured sample and c is the inverse luminescence lifetime.

Sample	Erbium concentrations									
	100%	97%	93%	90%	85%	80%	70%	50%	30%	10%
$\text{Er}_x\text{Y}_{1-x}(\text{L-1})_3$										
Risetime (μs)	0.46	0.46	0.48	0.47	0.46	0.47	0.51	0.50	0.50	
$\text{Er}_x\text{Y}_{1-x}(\text{L-2})_3$										
Risetime (μs)	0.34	0.40	0.36	0.40	0.36	0.36	0.34	0.33	0.39	0.40
$\text{Er}_x\text{Y}_{1-x}(\text{L-3})_3$										
Risetime (μs)	0.50	0.39	0.55	0.47	0.39	0.36	0.50	0.47	0.48	0.45
$\text{Er}_x\text{Y}_{1-x}(\text{L-4})_3$										
Risetime (μs)	0.46	0.37	0.43	0.43	0.56	0.56	0.49	0.52	0.54	0.37

Table 4.8 : Rise times of the Er^{3+} samples

We observed that the rise times within each family are approximately the same and the maximum rise time is about $\sim 0.50 \mu\text{s}$. This means that after the excitation pulse, it takes about $\sim 0.50 \mu\text{s}$ for the excitation energy to depopulate the $^2\text{H}_{11/2}$ level and transfer to the $^4\text{I}_{13/2}$ level where radiative emission takes place.

The average lifetimes, β values and quantum yields are shown in table 4.9. Average lifetimes shown in table 4.9 have an error of $\pm 15\%$ and have been calculated using the β values and equation 7.

Sample	Erbium concentrations									
	100%	97%	93%	90%	85%	80%	70%	50%	30%	10%
$\text{Er}_x\text{Y}_{1-x}(\text{L-1})_3$										
Lifetime (μs)	295	304	381	355	446	554	616	658	735	776
η (%)	3.7	3.8	4.8	4.4	5.6	6.9	7.7	8.2	9.2	9.7
β	0.87	0.82	0.89	0.86	0.92	0.94	1	1	1	1
$\text{Er}_x\text{Y}_{1-x}(\text{L-2})_3$										
Lifetime (μs)	222	187	230	312	393	434	496	576	677	669
η (%)	2.8	2.3	2.9	3.9	4.9	5.4	6.2	7.2	8.5	8.4
β	0.78	0.69	0.69	0.76	0.82	0.87	0.91	1	1	1
$\text{Er}_x\text{Y}_{1-x}(\text{L-3})_3$										
Lifetime (μs)	363	314	375	378	480	547	582	642	680	673
η (%)	4.5	3.9	4.7	4.7	6	6.8	7.3	8.0	8.5	8.4
β	0.86	0.79	0.79	0.82	0.89	1	1	1	1	1
$\text{Er}_x\text{Y}_{1-x}(\text{L-4})_3$										
Lifetime (μs)	343	437	540	606	556	597	629	659	717	707
η (%)	4.3	5.5	6.8	7.6	7.0	7.5	7.9	8.2	9.0	8.8
β	0.79	0.79	0.88	0.90	0.86	0.88	0.92	1	1	1

Table 4.9 : Average lifetimes, β values and quantum yields of diluted Er^{3+} samples

The luminescence lifetimes and rise times for $\text{Er}_x\text{Y}_{1-x}(\text{L-1})_3$, $\text{Er}_x\text{Y}_{1-x}(\text{L-2})_3$, $\text{Er}_x\text{Y}_{1-x}(\text{L-3})_3$ and $\text{Er}_x\text{Y}_{1-x}(\text{L-4})_3$ were measured at 1546 nm, 1538 nm, 1538 nm and 1537 nm, respectively. From table 4.9, it can be seen that the average lifetimes increase when the concentration of Er^{3+} decreases. This dilution has the effect of increasing the interionic distance between Er^{3+} ions and suppressing the effects of ion-ion interactions. The β values demonstrate a gradual increase as the Er^{3+} ions are diluted from 100% concentrations and β tends to 1 at lower concentrations. It can also be observed that samples with high concentration of Er^{3+} ($\sim >80\%$) demonstrate single exponential decay and as the concentration is reduced, the decay process tends towards being single exponential, with β being 1. This indicates that for the high Er^{3+} concentration samples, there is a distribution of

lifetimes across the sample, from the sites at the surface of the solid particle to the ions in the centre, and implies there may be some concentration dependent quenching occurring between the Er^{3+} ions. Lower β values suggest more stretching and hence more interactions between the ions. As the β value tends to unity for the low Er^{3+} concentration samples, it points to the fact that the distribution of lifetimes is homogenous across the sample and the probability that ion-ion interactions have been suppressed.

Based on the quantum efficiency ($\eta\%$) presented in table 4.9, and taking into considerations the lowest and highest values within each family, the effects of dilution have achieved between two and three-fold improvements in quantum efficiency.

The average lifetimes plots for all the samples are plotted and shown in figure 4.30. Figure 4.30 (a) is the Er^{3+} concentration ν lifetime plot for $\text{Er}_x\text{Y}_{1-x}(\text{L-1})_3$, figure 4.30 (b) is for $\text{Er}_x\text{Y}_{1-x}(\text{L-2})_3$, figure 4.30 (c) is for $\text{Er}_x\text{Y}_{1-x}(\text{L-3})_3$ and figure 4.30 (d) is for $\text{Er}_x\text{Y}_{1-x}(\text{L-4})_3$.

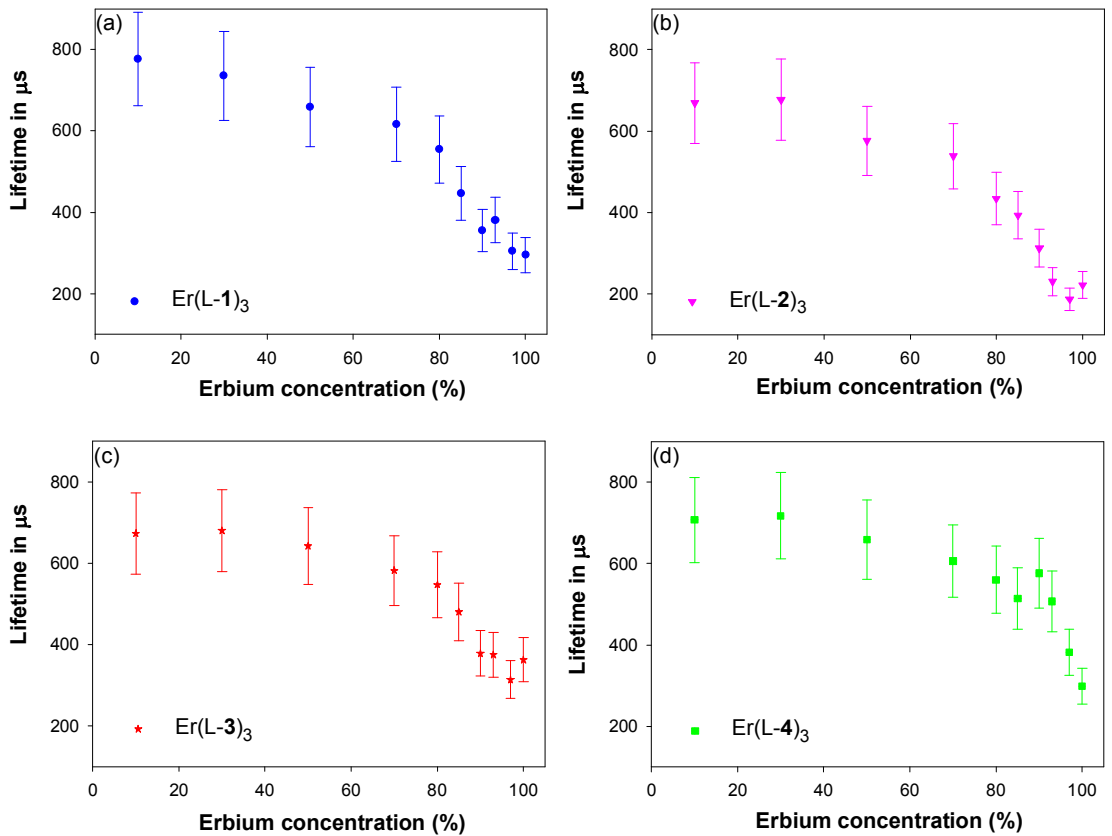


Figure 4.30 : Er^{3+} concentration v lifetime plots for (a) $\text{Er}_x\text{Y}_{1-x}(\text{L-1})_3$, (b) $\text{Er}_x\text{Y}_{1-x}(\text{L-2})_3$, (c) $\text{Er}_x\text{Y}_{1-x}(\text{L-3})_3$ and (d) $\text{Er}_x\text{Y}_{1-x}(\text{L-4})_3$

Each data point in the figure has an error of $\pm 15\%$. As the concentration of Er^{3+} ions increases, concentration quenching occurs which decreases the luminescence quantum yields. For our Er^{3+} samples, this concentration quenching process is evident from the increasing average lifetimes as the interionic distance increases between neighbouring Er^{3+} ions. Although upconversion processes are prevalent in Er^{3+} doped glasses,^{4,50} we could not detect any upconversion emissions at wavelength range of ~ 530 nm to 670 nm when these samples were excited at the common upconversion excitation wavelengths of 798 nm and 975 nm. Concentration quenching can also arise from the fact that at high Er^{3+} concentrations, the excitation energy can migrate from one ion to another and that increases the probability of the ion encountering a quenching centre. In such scenarios, the energy migrations give rise to a distribution of lifetimes and that is evident from the non-unity β values at high concentrations.

All the plots in figure 4.30 demonstrate similar shapes whereby the average lifetimes increased sharply from a 100% Er^{3+} sample to a 80% Er^{3+} sample. This suggests that for Er^{3+} concentrations greater than 80%, the interionic distance between the luminescence centres are most favourable for energy migration. At these high concentrations, Er^{3+} ions are most sensitive to its neighbouring Er^{3+} ions and any changes to its concentration will have a relatively significant effect on its lifetimes.

For Er^{3+} concentrations below 80%, the average lifetime increments are relatively gradual and for Er^{3+} concentrations of 30% and below, the lifetime values are approximately constant at $\sim 700 \mu\text{s}$. This led us to think that at the Er^{3+} concentration of 30%, the interionic distance between the luminescence centres is optimal due to the majority of Y^{3+} ions keeping the Er^{3+} ions apart. Thus, each Er^{3+} ion has minimal quenching effects on the next nearest Er^{3+} ion and the luminescence of each Er^{3+} ion is not affected by its neighbouring Er^{3+} ion. This suggests that $\sim 700 \mu\text{s}$ is the intrinsically limited lifetime for these Er^{3+} materials and that at this concentration, there is negligible energy migration between neighbouring Er^{3+} ions.

Although the absolute lifetimes of pure Er^{3+} in these organic hosts have not been determined, this set of results allow us to provide an upper limit to the Er^{3+} concentration that can be utilized in a device based on these materials. Figure 4.31 shows a combined plot of all the different diluted Er^{3+} samples against average lifetimes.

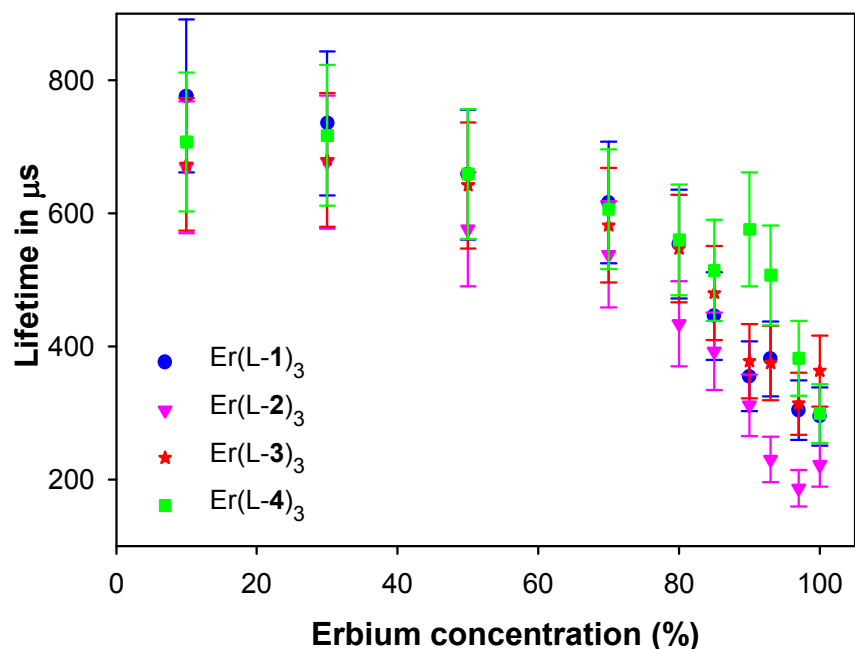


Figure 4.31 : Combined Er^{3+} concentration v lifetime plots of all the different diluted Er^{3+} samples

The similarity of the average lifetimes and the shape of the decay lifetime data can be seen from figure 4.31. One interesting feature of these samples as can be seen from figure 4.31 is that despite the increase in size from ligand L-1 to L-4, the average lifetimes of the samples at each concentration are identical. Since the effects of ion-ion interaction are strongly dependent on the ion concentration and can be related to the interionic distance between two or more similar ions, these results suggest that for the Er^{3+} phosphinates, the size of the ligand has minimal influence on the ion-ion distance. This has led us to conclude that for Er^{3+} , one dimensional quenching is prevalent across these samples, where the ions only interact with their neighbouring ions in one direction. Recall our discussions in section 4.4 (Figure 4.17) that these complexes are coordination polymers where the Ln^{3+} ions are bridged to one another and hence, along the backbone of the polymer, the Er-Er distance will not be affected by the size of the ligands.

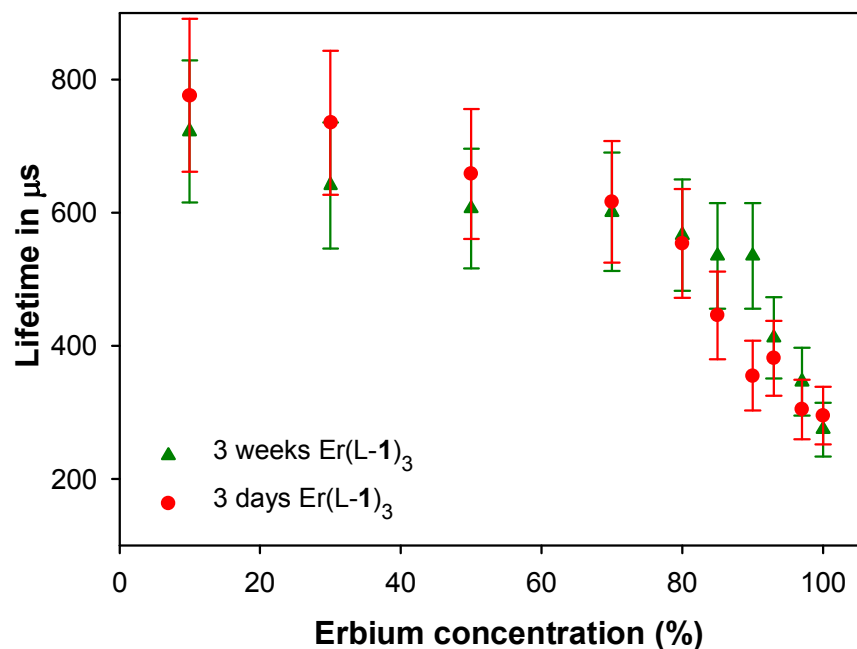


Figure 4.32 : Er^{3+} concentration v lifetime plots of Er^{3+} samples that have been kept for different periods of time

As mentioned earlier, all the samples were kept for about three days before filtering, washing and then drying them. To determine if the time between preparing the samples and filtering them makes any difference to their average lifetimes, a separate set of Er^{3+} complexes $\text{Er}(\text{L-1})_3$ was prepared and kept at room temperature for three weeks before filtering. The average lifetime results are plotted in figure 4.32. These samples exhibited similar average lifetimes and can be concluded that the time taken to grow these samples have minimal effects on their lifetimes.

4.9 Photoluminescence studies of Nd³⁺ phosphinate complexes

Figure 4.33 (a), (b), (c) and (d) shows the emission spectra of Nd(L-1)₃, Nd(L-2)₃, Nd(L-3)₃ and Nd(L-4)₃, respectively. These 100% Nd³⁺ samples were excited at 420 nm at 300 K. From these spectra, it can be observed that Nd³⁺ exhibits three possible emissions at ~876 nm, ~1056 nm and ~1320 nm corresponding to $^4F_{3/2} \longrightarrow ^4I_{9/2}$, $^4F_{3/2} \longrightarrow ^4I_{11/2}$ and $^4F_{3/2} \longrightarrow ^4I_{13/2}$ transitions²⁰, respectively. Due to Stark^{20,49} splitting of the energy levels, emission is observed at various wavelengths around this region. Similar to Er³⁺, these spectra have different number of peaks and that is due to the symmetry of the environment to the local crystal field.

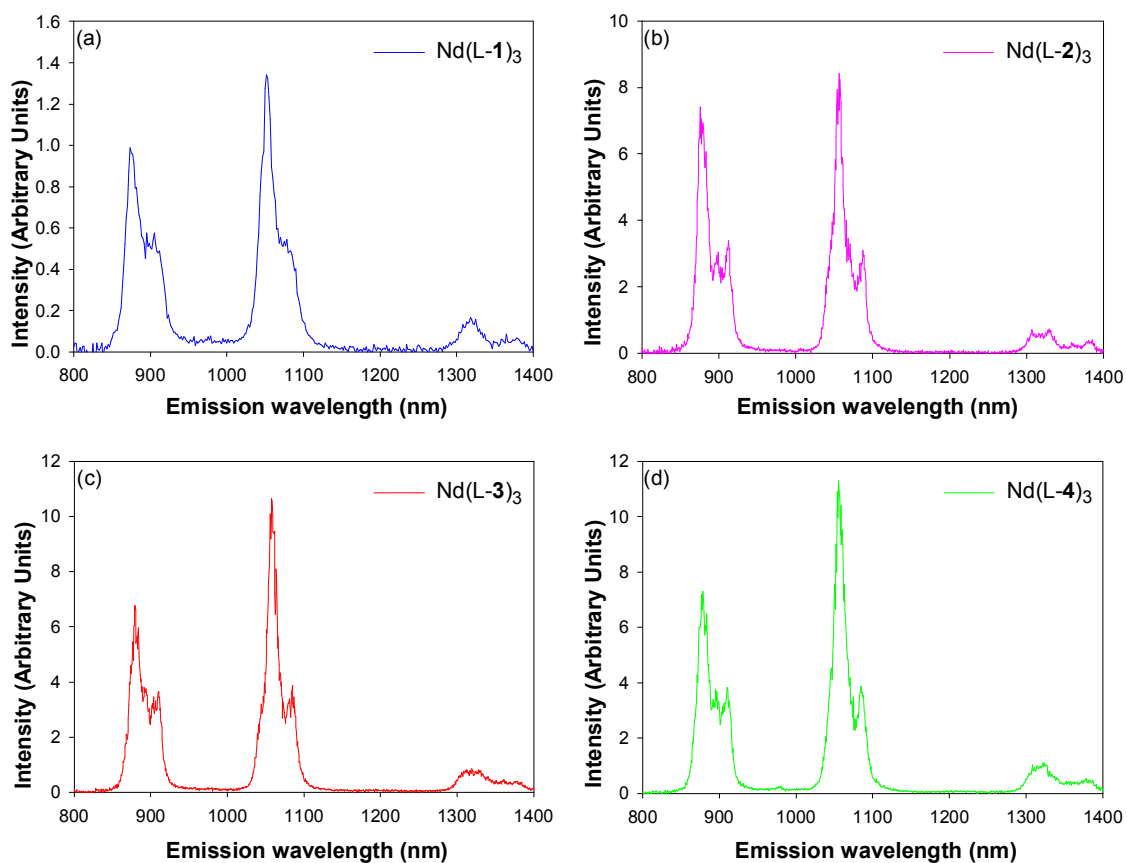


Figure 4.33 : Emission spectra of 100% (a) Nd(L-1)₃, (b) Nd(L-2)₃, (c) Nd(L-3)₃ and (d) Nd(L-4)₃

For Nd(L-1)₃ (Figure 4.33 (a)), the three main peaks are centred at 873 nm, 1052 nm and 1318 nm. Figure 4.33 (b) shows the emission spectrum of Nd(L-2)₃ and three sharp features can be observed around 900 nm with the highest peak at 876 nm and two other peaks at 897 nm and 912 nm. The peak with the highest intensity is at 1058 nm and a relatively smaller one at 1087 nm. A broad plateau with a peak at 1327 nm can also be seen. The emission spectra of Nd(L-3)₃ and Nd(L-4)₃ are rather similar in appearance. Two main peaks are centred at 876 nm and 1058 nm with other peaks at 904 nm, 1085 nm and 1320 nm for Nd(L-3)₃. For Nd(L-4)₃, the two main peaks are at 878 nm, and 1055 nm. Other peaks can also be seen at 910 nm, 1085 nm and 1322 nm.

For all the Nd³⁺ phosphinate samples, lifetime data can only be determined for the ${}^4F_{3/2} \longrightarrow {}^4I_{9/2}$ (~876 nm) and ${}^4F_{3/2} \longrightarrow {}^4I_{11/2}$ (~1056 nm) transitions. The ${}^4F_{3/2} \longrightarrow {}^4I_{13/2}$ (~1320 nm) transition was too weak for accurate lifetime measurements.

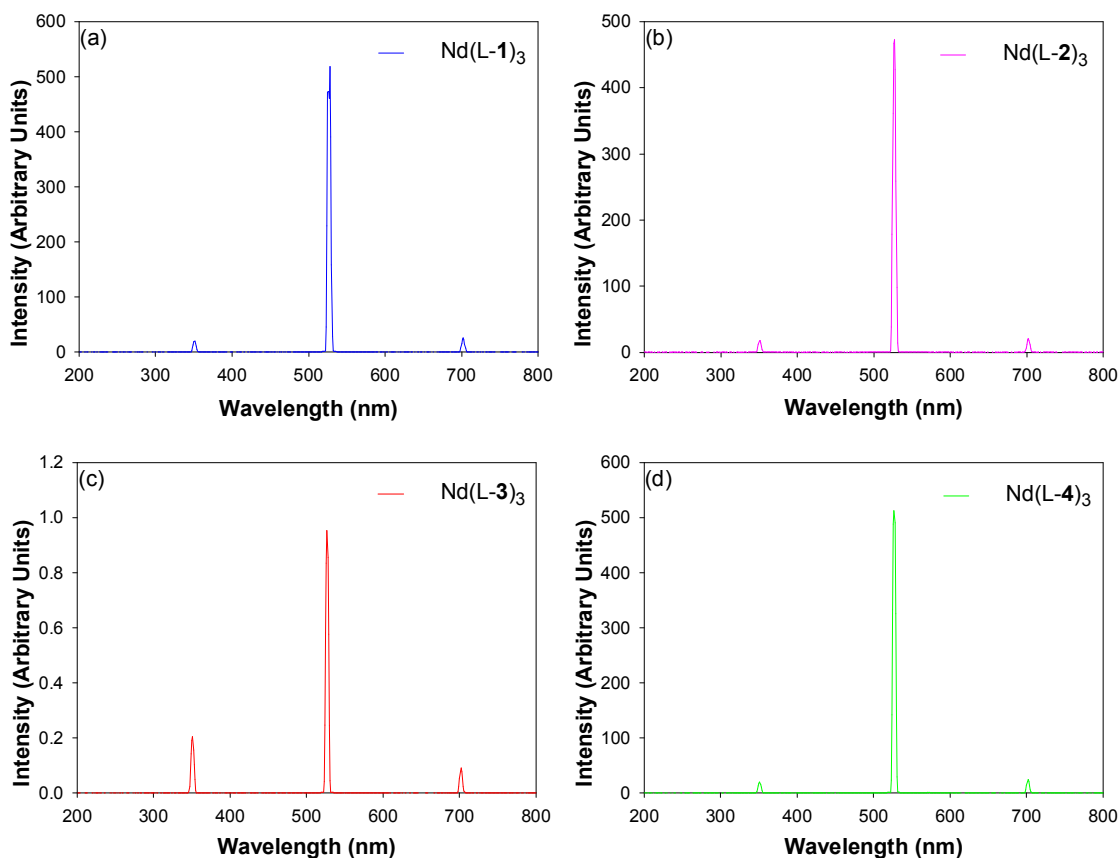


Figure 4.34 : Excitation spectra of 100% (a) Nd(L-1)₃, (b) Nd(L-2)₃, (c) Nd(L-3)₃ and (d) Nd(L-4)₃

Figure 4.34 (a), (b), (c) and (d) show the excitation spectra at the peak emission wavelength of ~1056 nm of 100% Nd(L-1)₃, Nd(L-2)₃, Nd(L-3)₃ and Nd(L-4)₃, respectively. All the spectra are identical with peaks at 351 nm, 527 nm and 702 nm. The strongest peak at 527 nm is attributed to the $^4G_{7/2} \longrightarrow ^4I_{9/2}$ transition whereas the peak at 702 nm can be attributed to the $^4F_{9/2} \longrightarrow ^4I_{9/2}$ transition and the peak at 351 nm is a consequence of the second order diffraction of the 702 nm peak.²⁰ Similar to the excitation spectra of Er³⁺ samples that we saw earlier, the relatively flat UV region implies that no sensitization from the ligands to the Nd³⁺ ions took place.

Figure 4.35 shows the luminescence lifetime data and fits of 100% Nd³⁺ samples with different phosphinate ligands. Unlike the Er³⁺ samples, in order to obtain a

good fit to the data, the first 30 - 40 data points out of 25,000 data points have to be removed from the luminescence lifetime data. Figure 4.35 (a), (c) and (e) show the luminescence lifetime data and fit of 100% Nd(L-1)₃, Nd(L-3)₃ and Nd(L-4)₃, respectively while figure 4.35 (b), (d) and (f) shows the corresponding truncated luminescence lifetime data and fit. All the Nd³⁺ samples with ligands L-1, L-3 and L-4 require part of the luminescence lifetime data to be truncated to obtain a reasonably good fit. However, all the luminescence lifetime data of Nd³⁺ samples with L-2 ligand can be fitted without any modifications (Figure 4.36). Data points that were truncated were highlighted in green in figure 4.35.

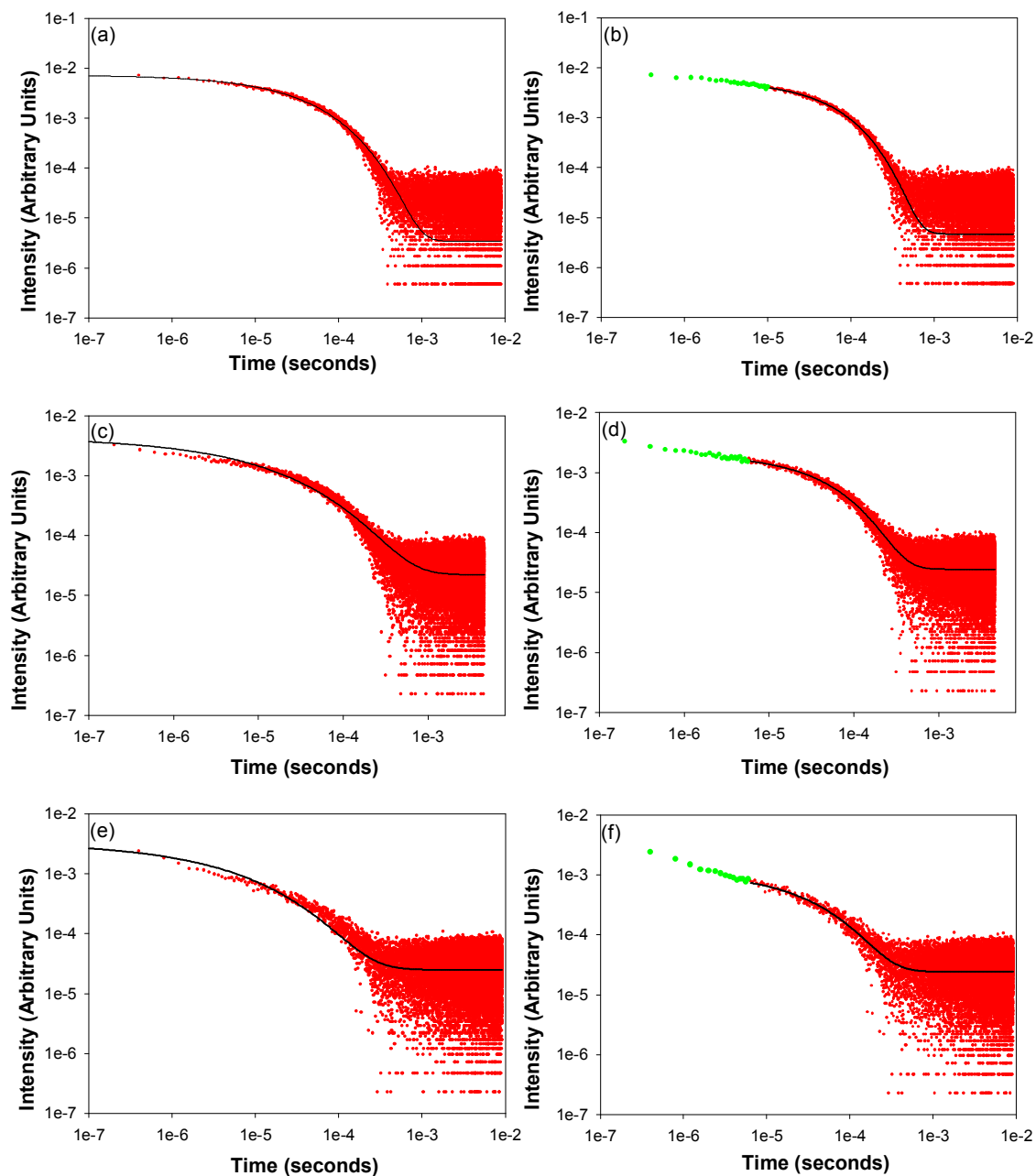


Figure 4.35 : Luminescence lifetime data and fit of 100% (a) Nd(L-1)_3 before truncation, (b) Nd(L-1)_3 after truncation, (c) Nd(L-3)_3 before truncation, (d) Nd(L-3)_3 after truncation, (e) Nd(L-4)_3 before truncation and (f) Nd(L-4)_3 after truncation

The truncated data revealed a fast lifetime component of the order of nanoseconds and it suggests that two or more different species of metal complexes are present

in these Nd³⁺ samples. Glover *et al*¹² reported the presence of a MeOH molecule in the crystal structure of $\{[(C_6F_5)_2P(O)]_2N\}_3Nd$. Despite the absence of any high energy vibrational bonds in the infrared spectrum of our Nd(L-1)₃, Nd(L-3)₃ and Nd(L-4)₃ samples, it is conceivable that solvent molecules have been coordinated to the Nd³⁺ ion, giving rise to the fast component that we observed in the luminescence lifetime data (Figure 4.35). Recall our discussions in chapter 2 that lifetimes in the nanosecond region are attributed to H₂O or solvent coordination on the Ln³⁺ ions.

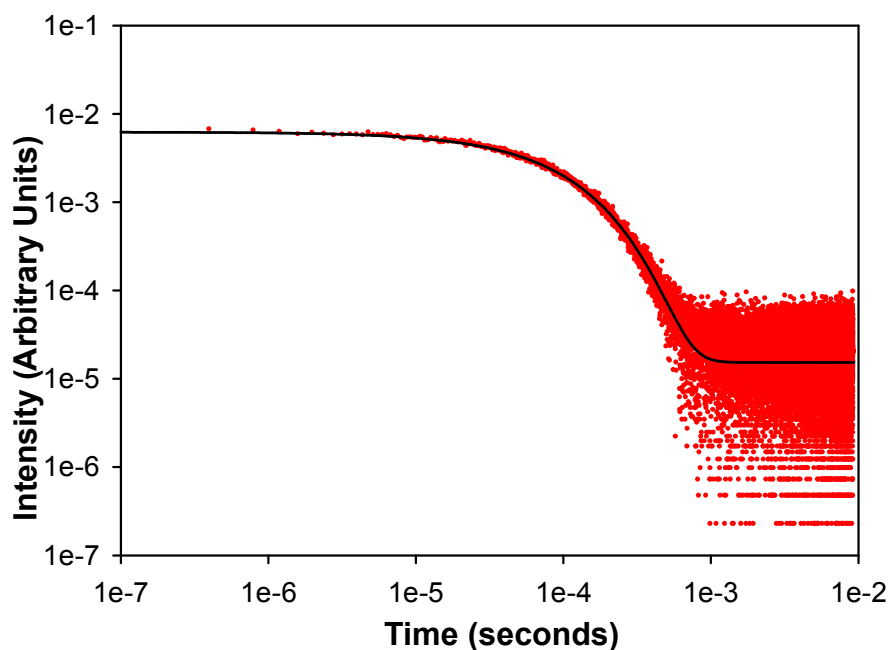


Figure 4.36 : Luminescence lifetime data and fit of 100% Nd(L-2)₃

Figure 4.36 shows the luminescence lifetime data and fit of 100% Nd(L-2)₃ and as can be seen, all the data points can be fitted using a stretched exponential function. The absence of any fast component in our Nd(L-2)₃ samples may be due to the fact that the CF₃ group on the para position of the aryl group has provided steric hindrance for any solvent molecules to be coordinated.

Average lifetimes at ~876 nm and ~1056 nm are identical and in this thesis, only the lifetimes of the ~1056 nm emission are presented. To illustrate the similarities,

table 4.10 shows the average lifetimes and figure 4.37 shows the luminescence lifetime data and fits of two different Nd³⁺ samples measured.

Compound	Lifetime of ${}^4F_{3/2} \longrightarrow {}^4I_{11/2}$ transition	Decay data	Lifetime of ${}^4F_{3/2} \longrightarrow {}^4I_{9/2}$ transition	Decay data
Nd(L-4) ₃ (100% Nd)	54 μs (1055 nm)	Figure 4.37 (a)	55 μs (878 nm)	Figure 4.37 (b)
Nd(L-3) ₃ (97% Nd)	49 μs (1058 nm)	Figure 4.37 (c)	50 μs (876 nm)	Figure 4.37 (d)

Table 4.10 : Average lifetime data for comparisons between ${}^4F_{3/2} \longrightarrow {}^4I_{11/2}$ and ${}^4F_{3/2} \longrightarrow {}^4I_{9/2}$ transitions

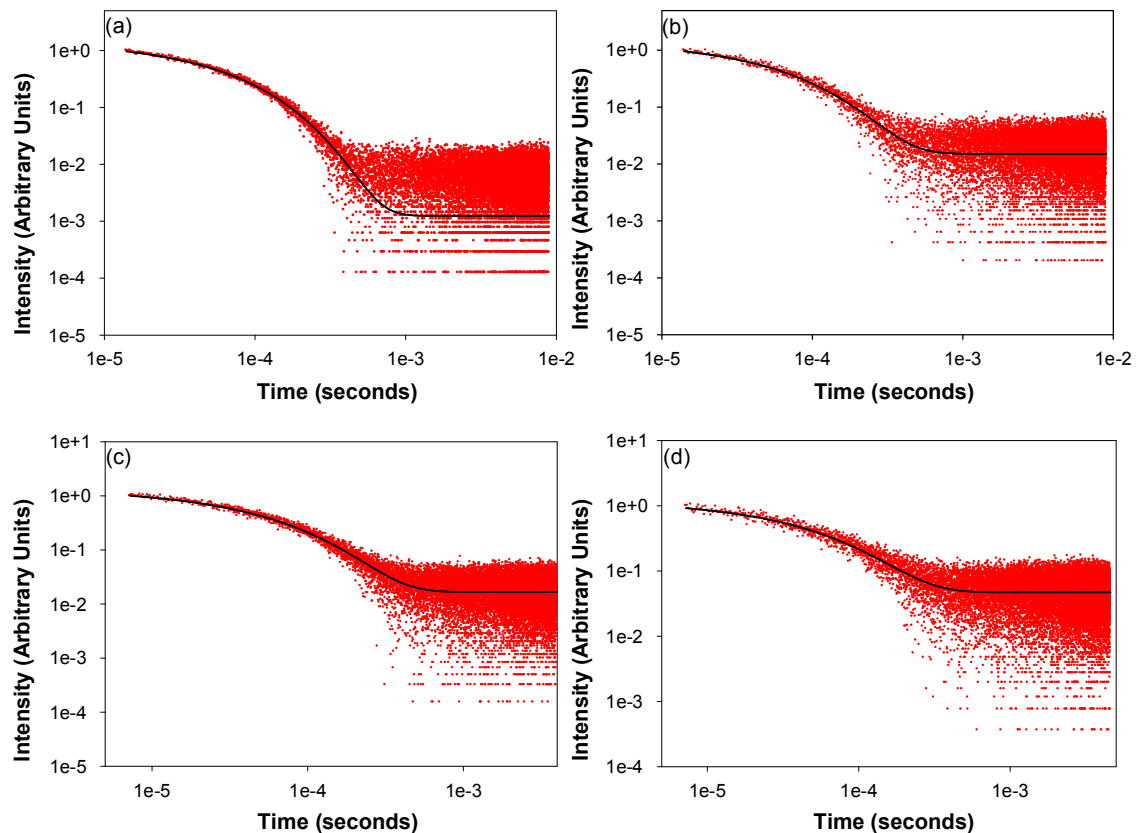


Figure 4.37 : Luminescence lifetime data and fit of (a) $\text{Nd(L-4)}_3 \text{ } ^4\text{F}_{3/2} \longrightarrow \text{}^4\text{I}_{11/2}$,
 (b) $\text{Nd(L-4)}_3 \text{ } ^4\text{F}_{3/2} \longrightarrow \text{}^4\text{I}_{9/2}$, (c) $\text{Nd}_{0.97}\text{Y}_{0.03}(\text{L-3})_3 \text{ } ^4\text{F}_{3/2} \longrightarrow \text{}^4\text{I}_{11/2}$ and
 (d) $\text{Nd}_{0.97}\text{Y}_{0.03}(\text{L-3})_3 \text{ } ^4\text{F}_{3/2} \longrightarrow \text{}^4\text{I}_{9/2}$ transitions

It can be seen from figure 4.37 that the luminescence data for the two transitions of Nd^{3+} are similar and that can be attributed to the fact that the NIR emission originates from the same energy level, $\text{}^4\text{F}_{3/2}$. The average lifetimes, β values and quantum yields of 100% Nd^{3+} samples are presented in table 4.11. These average lifetimes have an error of $\pm 15\%$.

Entry	Complex	Average lifetime	$\eta(\%)$	β value	Peak emission
1	Nd(L-1) ₃	38 μ s	15.2	0.60	1052 nm
2	Nd(L-2) ₃	76 μ s	30.4	0.92	1058 nm
3	Nd(L-3) ₃	45 μ s	18.0	0.77	1058 nm
4	Nd(L-4) ₃	54 μ s	21.6	0.74	1055 nm
5	Nd(L-5) ₃	1.36 μ s	0.5	0.50	1056 nm

Table 4.11 : Average lifetimes, β values and quantum yields of 100% Nd(L-1)₃, Nd(L-2)₃, Nd(L-3)₃, Nd(L-4)₃ and Nd(L-5)₃

From table 4.11, it can be seen that the average lifetimes of the 100% Nd³⁺ fluorinated complexes are in the region of between 38 μ s for Nd(L-1)₃ and 76 μ s for Nd(L-2)₃. They are also similar to those obtained for $\{[(C_6F_5)_2P(O)]_2N\}_3Nd$ with a lifetime of 46 μ s.¹² From our earlier work, Cs[Nd(HFA)]₄ has a major exponential lifetime of 1.65 μ s (92%) and a 8% contribution of 0.40 μ s. For a 98% deuterated Cs[Nd(HFA-*d*)]₄ sample, lifetimes of 4.20 μ s (96%) and 0.70 μ s (4%) were achieved. To compare the detrimental effects of the presence of high vibrational oscillators such as C–H bonds, Nd(L-5)₃ was measured. Similarly, about 30 data points had to be deleted before a fit with an average lifetime of 1.36 μ s and a β value of 0.50 could be obtained. This short average lifetime, which can be attributed to nonradiative decay pathways through the high vibrational energy C–H bonds, is identical to that obtained for $\{[(C_6H_5)_2P(O)]_2N\}_3Nd$ where a lifetime of 1.2 μ s is obtained in the solid state.¹³

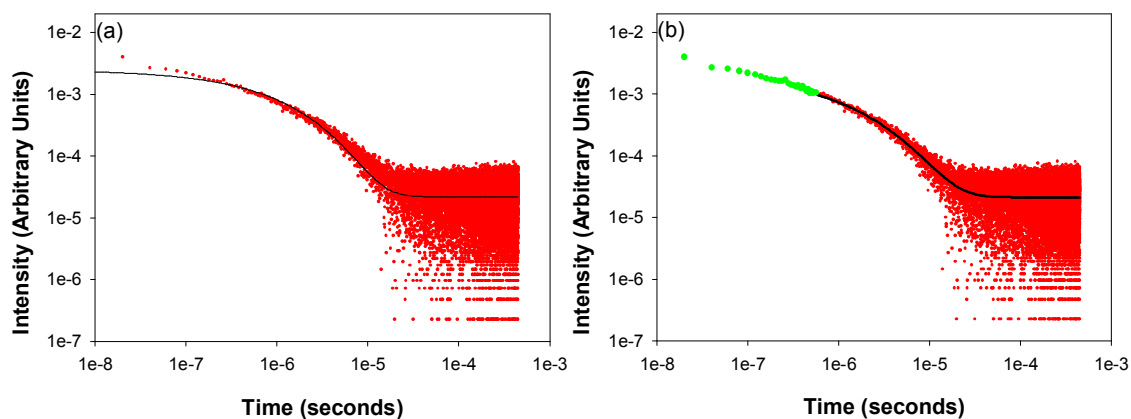


Figure 4.38 : Luminescence lifetime data and fit for 100% (a) Nd(L-5)_3 before any truncation and (b) after 30 points have been deleted

Figure 4.38 (a) shows the luminescence lifetime data and fit for 100% Nd(L-5)_3 before any truncation and figure 4.38 (b) shows the fit when 30 data points have been deleted. The truncated data are highlighted in green in figure 4.38.

The fact that these Nd^{3+} samples with L-1, L-3, L-4 and L-5 cannot be fitted using a single exponential fit suggests that there exists a number of different lifetimes and the Nd^{3+} ions are not in equivalent sites. Although the removal of high energy vibrational oscillators has improved the lifetimes by greater than an order of magnitude, the β values for all the samples are below unity and that implies that other quenching processes are involved in suppressing the luminescence lifetimes.

Assuming a natural lifetime of 0.25 ms,⁵¹ these Nd^{3+} fluorinated phosphinates demonstrate quantum yields of 15.2%, 30.4%, 18.0% and 21.6% for Nd(L-1)_3 , Nd(L-2)_3 , Nd(L-3)_3 and Nd(L-4)_3 , respectively. Although the long average lifetimes can be attributed to the exclusion of solvent molecules by the bulky ligands and the lower energy C–F bonds, the low quantum yields suggest that other quenching mechanisms are still present. Earlier, we discussed that these Ln^{3+} complexes have the tendency to interact with each other and that leads to lower quantum yield and efficiency. The only way to prevent this from occurring is to keep the luminescent centres apart and in the following section, we do this by diluting the Nd^{3+} complexes with Y^{3+} . Y^{3+} is optically inert and does not interact chemically with Nd^{3+} .

4.9.1 Effects of diluted Nd^{3+} samples

Ten Nd^{3+} samples were diluted with Y^{3+} and the results are shown in table 4.12. Average lifetimes shown in table 4.12 have an error of $\pm 15\%$ and have been calculated using the β values and equation 2. These samples are presented in the form, $\text{Nd}_x\text{Y}_{1-x}(\text{L-1} - \text{L-4})_3$, where x is the Nd^{3+} concentration, expressed as a percentage.

Each of these samples is excited at 420 nm to provide direct excitation into the $^2\text{P}_{1/2}$ level of the Nd^{3+} ion which rapidly decays to the $^4\text{F}_{3/2}$ level. Unlike the Er^{3+} samples, these samples have very fast rise times and could not be fitted with equation 8. Figure 4.39 is a representation of the rise time data observed for Nd^{3+} samples.

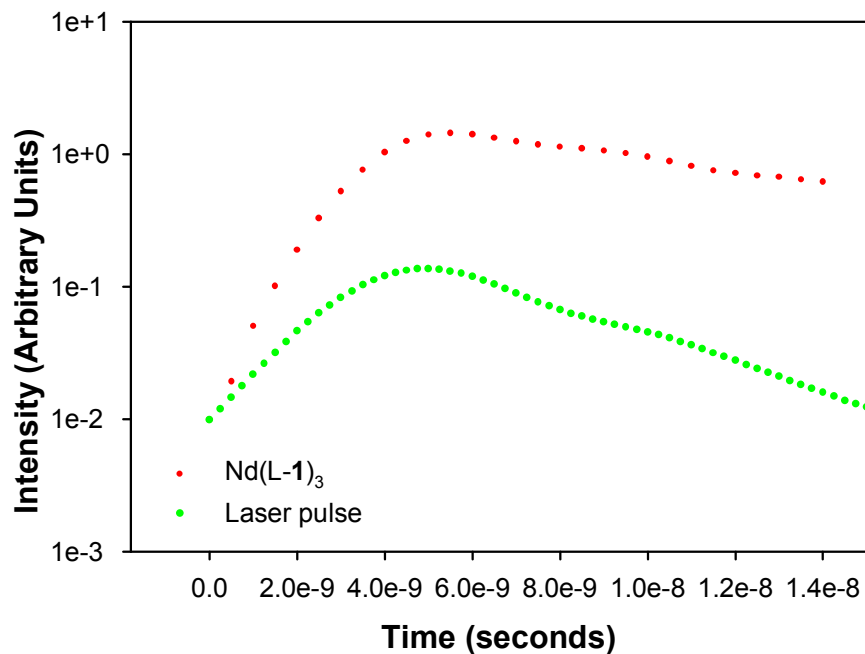


Figure 4.39 : Rise time data of $\text{Nd}(\text{L-1})_3$

It can be observed from figure 4.39 that the rise time of the $\text{Nd}(\text{L-1})_3$ sample is almost identical to that of the laser pulse. This implies that upon excitation of the

Nd^{3+} ions, they rapidly decay to the emitting level ${}^4\text{F}_{3/2}$ level and the decay time is in the order of a few nanoseconds and is comparable to that of the laser pulse.

Sample	Neodymium concentrations									
	100%	97%	93%	90%	85%	80%	70%	50%	30%	10%
$\text{Nd}_x\text{Y}_{1-x}(\text{L-1})_3$										
Lifetime (μs)	38	42	46	49	46	53	63	67	68	85
η (%)	15.2	16.8	18.4	19.6	18.4	21.2	25.2	26.8	27.2	34.0
β	0.60	0.59	0.61	0.62	0.58	0.60	0.56	0.54	0.54	0.58
$\text{Nd}_x\text{Y}_{1-x}(\text{L-2})_3$										
Lifetime (μs)	76	81	91	99	103	101	117	132	132	154
η (%)	30.4	32.4	36.4	39.6	41.2	40.4	46.8	52.8	52.8	61.6
β	0.92	0.91	0.87	0.91	0.92	0.88	0.90	0.89	0.85	0.87
$\text{Nd}_x\text{Y}_{1-x}(\text{L-3})_3$										
Lifetime (μs)	45	49	51	50	63	69	68	93	100	114
η (%)	18.0	19.6	20.4	20.0	25.2	27.6	27.2	37.2	40.4	45.6
β	0.77	0.69	0.73	0.67	0.82	0.79	0.73	0.72	0.78	0.71
$\text{Nd}_x\text{Y}_{1-x}(\text{L-4})_3$										
Lifetime (μs)	54	63	67	69	74	78	80	99	106	130
η (%)	21.6	25.2	26.8	27.6	29.6	31.2	32.0	39.6	42.4	52.0
β	0.74	0.78	0.73	0.77	0.79	0.74	0.75	0.74	0.75	0.79

Table 4.12 : Average lifetimes, β values and quantum yields of diluted Nd^{3+} samples

The rise times and decay lifetimes for $\text{Nd}_x\text{Y}_{1-x}(\text{L-1})_3$, $\text{Nd}_x\text{Y}_{1-x}(\text{L-2})_3$, $\text{Nd}_x\text{Y}_{1-x}(\text{L-3})_3$ and $\text{Nd}_x\text{Y}_{1-x}(\text{L-4})_3$ were measured at 1052 nm, 1058 nm, 1058 nm and 1055 nm, respectively. From table 4.12, it can be seen that the average lifetimes increase with decreasing Nd^{3+} concentration and this implies concentration quenching is prevalent among Nd^{3+} ions in organic hosts. Unlike Er^{3+} , none of the Nd^{3+} samples have β values of unity and no specific trends can be observed in the β values across the range of Nd^{3+} samples.

Comparing the β values, it can be seen that $\text{Nd}_x\text{Y}_{1-x}(\text{L-1})_3$ samples have the lowest β values in the region of ~ 0.60 and $\text{Nd}_x\text{Y}_{1-x}(\text{L-2})_3$ samples have the highest β values in the region of ~ 0.90 . However, within each family of samples, the β values are in the same region.

Based on the quantum yields ($\eta\%$) presented in table 4.12, and taking into considerations the lowest and highest values within each family, the effects of dilution have more than doubled the quantum efficiencies. The $\text{Nd}_x\text{Y}_{1-x}(\text{L-3})_3$ samples show the largest improvement (153%).

The average lifetimes plots for all the samples are plotted and shown in figure 4.40. Figure 4.40 (a) is the average lifetime plot for $\text{Nd}_x\text{Y}_{1-x}(\text{L-1})_3$, figure 4.40 (b) is for $\text{Nd}_x\text{Y}_{1-x}(\text{L-2})_3$, figure 4.40 (c) is for $\text{Nd}_x\text{Y}_{1-x}(\text{L-3})_3$ and figure 4.40 (d) is for $\text{Nd}_x\text{Y}_{1-x}(\text{L-4})_3$.

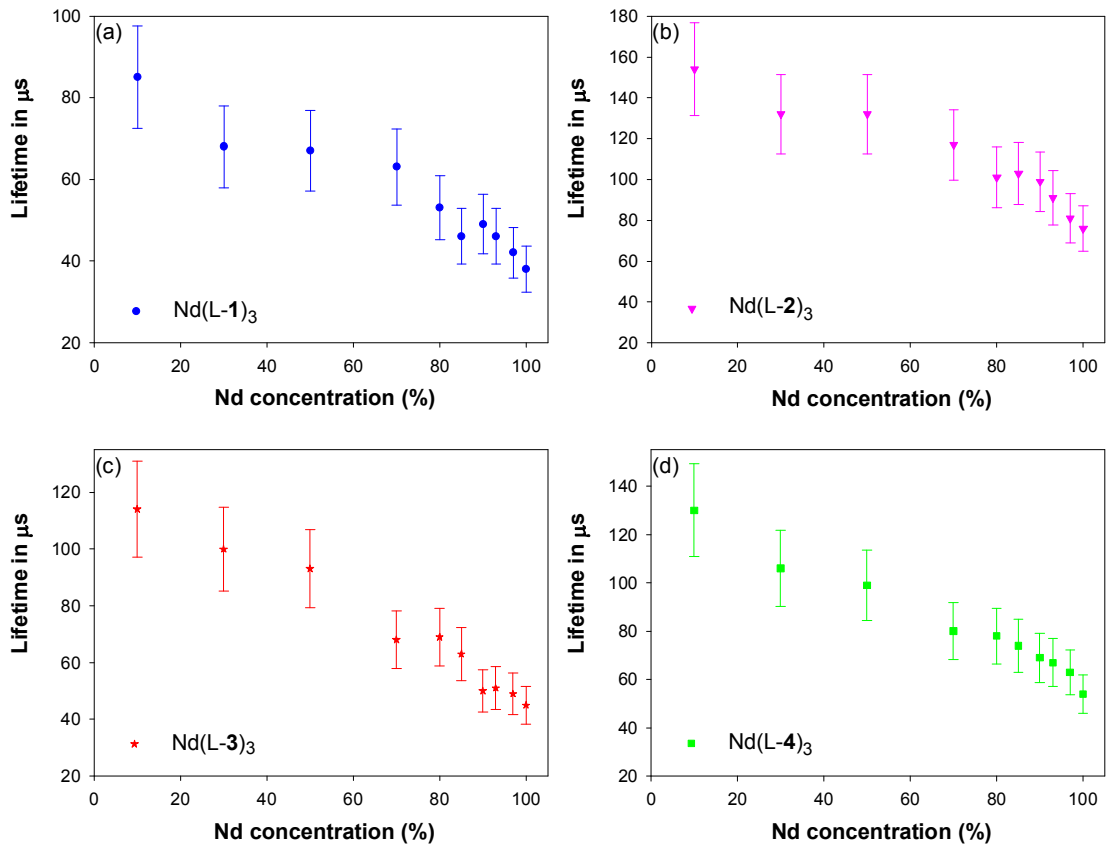


Figure 4.40 : Nd^{3+} concentration v lifetime plots for (a) $\text{Nd}_x\text{Y}_{1-x}(\text{L-1})_3$, (b) $\text{Nd}_x\text{Y}_{1-x}(\text{L-2})_3$, (c) $\text{Nd}_x\text{Y}_{1-x}(\text{L-3})_3$ and (d) $\text{Nd}_x\text{Y}_{1-x}(\text{L-4})_3$

Each data point on the figure has an error of $\pm 15\%$. All the plots in figure 4.40 demonstrate similar shapes whereby the average lifetimes increase with decreasing Nd^{3+} concentrations. Xiao *et al*³¹ observed upconversion luminescence at the region from 399 nm – 585 nm in the Nd^{3+} -doped crystalline silicon samples when they were excited at 700 nm. For our Nd^{3+} samples, no upconversion luminescence could be detected under similar conditions. Therefore, it can be assumed that energy migration or cross relaxation is the dominant concentration-dependent process. Unlike our Er^{3+} samples, the lifetimes at concentrations of 30% and below are not constant. However, the rate of change of lifetime does change at concentrations of about 80%. For all the Nd^{3+} samples, the β values remained below 1 and that implies the presence of a range of lifetimes, even at low Nd^{3+} concentrations. This may suggest that for Nd^{3+} , a neighbouring Nd^{3+} ion that is further away has greater quenching effect, relative to Er^{3+} .

Figure 4.41 shows a combined plot of all the different diluted Nd^{3+} samples against average lifetimes.

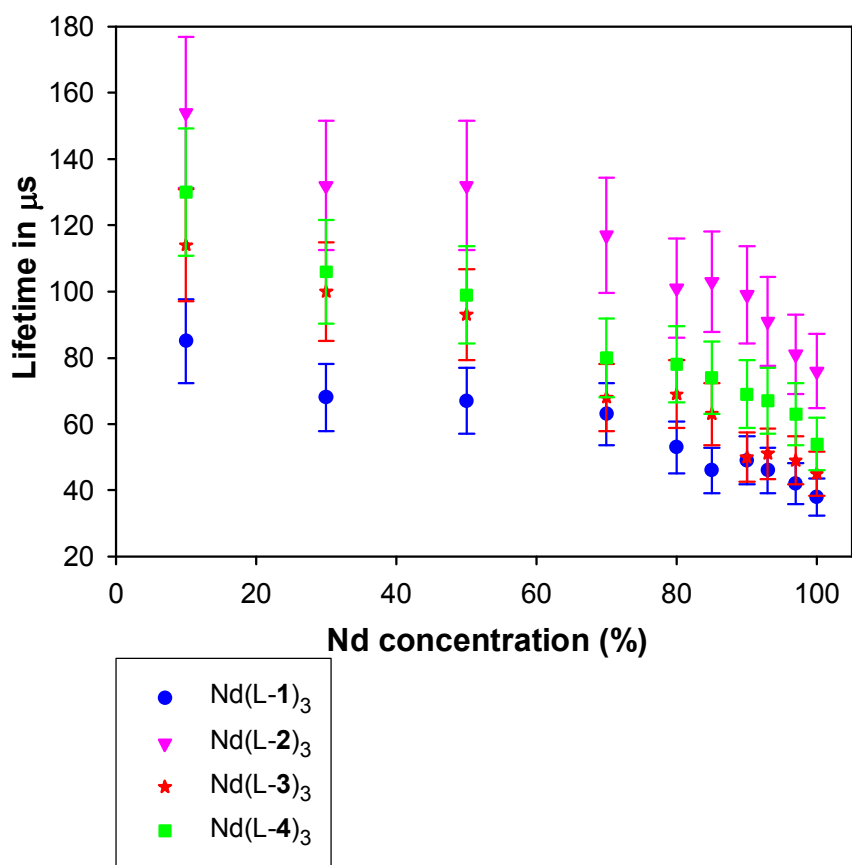


Figure 4.41 : Combined Nd^{3+} concentration ν lifetime plots of all the different diluted Nd^{3+} samples

From figure 4.41, it can be seen that the average lifetimes of each family of samples differ from one another, with the $\text{Nd}_x\text{Y}_{1-x}(\text{L-2})_3$ samples demonstrating the longest average lifetimes followed by $\text{Nd}_x\text{Y}_{1-x}(\text{L-4})_3$, $\text{Nd}_x\text{Y}_{1-x}(\text{L-3})_3$, and $\text{Nd}_x\text{Y}_{1-x}(\text{L-1})_3$. Since fitting the $\text{Nd}_x\text{Y}_{1-x}(\text{L-2})_3$ decay curves does not require any data to be truncated, it might account for the longest average lifetimes recorded. By looking at table 4.12, it can be observed that $\text{Nd}_x\text{Y}_{1-x}(\text{L-2})_3$ samples have the highest β values. The highest β values suggest that this family of samples demonstrate the least stretching and hence minimal energy migration which may be a contributing factor to the long radiative lifetimes. One possible explanation for this is that the bulky CF_3 group on L-2 provides a steric hindrance that prevents any solvent coordination and that limits the freedom of the excitation energy migration in these Nd^{3+} samples with the effect of longer luminescence lifetimes. Recall our earlier discussions in chapter 2 on the partially deuterated Nd^{3+} samples where we

concluded that Nd^{3+} are very sensitive to their surroundings. If solvent molecules are being coordinated to Nd^{3+} complexes with ligands L-1, L-3 and L-4, their sensitivity may account for the relatively lower average lifetimes than those with ligand L-2. Therefore, for the $\text{Nd}_x\text{Y}_{1-x}(\text{L-1})_3$, $\text{Nd}_x\text{Y}_{1-x}(\text{L-3})_3$ and $\text{Nd}_x\text{Y}_{1-x}(\text{L-4})_3$ samples, there seems to be two effects which affect the radiative lifetimes; quenching via solvent molecules (C–H bonds) and quenching via energy migration. These two effects might explain the fact that β is never 1.

It can be seen that $\text{Nd}_x\text{Y}_{1-x}(\text{L-1})_3$ samples have the shortest average lifetimes and by inspecting table 4.12, they exhibited the lowest β values. Lower β values are an indication that more stretching takes place which suggests that there is a greater tendency for the excitation energy to migrate from one site to another. Excessive migration of excitation energy leads to lower radiative lifetimes and less efficient quantum yields. It must be mentioned that the β values of the $\text{Nd}_x\text{Y}_{1-x}(\text{L-4})_3$ and $\text{Nd}_x\text{Y}_{1-x}(\text{L-3})_3$ samples are similar.

Based on the results seen in figure 4.41, it seems to suggest that the size of ligands for Nd^{3+} samples play a more significant role than that of Er^{3+} samples in varying the effects of ion-ion interaction. Due to the increment of the fluorinated phenyl groups, it can be assumed that the size of the ligands increase in the following order, L-4 > L-3 > L-1. Looking at figure 4.41 it can be seen that the lifetime curves are consistent with this argument where the average lifetimes of $\text{Nd}_x\text{Y}_{1-x}(\text{L-4})_3 > \text{Nd}_x\text{Y}_{1-x}(\text{L-3})_3 > \text{Nd}_x\text{Y}_{1-x}(\text{L-1})_3$.

Although the absolute lifetimes of Nd^{3+} in these organic hosts has not been determined, these set of results allow us to provide an upper limit to the Nd^{3+} concentration that can be utilized in a device based on these materials.

4.10 Photoluminescence studies of Yb³⁺ phosphinate complexes

Figure 4.42 shows the emission spectra of 100% Yb³⁺ samples excited at 460 nm at 300 K. From these spectra, it can be observed that Yb³⁺ exhibits an emission at 980 nm corresponding to the $^2F_{5/2} \longrightarrow ^2F_{7/2}$ transition.²⁰ To collect the luminescence lifetime data, these samples were excited at 960 nm and the emission was measured through a 980 nm interference filter. Only weak emissions were observed for Yb(L-1)₃ samples and the results have not been included in this thesis.

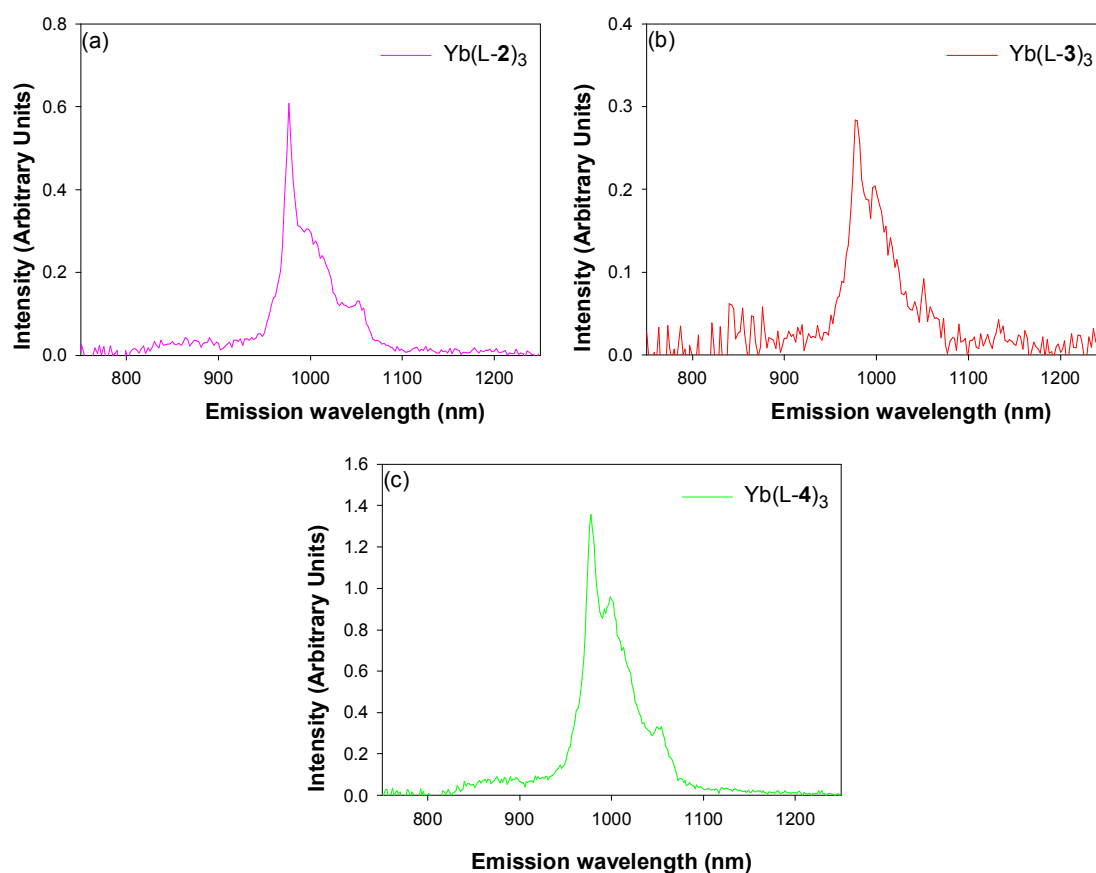


Figure 4.42 : Emission spectra of 100% (a) Yb(L-2)₃, (b) Yb(L-3)₃ and (c) Yb(L-4)₃

For all the Yb³⁺ samples, the main peak is centred at 980 nm. However, due to Stark^{20,49} splitting, other peaks can be observed. For Yb(L-2)₃ (Figure 4.42 (a)), one other peak can be seen at 1051 nm. Figure 4.42 (b) shows the emission

spectrum of Yb(L-3)_3 and another sharp feature can be observed at 998 nm. Peaks at 998 nm and 1032 nm can be observed for Yb(L-4)_3 (Figure 4.42 (c)).

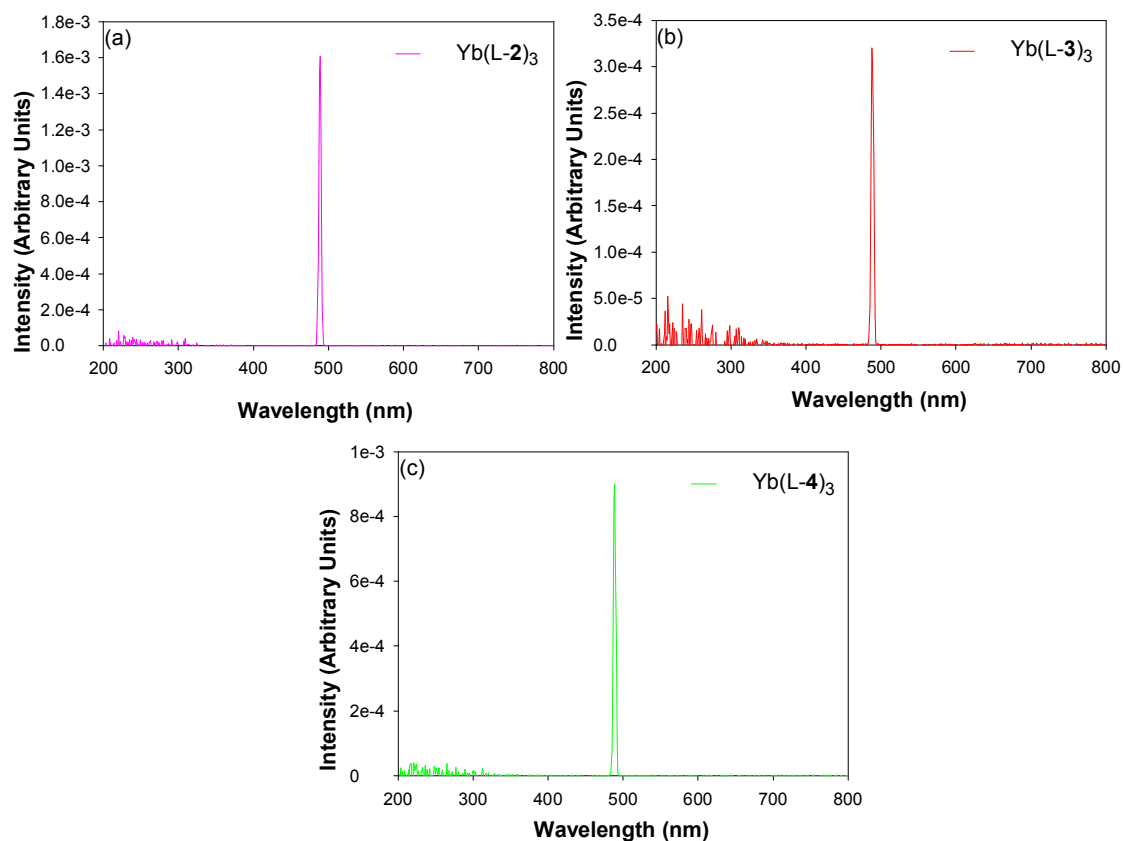


Figure 4.43 : Excitation spectra of 100% (a) Yb(L-2)_3 , (b) Yb(L-3)_3 and (c) Yb(L-4)_3

Figure 4.43 (a), (b) and (c) shows the excitation spectra at the peak emission wavelength of ~ 980 nm of 100% Yb(L-2)_3 , Yb(L-3)_3 and Yb(L-4)_3 , respectively. All the spectra are identical with a peak at 489 nm. The detector wavelength was at 980 nm and the signal at 489 nm was a consequence of the second order diffraction through the spectrometer. Weak signals can be seen between 200 and 300 nm, which correspond to the absorbance bands of the ligands discussed in section 4.6 (Figure 4.21). This implies that there is some sensitization of Yb^{3+} from the ligands.

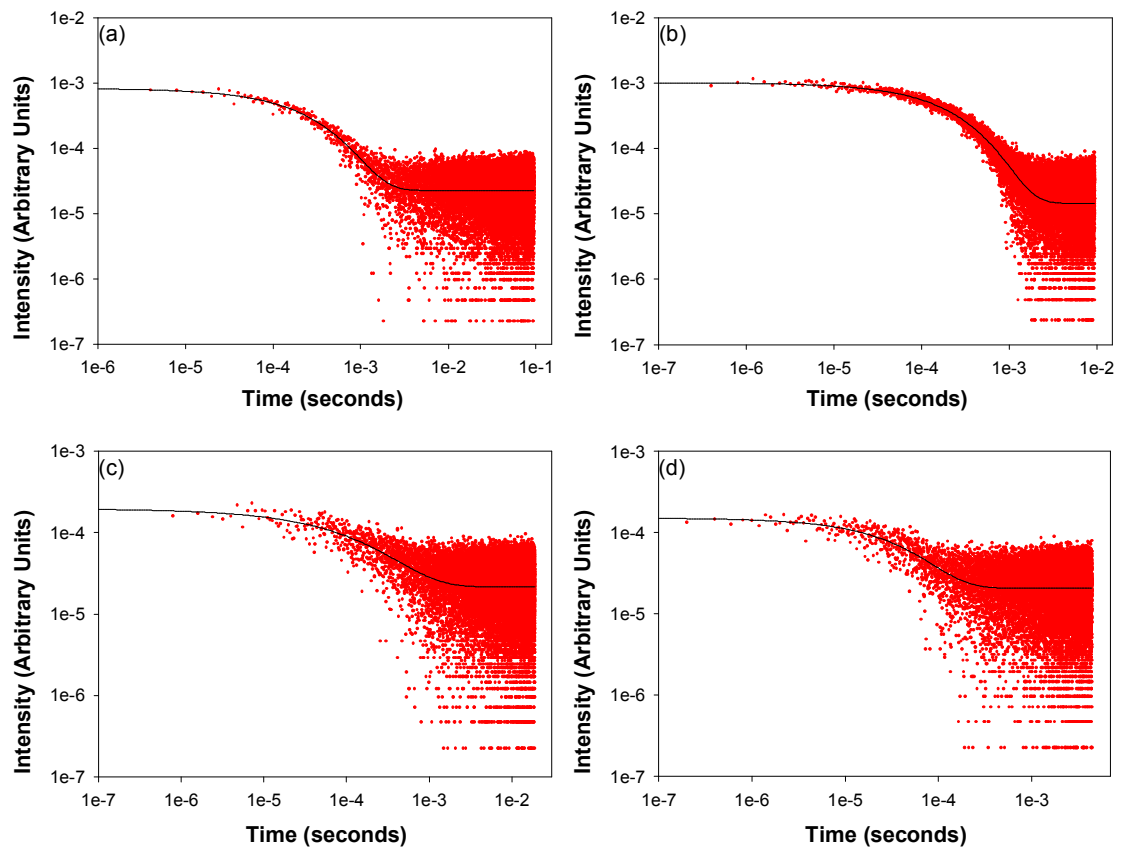


Figure 4.44 : Luminescence lifetime data and fit of 100% (a) Yb(L-2)_3 , (b) Yb(L-3)_3 , (c) Yb(L-4)_3 and (d) Yb(L-5)_3

Figure 4.44 shows the luminescence lifetime data and fit for 100% Yb(L-2)₃, Yb(L-3)₃, Yb(L-4)₃ and Yb(L-5)₃ at 980 nm, respectively. These samples cannot be fitted with a single exponential fit and a stretched exponential fit is used. The average lifetimes, β values and quantum yields are presented in table 4.13. These average lifetimes have an error of $\pm 15\%$.

Entry	Complex	Average lifetime	$\eta(\%)$	β value	Peak emission
1	Yb(L-2) ₃	287 μ s	14.4	0.72	980 nm
2	Yb(L-3) ₃	242 μ s	12.1	0.72	980 nm
3	Yb(L-4) ₃	201 μ s	10.1	0.54	980 nm
4	Yb(L-5) ₃	45 μ s	2.3	0.76	980 nm

Table 4.13 : Average lifetimes, β values and quantum yields of 100% Yb(L-2)₃, Yb(L-3)₃, Yb(L-4)₃ and Yb(L-5)₃

From table 4.13, it can be seen that the average lifetimes of the 100% Yb³⁺ fluorinated complexes are in the region of between 201 μ s for Yb(L-4)₃ and 287 μ s for Yb(L-2)₃. From our earlier work, Cs[Yb(HFA)]₄ has a single exponential lifetime of 22.6 μ s. For a 98% deuterated Cs[Yb(HFA-d)]₄ sample, a single lifetime of 289 μ s was achieved. To compare the detrimental effects of high vibrational oscillators such as C–H bonds, Yb(L-5)₃ is measured and an average lifetime of 45 μ s with a β value of 0.76 was achieved. This short lifetime can be attributed to nonradiative decay pathways through the high vibrational C–H bonds. Removal of high energy vibrational oscillators has improved the lifetimes by about an order of magnitude. C–F bonds have energy of 1200 cm⁻¹ and the emitting level of Yb³⁺ at ²F_{5/2} with an energy gap of 9700 cm⁻¹ is resonant with its 8th harmonic, rendering any high vibrational quenching less effective.

Assuming a natural lifetime of 2 ms,⁵¹ these fluorinated Yb³⁺ phosphinates demonstrate quantum yields of 14.4%, 12.1% and 10.1% for Yb(L-2)₃, Yb(L-3)₃ and Yb(L-4)₃, respectively. Although the long average lifetimes can be attributed to the exclusion of solvent molecules by the bulky ligands, the low quantum yields

suggest that other quenching mechanisms are still present. The β values obtained for these samples were below unity and that suggests that there is a distribution of lifetimes, which is indicative of ion-ion interactions. Earlier, we discussed that these Ln^{3+} complexes have the tendency to interact with each other and that leads to lower quantum yield and efficiency. The only way to prevent this from occurring is to keep the luminescent centres apart and in the following section, we do this by diluting the Yb^{3+} complexes with Y^{3+} .

4.10.1 Effects of diluted Yb^{3+} samples

Ten Yb^{3+} samples were diluted with Y^{3+} and the results are shown in table 4.14. Average lifetimes shown in table 4.14 have an error of $\pm 15\%$ and have been calculated using the β values and equation 7. These samples are presented in the form, $\text{Yb}_x\text{Y}_{1-x}(\text{L-2} - \text{L-4})_3$, where x is the Yb^{3+} concentration, expressed as a percentage.

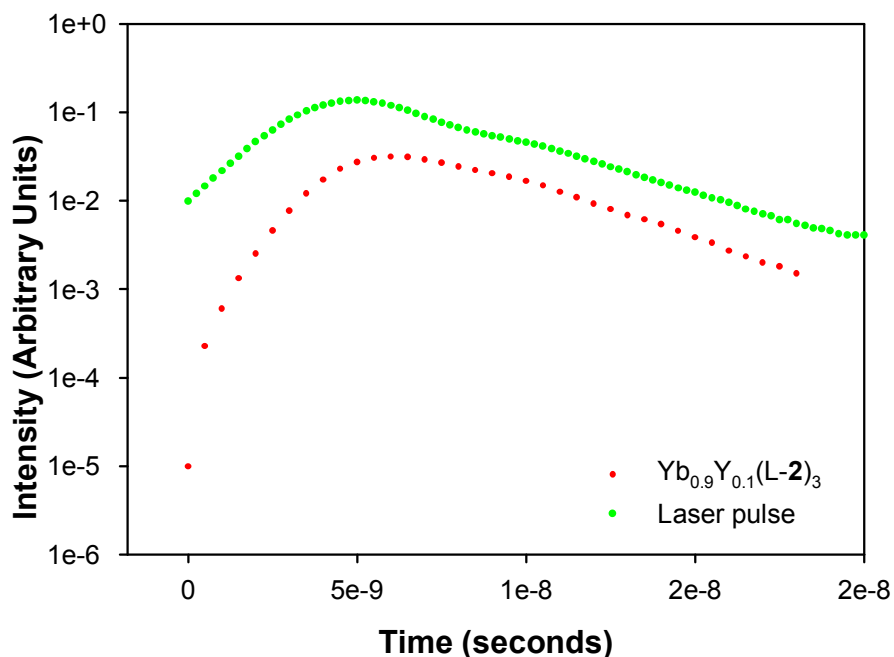


Figure 4.45 : Rise time data of $\text{Yb}_{0.9}\text{Y}_{0.1}(\text{L-2})_3$

Each of these samples is excited at 960 nm to provide direct excitation into the $^2F_{5/2}$ level of the Yb^{3+} ion. Consequently the rise times observed are the laser pulse shape. Figure 4.45 is a representation of the rise time data observed for Yb^{3+} samples.

Sample	Ytterbium concentrations									
	100%	97%	93%	90%	85%	80%	70%	50%	30%	10%
$Yb_xY_{1-x}(L-2)_3$										
Lifetime (μs)	287	540	598	375	590	1055	1080	1967	1723	
η (%)	14.4	27.0	29.9	18.8	29.5	52.8	54.0	98.4	86.2	
β	0.72	0.85	0.76	0.80	0.81	0.83	0.72	0.79	0.83	
$Yb_xY_{1-x}(L-3)_3$										
Lifetime (μs)	242	486	409	408	505	806	721	920	1223	1282
η (%)	12.1	24.3	20.5	20.4	25.3	40.3	36.1	46.0	61.2	64.1
β	0.72	0.83	0.72	0.76	0.76	0.79	0.81	0.74	0.79	0.77
$Yb_xY_{1-x}(L-4)_3$										
Lifetime (μs)	201	397	792	821	551	1103	1111	1362	1768	
η (%)	10.1	19.9	39.6	41.1	27.6	55.2	55.6	68.1	88.4	
β	0.54	0.67	0.71	0.65	0.70	0.73	0.79	0.78	0.90	

Table 4.14 : Average lifetimes, β values and quantum yields of diluted Yb^{3+} samples

For all the Yb^{3+} samples, the emissions observed were weaker than those for Er^{3+} and Nd^{3+} . This is due to the fact that the energy of the laser at the excitation wavelength was an order of magnitude lower. The rise times and decay lifetimes of all the samples were measured at 980 nm. These Yb^{3+} samples have similar characteristics to those of Nd^{3+} in that they do not have any β values of unity and the β values do not follow any specific trends. This indicates that for all the Yb^{3+} samples in table 4.14, there is a distribution of lifetimes across each sample from the sites at the surface to the ions in the centre and from what we have seen for Er^{3+} and Nd^{3+} samples, that has the implication of energy migration between the

Yb^{3+} ions. Note that the emissions for the 10% Yb^{3+} concentration of $\text{Yb}_x\text{Y}_{1-x}(\text{L-2})_3$ and $\text{Yb}_x\text{Y}_{1-x}(\text{L-4})_3$ were very weak and the lifetimes are not presented here.

Based on the quantum yields ($\eta\%$) presented in table 4.14, and taking into considerations the lowest and highest values within each family, the effects of dilution have achieved improvements of $>100\%$ in quantum efficiencies. The $\text{Yb}_x\text{Y}_{1-x}(\text{L-2})_3$ samples have the best performance with an approximately six-fold improvement.

The average lifetime plots for all the samples are shown in figure 4.46.

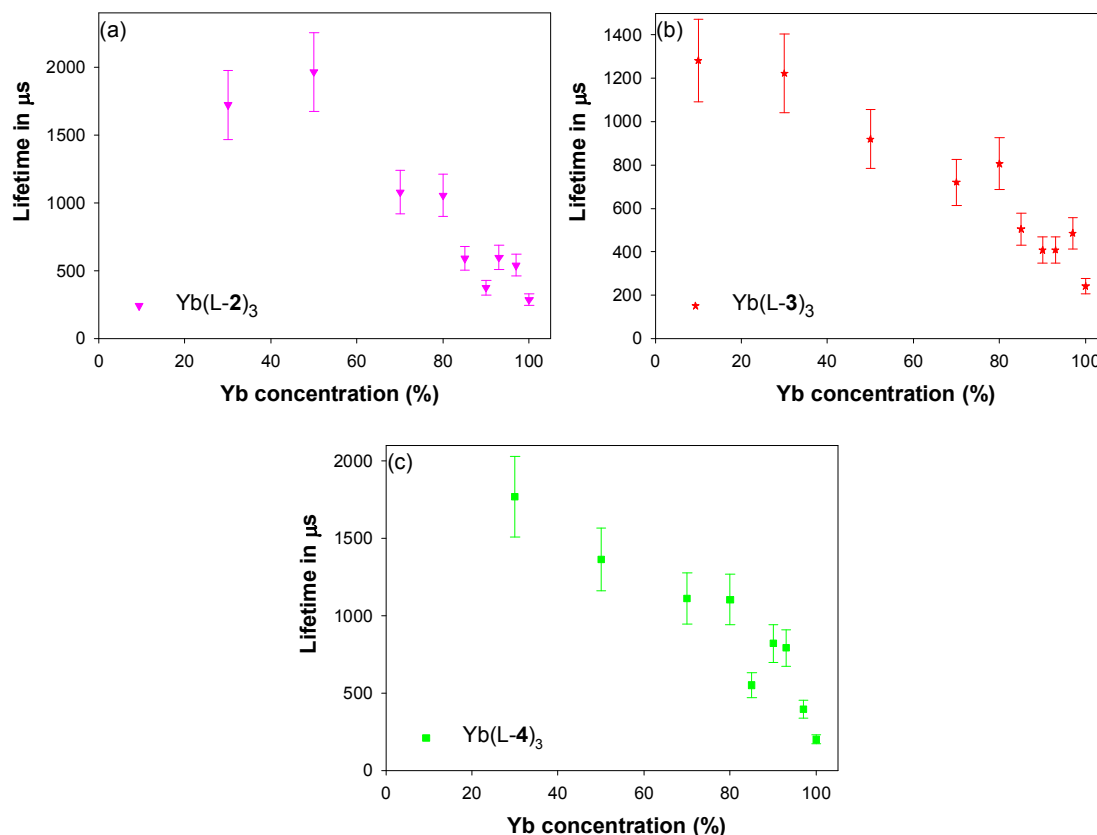


Figure 4.46 : Yb^{3+} concentration v lifetime plots for (a) $\text{Yb}_x\text{Y}_{1-x}(\text{L-2})_3$, (b) $\text{Yb}_x\text{Y}_{1-x}(\text{L-3})_3$ and (c) $\text{Yb}_x\text{Y}_{1-x}(\text{L-4})_3$

Each data point has an error of $\pm 15\%$. All the plots in figure 4.46 demonstrate a different behaviour to those for the Er^{3+} samples in that the average lifetimes do not seem to saturate at a particular concentration. Even at 30% Yb^{3+}

concentration, the average lifetime appears to be still increasing and that indicates that the luminescence centres are not emitting independently. From our data in figure 4.46, it suggests that relative to Er^{3+} , an Yb^{3+} ion is able to interact with one another over greater distances. This suggest that even at 30% Yb^{3+} concentration, the excitation energy of Yb^{3+} ions is still migrating and is consistent with the findings of Xu *et al*³². They reported that the 4f electrons of Yb^{3+} have a relatively strong interaction with their surroundings and the interactions between the 4f¹³ configurations of neighbouring Yb^{3+} ions is stronger than those of other Ln^{3+} ions. This implies that an Yb^{3+} ion is able to interact with another which is further away and that increases the likelihood of finding a quenching centre. The increased sensitivity of Yb^{3+} ions may explain why the data plots in figure 4.46 are slightly more scattered and also why the β values are randomized.

Bell *et al*³³ reported on cooperative luminescence at around 500 nm in Yb^{3+} doped phosphate glasses under 980 nm excitation. No cooperative luminescence was detected for all our Yb^{3+} samples under the same conditions.

Figure 4.47 shows a combined plot of all the different diluted Yb^{3+} samples against the average lifetimes.

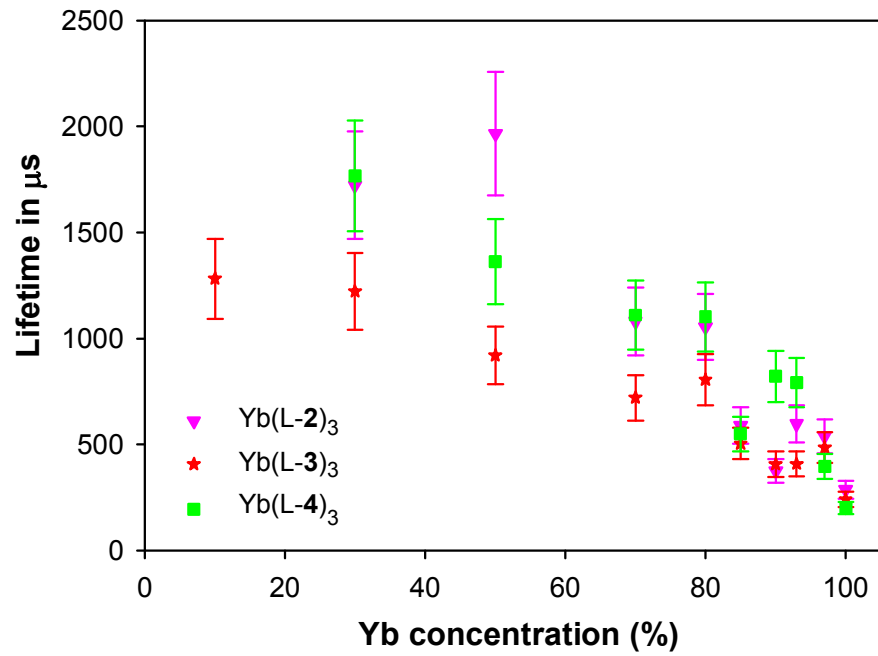


Figure 4.47 : Combined Yb³⁺ concentration v lifetime plots of all the different diluted Yb³⁺ samples

From figure 4.47, it can be seen that the average lifetimes of the Yb_xY_{1-x}(L-3)₃ samples are generally the lowest and the Yb_xY_{1-x}(L-2)₃ and Yb_xY_{1-x}(L-4)₃ samples have similar lifetimes.

4.11 Conclusions for chapter 4

In this chapter, we saw the advantages of eliminating high energy vibrational oscillators from the ligands that were coordinated to Er^{3+} , Nd^{3+} and Yb^{3+} ions. These fluorinated complexes demonstrated lifetime improvements by at least an order of magnitude over their non fluorinated analogues. Of all the 100% Ln^{3+} samples measured, the highest quantum efficiencies achieved were 4.5%, 30.4% and 14.4% for Er^{3+} , Nd^{3+} and Yb^{3+} , respectively. The rise times of Er^{3+} complexes were found to be $\sim 0.5 \mu\text{s}$ while for the Nd^{3+} and Yb^{3+} complexes, they were in the nanosecond region.

Diluting these samples with Y^{3+} is a way of suppressing concentration quenching, which is related to the interionic distance between centres. We saw for all the Er^{3+} , Nd^{3+} and Yb^{3+} samples that as the concentration of the emitting ions decreases, the decay lifetime increases. This is due to the fact that the interionic distances between emitting centres are bigger at lower Er^{3+} , Nd^{3+} and Yb^{3+} concentrations and that eliminates concentration quenching effects. No upconversion was detected for all our samples and energy migration is the dominant concentration quenching effect. For Er^{3+} samples, the best quantum efficiency achieved was 9.7% for a 10% $\text{Er}(\text{L-1})_3$. We also saw that the different ligands did not greatly affect the luminescence lifetimes and this can be attributed to one dimensional quenching. At high Er^{3+} concentration of $>80\%$, the average lifetime plots were steep, relative to the lower concentrations and that implies that at high Er^{3+} concentrations, the emitting ions were most sensitive to their neighbours. Luminescence lifetimes reached a saturation point at 30% Er^{3+} concentration and that suggests that the emitting ions are at an optimal distance apart and each emitting ion is not affected by any concentration quenching effect. The unity β values at low concentrations also imply the suppression of any ion-ion interactions.

To achieve reasonable lifetime fits for all the Nd^{3+} samples, except those with ligand, L-2, about 30 - 40 data points have to be truncated. We suspect that in those cases, solvent molecules might have coordinated to the ion, giving rise to the fast component. For Nd^{3+} samples, the best quantum efficiencies were achieved for the $\text{Nd}_x\text{Y}_{1-x}(\text{L-2})_3$ samples with the top efficiency at 61.6% for the 10%

Nd(L-2)₃ sample. Unlike Er³⁺ samples, each family of diluted samples had different lifetimes. None of the β values reached unity and that implies ion-ion interactions were present, even at low concentrations. We saw that the luminescence lifetimes of each family increase in the following order, Nd_xY_{1-x}(L-2)₃ > Nd_xY_{1-x}(L-4)₃ > Nd_xY_{1-x}(L-3)₃ > Nd_xY_{1-x}(L-1)₃ and this suggests that the size of ligands had an effect on concentration quenching in Nd³⁺ samples. The β values were the lowest for Nd_xY_{1-x}(L-1)₃ samples and highest for Nd_xY_{1-x}(L-2)₃ samples.

Similar to the Nd³⁺ samples, none of the β values for the Yb³⁺ samples reached unity and the best quantum efficiencies were achieved for the Yb_xY_{1-x}(L-2)₃ and Yb_xY_{1-x}(L-4)₃ samples. We suspect that the excitation energy for Yb³⁺ samples migrate over a greater distance and that results in the increasing lifetimes, even at 30% Yb³⁺ concentrations.

We have shown that concentration quenching can be related to interionic distances and the results in this chapter allow us to achieve optimal emitting ion concentrations for future device applications.

4.12 References for chapter 4

1. Choi; K. M., *Materials Chemistry and Physics*, 103, **2007**, 176
2. Zhang; X. Z., Zhang; D. M., Mu; S. K., Zhang; D. and Chen; C., *Applied Physics B*, 86, **2007**, 677
3. Zheng; Z., Liang; H., Ming; H., Zhang; Q. and Xie; J., *Optics Communications*, 233, **2004**, 149
4. Lin; H., Meredith; G., Jiang; S., Peng; X., Luo; T., Peyghambarian; N. and Pun; E. Y., *Journal of Applied Physics*, 93, **2003**, 186
5. Koughia; K., Munzar; M., Tonchev; D., Haugen; C. J., Decorby; R. G., McMullin; J. N. and Kasap; S. O., *Journal of Luminescence*, 112, **2005**, 92
6. Wang; J. S., Snitzer; E., Vogel; E. M. and Sigel; J. G. H., *Journal of Luminescence*, **1994**, 60/61, 145
7. Zheng; Y., Motevalli; M., Tan; R. H. C., Abrahams; I., Gillin; W. P. and Wyatt; P. B., *Polyhedron*, 27, **2008**, 1503
8. Birchall; J. M., Haszeldine; R. N., Nikokavouras; J. and Wilks; E. S., *Journal of Chemical Society. C*, **1971**, 562
9. Mancino; G., Ferguson; A. J., Beeby; A., Long; N. J. and Jones; T. S., *Journal of the American Chemical Society*, 127, **2005**, 524
10. Magennis; S. W., Parsons; S. and Pikramenou; Z., *Chemistry - A European journal*, 8, **2002**, 5761
11. Magennis; S. W., Ferguson; A. J., Bryden; T., Jones; T. S., Beeby; A. and Samuel; I. D. W., *Synthetic Metals*, 138, **2003**, 463

12. Glover; P., Bassett; A. P., Nockemann; P., Kariuki; B. M., Van Deun; R. and Pikramenou; Z., *Chemistry A European Journal*, 13, **2007**, 6308
13. Bassett; A. P., Van Deun; R., Nockemann; P., Glover; P. B., Kariuki; B. M., Van Hecke; K., Van Meervelt; L. and Pikramenou; Z., *Inorganic Chemistry*, 44, **2005**, 6140
14. Brown; M. R., Thomas; H., Williams; J. M., Woodward; R. J. and Shand; W. A., *Journal of Chemical Physics*, 51, **1969**, 3321
15. Johnson; L. F., Guggenheim; H. J., Rich; T. C. and Ostermayer; F. W., *Journal of Applied Physics*, 43, **1972**, 1125
16. Miniscalco; W. J., *Journal of Lightwave Technology*, 9, **1991**, 234
17. Kenyon; A. J., *Progress in Quantum Electronics*, 26, **2002**, 225
18. Desurvire; E., *Erbium-Doped Fiber Amplifiers – Principles and Applications*, John Wiley & Sons, Inc, New York, **1994**
19. An; H. L., Pun; E. Y. B., Lin; X. Z. and Liu; H. D., *IEEE Photonics Technology Letters*, 11, **1999**, 803
20. Becker; P. C., Olsson; N. A. and Simpson; J. R., *Erbium-Doped Fiber Amplifiers – Fundamentals and Technology*, Academic press, San Diego, **1999**
21. Ainslie; B. J., *Journal of Lightwave Technology*, 9, **1991**, 220
22. Ainslie; B. J., Craig; S. P. and Davey; S. T., *Material Letters*, 5, **1987**, 143
23. Ainslie; B. J., Craig; S. P., Davey; S. T. and Wakefield; B., *Material Letters*, 6, **1988**, 139

24. Ainslie; B. J., Craig; S. P., Wyatt; R. and Moulding; K., *Material Letters*, 8, **1989**, 204
25. Arai; K., Namikawa; H., Kumata; K., Tatsutoku; H., Ishii; Y. and Handa; T., *Journal of Applied Physics*, 59, **1986**, 3430
26. Kagi; N., Oyobe; A. and Nakamura; K., *IEEE Photonics Technology Letters*, 2, **1990**, 559
27. Shimizu; M., Yamada; M., Horiguchi; M. and Sugita; E., *IEEE Photonics Technology Letters*, 2, **1990**, 43
28. Van der Ziel; J. P., Van Uitert; L. G., Grodkiewicz; W. H. and Mikulyak; R. M., *Journal of Applied Physics*, 60, **1986**, 4262
29. Whitley; T. J., Millar; C. A., Wyatt; R., Brierley; M. C. and Szebesta; D., *Electronic Letters*, 27, **1991**, 1785
30. Mita; Y., Yoshida; T., Yagami; T. and Shionoya; S., *Journal of Applied Physics*, 71, **1992**, 938
31. Xiao; Z., Cheng; G., Zhang; T. and Xu; F., *Surface and coatings Technology*, 128-129, **2000**, 461
32. Xu; X., Zhao; Z., Song; P., Jiang; B., Zhou; G., Xu; J., Deng; P., Bourdet; G., Chanteloup; J. C., Zou; J. and Fulop; A., *Physica B*, 357, **2005**, 365
33. Bell; M. J. V., Quirino; W. G., Oliveira; S. L., de Sousa; D. F. and Nunes; L. A. O., *Journal of Physics: Condensed Matter*, 15, **2003**, 4877
34. Schaudel; B., Goldner; P., Prassas; M. and Auzel; F., *Journal of Alloys and Compounds*, 300-301, **2000**, 443

35. Comby; S. and Bünzli; J-C. G., *Handbook on the Physics and Chemistry of rare earths*, 37, **2007**
36. Qiu; X., Yu; K., Gao; C., Hou; C., He; J., Zhou; Z., Wei; W. and Peng; B., *Chemical Physics Letters*, 457, **2008**, 194
37. Lin; S., Feuerstein; R. J. and Mickelson; A. J., *Journal of Applied Physics*, 79, **1996**, 2868
38. Yanagida; S., Hasegawa; Y., Murakoshi; K., Wada; Y., Nakashima; N. and Yamanaka; T., *Coordination Chemistry Reviews*, 171, **1998**, 461
39. Orignac; X., Barbier; D., Du; X. M., and Almeida; R. M., *Applied Physics Letters*, 69, **1996**, 895
40. Wong; W. H., Chan; K. S. and Pun; E. Y. B., *Applied Physics Letters*, 87, **2005**, 011103
41. Wong; W. H., Pun; E. Y. B. and Chan; K. S., *Applied Physics Letters*, 84, **2004**, 176
42. da Vila; L. D., Gomes; L., Tarelho; L. V. G., Ribeiro; S. J. L. and Messadeq; Y., *Journal of Applied Physics*, 93, **2003**, 3878
43. Song; L., Hu; J., Wang; J., Liu; X. and Zhen; Z., *Photochemical & Photobiological Sciences*, 7, **2008**, 689
44. Oliver; K. W., Rettig; S. J., Thompson; R. C., Trotter; J. and Xia; S., *Journal of Fluorine Chemistry*, 83, **1997**, 47
45. Pearson; J., *MSc in Chemical Research thesis, QMUL*, **2007**
46. Grison; C., Comoy; C., Chatenet; D. and Coutrot; P., *Journal of Organometallic Chemistry*, 662, **2002**, 83

47. Dunstan; P. O. and Vicentini; G., *Anais da Academia Brasileira de Ciências*, 47, **1975**, 97
48. Lindsey; C. P. and Patterson; G. D., *Journal of Chemical Physics*, 73, **1980**, 3348
49. Dieke; G. H., *Spectra and Energy Levels of Rare Earth Ions*, **1968**, John Wiley & Sons, Inc
50. Zeng; F., Ren; G., Qiu; X. and Yang; Q., *Physica B*, 403, **2008**, 2417
51. Klink; S. I., Grave; L., Reinhoudt; D. N., Van Veggel; F. C. J. M., Werts; M. H. V., Geurts; F. A. J. and Hofstraat; J. W., *Journal Physical Chemistry A*, 104, **2000**, 5457

Chapter 5 – Experimental procedures and characterization data

5.1 General procedures

Melting points were measured using capillary tubes in a Gallenkamp melting point instrument or on a Reichert hot stage microscope melting point apparatus. The measurements were uncorrected and reported in degree Celsius (°C).

IR spectroscopy was done using a Shimadzu FTIR-8300 or Bruker Tensor 27 spectrometer using a thin film on sodium chloride (NaCl) plates or dispersed in potassium bromide (KBr) pellets.

^1H NMR and ^{31}P NMR spectra were recorded at room temperature on a Jeol JNM-EX270 (270 MHz for ^1H , 109.29 MHz for ^{31}P) or on a Bruker AMX 400 (400 MHz for ^1H , 161.97 MHz for ^{31}P). ^{19}F NMR spectra and ^{13}C NMR were recorded on a Bruker AMX 400 (376.46 MHz for ^{19}F , 100.62 MHz for ^{13}C). ^{13}C NMR and ^{31}P NMR spectra were recorded with proton decoupling. Chemical shifts are reported in ppm, relatively to TMS. In each case, the spectra are given as follows: δ (ppm), the multiplicity of the signals (s, singlet; d, doublet; t, triplet; q, quartet; quint, quintet; m, multiplet), the number of nuclei in the particular environment (deduced by integration), coupling constants measured in Hz and assignment of each signal.

Mass spectroscopy was performed by the EPSRC National Mass Spectrometry Service Centre, University of Wales, Swansea. SF-MALDI (Solvent-free Matrix-assisted laser desorption/ionisation) is a solvent-free ionisation technique that allows analysis of compounds that are insoluble or only soluble in less volatile solvents e.g. dimethyl sulphoxide.¹ SF-MALDI analysis of our perfluorinated Ln^{3+} complexes were carried out using a pentafluorobenzoic acid matrix. MALDI data were also collected on a Bruker Daltonics Auto flex instrument at Queen Mary, University of London. Elemental analysis was performed by Medac Ltd, Egham, Surrey.

Single crystal X-ray diffraction was carried out at Queen Mary, University of London using the Panalytical X'Pert Pro Diffractometer. The samples are run with the Cu tube set at 45 kV and 40 mA and the incident beam is normally collimated with 0.02 rad Soller slits, a 10 mm mask and $\frac{1}{4}$ ° divergence and scatter slits. The divergence slits are automated and set to a fixed value. The scattered beam is collimated by automated slits (fixed at $\frac{1}{2}$ °) and 0.02 rad Soller slits with a Ni filter to remove the Cu K β radiation. The detector is a Panalytical X'Celerator solid state detector which scans continuously over a 2.12 ° range.

X-ray powder diffraction was performed at Queen Mary, University of London. X-ray powder diffraction data for Cs[Nd(HFA)₄] was collected using an automated Philips PW1050/30 X-ray powder diffractometer with Ni-filtered CuK α radiation ($\lambda = 1.5418$ Å), in the range 5 – 70 ° 2 θ , in steps of 0.05 °, with a scan time of 10 s per step. X-ray powder diffraction data for Er[(C₆F₅)₂PO₂]₃ and Y[(C₆F₅)₂PO₂]₃ were collected on a PANalytical X'Pert X-ray diffractometer using Ni filtered CuK α radiation ($\lambda = 1.5418$ Å). Data were collected in flat plate θ/θ geometry over the range 5 – 154 °, in steps of 0.0167 °, with a scan time of 10 s per step. Calibration was carried out with an external Si standard.

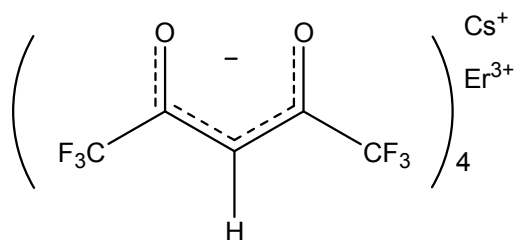
Solvents were rotary evaporated under reduced pressure using a Büchi R-114 Rotavapor. TLC was done using Merck silica gel 60 F₂₅₄ plates. Flash chromatography was performed using BDH silica gel of particle size 33 – 70 μ m.

Experiments which involved temperatures of –78 °C were achieved by freezing EtOAc with liquid nitrogen. Solid samples were dried *in vacuo* over P₂O₅ before characterisation.

THF was dried over sodium and benzophenone and distilled under nitrogen before use. Et₂O for Grignard experiments were dried over sodium wire. Triethylamine was distilled over calcium hydride to remove any traces of H₂O. All other commercially available products were used without further purification.

5.2 Preparation of Cs[Er(HFA)₄]

Caesium carbonate (0.43 g, 1.31 mmol) was dissolved in H₂O (5 mL) and then 1,1,1,5,5,5-hexafluoroacetylacetone (0.37 mL, 2.62 mmol) was added dropwise. A solution of erbium chloride hexahydrate (0.25 g, 0.66 mmol) in H₂O (5 mL) was then added to the mixture. The pink precipitate formed was filtered off and recrystallized from CH₃OH - H₂O to give Cs[Er(HFA)₄] (0.40 g, 53%) as a pale pink solid. Single X-ray diffraction was performed on this sample and the information is provided in Appendix A.



m.p. : 276 – 278 °C

IR (KBr, ν_{max} /cm⁻¹) : 2359, 2345, 1734, 1653, 1564, 1541, 1501, 1258, 1221, 1148, 1099

m/z (MALDI) : 992 (4%), 993 (1), 994 (96), 995 (91), 996 (100), 997 (23), 998 (56), 999 (11), 1000 (1)

HRMS (ESI⁻) *m/z* found 993.8828 (M – Cs⁺)

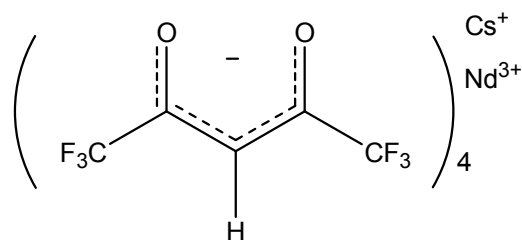
(C₂₀H₄F₂₄O₈¹⁶⁶Er requires 993.8831)

Found : C, 20.92; H, 0.34; N, 0%

(C₂₀H₄CsF₂₄O₈Er requires C, 21.29; H, 0.36%)

5.3 Preparation of Cs[Nd(HFA)₄]

Caesium carbonate (1.15 g, 3.53 mmol) was dissolved in H₂O (10 mL) and then 1,1,1,5,5,5-hexafluoroacetylacetone (1.00 mL, 7.07 mmol) was added dropwise. A solution of neodymium chloride hexahydrate (0.44 g, 1.77 mmol) in H₂O (5 mL) was then added to the mixture. The purple precipitate formed was filtered off and recrystallized from CH₃OH - H₂O to give Cs[Nd(HFA)₄] (1.10 g, 56%) as a pale purple solid. Powder X-ray diffraction was carried out to confirm the structure and was discussed in section 2.8 of chapter 2.



m.p. : 193 – 196 °C Lit² m.p. : 189 – 192 °C

IR (KBr, $\nu_{\text{max}}/\text{cm}^{-1}$) : 1647, 1618, 1541, 1497, 1254, 1153, 1096

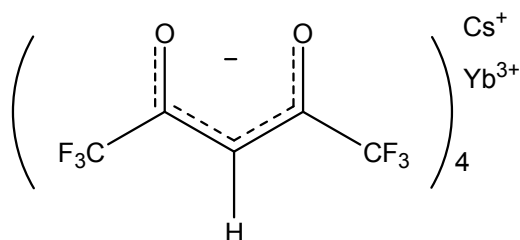
m/z (MALDI) : 970 (99%), 971 (66), 972 (100), 973 (51), 974 (73), 975 (15), 976 (23), 977 (5), 978 (21), 979 (4), 980 (1)

HRMS (ESI⁻) m/z found 969.8607 (M – Cs⁺)

(C₂₀H₄F₂₄O₈ ¹⁴²Nd requires 969.8606)

5.4 Preparation of Cs[Yb(HFA)₄]

Caesium carbonate (1.15 g, 3.53 mmol) was dissolved in H₂O (10 mL) and then 1,1,1,5,5,5-hexafluoroacetylacetone (1.00 mL, 7.07 mmol) was added dropwise. A solution of ytterbium chloride hexahydrate (0.69 g, 1.77 mmol) in H₂O (5 mL) was then added to the mixture. The white precipitate formed was filtered off and recrystallized from CH₃OH - H₂O to give Cs[Yb(HFA)₄] (0.25 g, 12%) as a white solid.



m.p. : 282 – 286 °C

IR (KBr, $\nu_{\text{max}}/\text{cm}^{-1}$) : 1655, 1566, 1543, 1258, 1223, 1150, 1099

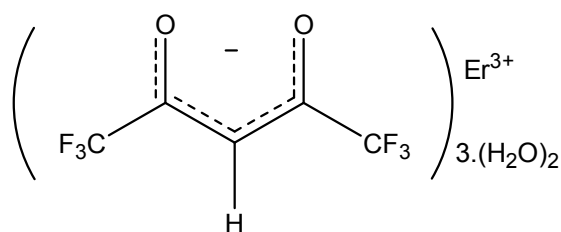
m/z (MALDI) : 998 (9%), 999 (43), 1000 (69), 1001 (59), 1002 (100), 1003 (20), 1004 (42), 1005 (9), 1006 (4)

HRMS (ESI⁻) m/z found : 1001.8937 (M – Cs⁺)

(C₂₀H₄F₂₄O₈¹⁷⁴Yb requires 1001.8917)

5.5 Preparation of [Er(HFA)₃(H₂O)₂] (Ref 3)

Diethyl ether (40 mL) was mixed with H₂O (1 mL) and then 1,1,1,5,5,5-hexafluoroacetylacetone (2.12 mL, 14.98 mmol) and ammonia (1.04 mL, 28%) were added. A solution of erbium chloride hexahydrate (1.91 g, 5.00 mmol) in H₂O (5 mL) was then added to the mixture. The pink precipitate formed was filtered off and recrystallized from toluene to give large pink needles (m.p. : 118 – 121 °C) which were confirmed to be [Er(HFA)₃(H₂O)₂] (1.59 g, 82%) by single crystal X-ray diffraction and elemental analysis. Appendix A shows the XRD crystallography data.



IR (KBr, $\nu_{\text{max}}/\text{cm}^{-1}$) : 2367, 2345, 1653, 1618, 1570, 1541, 1477, 1458, 1258, 1227, 1204, 1148, 1103

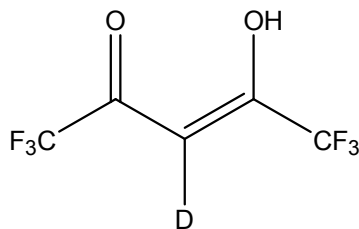
m/z (MALDI) : 992 (4%), 993 (2), 994 (100), 995 (85), 996 (96), 997 (18), 998 (34), 999 (9), 1000 (3)

Found : C, 21.61; H, 0.67%

(C₁₅H₇ErF₁₈O₈ requires C, 21.85; H, 0.86%)

5.6 Preparation of deuterated 1,1,1,5,5,5-hexafluoroacetylacetone⁴

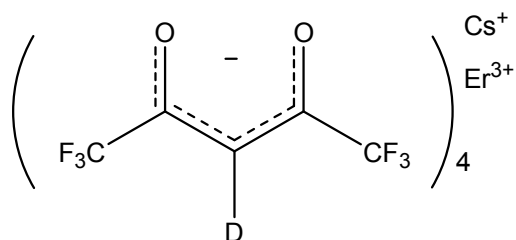
1,1,1,5,5,5-Hexafluoroacetylacetone (HHFA) (6 mL, 42.4 mmol) was dissolved in D₂O (30 mL) and left to stir for 45 min, during which time a white precipitate formed. Diethyl ether (30 mL) was then added and the solution was left to stir for 24 h. The D₂O was separated and then replaced with a fresh portion of D₂O (20 mL) and the mixture was left to stir for 1 h. The ether layer was transferred to another flask and P₂O₅ (4.00 g) was added and the mixture was refluxed for 1 h. Distillation at atmospheric pressure gave the title compound (3.77 g, 42%) as a colourless liquid, boiling point, 60 - 65 °C.



IR (KBr, ν_{\max} /cm⁻¹) : 2361, 2341, 1686, 1589, 1408, 1358, 1219, 1165, 1119, 1018
 δ_{F} (376MHz, CDCl₃) : 77.87 (s, 6F, CF₃)

5.7 Preparation of Cs[Er(HFA-d)₄]

Caesium carbonate (0.33 g, 1.00 mmol) was heated at 140 °C under vacuum for 2 h and then it was left to cool down under nitrogen before D₂O (5 mL) and hexafluoroacetylacetonone-d₂ (0.42 g, 2.00 mmol) were added to dissolve the dry Cs₂CO₃. Erbium chloride hexahydrate (0.19 g, 0.50 mmol) was dissolved in D₂O (2 mL) and then evaporated (process repeated twice) before being dissolved in CH₃OD (2 mL). Then the two solutions were mixed under nitrogen. The precipitate formed was filtered off to give Cs[Er(HFA-d)₄] (0.25 g, 48%) as a pale pink solid.



m.p. : 270 – 274 °C

IR (KBr, ν_{max} /cm⁻¹) : 2392, 2347, 1643, 1526, 1477, 1466, 1350, 1202, 1144, 1094

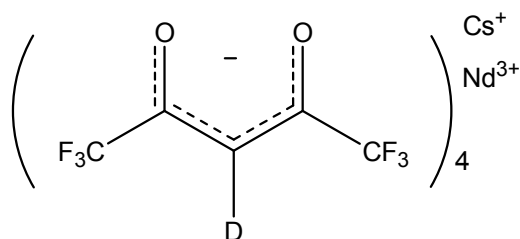
m/z (MALDI) : 994 (1.00%), 995 (1), 996 (6), 997 (14), 998 (100), 999 (92), 1000 (95), 1001 (26), 1002 (48), 1003 (10), 1004 (2)

HRMS (ESI⁻) *m/z* found : 997.9076

(C₂₀D₄F₂₄O₈ ¹⁶⁵Er requires 997.9082)

5.8 Preparation of Cs[Nd(HFA-*d*)₄]

Caesium carbonate (0.52 g, 1.60 mmol) was heated at 140 °C under vacuum for 2 h and then it was left to cool down under nitrogen before D₂O (5 mL) and hexafluoroacetylacetonone-*d*₂ (0.67 g, 3.20 mmol) were added to dissolve the dry Cs₂CO₃. Neodymium chloride hexahydrate (0.20 g, 0.80 mmol) was dissolved in D₂O (2 mL) and then evaporated (process repeated twice) before being dissolved in CH₃OD (2.00 mL). Then the two solutions were mixed under nitrogen. The precipitate formed was filtered off to give Cs[Nd(HFA-*d*)₄] (0.32 g, 35%) as a pale purple solid.



m.p. : 220 – 223 °C

IR (KBr, ν_{max} /cm⁻¹) : 2374, 2345, 2324, 1639, 1541, 1522, 1472, 1458, 1348, 1202, 1142

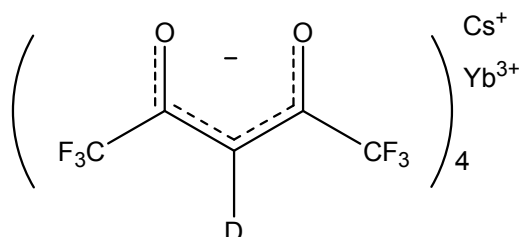
m/z (MALDI) : 972 (1%), 973 (11), 974 (100), 975 (70), 976 (96), 977 (54), 978 (71), 979 (16), 980 (24), 981 (6), 982 (22), 983 (1), 984 (1)

HRMS (ESI⁻) *m/z* found : 973.8845

(C₂₀D₄F₂₄O₈¹⁴¹Nd requires 973.8857)

5.9 Preparation of Cs[Yb(HFA-*d*)₄]

Caesium carbonate (0.52 g, 1.60 mmol) was heated at 140 °C under vacuum for 2 h and then it was left to cool down under nitrogen before D₂O (5 mL) and hexfluoroacetylacetonone-*d*₂ (0.67 g, 3.20 mmol) were added to dissolve the dry Cs₂CO₃. Ytterbium chloride hexahydrate (0.31 g, 0.80 mmol) was dissolved in D₂O (2 mL) and then evaporated (process repeated twice) before being dissolved in CH₃OD (2.00 mL). Then the two solutions were mixed under nitrogen. The precipitate formed was filtered off to give Cs[Yb(HFA-*d*)₄] (0.39 g, 28%) as a white solid.



m.p. : 284 – 290 °C

IR (KBr, ν_{\max} /cm⁻¹) : 2365, 2345, 1647, 1528, 1477, 1211, 1146, 1096

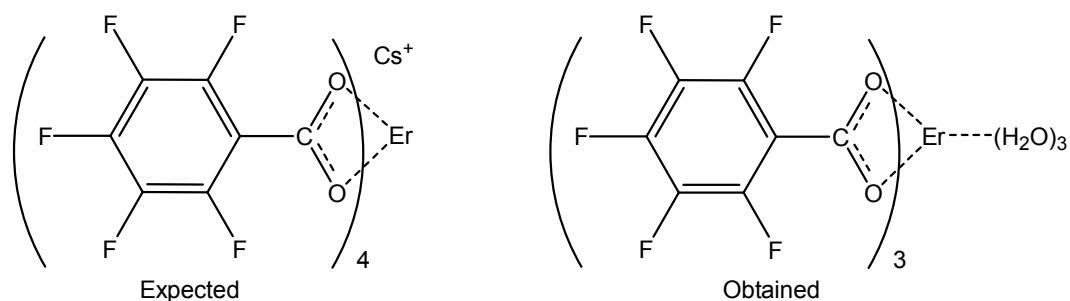
m/z (MALDI) : 1000 (1%), 1001 (2), 1002 (18), 1003 (55), 1004 (79), 1005 (71), 1006 (100), 1007 (26), 1008 (44), 1009 (8), 1010 (1)

HRMS (ESI⁻) *m/z* found : 1005.9152

(C₂₀D₄F₂₄O₈¹⁷⁴Yb requires 1005.9157)

5.10 Attempted preparation of Cs[Er(pentafluorobenzoate)₄]

Caesium carbonate (0.51 g, 1.57 mmol) was dissolved in H₂O (5 mL) and then pentafluorobenzoic acid (0.67 g, 3.14 mmol) was added. A solution of erbium chloride hexahydrate (0.30 g, 0.79 mmol) in H₂O (5 mL) was added to the mixture. The pink solution was evaporated to give pink solid, which was recrystallized from ethanol to give erbium(II)pentafluorobenzoate pentahydrate (0.22 g, 25%) as a pink solid, which was identified by single crystal X-ray diffraction (Appendix A).



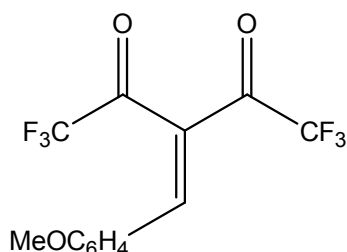
m.p. : >300 °C

IR (KBr, $\nu_{\max}/\text{cm}^{-1}$) : 3425, 2368, 2345, 1651, 1589, 1497, 1412, 1304, 1119, 1003, 941

HRMS (ESI ⁻) m/z found : 1010.8596 [(C₆F₅CO₂)₄Cs]⁻
(C₂₈¹⁶⁷ErF₂₀O₈ requires 1010.8589)

5.11 Preparation of 3-(4-methoxybenzylidene)-1,1,1,5,5,5-hexafluoropentane-2,4-dione⁵

4-Methoxybenzaldehyde (1.22 mL, 10.00 mmol), 1,1,1,5,5,5-hexafluoroacetylacetone (1.42 mL, 10.00 mmol) and acetic anhydride (10.00 mL, 105.00 mmol) were heated together at 80 °C for 23 h. The dark yellow liquid mixture was distilled under reduced pressure to give 3-(4-methoxybenzylidene)-1,1,1,5,5,5-hexafluoropentane-2,4-dione (2.01 g, 64%) as a yellow liquid.



b.p : 110 °C (3 mmHg), Lit⁵ b.p. : 120 °C (2 Torr)

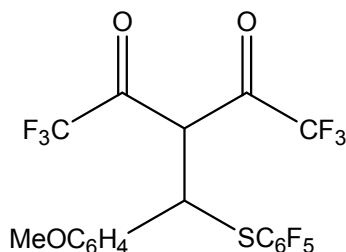
IR ($\nu_{\max}/\text{cm}^{-1}$) : 2847, 1751, 1686, 1589, 1566, 1516, 1312, 1273, 1207, 1146, 1011

Lit⁵ IR ($\nu_{\max}/\text{cm}^{-1}$) : 1750, 1690, 1590, 1560

δ_{H} (270 MHz, CDCl_3) : 3.88 (s, 3H, OCH_3), 6.94 – 6.97 (m, 2H, Ar), 7.39 – 7.42 (m, 2H, Ar), 7.96 (s, 1H, $\text{CH}=\text{C}$)

5.12 Preparation of 3-[(4-methoxyphenyl)(pentafluorophenylsulfanyl)methyl]-1,1,1,5,5,5-hexafluoro-pentane-2,4-dione

3-(4-Methoxybenzylidene) - 1,1,1,5,5,5-hexafluoropentane-2,4-dione (1.00 mL, 3.75 mmol) and pentafluorothiophenol (0.50 mL, 3.75 mmol) were stirred at room temperature for 15 min. The yellow solid which formed was recrystallized from Et₂O - petroleum spirit to give 3-[(4-methoxyphenyl)(pentafluorophenylsulfanyl)methyl]-1,1,1,5,5,5-hexafluoro-pentane-2,4-dione (1.42 g, 74%) as a white solid.



m.p. : 87 – 89 °C

IR (KBr, ν_{\max} /cm⁻¹) : 3425, 2361, 1774, 1612, 1489, 1304, 1265, 1180, 1088, 1034, 980

δ_{H} (270MHz, CDCl₃) : 3.77 (s, 3H, OMe), 5.00 (d, 1H, J = 11 Hz, CH), 5.25 (d, 1H, J = 11 Hz, CH), 6.77 (d, 2H, J = 9 Hz, Ar), 7.11 (d, 2H, J = 9 Hz, Ar)

δ_{F} (376MHz, CDCl₃) : -79.15 - -79.32 (m, 6F, CF₃CO), -131.78 (d, J = 18.8 Hz), -150.10 - -150.23 (m, 5F, C₆F₅)

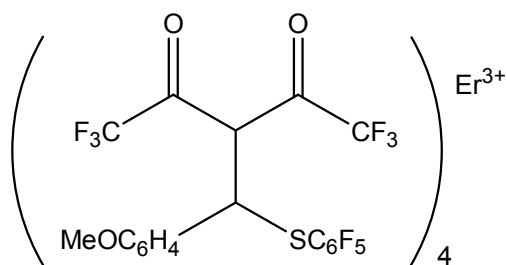
δ_{C} (100MHz, CDCl₃) : 52.99 (s, C-C), 55.66 (s, OCH₃), 59.95 (s, C-C), 114.67 (q, J = 291 Hz, CF₃), 114.86 (s, COMe), 115.24 (q, J = 291 Hz, CF₃), 126.81 (s, Ar), 129.58 (s, Ar), 134.22 – 149.33 (m, Ar), 160.66 (s, Ar), 181.07 (q, J = 20 Hz, C=O), 181.85 (q, J = 20 Hz, C=O)

Found : C, 43.17; H, 1.7; N, 0%

(C₁₉H₉F₁₁SO₃ requires C, 43.36; H, 1.72%)

5.13 Attempted preparation of Cs[Er(3-[(4-methoxyphenyl)(pentafluorophenylsulfanyl)methyl]-1,1,1,5,5,5-hexafluoro-pentane-2,4-dione)₄]

Caesium carbonate (0.16 g, 0.48 mmol) was dissolved in H₂O (10 ml) and then 3-[(4-methoxy-phenyl)-pentafluorophenylsulfanyl-methyl]-1,1,1,5,5,5-hexafluoro-pentane-2,4-dione (0.50 g, 0.95 mmol) was added. A solution of erbium chloride (0.09 g, 0.24 mmol) was added to the mixture. The yellow liquid mixture was rotary evaporated to give yellow solid, which was recrystallized from CH₃OH - H₂O to give a yellow solid (0.19 g). Luminescence studies on this material did not show significant amounts of Er³⁺ to be present.



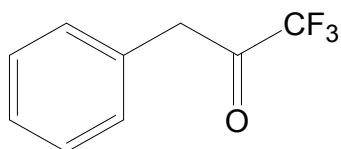
Expected

m.p. : 75 – 80 °C

IR (KBr, ν_{\max} /cm⁻¹) : 2370, 1734, 1647, 1516, 1481, 1458, 1259, 1159, 976

5.14 Preparation of 1,1,1-trifluoro-3-phenylpropan-2-one⁶

Magnesium turnings (2.50 g, 103.00 mmol) were left to stir overnight under nitrogen⁷ before dry Et₂O (50 mL) was added. A mixture of benzyl chloride (10.2 mL, 89.00 mmol) and dry Et₂O (10 mL) was added dropwise. The grey mixture was left to stir for 1 h at room temperature before being added to ethyl trifluoroacetate (16 mL, 133.5 mmol) which was cooled to -78 °C. The yellow liquid mixture was acidified using 2M HCl (6 mL). The aqueous layer was then extracted 3 times with Et₂O (50 mL). The organic layers were dried using anhydrous MgSO₄ and filtered. The solvent was evaporated under reduced pressure to give a pale yellow oil. Distillation under reduced pressure gave 1,1,1-trifluoro-3-phenylpropan-2-one (4.61 g, 27%) as a colourless liquid.



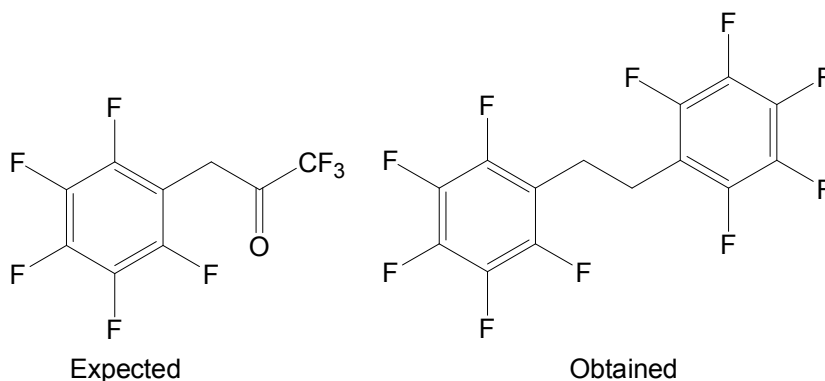
b.p. : 80 °C (approx. 15 mmHg), Lit⁸ b.p : 66 °C (16 mmHg)

IR ($\nu_{\max}/\text{cm}^{-1}$) : 3520, 3036, 2905, 1952, 1886, 1759, 1713, 1605, 1587, 1497, 1456, 1402, 1362, 1279, 1144, 1105, 1076, 1018, 1001

δ_{H} (270MHz, CDCl₃) : 4.00 (s, 2H, CH₂), 7.22 - 7.37 (m, 5H, C₆H₅)

5.15 Attempt to prepare 1,1,1-trifluoro-3-pentafluorophenyl-propan-2-one

Magnesium turnings (1.46 g, 60.0 mmol) were left to stir overnight under nitrogen⁷ before dry Et₂O (20 mL) was added. A mixture of 2,3,4,5,6 pentafluorobenzyl bromide (7.1 mL, 50 mmol) and dry Et₂O (10 mL) was added dropwise. The dark brown mixture was left to stir for 30 min at room temperature before being added to ethyl trifluoroacetate (10.7 mL, 90.0 mmol) which was cooled to -78 °C. The dark orange liquid mixture was acidified using 2M HCl (6 mL). The aqueous layer was then extracted 3 times with Et₂O (50 mL). The organic layers were dried using anhydrous MgSO₄ and filtered. The solvent was evaporated under reduced pressure to give 17.6 g of yellow solid. It was then recrystallized from hexane to give 1,2-bis(pentafluorophenyl) ethane (5.9 g, 63%) as a light yellow solid.



m.p. : 102 - 105 °C, Lit⁹ m.p. : 107 - 108 °C

IR ($\nu_{\max}/\text{cm}^{-1}$) : 3410, 2959, 2642, 2365, 1663, 1504, 1458, 1431, 1184, 1126, 968

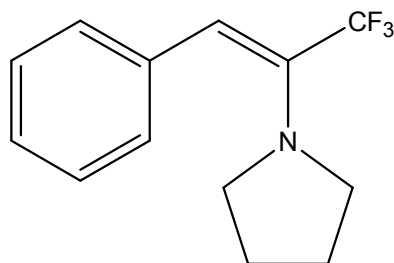
Lit⁹ IR ($\nu_{\max}/\text{cm}^{-1}$) : 1661 (C=C), 1506 (C=C)

δ_{H} (270MHz, CDCl₃) : 3.0 (s, 4H, CH₂)

Lit¹⁰ δ_{H} (270MHz, CDCl₃) : 3.0 (s, 4H, CH₂)

5.16 Preparation of (Z)-1-Phenyl-2-pyrrolidinyl-3,3,3-trifluoropropene¹¹

1,1,1-Trifluoro-3-phenylpropan-2-one (1.00 g, 5.30 mmol) and pyrrolidine (0.44 mL, 5.30 mmol) were refluxed in benzene (12 mL) for 1 h. A Dean and Stark trap apparatus was used to collect H₂O. The reaction mixture was evaporated under reduced pressure to give (Z)-1-phenyl-2-pyrrolidinyl-3,3,3-trifluoropropene (1.27 g, 93%) as a yellow liquid.



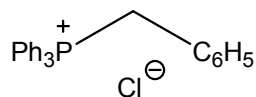
IR ($\nu_{\max}/\text{cm}^{-1}$): 3036, 2326, 1960, 1817, 1620, 1481, 1447, 1396, 1269, 1207, 1165, 1115, 1034

δ_{H} (270MHz, CDCl₃): 1.81 - 1.93 (m, 4H, NCH₂), 2.86 - 3.44 (m, 4H, CH₂), 6.15 (s, 1H, C-H), 7.28 - 7.39 (m, 5H, C₆H₅)

Lit¹¹ δ_{H} (CDCl₃): 1.7 (t), 3.05 (t), 6.15 (s), 7.3 (m)

5.17 Preparation of benzyl(triphenyl)phosphonium chloride¹²

Triphenylphosphine (50 g, 0.19 mol) was refluxed with benzyl chloride (21.9 mL, 0.19 mol) in toluene (200 mL) for 20 h under nitrogen. After cooling the mixture down, the white solid was filtered off to give the title compound (51.0 g, 67%).



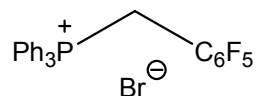
m.p. : >320 °C, Lit¹² m.p. : >300 °C

IR (KBr, $\nu_{\text{max}}/\text{cm}^{-1}$) : 3059, 2990, 2856, 2785, 2365, 2345, 1653, 1587, 1491, 1437, 1155, 1115, 995

δ_{H} (270MHz, CDCl_3) : 5.55 (d, 2H, $J = 14.4$ Hz, CH_2), 7.62 - 7.77 (m, 5H, C_6H_5)

5.18 Preparation of (pentafluorophenylmethyl)triphenylphosphonium bromide¹³

Triphenylphosphine (5.00 g, 19 mmol) was refluxed with pentafluorobenzyl bromide (2.69 mL, 19 mmol) in toluene (50 mL) for 20 h under nitrogen. The mixture was cooled and filtered to give the title compound (9.40 g, 95%) as a white solid.



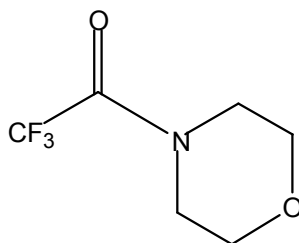
m.p. : 245 – 247 °C, Lit¹³ m.p. : 247 – 249 °C

IR (KBr, $\nu_{\text{max}}/\text{cm}^{-1}$) : 3013, 2855, 2365, 1653, 1585, 1522, 1506, 1485, 1435, 1391, 1308, 1113, 978, 964, 845

δ_{H} (270MHz, CDCl_3) : 5.71 (d, 2H, $J = 13$ Hz, CH_2), 7.67 - 7.87 (m, 5H, C_6H_5)

5.19 Preparation of 4-(Trifluoroacetyl)morpholine¹⁴

Morpholine (10.9 mL, 125 mmol) was added dropwise over 10 min to ice-cooled, stirred ethyl trifluoroacetate (14.9 mL, 125 mmol). The mixture was left to stir for 24 h under nitrogen at room temperature. Distillation under reduced pressure gave 4-(trifluoroacetyl)morpholine (21.28 g, 93%) as a colourless liquid.



b.p. : 100 °C (approx 15 mmHg), Lit¹⁴ b.p. : 47 °C (1 mmHg)

IR ($\nu_{\max}/\text{cm}^{-1}$) : 3535, 3375, 3161, 2930, 2768, 2718, 2689, 2480, 2363, 2228, 2133, 2016, 1958, 1705, 1558, 1510, 1437, 1391, 1364, 1279, 1117, 1028, 941, 897, 843

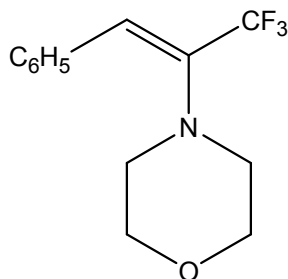
δ_{H} (270MHz, CDCl_3) : 3.44 - 3.55 (m, 8H, $\text{NCH}_2\text{CH}_2\text{O}$)

δ_{C} (100.6MHz, CDCl_3) : 43.6 (t, $J = 17$ Hz, C-N), 46.5 (t, $J = 3.1$ Hz, C-N),

66.3 – 66.7 (m, C-O), 116.6 (q, $J_{\text{C-F}} = 288$ Hz, CF_3), 155.5 (q, $J_{\text{C-F}} = 36$ Hz, C=O)

5.20 Preparation of 4-[2-phenyl-1-(trifluoromethyl)-vinyl]morpholine¹⁵

Benzyl(triphenyl)phosphonium chloride (15.9 g, 41.0 mmol) was added to a suspension of NaH (60% NaH in mineral oil; 1.7 g, 41.0 mmol) in dry toluene (30 mL). The colourless mixture was stirred for 3.5 h at 130 °C under nitrogen. 4-(Trifluoroacetyl)morpholine (7.5 g, 41.0 mmol) in dry toluene (10 mL) was added and the yellow mixture was left to stir for another 72 h, before it was evaporated under reduced pressure to give a pale orange solid. Petroleum spirit (b.p. : 40 – 60 °C) (30 mL) was added and left to stir for 30 min. Triphenylphosphine oxide and sodium chloride were filtered off. The pale yellow filtrate was concentrated and then purified by flash chromatography [94 : 6 petroleum spirit (b.p. : 40 - 60 °C) : Et₂O] to give 4-(2-phenyl-1-trifluoromethyl-vinyl)-morpholine (2.42g, 23%) as a yellow liquid. The ¹H NMR revealed a 5.2 : 1 ratio of the *Z* and *E* isomers.



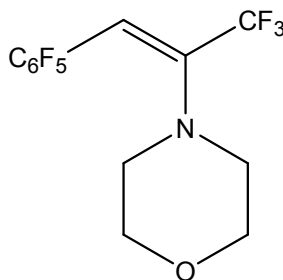
IR ($\nu_{\max}/\text{cm}^{-1}$) : 2863, 2855, 1636, 1489, 1450, 1377, 1327, 1261, 1165, 1119, 1015, 930, 907, 891, 849

δ_{H} (270MHz, CDCl₃) : 2.93 – 2.95 (m, 4H, H - 3,5), 3.74 – 3.98 (m, 4H, H - 2,6), 6.19 (s, 1H, HC=)(*E* isomer), 6.53 (s, 1H, HC=)(*Z* isomer), 7.25 – 7.72 (m, 5H, Ar)

Lit¹⁵ δ_{H} (CDCl₃) : 2.9 (m, 4H), 3.7 (m, 4H), 6.5 (s, 1H), 7.25 – 7.55 (m, 5H)

5.21 Preparation of 4-[2-(pentafluorophenyl)-1-(trifluoromethyl)vinyl]morpholine

(Pentafluorophenylmethyl)triphenylphosphonium bromide (12.0 g, 27.0 mmol) was added to a suspension of NaH (60% NaH in mineral oil; 1.06 g, 27.0 mmol) in dry toluene (30 mL). The yellow liquid mixture was stirred for 48 h at 150 °C under nitrogen. 4-(Trifluoroacetyl)morpholine (4.94 g, 27.0 mmol) in dry toluene (10 mL) was added and the dark yellow liquid mixture was left to stir for another 72 h, before it was evaporated under reduced pressure to give a dark yellow gel. Petroleum spirit (b.p. : 40 – 60 °C) (30 mL) was added and left to stir for 30 min. Triphenylphosphine oxide and sodium chloride were filtered off. The pale yellow filtrate was concentrated and then purified by flash chromatography [94 : 6 petroleum spirit (b.p. : 40 - 60 °C) : Et₂O] to give 4-[2-(pentafluorophenyl)-1-(trifluoromethyl)vinyl]morpholine (0.08g, 0.88%) as a pale yellow liquid.



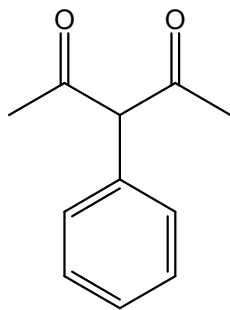
IR ($\nu_{\max}/\text{cm}^{-1}$) : 3364, 2970, 2862, 2692, 2361, 1643, 1497, 1443, 1373, 1288, 1173, 1126, 1026, 995, 941

δ_{H} (270MHz, CDCl₃) : 2.91 (t, 4H, $J = 4.7$ Hz, H - 3,5), 3.62 (t, 4H, $J = 4.7$ Hz, H - 2,6), 5.90 (s, 1H, HC=)

HRMS (EI +) m/z found : 347.0555 (M^+)
(C₁₃H₉F₈NO requires 347.0551)

5.22 Preparation of 3-phenyl-pentane-2,4-dione¹⁶

Acetylacetone (32.4 mL, 0.32 mol), iodobenzene (11.7 mL, 0.11 mol), potassium carbonate (58.05 g, 0.42 mmol), L-proline (2.42 g, 0.02 mol) and copper(I) iodide (2.00 g, 0.01 mol) were stirred together in DMSO (80 mL) for 6 h at 90 °C under N₂. The dark brown liquid mixture was then added to HCl (2M) and then extracted into EtOAc. The organic layer was dried using Na₂SO₄, filtered and then evaporated to give a dark brown liquid, which was purified by flash chromatography [7 : 1 petroleum spirit (b.p. : 30 - 40 °C) : EtOAc] to give a yellow liquid. Vacuum distillation of the yellow liquid gave 3-phenyl-pentane-2,4-dione (0.45 g, 0.7%) as a yellow solid.



b.p. : 100 °C (5 mmHg)

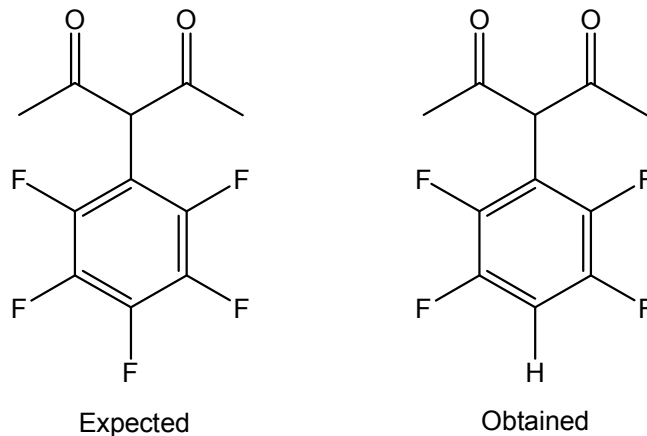
m.p. : 53 – 55 °C, Lit¹⁷ m.p. : 55 – 57 °C

IR (KBr, ν_{max} /cm⁻¹) : 3024, 2926, 2339, 1703, 1699, 1447, 1423, 1259, 1214, 1157, 1072, 976, 910, 841

δ_{H} (270MHz, CDCl₃) : 1.88 (s, 6H, CH₃), 7.17 – 7.37 (m, 5H, Ar), 16.67 (s, 1H, OH)

5.23 Reaction of acetylacetone with iodopentafluorobenzene

Acetylacetone (2.43 mL, 23.6 mmol), iodopentafluorobenzene (1.05 mL, 7.9 mmol), potassium carbonate (4.35 g, 31.5 mmol), L-proline (0.18 g, 1.6 mmol) and copper(I) iodide (0.15 g, 0.8 mmol) were stirred together in DMSO (15 mL) for 6 h at 100 °C. The dark brown liquid mixture was then added to HCl (2M) and then extracted into EtOAc. The organic layers were dried using Na₂SO₄, filtered and then evaporated to give a dark brown liquid, which was purified by flash chromatography [5 : 1 petroleum spirit (b.p. : 30 - 40 °C) : EtOAc] to give a yellow liquid. Distillation under reduced pressure gave 3-(2,3,5,6-tetrafluorophenyl)pentane-2,4-dione (0.26 g, 12%) as a yellow liquid.



b.p. : 100 °C (4 mm Hg)

IR (KBr, $\nu_{\text{max}}/\text{cm}^{-1}$) : 3067, 2986, 2324, 1738, 1614, 1495, 1398, 1312, 1242, 1175, 1123, 1047, 999, 934

δ_{H} (270MHz, CDCl₃) : 1.94 (s, 6H, CH₃), 7.09 – 7.12 (m, 1H, CH), 17.02 (s, 1H, OH)

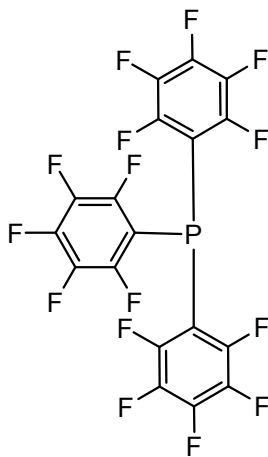
δ_{F} (376MHz, CDCl₃) : -139.2 - -140.0 (m, 2F, F - 3,5), -140.0 - -140.1 (m, 2F, F - 2,6)

HRMS (EI +) m/z found : 248.0452

(C₁₁H₈F₄O₂ requires 248.0455)

5.24 Preparation of tris(pentafluorophenyl)phosphine¹⁸

Magnesium turnings (1.25 g, 51.4 mmol) were stirred together with a small iodine crystal in Et₂O (20 mL) under nitrogen before a solution of pentafluorobromobenzene (6.3 mL, 50.5 mmol) in Et₂O (20 mL) was added dropwise. The reaction was exothermic and the mixture refluxed gently during the addition. Upon complete addition, the mixture was stirred for a further 1 h, after which all the magnesium had dissolved. A cannula was used to transfer the dark brown Grignard reagent to a solution of phosphorus trichloride (1.18 mL, 13.5 mmol) in Et₂O (20 mL). The mixture was stirred for 90 min at room temperature before HCl (2M) was added and the crude product was then extracted into Et₂O (3 x 50 mL). The combined organic layers were dried using MgSO₄ and then evaporated to give a brown solid, which was purified by flash chromatography [petroleum spirit (b.p. : 40 – 60 °C)] and then recrystallized from hexane to give the title compound (2.9 g, 40%) as a light brown solid.



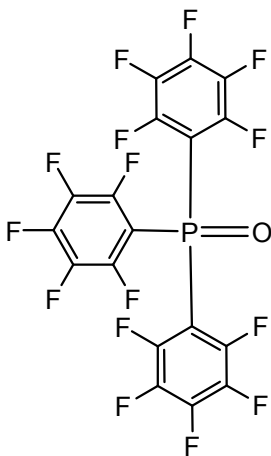
m.p. : 102 – 104 °C, Lit¹⁸ m.p. : 116 - 117 °C

IR (KBr, ν_{\max} /cm⁻¹) : 2916, 1643, 1520, 1474, 1389, 1296, 1084, 976, 853, 764

δ_{P} (109.3MHz, CDCl₃) : -73.3 (s)

5.25 Preparation of tris(pentafluorophenyl)phosphine oxide

This reaction was carried out behind a safety screen. Tris(pentafluorophenyl)phosphine (1 g, 1.9 mmol) was dissolved in TFA (10 mL) in an ice-bath. Aqueous H₂O₂ (35%) (0.33 mL, 3.76 mmol) was added and left to stir for 45 min before TLC (petrol) showed no sign of starting material. Sodium sulfite (0.85 g, 6.8 mmol) was added and TFA was removed under reduced pressure. Aqueous NaHCO₃ was added and the yellow solid was extracted into CHCl₃ (3 x 50 mL). The organic layer was evaporated to give the crude product which was then recrystallized from heptane to give tris(pentafluorophenyl)phosphine oxide (0.34 g, 33%) as a white solid.



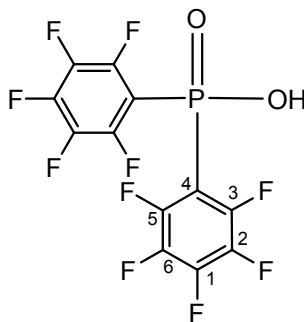
m.p. : 156 – 158 °C, Lit¹⁸ m.p. : 169 – 170 °C

IR (KBr, ν_{\max} /cm⁻¹) : 2924, 2372, 1651, 1520, 1497, 1389, 1300, 1234, 1099, 988, 837, 768, 733

δ_P (109.3MHz, CDCl₃) : -7.6 (s)

5.26 Preparation of bis(pentafluorophenyl)phosphinic acid

Tris(pentafluorophenyl)phosphine oxide (1.3 g, 2.37 mmol) was stirred in a mixture of H₂O (9 mL) and 1,4-dioxane (9 mL) before aqueous KOH (0.9M; 2.8 mmol) was added to give a colourless mixture of pH 14. After 30 min, TLC (CHCl₃) revealed the absence of starting material. H₂O and HCl (2M) was added to reduce the pH to 1. The solvent was removed under reduced pressure to give white solid. Brine was added and the product was extracted into Et₂O (3 x 50 mL), which was dried (Na₂SO₄) and then evaporated to give a white solid. Recrystallization from Et₂O - hexane gave the title compound as a white solid (0.6 g, 64%).



m.p. : 148 – 150 °C, Lit¹⁹ m.p. : 154 °C

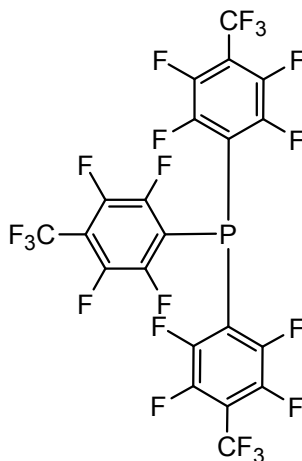
IR (KBr, ν_{\max} /cm⁻¹) : 3422, 1647, 1481, 1389, 1302, 1101, 982, 845, 731

δ_{P} (109.3MHz, CDCl₃) : 10.9 (s)

δ_{F} (376MHz, DMSO-*d*₆) : -130.6 (d, 4F, *J* = 21.4 Hz, F - 3,5), -146.27 (t, 2F, *J* = 21.8 Hz, F - 1), -157.6 - -158 (m, 4F, F - 2,6)

5.27 Preparation of tris(2,3,5,6-tetrafluoro-4(trifluoromethyl)phenyl)phosphine

Magnesium turnings (1.27 g, 53 mmol) were stirred together with a small iodine crystal in Et₂O (20 mL) under nitrogen before a solution of 4-bromo-2,3,5,6-tetrafluorobenzotrifluoride (8 mL, 51.9 mmol) in Et₂O (20 mL) was added dropwise. The reaction was exothermic and the mixture refluxed gently during the addition. Upon complete addition, the mixture was stirred for a further 1 h, after which all the magnesium had dissolved. A cannula was used to transfer the dark brown Grignard reagent to a solution of phosphorus trichloride (1.36 mL, 15.6 mmol) in Et₂O (20 mL). The mixture was stirred for 90 min at room temperature before HCl (2M; 10 mL) was added and then extracted into Et₂O (3 x 50 mL). The organic layer was evaporated to give a brown solid (9.2 g) and was subjected to flash chromatography [petroleum spirit (b.p. : 40 – 60 °C)] and then recrystallized from hexane to give the title compound (5.2 g, 49%) as a white solid.



m.p. : 105 – 106 °C, Lit²⁰ m.p. : 93 – 105 °C

IR (KBr, ν_{\max} /cm⁻¹) : 1651, 1589, 1474, 1420, 1327, 1258, 1188, 1150, 980, 937, 818

δ_{P} (109.3MHz, CDCl₃) : -71.1 (s)

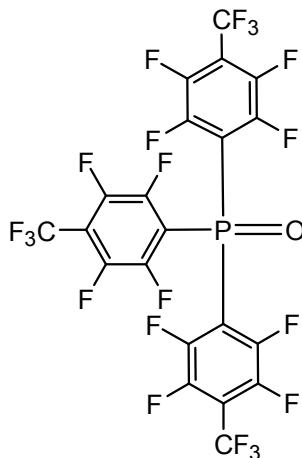
δ_{F} (376MHz, CDCl₆) : -57.9 (t, 9F, $J = 21.6$ Hz, CF₃), -128.6 - -128.7 (m, 6F, F - 3,5), -138.7 - -138.9 (m, 6F, F - 2,6)

HRMS (EI +) m/z found : 681.9399

(C₂₁F₂₁P (M⁺) requires 681.9397)

5.28 Preparation of tris(2,3,5,6-tetrafluoro-4(trifluoromethyl)phenyl)phosphine oxide

This reaction was carried out behind a safety screen. Tris(2,3,5,6-tetrafluoro-4(trifluoromethyl)phenyl)phosphine (5.14 g, 7.5 mmol) was dissolved in TFA (35 mL) in an ice-bath. Aqueous H₂O₂ (35%) (1.2 mL, 13.6 mmol) was added and left to stir for 45 min before TLC (petrol) showed no signs of starting material. Sodium sulfite (2.6 g, 20.6 mmol) was added and TFA was removed under reduced pressure to give white solid, which was extracted into CHCl₃ (3 x 50 mL). The organic layer was evaporated to give the crude product which was then recrystallized from EtOAc and petrol to give tris(2,3,5,6-tetrafluoro-4(trifluoromethyl)phenyl)phosphine oxide (1.43 g, 27%) as a white solid.



m.p. : 191 - 193 °C, Lit²⁰ m.p. : 192 - 194 °C

IR (KBr, ν_{\max} /cm⁻¹) : 1655, 1616, 1558, 1466, 1427, 1335, 1258, 1153, 1096, 976, 949

δ_{P} (109.3 MHz, CDCl₃) : -11.9 (s)

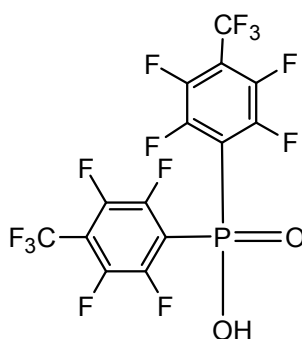
δ_{F} (376 MHz, CDCl₃) : -58.1 (t, 9F, $J = 21.8$ Hz, CF₃), -130.5 (t, 6F, $J = 16.4$ Hz, F - 3,5), -136.6 (d, 6F, $J = 20.5$ Hz, F - 2,6)

HRMS (EI +) m/z found : 697.9342

(C₂₁F₂₁PO (M⁺) requires 697.9346)

5.29 Preparation of bis[2,3,5,6-tetrafluoro-4(trifluoromethyl)phenyl]phosphinic acid

Tris(2,3,5,6-tetrafluoro-4(trifluoromethyl)phenyl)phosphine oxide (1.38 g, 1.98 mmol) was stirred in a mixture of H₂O (14 mL) and 1,4-dioxane (14 mL) for 15 min before aqueous KOH (0.9 mL, 3.52 mmol) was added to give a light yellow mixture of pH 12. After 30 min, TLC (CHCl₃) revealed the absence of starting material. H₂O and HCl (2M) were added to reduce the pH to 1. The solvent was removed under reduced pressure to give a white solid. Brine was added and the product was extracted into Et₂O (3 x 50 mL), dried, filtered and then evaporated to give 1.31 g of white solid. The crude product was recrystallized from Et₂O and hexane to give the title compound as a white solid (0.61 g, 62%).



m.p. : 194 - 196 °C, Lit²⁰ m.p. : 193 - 200 °C

IR (KBr, ν_{\max} /cm⁻¹) : 1701, 1647, 1570, 1460, 1420, 1340, 1175, 1148, 1074, 980, 953

δ_P (109.3MHz, DMSO-*d*₆) : -13.69 (s)

δ_F (376MHz, CDCl₃) : -58.16 (t, 6F, *J* = 21.8 Hz, CF₃), -131.77 - -131.87 (m, 4F, F - 3,5), -138.65 (d, 4F, *J* = 20.5 Hz, F - 2,6)

HRMS (EI -) *m/z* found : 496.9419

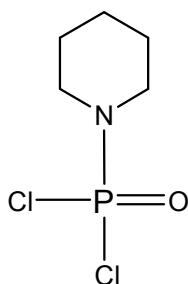
(C₁₄HF₁₄PO₂ (M-H⁺) requires 496.9418)

Found : C, 33.74; H, 0.13; N, <0.10%

(C₁₄F₁₄PO₂H requires C, 33.76; H, 0.20%)

5.30 Preparation of (piperidinylamido)phosphoric dichloride²¹

Triethylamine was distilled over calcium hydride to remove any traces of H₂O. Piperidine (4.52 mL, 45.7 mmol) was added to a solution of triethylamine (6.37 mL, 45.7 mmol) in Et₂O (9 mL) under nitrogen. The resultant colourless mixture was then transferred via a cannula to an ice-cooled solution of phosphoryl chloride (4.26 mL, 45.7 mmol) in Et₂O (9 mL). The reaction was exothermic and a white precipitate formed instantly. After stirring for 4 h, the mixture was filtered over MgSO₄ and the filtrate was rotary evaporated to give 8.39 g of yellow liquid. The crude product was distilled to give a colourless liquid of the title compound (5.26 g, 57%).



b. p. : 95 – 115 °C (approx 1 mmHg)

IR (KBr, $\nu_{\max}/\text{cm}^{-1}$) : 2941, 2858, 2363, 1466, 1452, 1445, 1379, 1344, 1277, 1205, 1165, 1107, 1072, 1024, 962, 853

Lit²¹ IR (KBr, $\nu_{\max}/\text{cm}^{-1}$) : 1270, 1034

δ_{H} (270MHz, CDCl₃) : 1.58 - 1.63 (m, 6H), 3.13 - 3.30 (m, 4H)

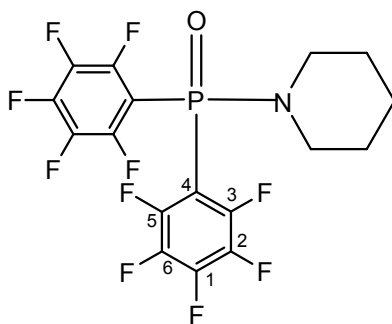
Lit²¹ δ_{H} (CDCl₃) : 1.59 - 1.72 (m, 6H), 3.20 - 3.40 (m, 4H)

δ_{P} (109.3MHz, CDCl₃) : 16.44 (s)

Lit²¹ δ_{P} (CDCl₃) : 13.4 (s)

5.31 Reaction of bromopentafluorobenzene with (piperidinylamido)phosphoric dichloride

This reaction was done behind a safety screen. A solution of n-butyllithium (11 mL, 17.6 mmol) in Et₂O (10 mL) was added dropwise over 30 min to a solution of bromopentafluorobenzene (2 mL, 16 mmol) in Et₂O (50 mL) at -78 °C under nitrogen. The reaction was exothermic and after 1 h, the mixture was transferred via cannula to a solution of (piperidinylamido)phosphoric dichloride (1.62 g, 8 mmol) in Et₂O (10 mL). 90 min later, the reaction was quenched with HCl (2M; 10 mL). Brine (5 mL) was added and the compound was extracted into Et₂O (3 x 50 mL), dried, filtered and then the organic layer was evaporated to give 4.62 g of light yellow oil. Aqueous KOH (0.25M; 20 mL) was then added and the mixture was extracted to Et₂O (3 x 50 mL) and then evaporated to give 3.45 g of white foam. The white foam was subject to flash chromatography (CH₂Cl₂) and 3 separate portions of colourless foam were isolated. Each of the colourless foam was separately recrystallized from EtOAc and hexane to give 1-[bis(pentafluorophenyl)phosphinoyl]piperidine (0.38 g, 10%), 1-[(nonafluorobiphenyl-4-yl)-pentafluorophenylphosphinoyl]piperidine (0.30 g, 6.2%) and 1-[bis(nonafluorobiphenyl-4-yl)-phosphinoyl]piperidine (0.57 g, 11.5%).



1-[bis(pentafluorophenyl)phosphinoyl]piperidine

m.p. : 96 – 97 °C

IR (KBr, ν_{\max} /cm⁻¹) : 2945, 2367, 1734, 1647, 1558, 1522, 1475, 1387, 1344, 1298, 1207, 1167, 1097, 978

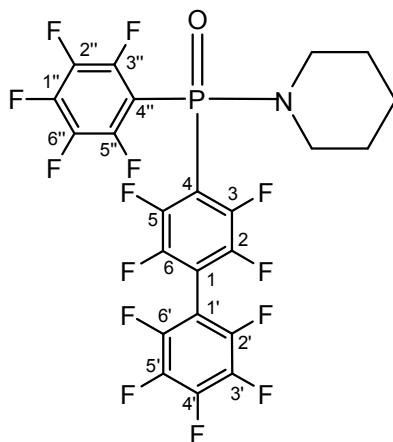
δ_{H} (270MHz, CDCl₃) : 1.55 - 1.61 (m, 6H), 3.14 - 3.16 (m, 4H)

δ_{P} (109.3MHz, CDCl₃) : 3.37 (s)

δ_{F} (376MHz, CDCl₃) : -133.77 - -133.89 (m, 2F, F - 1), -146.18 - -146.29 (m, 4F, F - 3,5), -159.70 - -159.88 (m, 4F, F - 2,6)

HRMS (ESI) *m/z* found : 465.0338

(C₁₇H₁₀F₁₀NOP (M-H⁺) requires 465.0335)



1-[(nonafluorobiphenyl-4-yl)-pentafluorophenyl]phosphinoyl]piperidine

m.p. : 146 – 147 °C

IR (KBr, ν_{max} /cm⁻¹) : 2945, 2368, 1684, 1647, 1523, 1481, 1460, 1375, 1344, 1298, 1263, 1229, 1165, 1132, 1099, 1065, 995, 984, 966, 845

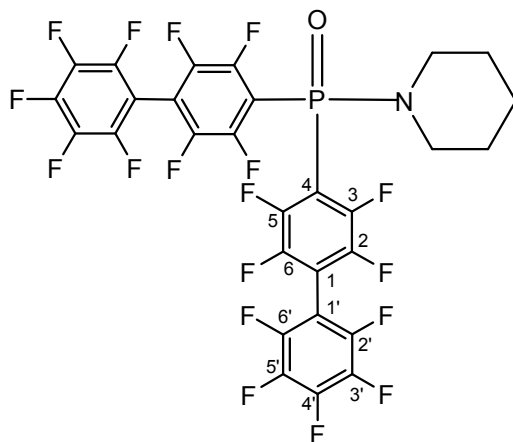
δ_{H} (270MHz, CDCl₃) : 1.56 - 1.72 (m, 6H), 3.18 - 3.23 (m, 4H)

δ_{P} (109.3MHz, CDCl₃) : 3.50 (s)

δ_{F} (376MHz, CDCl₃) : -133.37 - -133.49 (m, 2F, F - 3'', 5''), -133.80 (q, 2F, $J = 11.81$ Hz, F - 3, 5), -136.51 - -136.59 (m, 2F, F - 2'', 6''), -137.81 - -137.89 (m, 2F, F - 2, 6), -145.91 - -146.02 (m, 1F, F - 1''), -149.90 - -150.02 (m, 1F, F - 4'), -159.50 - -159.79 (m, 2F, F - 2', 6'), -160.95 - -161.11 (m, 2F, F - 3', 5')

HRMS (ESI) m/z found : 613.0264

(C₂₃H₁₀F₁₄NOP (M-H⁺) requires 613.0271)



1-[bis(nonafluorobiphenyl-4-yl)-phosphinoyl]piperidine

m.p. : 130 - 131 °C

IR (KBr, ν_{max} /cm⁻¹) : 2928, 2367, 1734, 1684, 1653, 1558, 1533, 1508, 1460, 1375, 1267, 1236, 1167, 1130, 1003, 966

δ_{H} (270MHz, CDCl₃) : 1.55 - 1.71 (m, 6H), 3.23 - 3.29 (m, 4H)

δ_{P} (109.3MHz, CDCl₃) : 3.65 (s)

δ_{F} (376MHz, CDCl₃) : -133.43 (q, 4F, $J = 12.0$ Hz, F - 3,5), -136.33 - -136.42 (m, 4F, F - 2,6), -137.76 - -137.83 (m, 4F, F - 2',6'), -149.88 (t, 2F, $J = 20.8$ Hz, F - 4'), -160.90 - -161.05 (m, 4F, F - 3',5')

HRMS (ESI) m/z found : 761.0209

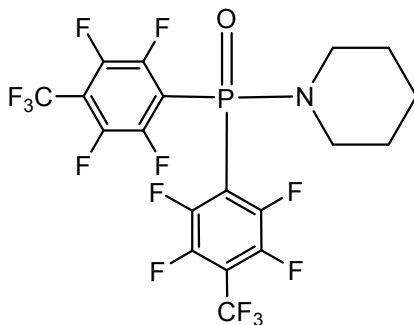
(C₂₉H₁₀F₁₈NOP (M⁻) requires 761.0207)

HRMS (ESI) m/z found : 760.0133

(C₂₉H₁₀F₁₈NOP (M-H)⁻) requires 760.0129)

5.32 Reaction of 4-bromo-2,3,5,6-tetrafluorobenzotrifluoride with (piperidinylamido)phosphoric dichloride

This reaction was done behind a safety screen. A solution of n-butyllithium (8.25 mL, 13.2 mmol) in Et₂O (10 mL) was added dropwise over 30 min to a solution of 4-bromo-2,3,5,6-tetrafluorobenzotrifluoride (2 mL, 13 mmol) in Et₂O (40 mL) at -78 °C under nitrogen. The reaction was exothermic and after 1 h, the mixture was transferred via cannula to a solution of (piperidinylamido)phosphoric dichloride (1.2 g, 6 mmol) in Et₂O (10 mL). 90 min later, the reaction was quenched with HCl (2M; 10 mL). Brine (5 mL) was added and the product was extracted into Et₂O (3 x 50 mL), dried, filtered and then the organic layer was evaporated to give 6.88 g of light yellow solid. The solid was subject to flash chromatography [6 : 1 petroleum spirit (b.p. : 40 – 60 °C) : CH₂Cl₂] and 2 separate portions of white solid were isolated. The white solid was separately recrystallized from EtOAc and hexane to give 1-[bis(2,3,5,6-tetrafluoro-4-trifluoromethylphenyl)-phosphinoyl]piperidine (0.57 g, 7.8%) and 1-[(2,3,5,6,3',6',2'',3'',5'',6''-decafluoro-4,5',4''-tris-trifluoromethyl-[1,1';4',1'']terphenyl-2'-yl)-(2,3,5,6-tetrafluoro-4-trifluoromethyl-phenyl) phosphinoyl]piperidine (0.72 g, 5.8%).



1-[bis(2,3,5,6-tetrafluoro-4-trifluoromethylphenyl)-phosphinoyl]piperidine

m.p. : 156 - 157 °C

IR (KBr, ν_{\max} /cm⁻¹) : 2946, 2364, 1700, 1653, 1461, 1324, 1242, 1156, 1070, 1026, 977, 948, 853

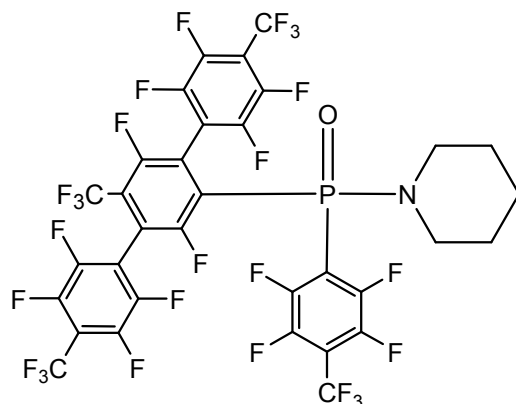
δ_{H} (270MHz, CDCl₃) : 1.55 - 1.70 (m, 6H), 3.16 - 3.23 (m, 4H)

δ_{P} (109.3MHz, CDCl₃) : 2.15 (s)

δ_{F} (376MHz, CDCl₃) : -57.95 (t, 6F, $J = 21.7$ Hz, CF₃), -132.24 (q, 4F, F - 3,5), -138.14 - -138.36 (m, 4F, F - 2,6)

HRMS (EI) m/z found : 566.0350

(C₂₉H₁₀F₁₈NOP (M+H)⁺) requires 566.0349)



1-[(2,3,5,6,3',6',2'',3'',5'',6''-decafluoro-4,5',4''-tris-trifluoromethyl-
[1,1';4',1'']terphenyl-2'-yl)-(2,3,5,6-tetrafluoro-4-trifluoromethyl-phenyl)-
phosphinoyl]piperidine

m.p. : 186 - 187 °C

IR (KBr, $\nu_{\text{max}}/\text{cm}^{-1}$) : 2950, 2361, 1700, 1653, 1502, 1476, 1403, 1342, 1326, 1294, 1222, 1144, 1064, 993, 979, 965, 957

δ_{H} (270MHz, CDCl_3) : 1.54 - 1.65 (m, 6H), 3.05 - 3.17 (m, 4H)

δ_{P} (109.3MHz, CDCl_3) : 4.55 (s)

δ_{F} (376MHz, CDCl_3) : -57.47 (t, 3F, $J = 21.8$ Hz, CF_3), -57.62 (t, 3F, $J = 21.8$ Hz, CF_3), -58.03 (t, 3F, $J = 21.7$ Hz, CF_3), -59.26 (d, 3F, $J = 21.4$ Hz, CF_3), -103.00 (d, 1F, $J = 15.5$ Hz, Ar), -110.59 - -110.81.1 (m, 1F, Ar), -132.50 - -132.58 (m, 2F, Ar), -137.30 - -137.98 (m, 2F, Ar), -138.01 - -138.26 (m, 2F, Ar), -138.50 - -138.59 (m, 2F, Ar), -139.04 - -139.21 (m, 2F, Ar), -139.57 - -139.73 (m, 2F, Ar)

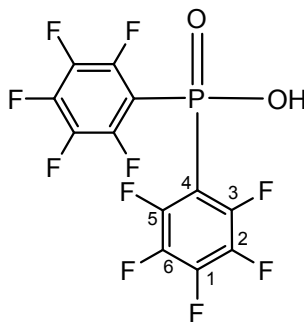
HRMS (ESI) m/z found : 979.0423

($\text{C}_{33}\text{H}_{10}\text{F}_{26}\text{NOP}(\text{M}+\text{NH}_4)^+$) requires 979.0423)

Appendix A shows the XRD crystallography data

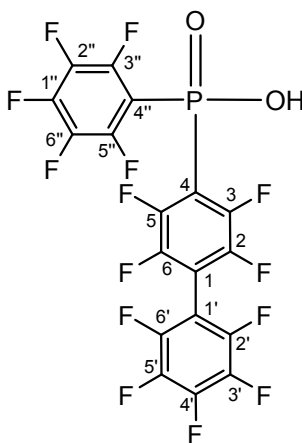
5.33 Preparation of bis(pentafluorophenyl)phosphinic acid via hydrolysis of 1-[bis(pentafluorophenyl)phosphinoyl]piperidine

1-[Bis(pentafluorophenyl)phosphinoyl]piperidine (300 mg, 0.65 mmol) was refluxed with HCl (2M; 12 mL) and acetic acid (12 mL). After 18 h, the solvent was evaporated and the white foam was extracted into Et₂O. After evaporation of Et₂O, 0.6 g of yellow solid was obtained. It was recrystallized from Et₂O and hexane to give the title compound (0.25 g, 98%) as a white solid. From the m. p., ¹⁹F NMR and ³¹P NMR data, this product was found to be identical with the material prepared by alkaline hydrolysis of tri(pentafluorophenyl)phosphine oxide (section 5.26).



5.34 Preparation of nonafluorobiphenyl-4-yl(pentafluorophenyl)phosphinic acid

1-[(Nonafluorobiphenyl-4-yl)-pentafluorophenylphosphinoyl]piperidine (300 mg, 0.49 mmol) was refluxed with HCl (2M; 12 mL) and acetic acid (12 mL). After 18 h, the solvent was evaporated and the white foam was extracted into Et₂O. After evaporation of the Et₂O extract, 0.32 g of yellow solid was obtained. This was recrystallized from Et₂O and hexane to give the title compound (0.16 g, 59%) as a white solid.



m.p. : 168 - 169 °C

IR (KBr, $\nu_{\max}/\text{cm}^{-1}$) : 2364, 1700, 1653, 1560, 1457, 1272, 1110, 983, 965

δ_{P} (109.3MHz, DMSO-*d*₆) : 7.98 (s)

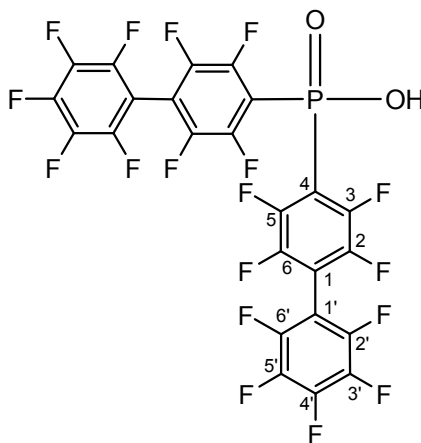
δ_{F} (376MHz, DMSO-*d*₆) : -129.97(d, 2F, $J = 11.33$ Hz, F - 3'',5''), -130.71 (d, 2F, $J = 21.74$ Hz, F - 3,5), -134.52 (s, 2F, F - 2'',6''), -134.79 (s, 2F, F - 2,6), -146.22 (t, 1F, $J = 21.8$ Hz, F - 1''), -146.97(t, 1F, $J = 21.23$ Hz, F - 4'), -157.22 - -157.32 (m, 2F, F - 2',6'), -158.08 - -158.17 (m, 2F, F - 3',5')

HRMS (EI) m/z found : 563.9825

(C₁₈HF₁₄O₂P (M+NH₄)⁺) requires 563.9829)

5.35 Preparation of bis(nonafluorobiphenyl-4-yl)phosphinic acid

1-[Bis-(2,3,5,6,2',3',4',5',6'-nonafluorobiphenyl-4-yl)phosphinoyl]piperidine (670 mg, 0.88 mmol) was refluxed with HCl (2M; 26 mL) and acetic acid (26 mL). After 18 h, the solvent was evaporated and the white foam was extracted with Et₂O. After evaporation of the Et₂O extract, 0.44 g of yellow solid was obtained. This was recrystallized from Et₂O and hexane to give the title compound (0.31 g, 51%) as a white solid.



m.p. : 136 - 137 °C

IR (KBr, ν_{\max} /cm⁻¹) : 2360, 1700, 1653, 1533, 1499, 1460, 1398, 1377, 1334, 1271, 1134, 1082, 995, 965

δ_P (109.3MHz, DMSO-*d*₆) : -10.81 (s)

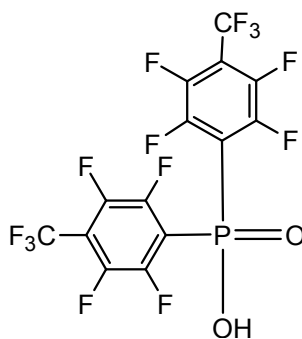
δ_F (376MHz, DMSO-*d*₆) : -130.08 - -130.18 (m, 4F, F - 3,5), -134.79 - -134.82 (m, 4F, F - 2,6), -134.86 - -134.92 (m, 4F, F - 2',6'), -146.28 (t, 2F, *J* = 22.22 Hz, F - 4'), -157.23 - -157.33 (m, 4F, F - 3',5')

HRMS (ESI -) *m/z* found : 692.9354

(C₂₄HF₁₈O₂P (M-H)) requires 692.9354)

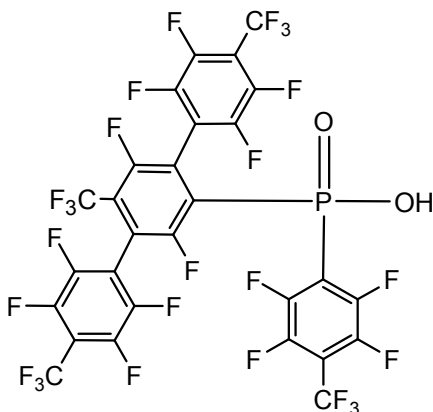
5.36 Preparation of bis[2,3,5,6-tetrafluoro-4(trifluoromethyl)phenyl]phosphinic acid via hydrolysis of 1-[bis-(2,3,5,6-tetrafluoro-4-trifluoromethylphenyl)phosphinoyl]piperidine

1-[Bis-(2,3,5,6-tetrafluoro-4-trifluoromethylphenyl)phosphinoyl]piperidine (540 mg, 0.96 mmol) was refluxed with HCl (2M; 23 mL) and acetic acid (23 mL). After 18 h, the solvent was evaporated and the white foam was extracted with Et₂O. After evaporation of the Et₂O extract, 0.67 g of colourless solid was obtained. This was recrystallized from EtOAc and hexane to give the title compound (0.23 g, 48%) as a white solid. From the m. p., ¹⁹F NMR, ³¹P NMR and mass spectroscopy data, this product was found to be identical with the material prepared by alkaline hydrolysis of tris(2,3,5,6-tetrafluoro-4(trifluoromethyl)phenyl)phosphine oxide (section 5.29).



5.37 Preparation of 1-[(2,3,5,6,3',6',2'',3'',5'',6''-decafluoro-4,5',4''-tris-trifluoromethyl[1,1';4',1'']terphenyl-2'-yl)-(2,3,5,6-tetrafluoro-4-trifluoromethyl-phenyl)]phosphinic acid

1-[(2,3,5,6,3',6',2'',3'',5'',6''-decafluoro-4,5',4''-tris-trifluoromethyl[1,1';4',1'']terphenyl-2'-yl)-(2,3,5,6-tetrafluoro-4-trifluoromethyl-phenyl)phosphinoyl]-piperidine (360 mg, 0.37 mmol) was refluxed with HCl (7 mL) and trifluoroacetic acid (7 mL). After 18 h, the solvent was evaporated and the white foam was extracted into Et₂O. After evaporation of Et₂O, 0.44 g of white solid was obtained. It was recrystallized from EtOAc and hexane to give (0.23 g, 41.8%) of white solid.



m.p. : 126 - 128 °C

IR (KBr, ν_{\max} /cm⁻¹) : 2928, 2372, 1663, 1501, 1404, 1342, 1327, 1292, 1223, 1153, 1072, 995, 964

δ_P (109.3MHz, DMSO-*d*₆) : -11.23 (s)

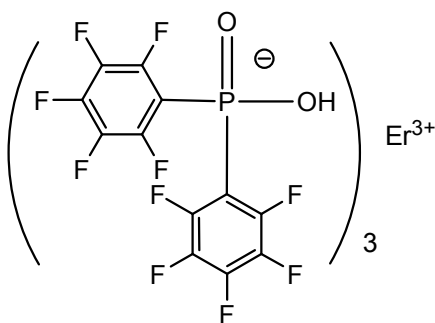
δ_F (376MHz, DMSO-*d*₆) : -52.38 (s, 6F, CF₃), -52.86 (s, 3F, CF₃), -54.29 (s, 3F, CF₃), -100.09 (s, 1F, Ar), -111.45 (s, 1F, Ar), -129.84(s, 2F, Ar), -133.56 (s, 2F, Ar), -134.69 (s, 2F, Ar), -137.31 (s, 2F, Ar), -138.23 (s, 2F, Ar), -139.96(s, 2F, Ar)

HRMS (ESI) *m/z* found : 892.9221

(C₂₈HF₂₆O₂P (M-H)) requires 892.9226)

5.38 Preparation of erbium(III) bis(pentafluorophenyl)phosphinate

Erbium chloride hexahydrate (54.6 mg, 0.14 mmol) was dissolved in H₂O (3 mL) in a vial before a layer of pure H₂O (1 mL) was added to form a layer above it. A solution of bis(pentafluorophenyl)phosphinic acid (170.8 mg, 0.43 mmol) dissolved in Et₂O (3 mL) and MeOH (2 mL) was then added dropwise to the mixture in the vial and a very fine layer of precipitate formed immediately. After 3 days, the precipitate had grown to form a dense layer and it was filtered off. The pink solid was washed with H₂O, Et₂O and MeOH and dried over P₂O₅ to give erbium(III) bis(pentafluorophenyl)phosphinate (0.15 g, 76%). Powder X-ray diffraction data was obtained and was discussed in section 4.4 of chapter 4.



m.p. : >360 °C

IR (KBr, ν_{\max} /cm⁻¹) : 1647, 1528, 1489, 1393, 1304, 1204, 1111, 1084, 1034, 980, 849

m/z (SF-MALDI[+], observed) : 2315.6 (Er₂[(C₆F₅)₂PO₂]₅⁺, 5%), 2316.6 (38), 2317.6 (61), 2318.6 (100), 2319.6 (83), 2320.6 (75), 2321.6 (59), 2322.6 (38), 2323.6 (34), 2324.6 (15); (theoretical) 2315.6 (Er₂[(C₆F₅)₂PO₂]₅⁺, 4%), 2316.6 (35), 2317.6 (65), 2318.6 (100), 2319.6 (88), 2320.6 (87), 2321.6 (62), 2322.6 (48), 2323.6 (22), 2324.6 (13)

m/z (SF-MALDI[-], observed) : 1751.7 (Er[(C₆F₅)₂PO₂]₄⁻, 4%), 1753.7 (74), 1754.7 (98), 1755.7 (100), 1756.7 (42), 1757.7 (43), 1758.7 (22); (theoretical) 1751.7 (Er[(C₆F₅)₂PO₂]₄⁻, 4%), 1753.7 (76), 1754.7 (92), 1755.7 (100), 1756.7 (43), 1757.7 (45), 1758.7 (20)

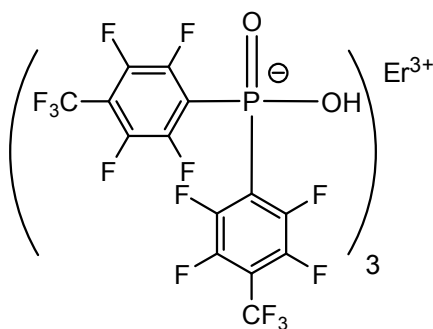
m/z (SF-MALDI[-], observed) : 396.9 ((C₆F₅)₂PO₂⁻, 100%), 397.1 (18), 397.9 (15), 398.9 (2); (theoretical) 396.9 ((C₆F₅)₂PO₂⁻, 100%), 398.0 (13), 398.9 (1)

Found : C, 31.26; H, <0.10; N, <0.10%

(C₃₆F₃₀O₆ErP₃ requires C, 31.83%)

5.39 Preparation of erbium(III) bis(2,3,5,6-tetrafluoro-4(trifluoromethyl)phenyl)phosphinate

Erbium chloride hexahydrate (25 mg, 0.067 mmol) was dissolved in H₂O (5 mL) in a vial before a layer of pure H₂O (1 mL) was added to form a layer above it. A solution of bis(2,3,5,6-tetrafluoro-4(trifluoromethyl)phenyl)phosphinic acid (100 mg, 0.2 mmol) dissolved in Et₂O (1 mL) and MeOH (1 mL) was then added dropwise to the mixture in the vial and a very fine layer of precipitate formed immediately. After 3 days, the precipitate had grown to form a dense layer and it was filtered off. The pink solid was washed with H₂O, Et₂O and MeOH and dried over P₂O₅ to give erbium(III) bis(2,3,5,6-tetrafluoro-4(trifluoromethyl)phenyl)phosphinate (94 mg, 86%).



m.p. : >360 °C

IR (KBr, $\nu_{\max}/\text{cm}^{-1}$) : 1491, 1464, 1331, 1213, 1167, 1094, 976, 957

m/z (SF-MALDI[+], observed) : 2816.4 ($\text{Er}_2[(\text{C}_7\text{F}_7)_2\text{PO}_2]_5^+$, 18%), 2817.4 (49), 2818.4 (100), 2819.4 (75), 2820.4 (65), 2821.4 (57), 2822.4 (45), 2823.4 (17), 2824.4 (17); (theoretical) 2816.6 ($\text{Er}_2[(\text{C}_7\text{F}_7)_2\text{PO}_2]_5^+$, 33%), 2817.6 (64), 2818.6 (100), 2819.6 (93), 2820.6 (91), 2821.6 (68), 2822.6 (52), 2823.6 (26), 2824.6 (15)

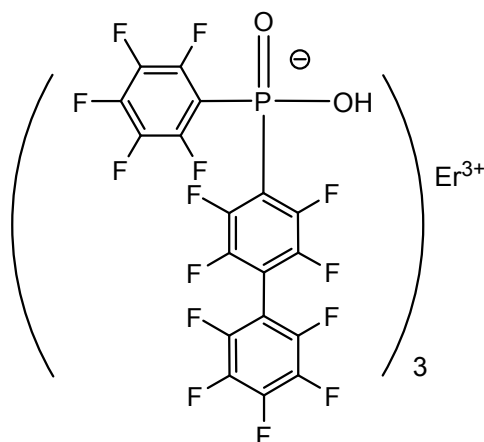
m/z (SF-MALDI[-], observed) : 2151.7 ($\text{Er}[(\text{C}_7\text{F}_7)_2\text{PO}_2]_4^-$, 3%), 2152.7 (3), 2153.7 (70), 2154.7 (92), 2155.7 (100), 2156.7 (50), 2157.7 (40), 2158.7 (19), 2159.7 (5); (theoretical) 2151.7 ($\text{Er}[(\text{C}_7\text{F}_7)_2\text{PO}_2]_4^-$, 4%), 2152.7 (3), 2153.7 (70), 2154.7 (92), 2155.7 (100), 2156.7 (48), 2157.7 (46), 2158.7 (23), 2159.7 (7)

m/z (SF-MALDI[-], observed) : 494.9 ($(\text{C}_7\text{F}_7)_2\text{PO}_2^-$, 4%), 496.9 (100), 497.9 (15); (theoretical) 496.9 ($(\text{C}_7\text{F}_7)_2\text{PO}_2^-$, 100%), 497.9 (15)

Found : C, 30.87%
($\text{C}_{42}\text{F}_{42}\text{O}_6\text{ErP}_3$ requires C, 30.42%)

5.40 Preparation of erbium(III) (nonafluorobiphenyl-4-yl)(pentafluorophenyl)phosphinate

Erbium chloride hexahydrate (18.6 mg, 0.049 mmol) was dissolved in H₂O (3 mL) in a vial before a layer of pure H₂O (1 mL) was added to form a layer above it. A solution of (nonafluorobiphenyl-4-yl)(pentafluorophenyl)phosphinic acid (80 mg, 0.15 mmol) dissolved in Et₂O (3 mL) and MeOH (2 mL) was then added dropwise to the mixture in the vial and a very fine layer of precipitate formed immediately. After 3 days, the precipitate had grown to form a dense layer and it was filtered off. The pink solid was washed with H₂O, Et₂O and MeOH and dried over P₂O₅ to give erbium(III) (nonafluorobiphenyl-4-yl)(pentafluorophenyl)phosphinate (59.6 mg, 68%).



m.p. : >300 °C

IR (KBr, ν_{\max} /cm⁻¹) : 1647, 1528, 1489, 1466, 1396, 1304, 1273, 1211, 1134, 1111, 1088, 1007, 968

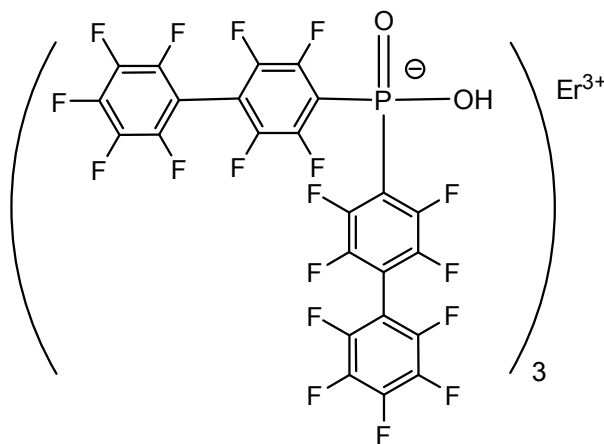
m/z (SF-MALDI[+], observed) : 3055.7 (Er₂(C₁₈F₁₄O₂P)₅⁺, 4%), 3056.6 (18), 3057.6 (57), 3058.6 (85), 3059.6 (100), 3060.7 (82), 3061.6 (66), 3062.7 (55), 3063.7 (40), 3064.6 (16), 3065.7 (10), 3066.7 (8), 3067.7 (5), 3069.1(6); (theoretical) 3054.6 (Er₂(C₁₈F₁₄O₂P)₅⁺, 3%), 3055.6 (4), 3056.6 (30), 3057.6 (60), 3058.6 (99), 3059.6 (100), 3060.6 (98), 3061.6 (77), 3062.6 (60), 3063.6 (35), 3064.6 (19), 3065.6 (10), 3066.6 (4)

m/z (SF-MALDI[-], observed) : 2343.7 (Er(C₁₈F₁₄O₂P)₄⁻, 7%), 2344.7 (13), 2345.7 (46), 2346.7 (87), 2347.7 (100), 2348.7 (54), 2349.7 (43), 2350.7 (34), 2351.7 (9), 2352.7 (7) (theoretical) 2343.7 (Er(C₁₈F₁₄O₂P)₄⁻, 3%), 2344.7 (2), 2345.7 (60), 2346.7 (89), 2347.7 (100), 2348.7 (58), 2349.7 (48), 2350.7 (27), 2351.7 (11), 2352.7 (3)

m/z (SF-MALDI[-], observed) : 544.9 (C₁₈F₁₄PO₂⁻, 100%), 545.1 (16), 545.9 (21), 546.1 (3), 546.9 (3); (theoretical) 544.9 (C₁₈F₁₄PO₂⁻, 100%), 545.9 (20), 546.9 (2)

5.41 Preparation of erbium(III) bis(nonafluorobiphenyl-4-yl)phosphinate

Erbium chloride hexahydrate (36.7 mg, 0.096 mmol) was dissolved in H₂O (3 mL) in a vial before a layer of pure H₂O (1 mL) was added to form a layer above it. A solution of bis(nonafluorobiphenyl-4-yl)phosphinic acid (0.2 g, 0.29 mmol) dissolved in Et₂O (3 mL) and MeOH (2 mL) was then added dropwise to the mixture in the vial and a very fine layer of precipitate formed immediately. After 3 days, the precipitate had grown to form a dense layer and it was filtered off. The pink solid was washed with H₂O, Et₂O and MeOH and dried over P₂O₅ to give erbium(III) bis(nonafluorobiphenyl-4-yl)phosphinate (0.14 g, 66%).



m.p. : >300 °C

IR (KBr, ν_{\max} /cm⁻¹) : 1655, 1531, 1501, 1458, 1400, 1381, 1335, 1273, 1211, 1134, 1092, 1003, 968

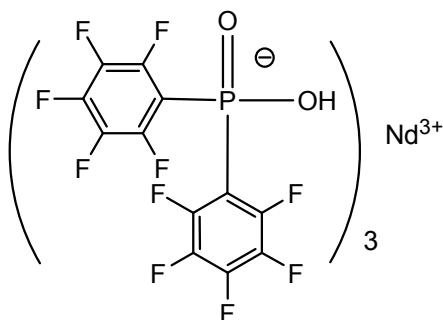
m/z (SF-MALDI[+], observed) : 3794.7 (Er₂(C₂₄F₁₈O₂P)₅⁺, 3%), 3795.6 (2), 3796.6 (16), 3797.6 (36), 3798.6 (78), 3799.6 (84), 3800.6 (100), 3801.6 (50), 3802.6 (49), 3803.6 (35), 3804.6 (27), 3805.6 (13), 3806.6 (11), 3807.8 (7), 3808.6 (6), 3810.7 (8); (theoretical) 3794.5 (Er₂(C₂₄F₁₈O₂P)₅⁺, 2%), 3795.5 (4), 3796.5 (23), 3797.5 (53), 3798.5 (88), 3799.5 (99), 3800.5 (100), 3801.5 (86), 3802.5 (68), 3803.5 (44), 3804.5 (27), 3805.6 (14), 3806.6 (6), 3807.6 (2)

m/z (SF-MALDI[-], observed) : 2937.8 (Er(C₂₄F₁₈O₂P)₄⁻, 44%), 2938.8 (49), 2939.8 (100), 2940.8 (50), 2941.8 (32), 2942.8 (22), 2943.8 (12) (theoretical) 2935.7 (Er(C₂₄F₁₈O₂P)₄⁻, 2%), 2936.7 (3), 2937.7 (49), 2938.7 (84), 2939.7 (100), 2940.7 (70), 2941.7 (54), 2942.7 (35), 2943.7 (15), 2944.7 (6)

m/z (SF-MALDI[-], observed) : 692.9 (C₂₄F₁₈PO₂⁻, 100%), 693.1 (25), 693.9 (40), 694.1 (7), 694.9 (5); (theoretical) 692.9 (C₂₄F₁₈PO₂⁻, 100%), 693.9 (27), 694.9 (3)

5.42 Preparation of neodymium(III) bis(pentafluorophenyl)phosphinate

Neodymium chloride hexahydrate (2.5 mg, 0.01 mmol) was dissolved in H₂O (1 mL) in a vial before a layer of pure H₂O (1 mL) was added to form a layer above it. A solution of bis(pentafluorophenyl)phosphinic acid (11.9 mg, 0.03 mmol) dissolved in Et₂O (1 mL) and MeOH (1 mL) was then added dropwise to the mixture in the vial and a very fine layer of precipitate formed immediately. After 3 days, the precipitate had grown to form a dense layer and it was filtered off. The light purple solid was washed with H₂O, Et₂O and MeOH and dried over P₂O₅ to give neodymium(III) bis(pentafluorophenyl)phosphinate (6.5 mg, 49%).



m.p. : >360 °C

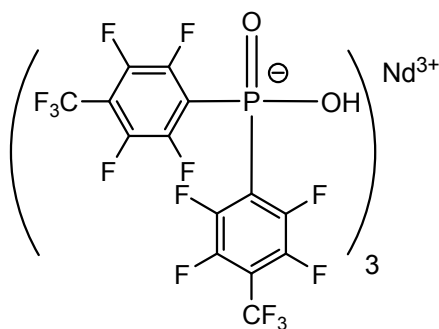
IR (KBr, ν_{\max} /cm⁻¹) : 1648, 1525, 1488, 1478, 1391, 1305, 1195, 1108, 1076, 1031, 979

m/z (SF-MALDI[+], observed) : 2268.5 (Nd₂[(C₆F₅)₂PO₂]₅⁺, 25%), 2269.5 (34), 2270.5 (63), 2271.5 (78), 2272.5 (100), 2273.5 (72), 2274.5 (79), 2275.5 (50), 2276.5 (49), 2277.5 (44), 2278.5 (35), 2279.5 (15), 2280.5 (12), 2281.5 (6), 2282.5 (9), 2283.6 (4); (theoretical) 2268.6 (Nd₂[(C₆F₅)₂PO₂]₅⁺, 26%), 2269.6 (42), 2270.6 (74), 2271.6 (79), 2272.6 (100), 2273.6 (84), 2274.6 (82), 2275.6 (55), 2276.6 (54), 2277.6 (37), 2278.6 (32), 2279.6 (20), 2280.6 (15), 2281.6 (8), 2282.6 (5), 2283.6 (3)

m/z (SF-MALDI[-], observed) : 1729.7 (Nd[(C₆F₅)₂PO₂]₄⁻, 87%), 1730.7 (89), 1731.7 (100), 1732.7 (90), 1733.7 (91), 1734.7 (30), 1735.7 (28), 1736.7 (17), 1737.7 (20), 1738.7 (18); (theoretical) 1729.7 (Nd[(C₆F₅)₂PO₂]₄⁻, 78%), 1730.7 (77), 1731.7 (100), 1732.7 (68), 1733.7 (75), 1734.7 (33), 1735.7 (26), 1736.7 (11), 1737.7 (20), 1738.7 (10), 1739.7 (3)

5.43 Preparation of neodymium(III) bis(2,3,5,6-tetrafluoro-4(trifluoromethyl)phenyl)phosphinate

Neodymium chloride hexahydrate (5 mg, 0.02 mmol) was dissolved in H₂O (1 mL) in a vial before a layer of pure H₂O (1 mL) was added to form a layer above it. A solution of bis(2,3,5,6-tetrafluoro-4(trifluoromethyl)phenyl)phosphinic acid (30 mg, 0.06 mmol) dissolved in Et₂O (1 mL) and MeOH (1 mL) was then added dropwise to the mixture in the vial and a very fine layer of precipitate formed immediately. After 3 days, the precipitate had grown to form a dense layer and it was filtered off. The light purple solid was washed with H₂O, Et₂O and MeOH and dried over P₂O₅ to give neodymium(III) bis(2,3,5,6-tetrafluoro-4(trifluoromethyl)phenyl)phosphinate (11 mg, 34%).



m.p. : >360 °C

IR (KBr, $\nu_{\max}/\text{cm}^{-1}$) : 1655, 1597, 1464, 1426, 1387, 1332, 1256, 1208, 1164, 1086, 977, 956

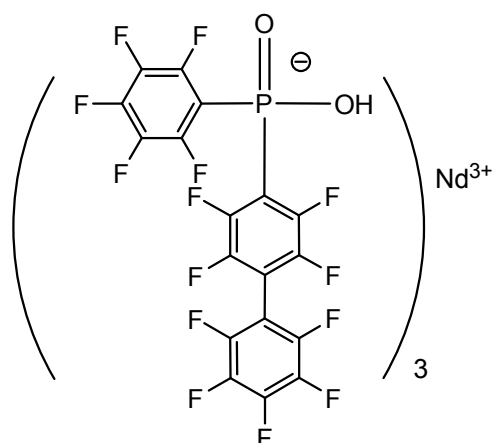
m/z (SF-MALDI[+], observed) : 2768.5 (Nd₂[(C₇F₇)₂PO₂]₅⁺, 24%), 2769.5 (48), 2770.5 (82), 2771.5 (89), 2772.5 (100), 2773.6 (94), 2774.5 (85), 2775.5 (68), 2776.5 (61), 2777.5 (35), 2778.5 (36), 2779.5 (25), 2780.6 (24), 2781.5 (9), 2782.9 (5); (theoretical) 2768.5 (Nd₂[(C₇F₇)₂PO₂]₅⁺, 24%), 2769.5 (41), 2770.5 (72), 2771.5 (82), 2772.5 (100), 2773.5 (86), 2774.5 (84), 2775.5 (60), 2776.5 (58), 2777.5 (40), 2778.5 (33), 2779.5 (21), 2780.5 (16), 2781.5 (9), 2782.5 (6)

m/z (SF-MALDI[-], observed) : 2129.7 (Nd[(C₇F₇)₂PO₂]₄⁻, 87%), 2130.7 (85), 2131.7 (100), 2132.7 (68), 2133.7 (70), 2134.7 (40), 2135.7 (28), 2136.7 (10), 2137.7 (10), 2138.6 (11); (theoretical) 2129.7 (Nd[(C₇F₇)₂PO₂]₄⁻, 74%), 2130.7 (79), 2131.7 (100), 2132.7 (73), 2133.7 (76), 2134.7 (37), 2135.7 (28), 2136.7 (12), 2137.7 (20), 2138.7 (11), 2139.7 (4)

m/z (SF-MALDI[-], observed) : 496.9 ((C₇F₇)₂PO₂⁻, 100%), 497.1 (11), 497.9 (17), 498.9 (2); (theoretical) 496.9 ((C₇F₇)₂PO₂⁻, 100%), 497.9 (15)

5.44 Preparation of neodymium(III) (nonafluorobiphenyl-4-yl)(pentafluorophenyl)phosphinate

Neodymium chloride hexahydrate (2.5 mg, 0.01 mmol) was dissolved in H₂O (1 mL) in a vial before a layer of pure H₂O (1 mL) was added to form a layer above it. A solution of (nonafluorobiphenyl-4-yl)(pentafluorophenyl)phosphinic acid (16 mg, 0.03 mmol) dissolved in Et₂O (1 mL) and MeOH (1 mL) was then added dropwise to the mixture in the vial and a very fine layer of precipitate formed immediately. After 3 days, the precipitate had grown to form a dense layer and it was filtered off. The light purple solid was washed with H₂O, Et₂O and MeOH and dried over P₂O₅ to give neodymium(III) (nonafluorobiphenyl-4-yl)(pentafluorophenyl)phosphinate (7 mg, 39%).



m.p. : >300 °C

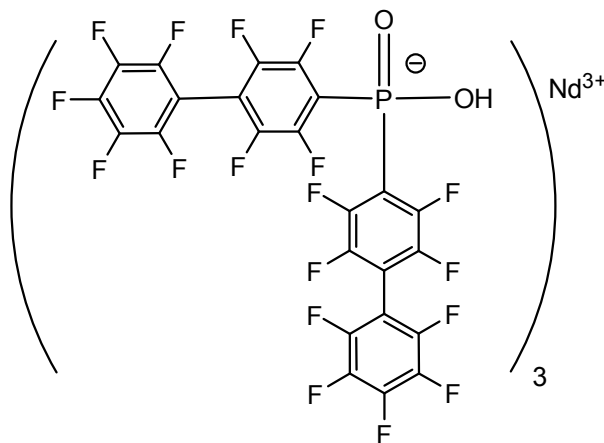
IR (KBr, ν_{\max} /cm⁻¹) : 1657, 1647, 1531, 1504, 1483, 1462, 1396, 1333, 1304, 1271, 1206, 1135, 1108, 1082, 1038, 1006, 983, 968

m/z (SF-MALDI[+], observed) : 3008.5 Nd₂(C₁₈F₁₄O₂P)₅⁺, 23%), 3009.5 (40), 3010.5 (45), 3011.5 (84), 3012.5 (79), 3013.5 (88), 3014.5 (100), 3015.5 (74), 3016.5 (49), 3017.5 (36), 3018.5 (41), 3019.5 (32), 3020.5 (17), 3021.5 (16), 3022.7 (9), 3023.5 (9), 3024.5 (7); (theoretical) 3008.5 Nd₂(C₁₈F₁₄O₂P)₅⁺, 20%), 3009.5 (39), 3010.5 (69), 3011.5 (82), 3012.5 (100), 3013.5 (94), 3014.5 (87), 3015.5 (68), 3016.5 (61), 3017.5 (46), 3018.5 (39), 3019.5 (26), 3020.5 (20), 3021.5 (12), 3022.5 (6), 3023.5 (4), 3024.5 (3), 3025.5 (2)

m/z (SF-MALDI[-], observed) : 2321.7 (Nd(C₁₈F₁₄O₂P)₄⁻, 35%), 2322.7 (39), 2323.7 (100), 2324.7 (59), 2325.8 (59), 2326.5 (18), 2327.5 (9), 2329.5 (20), 2329.6 (15), 2329.7 (14), 2331.9 (4), 2333.5 (9) (theoretical) 2321.7 (Nd(C₁₈F₁₄O₂P)₄⁻, 64%), 2322.7 (80), 2323.7 (100), 2324.7 (80), 2325.7 (78), 2326.7 (46), 2327.7 (32), 2328.7 (17), 2329.7 (20), 2330.7 (14), 2331.7 (6), 2332.7 (2)

5.45 Preparation of neodymium(III) bis(nonafluorobiphenyl-4-yl)phosphinate

Neodymium chloride hexahydrate (2.5 mg, 0.01 mmol) was dissolved in H₂O (1 mL) in a vial before a layer of pure H₂O (1 mL) was added to form a layer above it. A solution of bis(nonafluorobiphenyl-4-yl)phosphinic acid (20.9 mg, 0.03 mmol) dissolved in Et₂O (1 mL) and MeOH (1 mL) was then added dropwise to the mixture in the vial and a very fine layer of precipitate formed immediately. After 3 days, the precipitate had grown to form a dense layer and it was filtered off. The light purple solid was washed with H₂O, Et₂O and MeOH and dried over P₂O₅ to give neodymium(III) bis(nonafluorobiphenyl-4-yl)phosphinate (10 mg, 45%).



m.p. : >300 °C

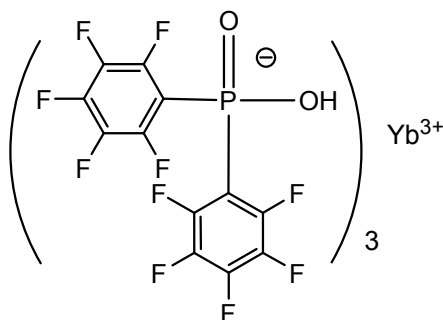
IR (KBr, ν_{\max} /cm⁻¹) : 1658, 1581, 1533, 1502, 1461, 1399, 1380, 1335, 1272, 1206, 1135, 1085, 1038, 1004, 968

m/z (SF-MALDI[+], observed) : 3748.5 (Nd₂(C₂₄F₁₈O₂P)₅⁺, 10%), 3749.5 (34), 3750.5 (66), 3751.5 (80), 3752.5 (94), 3753.5 (100), 3754.5 (75), 3755.5 (54), 3756.4 (56), 3757.5 (49), 3758.4 (38), 3759.5 (40), 3760.5 (16), 3761.5 (15), 3762.4 (14), 3763.5 (10), 3764.6 (8), 3765.6 (4), 3766.5 (9); (theoretical) 3748.5 (Nd₂(C₂₄F₁₈O₂P)₅⁺, 15%), 3749.5 (35), 3750.5 (64), 3751.5 (81), 3752.5 (100), 3753.5 (99), 3754.5 (94), 3755.5 (77), 3756.5 (67), 3757.5 (53), 3758.5 (43), 3759.5 (30), 3760.5 (22), 3761.5 (14), 3762.5 (9), 3763.5 (5)

m/z (SF-MALDI[-], observed) : 2913.7 (Nd(C₂₄F₁₈O₂P)₄⁻, 58%), 2914.7 (94), 2915.7 (100), 2916.7 (82), 2917.7 (83), 2918.7 (50), 2919.7 (36), 2920.7 (13), 2921.7 (39), 2922.7 (15), 2923.8 (9), 2926.6 (12) (theoretical) 2913.6 (Nd(C₂₄F₁₈O₂P)₄⁻, 52%), 2914.6 (78), 2915.7 (100), 2916.7 (88), 2917.7 (84), 2918.7 (54), 2919.7 (36), 2920.7 (20), 2921.7 (19), 2922.7 (14), 2923.7 (7)

5.46 Preparation of ytterbium(III) bis(pentafluorophenyl)phosphinate

Ytterbium chloride hexahydrate (3.9 mg, 0.01 mmol) was dissolved in H₂O (1 mL) in a vial before a layer of pure H₂O (1 mL) was added to form a layer above it. A solution of bis(pentafluorophenyl)phosphinic acid (11.9 mg, 0.03 mmol) dissolved in Et₂O (1 mL) and MeOH (1 mL) was then added dropwise to the mixture in the vial and a very fine layer of precipitate formed immediately. After 3 days, the precipitate had grown to form a dense layer and it was filtered off. The white solid was washed with H₂O, Et₂O and MeOH and dried over P₂O₅ to give ytterbium(III) bis(pentafluorophenyl)phosphinate (8 mg, 58%).



m.p. : >360 °C

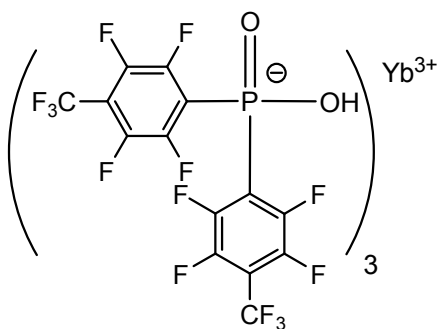
IR (KBr, ν_{max} /cm⁻¹) : 1649, 1526, 1488, 1478, 1392, 1305, 1204, 1111, 1084, 1033, 979

m/z (SF-MALDI[+], observed) : 2326.6 (Yb₂[(C₆F₅)₂PO₂]₅⁺, 12%), 2327.6 (32), 2328.6 (58), 2329.6 (80), 2330.6 (100), 2331.6 (89), 2332.6 (82), 2333.6 (55), 2334.6 (54), 2335.6 (33), 2336.7 (12), 2337.7 (10); (theoretical) 2325.6 (Yb₂[(C₆F₅)₂PO₂]₅⁺, 4%), 2326.6 (14), 2327.6 (32), 2328.6 (55), 2329.6 (82), 2330.6 (100), 2331.6 (95), 2332.6 (96), 2333.6 (61), 2334.6 (50), 2335.6 (25), 2336.6 (12), 2337.6 (5)

m/z (SF-MALDI[-], observed) : 1757.7 (Yb[(C₆F₅)₂PO₂]₄⁻, 7%), 1758.7 (40), 1759.7 (75), 1760.7 (74), 1761.7 (100), 1762.7 (54), 1763.7 (53), 1764.7 (19); (theoretical) 1757.7 (Yb[(C₆F₅)₂PO₂]₄⁻, 7%), 1758.7 (36), 1759.7 (68), 1760.7 (68), 1761.7 (100), 1762.7 (46), 1763.7 (43), 1764.7 (18), 1765.7 (5)

5.47 Preparation of ytterbium(III) bis(2,3,5,6-tetrafluoro-4(trifluoromethyl)phenyl)phosphinate

Ytterbium chloride hexahydrate (2.7 mg, 0.007 mmol) was dissolved in H₂O (1 mL) in a vial before a layer of pure H₂O (1 mL) was added to form a layer above it. A solution of bis(2,3,5,6-tetrafluoro-4(trifluoromethyl)phenyl)phosphinic acid (10 mg, 0.02 mmol) dissolved in Et₂O (1 mL) and MeOH (1 mL) was then added dropwise to the mixture in the vial and a very fine layer of precipitate formed immediately. After 3 days, the precipitate had grown to form a dense layer and it was filtered off. The white solid was washed with H₂O, Et₂O and MeOH and dried over P₂O₅ to give ytterbium(III) bis(2,3,5,6-tetrafluoro-4(trifluoromethyl)phenyl)phosphinate (8 mg, 69%).



m.p. : >300 °C

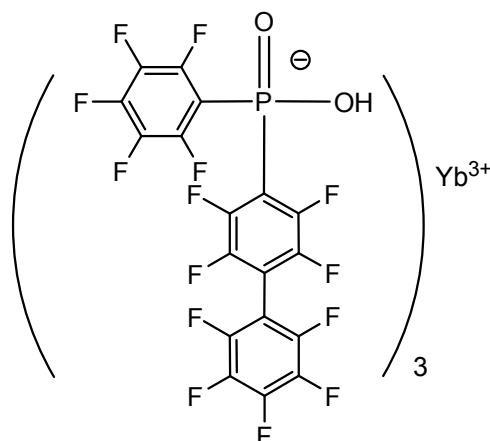
IR (KBr, ν_{\max} /cm⁻¹) : 1655, 1598, 1465, 1427, 1388, 1332, 1256, 1215, 1168, 1095, 978, 956

m/z (SF-MALDI[+], observed) : 2826.7 (Yb₂[(C₇F₇)₂PO₂]₅⁺, 7%), 2827.6 (27), 2828.6 (48), 2829.6 (68), 2830.6 (97), 2831.6 (100), 2832.6 (84), 2833.6 (61), 2834.6 (50), 2835.6 (27), 2836.6 (20), 2838.7 (9), 2840.7 (7), 2842.8 (4); (theoretical) 2825.6 (Yb₂[(C₇F₇)₂PO₂]₅⁺, 3%), 2826.6 (12), 2827.6 (30), 2828.6 (54), 2829.6 (81), 2830.6 (100), 2831.6 (98), 2832.6 (99), 2833.6 (65), 2834.6 (53), 2835.6 (27), 2836.6 (15), 2837.6 (6), 2838.6 (2)

m/z (SF-MALDI[-], observed) : 2157.7 (Yb[(C₇F₇)₂PO₂]₄⁻, 5%), 2158.7 (34), 2159.7 (64), 2160.7 (72), 2161.7 (100), 2162.7 (45), 2163.7 (44), 2164.7 (20); (theoretical) 2157.7 (Yb[(C₇F₇)₂PO₂]₄⁻, 6%), 2158.7 (34), 2159.7 (66), 2160.7 (70), 2161.7 (100), 2162.7 (52), 2163.7 (44), 2164.7 (21), 2165.7 (7)

5.48 Preparation of ytterbium(III) (nonafluorobiphenyl-4-yl)(pentafluorophenyl)phosphinate

Ytterbium chloride hexahydrate (3.9 mg, 0.01 mmol) was dissolved in H₂O (1 mL) in a vial before a layer of pure H₂O (1 mL) was added to form a layer above it. A solution of (nonafluorobiphenyl-4-yl)(pentafluorophenyl)phosphinic acid (16 mg, 0.03 mmol) dissolved in Et₂O (1 mL) and MeOH (1 mL) was then added dropwise to the mixture in the vial and a very fine layer of precipitate formed immediately. After 3 days, the precipitate had grown to form a dense layer and it was filtered off. The white solid was washed with H₂O, Et₂O and MeOH and dried over P₂O₅ to give ytterbium(III) (nonafluorobiphenyl-4-yl)(pentafluorophenyl)phosphinate (7 mg, 38%).



m.p. : >300 °C

IR (KBr, ν_{\max} /cm⁻¹) : 1649, 1531, 1504, 1486, 1462, 1397, 1333, 1304, 1272, 1213, 1135, 1111, 1089, 1037, 1006, 984, 969

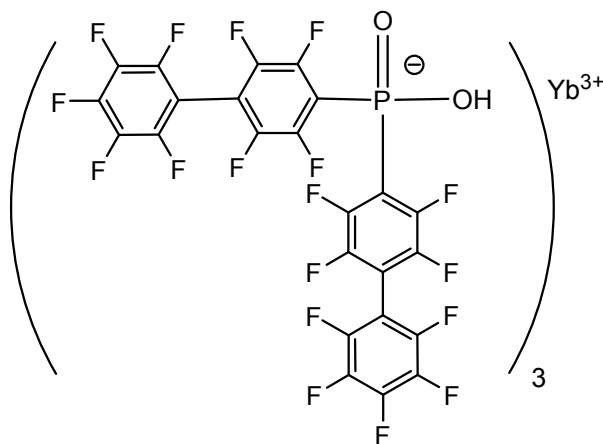
m/z (SF-MALDI[+], observed) : 3065.5 (Yb₂(C₁₈F₁₄O₂P)₅⁺, 5%), 3066.5 (8), 3067.5 (32), 3068.5 (52), 3069.5 (84), 3070.5 (100), 3071.5 (95), 3072.5 (90), 3073.5 (74), 3074.5 (65), 3075.5 (38), 3076.5 (21), 3077.6 (11); (theoretical) 3065.6

(Yb₂(C₁₈F₁₄O₂P)₅⁺, 3%), 3066.6 (11), 3067.6 (26), 3068.6 (49), 3069.6 (76), 3070.6 (96), 3071.6 (100), 3072.6 (99), 3073.6 (74), 3074.6 (57), 3075.6 (33), 3076.6 (18), 3077.6 (8), 3078.6 (3)

m/z (SF-MALDI[-], observed) : 2349.7 (Yb(C₁₈F₁₄O₂P)₄⁻, 15%), 2350.7 (38), 2351.7 (66), 2352.7 (99), 2353.7 (100), 2354.7 (65), 2355.7 (80), 2356.7 (44), 2357.7 (11), 2358.7 (9) (theoretical) 2349.7 (Yb(C₁₈F₁₄O₂P)₄⁻, 6%), 2350.7 (32), 2351.7 (65), 2352.7 (73), 2353.7 (100), 2354.7 (62), 2355.7 (47), 2356.7 (26), 2357.7 (10), 2358.7 (3)

5.49 Preparation of ytterbium(III) bis(nonafluorobiphenyl-4-yl)phosphinate

Ytterbium chloride hexahydrate (3.9 mg, 0.01 mmol) was dissolved in H₂O (1 mL) in a vial before a layer of pure H₂O (1 mL) was added to form a layer above it. A solution of bis(nonafluorobiphenyl-4-yl)phosphinic acid (20.9 mg, 0.03 mmol) dissolved in Et₂O (1 mL) and MeOH (1 mL) was then added dropwise to the mixture in the vial and a very fine layer of precipitate formed immediately. After 3 days, the precipitate had grown to form a dense layer and it was filtered off. The white solid was washed with H₂O, Et₂O and MeOH and dried over P₂O₅ to give ytterbium(III) bis(nonafluorobiphenyl-4-yl)phosphinate (9 mg, 40%).



m.p. : >300 °C

IR (KBr, ν_{max} /cm⁻¹) : 1658, 1579, 1534, 1502, 1461, 1399, 1379, 1334, 1272, 1214, 1136, 1093, 1039, 998, 967

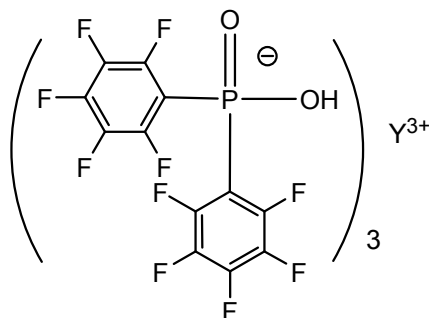
m/z (SF-MALDI[+], observed) : 3806.5 (Yb₂(C₂₄F₁₈O₂P)₅⁺, 8%), 3807.5 (18), 3808.5 (43), 3809.5 (65), 3810.5 (78), 3811.5 (98), 3812.5 (100), 3813.5 (86), 3814.5 (71), 3815.5 (40), 3816.5 (30), 3817.6 (16), 3818.5 (9); (theoretical) 3806.5

(Yb₂(C₂₄F₁₈O₂P)₅⁺, 8%), 3807.5 (22), 3808.5 (42), 3809.6 (68), 3810.6 (90), 3811.6 (99), 3812.6 (100), 3813.6 (80), 3814.6 (62), 3815.6 (40), 3816.6 (24), 3817.6 (12), 3818.6 (5)

m/z (SF-MALDI[-], observed) : 2941.6 (Yb(C₂₄F₁₈O₂P)₄⁻, 9%), 2942.6 (34), 2943.6 (50), 2944.6 (71), 2945.7 (100), 2946.7 (89), 2947.6 (60), 2948.7 (36), 2949.7 (20); (theoretical) 2941.7 (Yb(C₂₄F₁₈O₂P)₄⁻, 5%), 2942.7 (26), 2943.7 (60), 2944.7 (75), 2945.7 (100), 2946.7 (75), 2947.7 (55), 2948.7 (34), 2949.7 (15), 2950.7 (5), 2951.7 (2)

5.50 Preparation of yttrium(III) bis(pentafluorophenyl)phosphinate

Yttrium chloride hexahydrate (3 mg, 0.01 mmol) was dissolved in H₂O (1 mL) in a vial before a layer of pure H₂O (1 mL) was added to form a layer above it. A solution of bis(pentafluorophenyl)phosphinic acid (11.9 mg, 0.03 mmol) dissolved in Et₂O (1 mL) and MeOH (1 mL) was then added dropwise to the mixture in the vial and a very fine layer of precipitate formed immediately. After 3 days, the precipitate had grown to form a dense layer and it was filtered off. The white solid was washed with H₂O, Et₂O and MeOH and dried over P₂O₅ to give yttrium(III) bis(pentafluorophenyl)phosphinate (7 mg, 55%). Powder X-ray diffraction data was obtained and was discussed in section 4.4 of chapter 4.



m.p. : >360 °C

IR (KBr, ν_{\max} /cm⁻¹) : 1648, 1526, 1489, 1478, 1392, 1305, 1204, 1111, 1083, 1032, 979

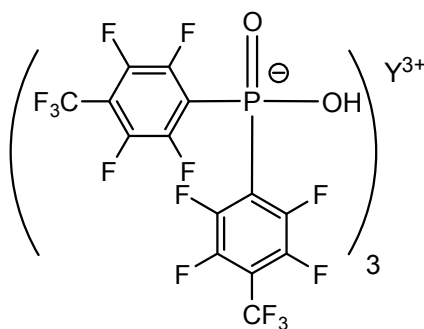
m/z (SF-MALDI[+], observed) : 2162.5 (Y₂[(C₆F₅)₂PO₂]₅⁺, 100%), 2163.5 (56), 2164.6 (32), 2165.6 (11) (theoretical) 2162.5 (Y₂[(C₆F₅)₂PO₂]₅⁺, 100%), 2163.6 (68), 2164.6 (25), 2165.6 (7)

m/z (SF-MALDI[-], observed) : 1676.7 (Y[(C₆F₅)₂PO₂]₄⁻, 100%), 1677.0 (9), 1677.7 (54), 1678.0 (8), 1678.7 (12); (theoretical) 1676.7 (Y[(C₆F₅)₂PO₂]₄⁻, 100%), 1677.7 (54), 1678.7 (16), 1679.7 (3)

m/z (SF-MALDI[-], observed) : 396.9 (C₁₂F₁₀PO₂⁻, 100%), 397.1 (17), 397.9 (13), 398.4 (2), 398.9 (5), 399.0 (16), 400.0 (3), 400.7 (2), 401.9 (2); (theoretical) 396.9 (C₁₈F₁₄PO₂⁻, 100%), 398.0 (14)

5.51 Preparation of yttrium(III) bis(2,3,5,6-tetrafluoro-4(trifluoromethyl)phenyl)phosphinate

Yttrium chloride hexahydrate (3 mg, 0.01 mmol) was dissolved in H₂O (1 mL) in a vial before a layer of pure H₂O (1 mL) was added to form a layer above it. A solution of bis(2,3,5,6-tetrafluoro-4(trifluoromethyl)phenyl)phosphinic acid (15 mg, 0.03 mmol) dissolved in Et₂O (1 mL) and MeOH (1 mL) was then added dropwise to the mixture in the vial and a very fine layer of precipitate formed immediately. After 3 days, the precipitate had grown to form a dense layer and it was filtered off. The white solid was washed with H₂O, Et₂O and MeOH and dried over P₂O₅ to give yttrium(III) bis(2,3,5,6-tetrafluoro-4(trifluoromethyl)phenyl)phosphinate (8 mg, 51%).



m.p. : >300 °C

IR (KBr, $\nu_{\max}/\text{cm}^{-1}$) : 1655, 1597, 1487, 1465, 1426, 1388, 1332, 1256, 1217, 1167, 1093, 978, 956

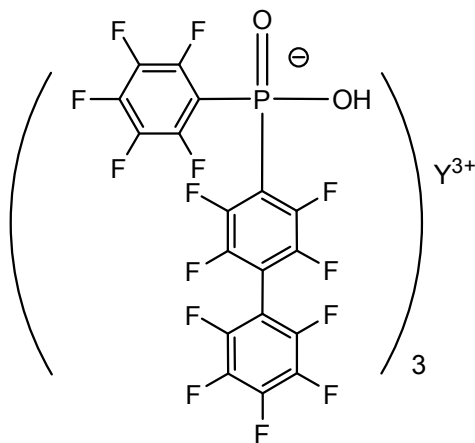
m/z (SF-MALDI[+], observed) : 2662.5 (Y₂[(C₇F₇)₂PO₂]₅⁺, 100%), 2663.5 (66), 2664.5 (26), 2665.5 (10), 2666.4 (6); (theoretical) 2662.5 (Y₂[(C₇F₇)₂PO₂]₅⁺, 100%), 2663.5 (78), 2664.5 (34), 2665.5 (9), 2666.5 (2)

m/z (SF-MALDI[-], observed) : 2076.7 (Y[(C₇F₇)₂PO₂]₄⁻, 100%), 2077.1 (11), 2077.7 (61), 2078.0 (5), 2078.7 (17); (theoretical) 2076.7 (Y[(C₇F₇)₂PO₂]₄⁻, 100%), 2077.7 (64), 2078.7 (22), 2079.7 (6)

m/z (SF-MALDI[-], observed) : 496.9 (C₁₄F₁₄PO₂⁻, 100%), 497.0 (4), 497.1 (15), 497.9 (20), 498.9 (2), 499.5 (1); (theoretical) 496.9 (C₂₄F₁₈PO₂⁻, 100%), 497.9 (15)

5.52 Preparation of yttrium(III) (nonafluorobiphenyl-4-yl)(pentafluorophenyl)phosphinate

Yttrium chloride hexahydrate (3 mg, 0.01 mmol) was dissolved in H₂O (1 mL) in a vial before a layer of pure H₂O (1 mL) was added to form a layer above it. A solution of (nonafluorobiphenyl-4-yl)(pentafluorophenyl)phosphinic acid (16 mg, 0.03 mmol) dissolved in Et₂O (1 mL) and MeOH (1 mL) was then added dropwise to the mixture in the vial and a very fine layer of precipitate formed immediately. After 3 days, the precipitate had grown to form a dense layer and it was filtered off. The white solid was washed with H₂O, Et₂O and MeOH and dried over P₂O₅ to give yttrium(III) (nonafluorobiphenyl-4-yl)(pentafluorophenyl)phosphinate (8 mg, 47%).



m.p. : >300 °C

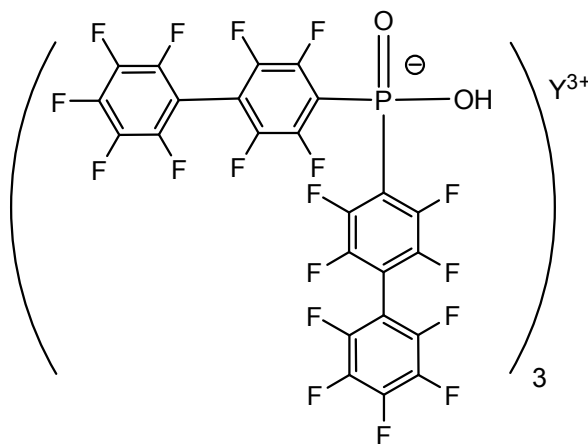
IR (KBr, ν_{\max} /cm⁻¹) : 1648, 1531, 1504, 1486, 1462, 1396, 1333, 1304, 1271, 1212, 1135, 1110, 1088, 1037, 1006, 984, 969

m/z (SF-MALDI[+], observed) : 2902.5 (Y₂(C₁₈F₁₄O₂P)₅⁺, 89%), 2903.5 (100), 2904.5 (42), 2905.5 (16), 2906.5 (7), 2907.1 (4), 2907.6 (6), 2908.9 (3), 2910.5 (8); (theoretical) 2902.5 (Y₂(C₁₈F₁₄O₂P)₅⁺, 99%), 2903.5 (100), 2904.5 (52), 2905.5 (19), 2906.5 (5)

m/z (SF-MALDI[-], observed) : 2268.7 (Y(C₁₈F₁₄O₂P)₄⁻, 100%), 2269.7 (79), 2270.7 (25), 2271.7 (24), 2272.7 (5); (theoretical) 2268.7 (Y(C₁₈F₁₄O₂P)₄⁻, 100%), 2269.7 (80), 2270.7 (34), 2271.7 (10), 2272.7 (2)

5.53 Preparation of yttrium(III) bis(nonafluorobiphenyl-4-yl)phosphinate

Yttrium chloride hexahydrate (3 mg, 0.01 mmol) was dissolved in H₂O (1 mL) in a vial before a layer of pure H₂O (1 mL) was added to form a layer above it. A solution of bis(nonafluorobiphenyl-4-yl)phosphinic acid (20.9 mg, 0.03 mmol) dissolved in Et₂O (1 mL) and MeOH (1 mL) was then added dropwise to the mixture in the vial and a very fine layer of precipitate formed immediately. After 3 days, the precipitate had grown to form a dense layer and it was filtered off. The white solid was washed with H₂O, Et₂O and MeOH and dried over P₂O₅ to give yttrium(III) bis(nonafluorobiphenyl-4-yl)phosphinate (7 mg, 33%).



m.p. : >300 °C

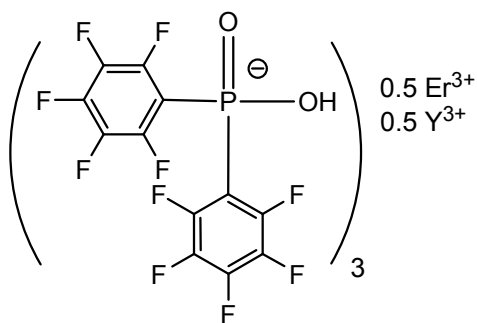
IR (KBr, ν_{\max} /cm⁻¹) : 1658, 1579, 1533, 1503, 1461, 1399, 1381, 1335, 1273, 1214, 1136, 1092, 1038, 1004, 968, 901

m/z (SF-MALDI[+], observed) : 3642.5 (Y₂(C₂₄F₁₈O₂P)₅⁺, 79%), 3643.5 (100), 3644.5 (77), 3645.5 (34), 3646.5 (19), 3647.5 (6) (theoretical) 3642.5 (Y₂(C₂₄F₁₈O₂P)₅⁺, 76%), 3643.5 (100), 3644.5 (69), 3645.5 (33), 3646.5 (13), 3647.5 (4)

m/z (SF-MALDI[-], observed) : 2860.6 (Y(C₂₄F₁₈O₂P)₄⁻, 100%), 2861.6 (95), 2862.6 (45), 2863.7 (19), 2864.2 (14) (theoretical) 2860.6 (Y(C₂₄F₁₈O₂P)₄⁻, 94%), 2861.6 (100), 2862.6 (57), 2863.7 (21), 2864.7 (7), 2865.7 (2)

5.54 Preparation of erbium (50%) yttrium (50%)(III) bis(pentafluorophenyl)phosphinate

Erbium chloride hexahydrate (2 mg, 0.005 mmol) was dissolved in H₂O (0.5 mL) in a vial before an aqueous solution of yttrium chloride hexahydrate (1.5 mg, 0.005 mmol) in H₂O (0.5 mL) was added. A layer of pure H₂O (1 mL) was added to form a layer above it. A solution of bis(pentafluorophenyl)phosphinic acid (11.9 mg, 0.03 mmol) dissolved in Et₂O (1 mL) and MeOH (1 mL) was then added dropwise to the mixture in the vial and a very fine layer of precipitate formed immediately. After 3 days, the precipitate had grown to form a dense layer and it was filtered off. The white solid was washed with H₂O, Et₂O and MeOH and dried over P₂O₅ to give erbium (50%) yttrium (50%)(III) bis(pentafluorophenyl)phosphinate (8 mg, 61%).



m.p. : >320 °C

IR (KBr, ν_{\max} /cm⁻¹) : 1649, 1526, 1490, 1477, 1392, 1305, 1203, 1110, 1083, 1033, 979

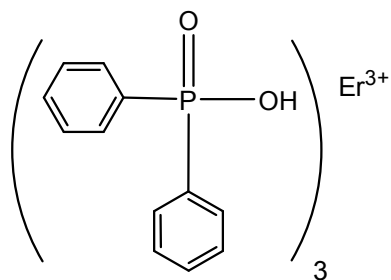
m/z (SF-MALDI[+], observed) : 2237.6 (YEr[(C₆F₅)₂PO₂]₅⁺, 4%), 2239.6 (60), 2240.6 (94), 2241.6 (100), 2242.6 (46), 2243.0 (4), 2243.6 (42), 2244.6 (25), 2245.6 (8), 2246.7 (4) (theoretical) 2237.6 (YEr[(C₆F₅)₂PO₂]₅⁺, 4%), 2238.6 (2), 2239.6 (68), 2240.6 (90), 2241.6 (100), 2242.6 (51), 2243.6 (46), 2244.6 (24), 2245.6 (8), 2246.6 (3)

m/z (SF-MALDI[+], observed) : 2314.6 (Er₂[(C₆F₅)₂PO₂]₅⁺, 4%), 2315.6 (3), 2316.6 (34), 2317.6 (68), 2318.6 (100), 2319.6 (97), 2320.6 (88), 2321.6 (68), 2322.6 (53), 2323.7 (20), 2324.6 (20), 2325.6 (6); (theoretical) 2314.6 (Er₂[(C₆F₅)₂PO₂]₅⁺, 4%), 2315.6 (5), 2316.6 (35), 2317.6 (64), 2318.6 (100), 2319.6 (88), 2320.6 (87), 2321.6 (63), 2322.6 (48), 2323.6 (22), 2324.6 (13), 2325.6 (6), 2326.6 (3)

m/z (SF-MALDI[-], observed) : 1676.7 (Y[(C₆F₅)₂PO₂]₄⁻, 100%), 1677.7 (48), 1678.7 (9); (theoretical) 1676.7 (Y[(C₆F₅)₂PO₂]₄⁻, 100%), 1677.7 (54), 1678.7 (16), 1679.7 (4)

m/z (SF-MALDI[-], observed) : 1753.7 (Er[(C₆F₅)₂PO₂]₄⁻, 72%), 1754.7 (83), 1755.7 (100), 1756.7 (34), 1757.7 (44), 1758.7 (16); (theoretical) 1751.7 (Er[(C₆F₅)₂PO₂]₄⁻, 4%), 1752.7 (2), 1753.7 (76), 1754.7 (92), 1755.7 (100), 1756.7 (43), 1757.7 (45), 1758.7 (21), 1759.7 (5), 1760.7 (1)

5.55 Preparation of erbium(III) diphenylphosphinate



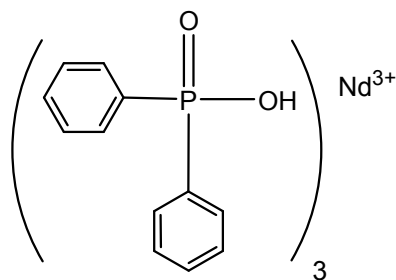
Erbium chloride hexahydrate (20 mg, 0.05 mmol) was dissolved in H₂O (1 mL) in a vial before a layer of pure H₂O (1 mL) was added to form a layer above it. A solution of diphenylphosphinic acid (34 mg, 0.16 mmol) dissolved in Et₂O (1 mL) and MeOH (1 mL) was then added dropwise to the mixture in the vial and a very fine layer of precipitate formed immediately. After 3 days, the precipitate had grown to form a dense layer and it was filtered off. The pink solid was washed with H₂O, Et₂O and MeOH and dried over P₂O₅ to give erbium(III) diphenylphosphinate (18.2 mg, 42%).

m.p. : >320 °C, Lit²² m.p. : >250 °C

IR (KBr, ν_{max} /cm⁻¹) : 3075, 3054, 3024, 3011, 1593, 1574, 1485, 1437, 1384, 1334, 1310, 1283, 1150, 1135, 1057, 1024, 998

Lit²² IR (KBr, ν_{max} /cm⁻¹) : 3380, 1620, 1155 – 1138, 1060

5.56 Preparation of neodymium(III) diphenylphosphinate



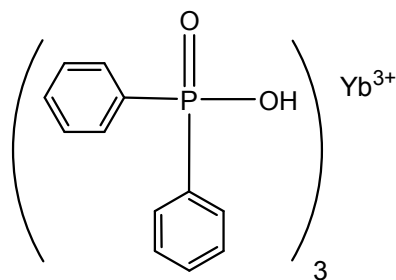
Neodymium chloride hexahydrate (13 mg, 0.05 mmol) was dissolved in H₂O (1 mL) in a vial before a layer of pure H₂O (1 mL) was added to form a layer above it. A solution of diphenylphosphinic acid (34 mg, 0.16 mmol) dissolved in Et₂O (1 mL) and MeOH (1 mL) was then added dropwise to the mixture in the vial and a very fine layer of precipitate formed immediately. After 3 days, the precipitate had grown to form a dense layer and it was filtered off. The pink solid was washed with H₂O, Et₂O and MeOH and dried over P₂O₅ to give neodymium(III) diphenylphosphinate (20 mg, 48%).

m.p. : >320 °C, Lit²² m.p. : >250 °C

IR (KBr, ν_{max} /cm⁻¹) : 3091, 3075, 3055, 3022, 3011, 1967, 1907, 1832, 1775, 1673, 1614, 1593, 1573, 1485, 1437, 1384, 1332, 1309, 1283, 1138, 1070, 1048, 1022, 997

Lit²² IR (KBr, ν_{max} /cm⁻¹) : 3380, 1620, 1137, 1050

5.57 Preparation of ytterbium(III) diphenylphosphinate



Ytterbium chloride hexahydrate (20.3 mg, 0.05 mmol) was dissolved in H₂O (1 mL) in a vial before a layer of pure H₂O (1 mL) was added to form a layer above it. A solution of diphenylphosphinic acid (34 mg, 0.16 mmol) dissolved in Et₂O (1 mL) and MeOH (1 mL) was then added dropwise to the mixture in the vial and a very fine layer of precipitate formed immediately. After 3 days, the precipitate had grown to form a dense layer and it was filtered off. The pink solid was washed with H₂O, Et₂O and MeOH and dried over P₂O₅ to give ytterbium(III) diphenylphosphinate (29 mg, 48%).

m.p. : >320 °C, Lit²² m.p. : >250 °C

IR (KBr, $\nu_{\text{max}}/\text{cm}^{-1}$) : 3075, 3054, 3024, 3011, 1967, 1908, 1832, 1774, 1742, 1676, 1654, 1593, 1574, 1485, 1437, 1384, 1333, 1311, 1284, 1153, 1059, 1024, 998

Lit²² IR (KBr, $\nu_{\text{max}}/\text{cm}^{-1}$) : 3400, 1620, 1158 - 1135, 1062

5.58 References for chapter 5

1. Wyatt; M. F., *EPSRC National Mass Spectrometry Service Centre Application Notes*, Swansea University, 5, **2008**
2. Danford; M. D., Burns; J. H., Higgins; C. E., Stokely Jr; J. R. and Baldwin; W. H., *Inorganic Chemistry*, 9, **1970**, 1953
3. Richardson; M. F., Wagner; W. F. and Sands; D. E., *Journal of Inorganic and Nuclear Chemistry*, 30, **1968**, 1968
4. Ogoshi; H. and Nakamoto; K., *Journal of Chemical Physics*, 45, **1996**, 3113
5. Zhu; S. Z., Xu; B. and Zhang; J., *Journal of Fluorine Chemistry* 74, **1995**, 167
6. Felix; C., Laurent; A. and Mison; P., *Journal of Fluorine Chemistry*, 70, **1995**, 71
7. Baker; K. V., Brown; J. M., Hughes; N., Skarnulis; A. J. and Sexton; A., *Journal of Organic Chemistry*, 56, **1991**, 698
8. Herkes; F. E. and Burton; D. J., *Journal of Organic Chemistry*, 32, **1967**, 1311
9. Birchall; J. M. and Haszeldine; R. N., *Journal of Chemical Society*, **1961**, 3719
10. Krafczyk; R., Thönnessen; H., Jones; P. G. and Schmutzler; R., *Journal of Fluorine Chemistry*, 83, **1997**, 159
11. Bégué; J-P., Bonnet-Delpon; D., Bouvet; D and Rock. M. H., *Journal of Chemical Society, Perkin Transactions*, 1, **1998**, 1797

12. Grayson; M. and Keough; P. T., *Journal of the American Chemical Society*, 82, **1960**, 3919
13. Filler; R. and Heffern; E. W., *Journal of Organic Chemistry*, 32, **1967**, 3249
14. Joullie; M. M., *Journal of American Chemical Society*, 77, **1955**, 6662
15. Bégué; J-P. and Mesureur ; D, *Synthesis*, 4, **1989**, 309
16. Jiang; Y., Wu; N., Wu; H. and He; M., *Synlett*, 18, **2005**, 2731
17. Barton; D. H. R., Blazejewski; J-C, Charpiot; B., Finet; J-P. and Motherwell; W. B., *Journal of the Chemical Society, Perkin Transactions 1*, **1985**, 2667
18. Wall; L. A., Donadio; R. E. and Pummer; W. J., *Journal of the American Chemical Society*, 82, **1960**, 4846
19. Oliver; K. W., Rettig; S. J., Thompson; R. C., Trotter; J. and Xia; S., *Journal of Fluorine Chemistry*, 83, **1997**, 47
20. Pearson; J., *MSc in Chemical Research thesis, QMUL*, **2007**
21. Grison; C., Comoy; C., Chatenet; D. and Coutrot; P., *Journal of Organometallic Chemistry*, 662, **2002**, 83
22. Dunstan; P. O. and Vicentini; G., *Anais da Academia Brasileira de Ciências*, 47, **1975**, 97

Chapter 6 – Conclusions and future work

6.1 Conclusion

This thesis has presented the developments of organic Ln^{3+} complexes for use as optical amplifying materials in integrated optical devices. We began by studying Ln^{3+} HFA complexes and observed an improvement in the luminescence lifetimes when H_2O or solvent molecules were excluded in the coordination sphere. O–H and C–H bonds have high vibrational energy and they are present in the HFA ligand. By deuterating the Ln^{3+} HFA complexes, improvements of at least 150% were observed for these complexes. By partially deuterating the Er^{3+} samples, we deduced that the rapid luminescence quenching is strongly dependent on the immediate local environment with only a secondary effect due to more distant C–H oscillators. This set of results contradicts the continuous medium approximation model adopted by Quochi *et al.*¹ For Nd^{3+} and Yb^{3+} ions, we observed single exponential decay for the anhydrous ions at all deuteration levels and the rate constant for quenching was found to vary linearly with deuteration levels. We were also the first to quantify the detrimental effects of hydrogen and from our studies, we have shown that any hydrogen within ~ 20 Å away will effectively quench the luminescence lifetime. Even when the hydrogen is ~ 20 Å away, the obtained lifetime of 100 μs lifetime is not sufficient to develop useful telecommunication devices and that warranted the need to synthesize fully halogenated molecules.

Our quest to obtain fully halogenated Ln^{3+} complexes began when we first reacted pentafluorobenzoic acid with erbium(III) chloride in a 4:1 ligand to Ln^{3+} ratio. The results are consistent with those of Roh *et al.*² where 3 : 1 tris complexes were obtained. Single X-ray diffraction revealed the formation of erbium(III) pentafluorobenzoate pentahydrate. Proceeding that, we prepared and characterized a novel β -diketone, 3-[(4-methoxyphenyl)(pentafluorophenylsulfanyl) methyl] -1,1,1,5,5,5-hexafluoro-pentane-2,4-dione) but unfortunately, we were unable to characterize any erbium complexes derived from this partially fluorinated ligand. Three methodologies (Grignard chemistry, Wittig chemistry and some experiments involving catalytic arylation of diketones) were adopted to prepare 1,1,1,5,5,5-hexafluoro-3(pentafluorophenyl)pentane-2,4-dione.

None of these experiments led to the desired β -diketone and this was attributed to the electron withdrawing nature of the CF_3 groups. In the course of these experiments, we observed an unexpected reductive defluorination, at position 4, in the copper catalyzed arylation of 2,5-pentanedione by iodopentafluorobenzene.

In the final results and discussions chapter (Chapter 4), we synthesized four fully fluorinated organic ligands and upon chelating each ligand to the three Ln^{3+} ions under investigation, the fluorinated complexes demonstrated lifetimes of at least an order of magnitude higher than their non fluorinated analogues. Concentration quenching^{3,4,5} is a well known phenomenon which decreases the luminescence efficiency and we overcame that by diluting the Ln^{3+} samples with Y^{3+} . Effectively, that increases the interionic distance between the emitting centres and we saw that for all the Er^{3+} , Nd^{3+} and Yb^{3+} samples, the luminescence lifetimes increase with decreasing Ln^{3+} concentrations.

This thesis has presented the detrimental effects of high vibrational oscillators and high concentration of emitting ions towards luminescence quenching. We have shown that fluorination and dilution have significantly improved the quantum efficiencies. Due to the insolubility of these fully fluorinated phosphonate complexes, we were not able to obtain any crystal structures. Any future work should be directed towards improving the solubility of these complexes to obtain useful crystallography data and the solubility would also allow these complexes to be processed as useful devices. More work should also be focused on obtaining fully fluorinated β -diketonate complexes with chromophores. It would also be interesting to synthesize Ln^{3+} complexes with fully fluorinated ligands such as phthalocyanines and quinolines. It has been reported that phthalocyanines⁷ form stable sandwich complexes and due to their bulkiness, emitting centers can be kept apart whilst maintaining an optimal level of ion concentration. Similar to the phthalocyanines, quinolines have a high degree of conjugation and that might allow the ligands to absorb in the near UV wavelengths and hence providing an efficient sensitization pathway.

6.2 References for chapter 6

1. Quochi; F., Orru; R., Cordella; F., Mura; A., Bongiovanni; G., Artzsu; F., Deplano; P., Mercuri; M. L., Pilia; L. and Serpe; A., *Journal of Applied Physics*, 99, **2006**, 053520
2. Roh; S-G., Oh; J. B., Nah; M-K., Baek; N. S., Lee; Y. and Kim; H. K., *Bulletin of the Korean Chemical Society*, 25, **2004**, 1503
3. Ainslie; B. J., *Journal of Lightwave Technology*, 9, **1991**, 220
4. Ainslie; B. J., Craig; S. P. and Davey; S. T., *Material Letters*, 5, **1987**, 143
5. Ainslie; B. J., Craig; S. P., Davey; S. T. and Wakefield; B., *Material Letters*, 6, **1988**, 139
6. Xu; X., Zhao; Z., Song; P., Jiang; B., Zhou; G., Xu; J., Deng; P., Bourdet; G., Chanteloup; J. C., Zou; J. and Fulop; A., *Physica B*, 357, **2005**, 365
7. Kimura; T, Kumasaka; J. and Namauo; T., *European Journal of Organic Chemistry*, 30, **2008**, 5079

Abbreviations

6FDA	2, 2'-Bis(3, 4- dicarboxyphenyl)hexafluoropropane
AIQ	Tris(8-hydroxyquinolino)-aluminum(III)
Al ₂ O ₃	Aluminium oxide
BA	1-Benzoylacetone
BaO	Barium oxide
Bp	Boiling point
BPM	2,2'-Bipyrimidine
BPTZ	Bis-bidentate bridging ligand 3,6-bis(2-pyridyl)tetrazine
BTFA	4,4,4-Trifluoro-1-phenyl-1,3-butanedione
C ₆ F ₅ SH	Pentafluorothiophenol
CDCl ₃	Deuterated chloroform
CD ₃ OD	Deuterated Methanol (4 deuteriums)
CD ₃ OH	Deuterated Methanol (3 deuteriums)
Ce	Cerium
CF ₃ CO ₂ CH ₂ CH ₃	Ethyl trifluoroacetate
(CH ₃ CH ₂) ₂ O·BF ₃	Boron trifluoride diethyl ether
CH ₂ Cl ₂	Dichloromethane
CH ₃ COCH ₃	Acetone
(CH ₃ CO) ₂ O	Acetic anhydride
CH ₃ OD	Deuterated Methanol (1 deuterium)
CH ₃ OH	Methanol
CHCl ₃	Chloroform
Cl	Chloride
ClO ₄	Perchlorate
Cs ₂ CO ₃	Caesium carbonate
Cs	Caesium
Cu	Copper
D ₂ O	Deuterated water
DBM	Dibenzoylmethane
DCM	Dichloromethane
DMF	Dimethylformamide
DMSO	Dimethyl sulfoxide
DMSO- <i>d</i> ₆	Deuterated dimethyl sulfoxide
DPP	2,3-Bis(2-pyridyl)pyrazine
DTPA	Diethylenetriaminepentaacetic acid
EDFA	Erbium-Doped Fiber Amplifier
EDWA	Erbium-Doped Waveguide Amplifiers
EDX	Energy dispersive X-ray
EI	Electron impact
Er	Erbium
Er ₂ O ₃	Erbium oxide
ErQ	Erbium(III) tris(8-hydroxyquinolate)
ESA	Excited state absorption
ESI	Electron spray ionization

Et ₂ O	Diethyl ether
ET	Energy transfer
EtOAc	Ethyl acetate
Eu	Europium
Gd	Gadolinium
H ₂ O	Water
HCl	Hydrochloric acid
HFA	1,1,1,5,5,5-Hexafluoroacetylacetone
HFA- <i>d</i>	1,1,1,5,5,5-Hexafluoroacetylacetone (deuterated)
HF-tpip	Tetrakis(pentafluorophenyl)imidodiphosphinate
Hg	Mercury
IO	Integrated Optics
IR	Infrared
Ir	Iridium
ISC	Intersystem crossing
K ₂ CO ₃	Potassium carbonate
K	Rate constant
K ₂ O	Potassium oxide
KBr	Potassium bromide
KOH	Potassium hydroxide
L	Ligand
LED	Light-emitting diode
LMCT	Ligand-to-Metal charge transfer
Ln	Lanthanide
<i>m/e</i>	Mass/charge ratio
M	Molar concentration
MALDI	Matrix-assisted laser desorption/ionization
MCVD	Modified chemical vapour deposition
MeCN	Acetonitrile
MeOH	Methanol
Mg	Magnesium
MgSO ₄	Magnesium sulfate
MLCT	Metal-to-Ligand charge transfer
mm	Millimetres
MOCVD	Metal-organic chemical vapour deposition
Mol	Mole (chemistry)
Mp	Melting point
N ₂	Nitrogen
Na	Sodium
Na ₂ O	Sodium oxide
Na ₂ SO ₄	Sodium sulfate
NaCl	Sodium chloride
NaH	Sodium hydride
Nd	Neodymium

Nd:YAG	Neodymium-doped yttrium aluminium garnet
NIR	Near-Infrared
NMR	Nuclear Magnetic Resonance
NO ₃	Nitrate
OAc	Acetate
OPO	Optical parametric oscillator
Os	Osmium
P ₂ O ₅	Phosphorus pentoxide
PL	Photoluminescence
PMDA	Pyromellitic dianhydride
PMMA	Poly(methyl methacrylate)
PMT	Photomultiplier tube
Pt	Platinum
Q	Quantum yield
RE	Rare earth
Re	Rhenium
Ru	Ruthenium
SEM	Scanning Electron Microscope
SF	Solvent free
SiO ₂	Silicon dioxide
SM	Samarium
τ	Lifetime
Tb	Terbium
TFDB	2, 2'-Bis(trifluoromethyl)-4, 4'-diaminobiphenyl
THF	Tetrahydrofuran
TLC	Thin layer chromatography
Tm	Thulium
TTA	Thenoyl(trifluoro)acetone
TOF	Time of flight
TPTZ	2,4,6-Tri(2-pyridyl)-1,3,5-triazine
UC	Upconversion
UV	Ultraviolet
WDM	Wavelength division multiplexing
Xe	Xenon
XRD	X-ray diffraction
Yb	Ytterbium
Yb ₂ O ₃	Ytterbium oxide

Appendix A

XRD data for the anion [Er(HFA)₄]⁻ in the Cs⁺ salt

Crystal data and structure refinement.

Empirical formula	C ₂₀ H ₄ Cs Er F ₂₄ O ₈
Formula weight	1128.40
Temperature	160(2) K
Wavelength	0.71073 Å
Crystal system	Orthorhombic
Space group	P bcn
Unit cell dimensions	a = 8.534(3) Å α = 90°. b = 21.189(5) Å β = 90°. c = 17.251(8) Å γ = 90°.
Volume	3119(2) Å ³
Z	4
Density (calculated)	2.403 Mg/m ³
Absorption coefficient	4.027 mm ⁻¹
F(000)	2108
Crystal size	0.30 x 0.17 x 0.10 mm ³
Theta range for data collection	2.26 to 25.48°.
Index ranges	-4 ≤ h ≤ 10, -2 ≤ k ≤ 25, 0 ≤ l ≤ 20
Reflections collected	3057
Independent reflections	2890 [R(int) = 0.0102]
Completeness to theta = 25.48°	99.5 %
Max. and min. transmission	0.6889 and 0.3779
Refinement method	Full-matrix least-squares on F ²
Data / restraints / parameters	2890 / 0 / 245
Goodness-of-fit on F ²	0.970
Final R indices [I > 2σ(I)]	R1 = 0.0430, wR2 = 0.1044
R indices (all data)	R1 = 0.1010, wR2 = 0.1288
Largest diff. peak and hole	1.191 and -1.301 e.Å ⁻³

XRD data for [Er(HFA)₃(H₂O)₂]

Crystal data and structure refinement.

Empirical formula	C ₁₅ H ₇ Er F ₁₈ O ₈
Formula weight	824.47
Temperature	120(2) K
Wavelength	0.71073 Å
Crystal system	Triclinic
Space group	P-1
Unit cell dimensions	a = 9.90590(10) Å α = 67.9090(10)°. b = 11.5257(2) Å β = 73.7910(10)°. c = 12.3039(2) Å γ = 76.0860(10)°.
Volume	1235.32(3) Å ³
Z	2
Density (calculated)	2.217 Mg/m ³
Absorption coefficient	3.572 mm ⁻¹
F(000)	782
Crystal size	0.12 x 0.07 x 0.03 mm ³
Theta range for data collection	3.07 to 27.56°.
Index ranges	-12<=h<=12, -14<=k<=14, -15<=l<=15
Reflections collected	27543
Independent reflections	5641 [R(int) = 0.0382]
Completeness to theta = 27.56°	99.1 %
Max. and min. transmission	0.9004 and 0.6738
Refinement method	Full-matrix least-squares on F ²
Data / restraints / parameters	5641 / 4 / 396
Goodness-of-fit on F ²	1.073
Final R indices [I>2sigma(I)]	R1 = 0.0265, wR2 = 0.0670
R indices (all data)	R1 = 0.0276, wR2 = 0.0678
Extinction coefficient	0.0016(5)
Largest diff. peak and hole	1.335 and -0.928 e.Å ⁻³

XRD data for [Er(C₆F₅CO₂)₃(H₂O)₅]

Crystal data and structure refinement.

Empirical formula	C ₂₁ H ₁₂ Er F ₁₅ O ₁₂
Formula weight	908.57
Temperature	120(2) K
Wavelength	0.71073 Å
Crystal system	Triclinic
Space group	P 1
Unit cell dimensions	a = 7.4873(3) Å α = 87.927(2)°. b = 9.6844(4) Å β = 82.361(2)°. c = 18.6136(7) Å γ = 79.274(2)°.
Volume	1314.23(9) Å ³
Z	2
Density (calculated)	2.296 Mg/m ³
Absorption coefficient	3.365 mm ⁻¹
F(000)	874
Crystal size	0.14 x 0.09 x 0.02 mm ³
Theta range for data collection	3.06 to 27.68°.
Index ranges	-9<=h<=9, -12<=k<=11, -24<=l<=24
Reflections collected	19199
Independent reflections	6010 [R(int) = 0.0480]
Completeness to theta = 27.68°	97.6 %
Absorption correction	Semi-empirical from equivalents
Max. and min. transmission	0.9358 and 0.6502
Refinement method	Full-matrix least-squares on F ²
Data / restraints / parameters	6010 / 3 / 490
Goodness-of-fit on F ²	1.102
Final R indices [I>2sigma(I)]	R1 = 0.0393, wR2 = 0.0780
R indices (all data)	R1 = 0.0467, wR2 = 0.0816
Largest diff. peak and hole	1.090 and -0.846 e.Å ⁻³

XRD data for 1-[(2,3,5,6,3',6',2'',3'',5'',6''-decafluoro-4,5',4''-tris-trifluoromethyl-[1,1';4',1'']terphenyl-2'-yl)-(2,3,5,6-tetrafluoro-4-trifluoromethyl-phenyl)-phosphinoyl]piperidine

Crystal data and structure refinement.

Empirical formula	C ₃₃ H ₁₀ F ₂₆ N O P
Formula weight	961.39
Temperature	120(2) K
Wavelength	0.71073 Å
Crystal system	Monoclinic
Space group	P 2 ₁ /c
Unit cell dimensions	a = 12.6809(4) Å α = 90°. b = 12.4939(4) Å β = 104.634(2)°. c = 21.6979(7) Å γ = 90°.
Volume	3326.16(18) Å ³
Z	4
Density (calculated)	1.920 Mg/m ³
Absorption coefficient	0.263 mm ⁻¹
F(000)	1888
Crystal size	0.22 x 0.03 x 0.02 mm ³
Theta range for data collection	3.26 to 27.60°.
Index ranges	-16 ≤ h ≤ 16, -16 ≤ k ≤ 16, -27 ≤ l ≤ 28
Reflections collected	31395
Independent reflections	7580 [R(int) = 0.0728]
Completeness to theta = 27.60°	98.1 %
Max. and min. transmission	0.9948 and 0.9444
Refinement method	Full-matrix least-squares on F ²
Data / restraints / parameters	7580 / 0 / 569
Goodness-of-fit on F ²	1.154
Final R indices [I > 2σ(I)]	R1 = 0.0748, wR2 = 0.1129
R indices (all data)	R1 = 0.1427, wR2 = 0.1382
Largest diff. peak and hole	0.505 and -0.438 e.Å ⁻³